ISSN 1451 - 9372 (Print)
ISSN 2217 - 7434 (Online)
JANUARY-MARCH 2024
Vol.30, Number 1, 1-88

Chemical Industry & Chemical Engineering Quarterly

The AChE Journal for Chemical Engineering,
Biochemical Engineering, Chemical Technology,
New Materials, Renewable Energy and Chemistry
www.ache.org.rs/ciceq

Journal of the
Association of Chemical Engineers of
Serbia, Belgrade, Serbia

Chemical Industry & Chemical Engineering
CI&CEQuarterly

Journal of the
Association of Chemical Engineers of
Serbia, Belgrade, Serbia

Chemical Industry & Chemical Engineering Quarterly

Vol. 30 Belgrade, January-March 2024 No. 1

Chemical Industry & Chemical Engineering Quarterly (ISSN 1451-9372) is published quarterly by the Association of Chemical Engineers of Serbia, Kneza Miloša 9/I, 11000 Belgrade, Serbia

Editor:
Vlada B. Veljković
veljkovic@yahoo.com

Editorial Office:
Kneza Miloša 9/I, 11000 Belgrade, Serbia
Phone/Fax: +381 (0)11 3240 018
E-mail: shi@ache.org.rs
www.ache.org.rs

For publisher:
Ivana T. Drvenica

Secretary of the Editorial Office:
Slavica Desnica

Marketing and advertising:
AChE Marketing Office
Kneza Miloša 9/I, 11000 Belgrade, Serbia
Phone/Fax: +381 (0)11 3240 018

Publication of this Journal is supported by the Ministry of Education, Science and Technological Development of the Republic of Serbia

Subscription and advertisements make payable to the account of the Association of Chemical Engineers of Serbia, Belgrade, No. 205-2172-71, Komercijalna banka a.d., Beograd

Computer typeface and paging:
Marija B. Tasić

Journal manager:
Aleksandar B. Dekanski

Printed by:
Faculty of Technology and Metallurgy, Research and Development Centre of Printing Technology, Karnegijeva 4, P.O. Box 3503, 11120 Belgrade, Serbia

Abstracting/Indexing:
Articles published in this Journal are indexed in *Thompson Reuters* products: *Science Citation Index - Expanded*™ - access *via Web of Science*®, part of *ISI Web of Knowledge*℠

CONTENTS

The activities of the Association of Chemical Engineers of Serbia are supported by:

MINISTRY OF SCIENCE, TECHNOLOGICAL DEVELOPMENT AND INNOVATION OF REPUBLIC OF SERBIA

Faculty of Technology and Metallurgy, University of Belgrade

Faculty of Science, University of Novi Sad

Institute for Technology of Nuclear and Other Mineral Raw Materials, Bekgrade

Faculty of Technology, University of Novi Sad

Institute of Chemistry, Technology and Metallurgy, University of Belgrade

Faculty of Technical Sciences University of Novi Sad

Faculty of Technology, University of Niš, Leskovac

Faculty of Technical Sciences, University of Priština, Kosovska Mitrovica

IMS Institute, Belgrade

DCP HEMIGAL
Leskovac

Elixir Prahovo

CI&CEQ
Chemical Industry & Chemical Engineering Quarterly

Available online at
Association of the Chemical Engineers of Serbia AChE
www.ache.org.rs/CICEQ

Chem. Ind. Chem. Eng. Q. 30 (1) 1–10 (2024) CI&CEQ

SEMA AKYALCIN[1]
LEVENT AKYALCIN[1]
MORTEN BJØRGEN[2]

CATALYTIC PERFORMANCE OF DESILICATED HZSM-12 FOR BENZYLATION REACTION OF BENZENE WITH BENZYL ALCOHOL

[1]Department of Chemical Engineering, Faculty of Engineering, Eskisehir Technical University, Eskisehir, Turkey

[2]Department of Life Sciences and Health, Faculty of Health Sciences, Oslo Metropolitan University, Oslo, Norway

SCIENTIFIC PAPER

UDC 547:66:549.67

Article Highlights

- In the benzylation reaction, desilicated HZSM-12 showed better catalytic activity than HZSM-12
- The effects of reaction parameters were investigated
- The organic species deposited on the catalyst decreased the activity of the desilicated HZSM-12

Abstract

The catalytic production of diphenylmethane from the reaction of benzene with benzyl alcohol was investigated using HZSM-12 and desilicated HZSM-12 that was obtained by treating ZSM-12 with 0.2M NaOH solution at 85 °C for 60 min. The untreated and alkaline treated ZSM-12 zeolites were characterized by X-ray diffraction, nitrogen adsorption/desorption isotherms, scanning electron microscopy, inductively coupled plasma optical emission spectrometry, and temperature-programmed desorption of ammonia. The desilicated HZSM-12 showed promising catalytic performance with benzyl alcohol conversion of 100% and the selectivity to diphenylmethane of 74% and 87% in 4 h and 8 h reaction time, respectively. The reaction parameters affecting benzyl alcohol conversion and product distribution were also presented. The activities of fresh and regenerated catalysts were compared, and characterization results indicated that the occluded organic molecules decreased the number of acidic sites of the catalyst after the reaction and regeneration.

Keywords: benzyl alcohol, benzylation, catalyst deactivation, desilication, diphenylmethane, ZSM-12.

The benzylated aromatics are produced via the reaction of benzene (B) with benzyl alcohol (BA) or benzyl chloride [1,2]. An essential chemical compound obtained from the benzylation of benzene is diphenylmethane (DPM), and it is used as a fixative and a scenting soap in the fragrance industry, a plasticizer for dyes, and a synergist in some insecticides [2,3]. DPM is also employed to improve the thermal stability of polyester and the stability and lubricating properties of jet fuels [2,3]. During the synthesis of DPM, using less reactive benzyl alcohol instead of benzyl chloride as a benzylation agent is an eco-friendly process since the formation of HCl as a by-product is avoided [4]. The benzylation reaction pathway in the presence of the catalyst [1] is given in Figure 1.

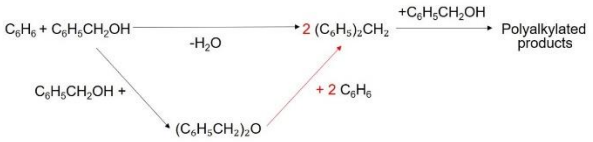

Figure 1. Benzylation reaction pathway of benzene with benzyl alcohol.

The benzylation reaction also forms dibenzyl ether (DBE) and polyalkylated products (PAB). Therefore, choosing the proper catalyst for the reaction is

Correspondence: S. Akyalcin, Department of Chemical Engineering, Eskisehir Technical University, 26555, Eskisehir, Turkey.
E-mail: sdogruel@eskisehir.edu.tr
Paper received: 20 June, 2022
Paper revised: 23 February, 2023
Paper accepted: 17 March, 2023

https://doi.org/10.2298/CICEQ220620006A

essential, which maximizes the selectivity of the desired monobenzylated aromatics. Additionally, benzyl alcohol usage instead of benzyl chloride requires a stronger acid catalyst having good catalytic activity [2,4].

Benzylation reactions are generally performed in the presence of homogeneous acid catalysts such as $AlCl_3$, $FeCl_3$, and H_2SO_4 [5]. These catalysts cause several problems: difficulty separating and recovering the catalyst and corrosion problems. Therefore, replacing these homogeneous catalysts with heterogeneous catalysts is highly desirable.

In benzylation reactions, zeolites such as H-Beta, Mordenite, HY, and HZSM-5 are used as heterogeneous catalysts due to their strong acidity, large surface area, and stable porous structure [2,6–9]. However, the catalytic performance of zeolites can be limited because of their microporous channel structure. The reduction of particle size from the micrometer to the nanometer scale and the formation of mesopores in zeolite by post-synthesis treatments improve accessibility and molecular transport in catalysis [10,11]. Among the post-synthesis treatment, desilication is a widely applied preparation method to prepare mesoporous zeolites due to the combination of efficiency and simplicity [11,12].

Leng *et al.* [1] prepared hierarchical mordenites using a sequential post-treatment method based on a commercial mordenite with a Si/Al molar ratio of 15. They report that acid-base-acid-leached mordenite exhibited the highest catalytic activity, with a BA conversion of 99.6%, compared to untreated mordenite (BA conversion of 6.1%), acid-leached mordenite (BA conversion of 40.2%), and acid-base-leached mordenite (BA conversion of 28.8%) under the same reaction conditions in the benzylation of benzene with benzyl alcohol [1]. They stated that the enhanced catalytic performance was attributed to more accessible acid sites and much better mass transfer ability from rich mesoporosity in acid-base-acid-leached mordenite [1]. Wang *et al.* [6] prepared the hierarchical Beta by base treatment of a commercial Beta with a Si/Al molar ratio of 12.5. They report that the desilicated catalyst exhibited much poorer catalytic activity than the untreated catalyst due to the significant loss of total acidity [6]. They state that the subsequent acid treatment after desilication can significantly recover zeolite Beta's acidity and improve the desilicated Beta's catalytic performance in some acid-catalytic reactions [6]. Wang *et al.* [13] synthesized mesoporous aluminosilicates (ZM) by assembling zeolitic subunits obtained by the controllable desilication of nano-sized ZSM-5 zeolite particles in Na_2SiO_3 aqueous solution, with cetyltrimethylammonium bromide (CTAB) as the template. They report that ZM possessed a mesoporous structure similar to MCM-41, and ZSM-5 subunits were present in the pore walls [13]. They state that HZM exhibited much higher catalytic activity with a BA conversion of 78% than HAl-MCM-41 (BA conversion of 21%) and HZSM-5 (BA conversion of 8%) in 10 h reaction time under the same reaction conditions in the liquid phase benzylation of benzene with benzyl alcohol [13]. Candu *et al.* [2] investigated the liquid phase benzylation of benzene to diphenylmethane over various catalysts (mordenite and beta zeolites with Si/Al of 10.8 and 35.8). They report that the observed difference in the BA conversion for Beta zeolite (Si/Al=10.8) and mordenite (Si/Al=10.0), whose Si/Al molar ratio is close to each other, is quite low (48.4% for Beta zeolite versus 44.5% for mordenite) while the selectivity to DPM was 30.9% for Beta zeolite and 3.1% for mordenite. However, the BA conversion on Beta zeolite (Si/Al = 35.8) was almost 66% with 22% DPM selectivity. They stated that both the activity and selectivity were affected by the Si/Al molar ratio for both zeolites, and a higher Si/Al molar ratio was found to allow an increased benzyl alcohol conversion. The conversion of BA and product distribution largely depends on the zeolite nature and the experimental conditions [2].

ZSM-12 zeolite is a desirable catalyst for the petrochemical industry, including alkylation of benzene with propene [14], disproportionation of alkyl aromatic hydrocarbons [15], cracking, hydrocracking [16], isomerization reactions [17], and other petroleum refining processes [16]. ZSM-12 can potentially apply in catalysis due to their unidirectional twelve-membered ring linear channel system and strong acidic character [18]. Akyalcin *et al.* [19] prepared the mesoporous ZSM-12 samples by desilication of ZSM-12 under various NaOH concentrations (0.2 M, 0.4 M, and 0.6 M) at different temperatures (35 °C, 65 °C, and 85 °C) and treatment times (15 min, 30 min, and 60 min), and Taguchi's design of experiment was applied to investigate the influence of desilication parameters. They report that the zeolite treated with 0.2 M NaOH at 85 °C for 60 min shows higher catalytic activity than the other desilicated samples in the benzylation of benzene to diphenylmethane under constant reaction conditions [19].

This study assessed the catalytic performances of HZSM-12 and desilicated HZSM-12 in the benzylation reaction of benzene with environmentally friendly benzyl alcohol as an alkylating agent. The effects of reaction temperature, catalyst loading, and benzene to benzyl alcohol molar ratio on conversion and the selectivity of DPM, DBE, and PAB were determined. Additionally, the reusability of the desilicated HZSM-12

was tested. XRD and NH_3-TPD characterized the fresh, spent, and regenerated samples to evaluate the impact of deactivation and regeneration on the properties of the catalyst.

MATERIAL AND METHODS

Catalyst synthesis

ZSM-12 was hydrothermally synthesized with LUDOX HS-40 colloidal silica (40 wt.%, Sigma Aldrich), sodium aluminum oxide (Sigma Aldrich, technical grade), tetraethylammonium hydroxide (TEAOH, 35 wt.%, Aldrich), and deionized water according to the method proposed by Gopal *et al.* [20] and Hou *et al.* [21]. The gel prepared with the composition of Na_2O: Al_2O_3: 80 SiO_2:12.7 TEAOH: 1040 H_2O was transferred into a 125 mL Parr Teflon lined autoclave, and the zeolite was crystallized at 160 °C for 5.5 days. Thus, the solid product was filtered, washed with deionized water, and dried at 100 °C overnight. The as-synthesized zeolite was calcined in static air at 520 °C for four hours to remove the template.

The calcined zeolite was treated in 0.2 M NaOH solution (in the proportion of 20 mL/g) at 85 °C for 60 minutes, and then it was filtered, washed with deionized water, and dried overnight at room temperature. After that, the zeolite samples (ZSM-12 and desilicated ZSM-12) were ion exchanged three times with a fresh 1 M NH_4NO_3 (in the proportion of 20 mL/g) for two hours at 75 °C, followed by calcination at 520 °C for four hours. The final H-form of ZSM-12 and desilicated ZSM-12 were labeled as HZSM-12 and desilicated HZSM-12.

Catalyst characterization

The X-ray powder diffraction (XRD) patterns of the samples were collected on a Rigaku MiniFlex 600 Diffractometer using a CuKα X-ray source (40 kV, 15 mA). The XRD analysis was carried out from 5° to 40° 2θ at a scanning rate of 1.2°/min.

Nitrogen adsorption/desorption isotherms were measured at 77 K on a Quantachrome Autosorb IQ-MP-XR instrument to determine the textural properties of the samples. The samples were outgassed in a vacuum at 200 °C for four hours before measurements.

The elemental compositions of the catalysts were determined by inductively coupled plasma optical emission spectrometry (ICP-OES) in a Perkin-Elmer Optima 4300DV device.

Scanning electron microscope (SEM) images of the samples coated with a gold layer were obtained using Zeiss Supra 50 VP microscope.

The acidic behavior of the samples was determined by NH_3-TPD measurements, which were accomplished on a Quantachrome Autosorb IQ-Chemi-XR instrument. For the analysis, the sample was pre-treated in helium flow at 500°C for two hours to remove moisture. The sample was then cooled to 100 °C and saturated with pure ammonia flow for 30 min. After the adsorption, physisorbed ammonia was purged using helium flow at 100 °C for 60 min. Finally, the NH_3-TPD profile was recorded under helium flow (30 mL/min) by heating the sample from 100 °C to 600 °C at a ramp rate of 10 °C/min.

The thermogravimetric analyses (TGA) of the fresh and spent catalysts were conducted on a Perkin Elmer STA 6000 instrument heated from 30 °C to 900 °C (10 °C/min) under airflow (50 mL/min).

Catalytic activity test

Under solvent-free conditions, the benzylation reaction was performed in a laboratory-scale reactor described previously [19,22]. The experiments were conducted at different reaction temperatures of 60 °C–80 °C, catalyst loading of 0 mg/mL–4.9 mg/mL, and benzene to benzyl alcohol molar ratio of 21/1 to 98/1. In a typical experiment, benzene was placed in the reactor, heated, and magnetically stirred. When benzene reached the desired temperature, a fresh catalyst and benzyl alcohol (BA) were added to the reactor. Then the first sample was taken from the reactor to determine the initial composition of the reaction mixture. The samples taken at different time intervals from the reactor were put into the centrifuge tubes in an ice bath and then centrifuged to separate the catalyst from the samples. The samples were analyzed using Agilent HP 7890 gas chromatography, equipped with FID and HP-5 column. The following temperature program was employed: isothermal at 50 °C for 2 min, heating at 20 °C/min to 250 °C, and isothermal at 250 °C for 6 min. Quantification of B, BA, DPM, and DBE was done using the internal standard calibration method. The amount of PAB was calculated using reaction stoichiometry (Figure 1). The product selectivity was determined as the moles of product formed divided by the moles of benzyl alcohol reacted.

RESULTS AND DISCUSSION

Catalyst characterization

The XRD patterns of HZSM-12 and desilicated HZSM-12 samples are shown in Figure 2. All of the peaks observed at 7.4°, 8.8°, 20.8°, and 23.1° of 2θ are attributed to the phases of the ZSM-12 zeolite [16,19–21].

XRD peak positions of the desilicated HZSM-12 are very close to that of HZSM-12. Figure 2 shows that

although the crystal structure of the sample is preserved after alkali treatment, the peak intensities of the desilicated HZSM-12 decrease slightly due to the removal of Si from the zeolite framework, in accord with Wei and Smirniotis [23].

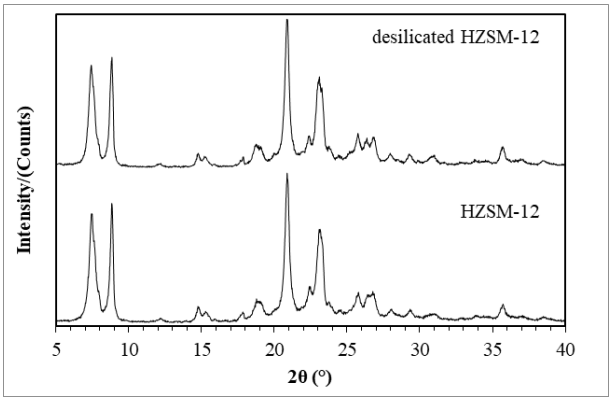

Figure 2. XRD patterns of HZSM-12 and desilicated HZSM-12.

The SEM images for HZSM-12 and desilicated HZSM-12 are shown in Figure S1. The zeolite samples consist of about 1 μm crystallites. HZSM-12 agglomerates are formed by nanocrystals with sizes determined by the Scherrer equation [24] of about 22 nm. These findings are compatible with the reports given in the literature [20,21,25]. As seen in Figure S1, there are no significant differences among the samples.

The N_2 adsorption/desorption isotherms and pore size distribution curves of HZSM-12 and desilicated HZSM-12 are given in Figure S2. N_2 adsorption/desorption measurement for the HZSM-12 resulted in a type I isotherm, indicating a microporous material [26] with a narrow hysteresis loop between 0.4 and 0.8 that implies the presence of some mesoporosity. The presence of mesopores in HZSM-12 with a mean pore diameter of about 4.3 nm (Figure S2) could be generated due to voids between the nanocrystals that form the agglomerates [25]. On the other hand, the N_2 adsorption/desorption isotherm of the desilicated HZSM-12 represents type I and type IV behavior with the rather pronounced hysteresis loop. Those are associated with capillary condensation in the mesopore structure [26]. As seen in Figure S2, the desilicated HZSM-12 shows a bimodal mesopore distribution with mean diameters of 6.5 nm and 9.5 nm. The results of N_2 adsorption and desorption analysis are given in Table 1.

As seen from Table 1, the desilicated HZSM-12 shows a lower micropore volume (0.06 cm^3/g) than HZSM-12 (0.11 cm^3/g), which is also in compliance with the slight crystallinity loss observed by XRD. The decrease in micropore volume is coupled with increased external surface area (127 m^2/g to 146 m^2/g) and mesopore volume (0.11 cm^3/g to 0.26 cm^3/g). Alkaline treatment of ZSM-12 leads to a significant increase in mesopore formation, resulting from the preferential dissolution of Si from the zeolite framework [27,28]. Indeed, ICP-OES analysis results show that the alkaline treatment of ZSM-12 leads to the preferential removal of silicon from the zeolite lattice.

Table 1. Elemental composition and N_2 sorption characteristics of the samples.

Sample	HZSM-12	Desilicated HZSM-12
Si/Al[a]	40.8	32.9
S_{BET} (m^2/g)	384	338
S_{ext}[b] (m^2/g)	127	146
S_{micro}[b] (m^2/g)	257	192
S_{meso}[c] (m^2/g)	64	127
V_{micro}[b] (cm^3/g)	0.11	0.06
V_{meso}[c] (cm^3/g)	0.11	0.26
V_{total}[d] (cm^3/g)	0.25	0.37

[a]ICP-OES; [b]t-Method; [c]BJH Method (adsorption branch); [d]Volume absorbed at p/p_0=0.99.

NH_3-TPD was used to determine the strength and number of the acidic sites of HZSM-12 and desilicated HZSM-12. Two desorption peaks characterize the NH_3-TPD profiles of the samples given in Figure S3; a low-temperature peak below 300 °C and a high-temperature peak at 300 °C–550 °C. The low-temperature peak is assigned to the weak acidic sites, commonly attributed to silanol groups at the external surface or in lattice defects, and OH groups bonded to extra-framework aluminum species [29]. The high-temperature peak has been attributed to NH_3 adsorbed on the strong acid sites generated by framework tetrahedral aluminum species [29]. The quantities of weak and strong acid sites were determined by integrating the area under each peak shown in Figure S3; the results are given in Table 2.

Table 2. Amount of acid sites for the samples.

Sample	Amount of acid sites (mmol/g)		
	Weak	Strong	Total
HZSM-12	0.39(206.1)*	0.31(406.9)*	0.70
Desilicated HZSM-12	0.47 (178.9)	0.28 (387.4)	0.75
Spent catalyst	0.46 (172.1)	0.07 (348.6)	0.53
Regenerated catalyst	0.46 (181.1)	0.13 (387.4)	0.59

*T_{max} is given in parenthesis

The results given in Table 2 show that the number of weak acidic silanol groups increases due to the alkaline treatment of ZSM-12. Although the number of strong acidic sites remains virtually unchanged, the high-temperature peak is shifted to the lower temperature due to the lower intrinsic acidity of the Brønsted sites [30]. ICP-OES analysis of the samples shows that the desilicated HZSM-12 contains more aluminum than HZSM-12, and the Si/Al ratios of ZSM-12 samples decreased from 40.8 to 32.9 after the alkaline treatment of ZSM-12. The results of ICP-OES and NH_3-TPD analyses show that the geometric arrangement of aluminum atoms in the zeolite framework affects the acidity of the catalyst. It was

reported that, during the alkali treatment, some framework aluminum species responsible for forming the strong acid sites were re-distributed as extra-framework aluminum species due to the leaching of the framework siliceous species [31–33]. However, our previous study shows that the mesopores obtained in the specified desilication condition were successfully introduced without decreasing the strong Brønsted acidity [19]. Svelle *et al.* [34] stated that the mode of mesopore formation, i.e., concerning where and to which extent the alkaline solution attacks each zeolite particle, is elusive. They demonstrated that the mesopore formation according to both the Al-directed dissolution of siliceous areas and selective dissolution or etching along boundaries, intergrowths, and defects within each particle is important [34].

Catalytic activity

Catalytic performances of HZSM-12 and desilicated HZSM-12 were evaluated by the benzylation reaction of benzene with benzyl alcohol at 80 °C, 56/1 molar ratio of B to BA, and 2.5 mg/mL of catalyst loading. The conversion of benzyl alcohol over HZSM-12 and desilicated HZSM-12 is shown in Figure 3.

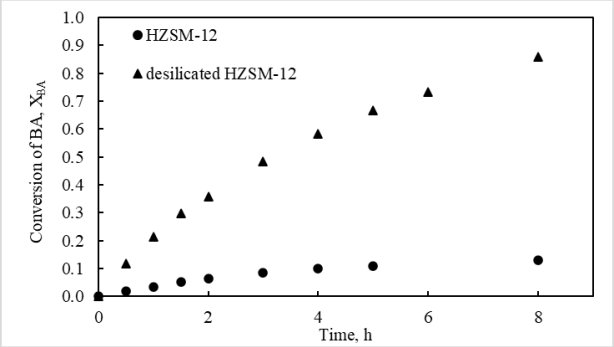

Figure 3. Catalytic activities of HZSM-12 and desilicated HZSM-12 in the benzylation reaction of benzene with benzyl alcohol at 80 °C, 2.5 mg/mL of catalyst loading, and 56/1 molar ratio of B to BA.

As shown in Figure 3, the alkaline-treated catalyst sample shows substantially higher catalytic activity than the untreated ZSM-12. To explain why the desilicated HZSM-12 exhibited higher catalytic activity in the reaction, the relationship between the structural properties and the catalytic performances of the catalyst needs to be discussed. It is known that ZSM-12 has a one-dimensional channel system with a 12-membered ring pore channel of 0.57 nm x 0.61 nm [19,21]. The molecular size of benzene (0.5 nm), benzyl alcohol (0.7 nm), DPM (0.9 nm), and DBE (1.2 nm) is close to or larger than the pore size of untreated ZSM-12 [35]. Such a pore size is inadequate for mass transfer to increase the conversion of BA into DPM. In the benzylation of benzene with benzyl alcohol, two reaction step is proposed to form DPM (Figure 1): (1) the direction formation of DPM by the alkylation of benzene with benzyl alcohol; (2) the conversion of DBE formed by the self-condensation of benzyl alcohol to DPM. Therefore, mass transfer ability is an important factor that affects the catalytic performance of the catalyst. As listed in Table 1, the desilicated HZSM-12 has a higher mesopore volume and external surface area than HZSM-12. Additional mesopores and external surface area will likely improve the mass transfer ability. Furthermore, the accessibility of acid sites is naturally vital in this reaction. The catalyst performs better in the benzylation reaction with higher mass transfer ability and more accessible acid sites. These results comply with the literature findings [1,6,8,19]. Akyalcin *et al.* [19] stated that ZSM-12, treated with 0.2 M NaOH at 85 °C for 60 min, exhibits a 10-fold enhancement of the catalytic activity compared to microporous HZSM-12 for the benzylation reaction of benzene with benzyl alcohol. In this study, the difference in the catalytic performance of the desilicated HZSM-12 can be explained by the strength of strong acid sites of the catalyst since the stronger acid sites are required to polarize benzyl alcohol into an electrophile that attacks the benzene ring [2]. When the maximum temperature (T_{max}) for the NH_3 desorption peak of the samples given in Table 2 is investigated, the shift of the second peak to a lower temperature for desilicated HZSM-12 indicates a decrease in the acid strength of the strong acid sites. This case leads to somewhat lower catalytic activity in converting benzyl alcohol to diphenylmethane. Milina *et al.* [36] stated that both compositional and porosity variations induced by alkaline treatment contribute to the catalytic performance of desilicated ZSM-5 in the liquid phase alkylation of toluene with benzyl alcohol. Svelle *et al.* [34] stated that the comparison of catalyst performance between mesoporous samples of ZSM-5 in the methanol to hydrocarbons reaction is not straightforward, as the Si/Al ratio, distribution of intergrowths/defects, mesoporosity, particle size, and other characteristics influence activity and deactivation rates in an interdependent manner. Consequently, the catalytic performance of the catalyst for the reaction of benzene with benzyl alcohol could be attributed to the synergic effect of mass transfer efficiency and surface acidity.

The effects of reaction parameters (reaction temperature, catalyst loading, and benzene to benzyl alcohol molar ratio) on the BA conversion and the DPM, DBE, and PAB selectivity were investigated using desilicated HZSM-12.

Effect of reaction temperature

Investigation to the effect of reaction temperature

on the reaction rate, the benzylation reaction was performed at 60°C, 70°C, 75°C, and 80 °C, with 3.9 mg/mL of catalyst loading and 56/1 molar ratio of B to BA. The results are shown in Figure 4a.

As shown in Figure 4a, the influence of reaction temperature on the BA conversion is quite strong.

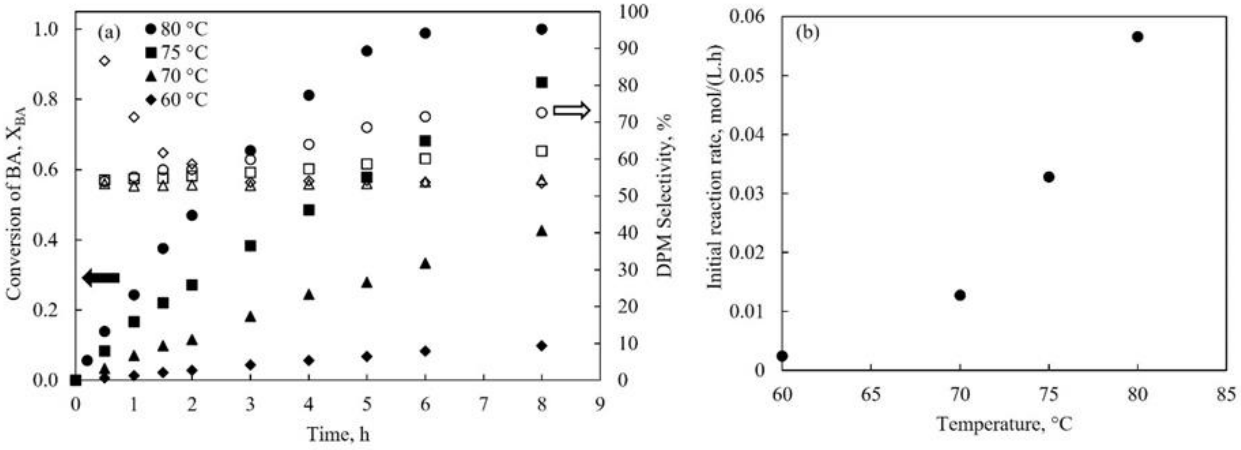

Figure 4. Effect of reaction temperature (a) on the benzyl alcohol conversion and DPM selectivity (b) on the initial reaction rate (3.9 mg/mL of catalyst loading, 56/1 molar ratio of B to BA).

The initial reaction rate shown in Figure 4b was calculated from Eq. 1 using a conversion of less than 10%, and the reaction rate can be considered a linear function of time.

$$-r_{BA_0} = C_{BA_0} \frac{x_{BA}}{t} \quad (1)$$

Figure 4b indicates that the reaction rate increases exponentially with the temperature, indicating that external and internal diffusion resistances can be neglected during the reaction since a chemical change is more temperature sensitive than a physical change [37]. Increasing the reaction temperature led to increased BA conversion, which increased the selectivity to DPM. For example, at 70 °C, the BA conversion was 24% after a reaction time of 4 h; at 80 °C, the BA conversion reached 81%. Therefore, the selectivity to DPM increased from 53% to 64%, paralleling the BA conversion. When the reaction time at 80 °C was increased from 4 h to 8 h, the selectivity to DPM was increased from 64% to 73%. However, at the same conversion, the change in the reaction temperature did not prominently change (~1%) in the selectivity to DPM. Therefore, 80 °C was suggested as the optimal reaction temperature under the atmospheric pressure by considering the obtained conversion and selectivity for the benzylation of benzene with benzyl alcohol in the presence of desilicated HZSM-12.

Effect of catalyst loading

The effect of catalyst loading on the reaction rate was investigated by performing the reaction in the presence of desilicated HZSM-12 at 0 mg/mL–4.9 mg/mL of varying catalyst loadings, 56/1 molar ratio of B to BA, and T=80 °C. The results are given in Figure 5a.

Figure 5a indicates that the conversion of BA increases with an increase in the catalyst loading. The initial reaction rate, $-r_{BA_0}$, versus catalyst loading, is given in Figure 5b. As can be seen in Figure 5b, the initial reaction rate linearly increases with catalyst loading, as expected, since the active sites of the catalyst are proportional to the amount of catalyst, and the mathematical expression can be given by:

$$-r_{BA_0}\,(mol/L\,h) = 0.0152\; C_{cat}\,(mg/mL) \quad (2)$$

When the reaction was carried out without a catalyst, no conversion was observed at a reasonable time. Thus, the reaction rate was considered negligible without the catalyst. This result is compatible with the report by Narender *et al.* [38]. The effect of catalyst loading on the BA conversion and product selectivities for 4 h and 8 h reaction time was given in Figure 5c.

Figure 5c indicates that the formation of DPM increases with DBE consumption, and PAB was also formed during the reaction. When the catalyst loading increased from 2.5 mg/mL to 4.9 mg/mL for 4 h reaction time, the BA conversion increased from 58% to 98%, and the selectivity towards DPM increased from 55% to 69%, paralleling the BA conversion. Under the same reaction conditions, the DPM and PAB selectivities increased with a longer reaction time. After 8 h reaction time, the DPM and PAB selectivities were 78% and 7%, respectively. The results show that the increase in the

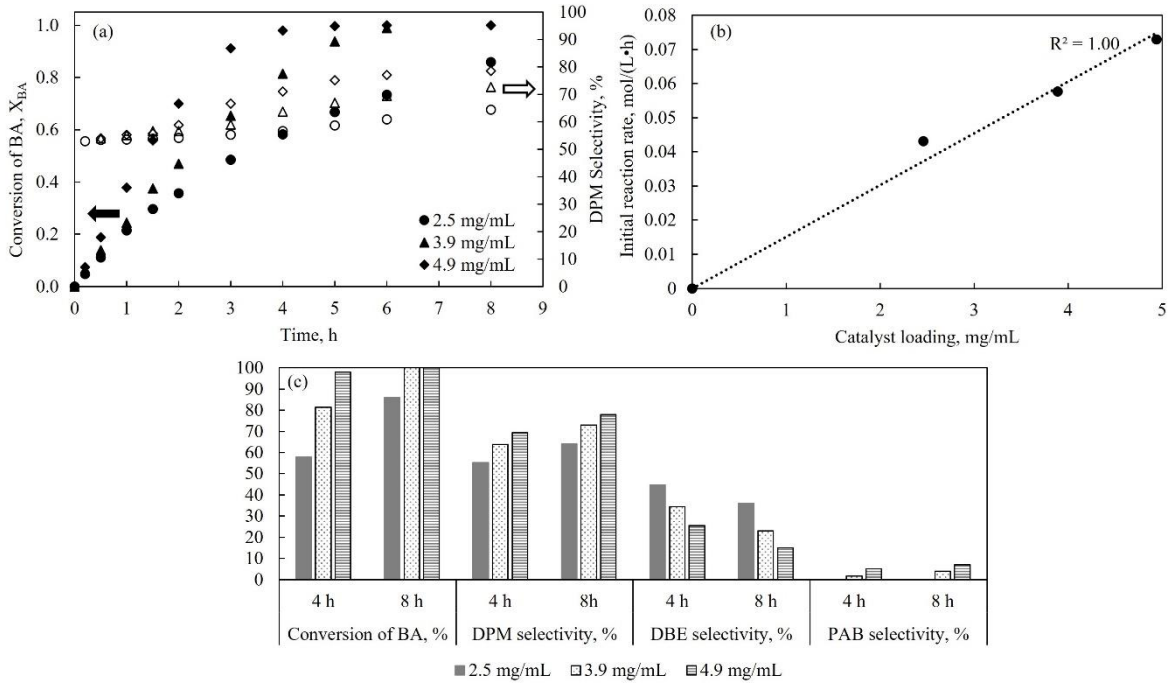

Figure 5. Effect of catalyst loading (a) on the BA conversion and DPM selectivity (b) on the initial reaction rate at 80 °C, and 56/1 molar ratio of B to BA (c) on the BA conversion and product selectivities for 4 h and 8 h reaction time at 80 °C, 56/1 molar ratio of B to BA.

catalyst loading did not significantly change the selectivity to DPM at the same conversion since increasing the catalyst loading provides the same effect on the rate of side reactions (Figure 1). Therefore, further experiments were performed with low catalyst loading (2.5 mg/mL) to reduce PAB formation.

Effect of benzene to benzyl alcohol molar ratio

The benzylation reactions were carried out at B to BA molar ratios of 21/1, 56/1, and 98/1 while maintaining 2.5 mg/mL of catalyst loading and the reaction temperature at 80 °C. The effects of the B to BA molar ratio on the BA conversion are given in Figure 6a.

Figure 6a shows that increasing the molar ratio of B to BA increased the conversion of benzyl alcohol. It is an expected result since the concentration of BA is relatively high, with the B to BA molar ratio of 21/1. The effects of the B to BA molar ratio on the BA conversion and product selectivities are given in Figure 6b.

Figure 6b shows the conversion of BA increases from 12% to 100% with the increase of B to BA molar ratio from 21/1 to 98/1. The DPM selectivity also changes with the B to BA molar ratio. The DPM selectivity increased from 74% to 87% (98/1 molar ratio of B to BA) with increasing reaction time from 4 h to 8 h; since the DPM formation increases steadily with the DBE consumption. No poly-alkylated products were obtained during the reaction at the prescribed condition.

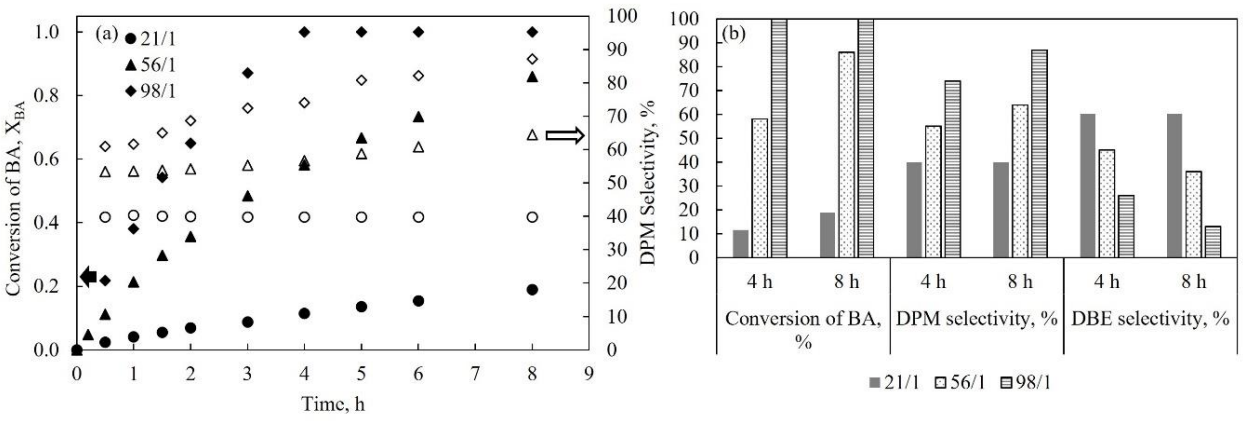

Figure 6. Effect of B to BA molar ratio (a) on the BA conversion and DPM selectivity (b) product selectivities at 80 °C, and 2.5 mg/mL of catalyst loading.

Catalyst reusability and deactivation

After completion of the benzylation reaction, the catalyst was filtered from the reaction mixture and dried. This catalyst was denoted as a “spent catalyst.” Before reusing this catalyst in the benzylation reaction, the spent catalyst was calcined at 520 °C for four hours under static air. The obtained catalyst was named a "regenerated catalyst." The reaction was performed at 80 °C and 56/1 molar ratio of B to BA in the presence of the regenerated catalyst with 2.5 mg/mL of catalyst loading to compare the catalytic activity of the fresh and regenerated catalyst. The conversion of benzyl alcohol dropped from 86% (fresh catalyst) to 45% (regenerated catalyst) for 8 h reaction time, while the DPM selectivity varies from 64% (fresh catalyst) to 56% (regenerated catalyst). The change of the acidic sites of the catalyst after regeneration can explain this activity difference. To determine the differences in the acid amount and the acid strength of the fresh, spent, and regenerated catalysts, the NH_3-TPD profiles given in Figure S4 were obtained. Table 2 indicates that after the eight hours reaction time of the fresh catalyst, the total acid sites on the catalyst significantly reduced, and a higher loss of strong acid sites occurred, which means that strong acid sites are more active in the benzylation of benzene with benzyl alcohol. Yoo and Smirniotis [39] stated that ZSM-12 was deactivated due to site coverage during the alkylation of isobutene with 2-butene at 80 °C and 300 psig. In this study, the occluded organic species formed on the catalyst during the reaction deactivated the catalyst, as was confirmed by the TGA analysis shown in Figure 7. From the recorded profiles, the weight loss before 200 °C is attributed to the desorption of the adsorbed water, and the weight loss of 4.5 wt% between 200 °C and 400 °C is associated with the desorption/decomposition of adsorbed organic compounds generated during the reaction. The weight loss of 5.5 wt% above 400 °C is attributed to the decomposition/oxidation of larger-sized organic molecules generated during the reaction [40,41].

Kim *et al.* [40] stated that the conventional zeolite deactivated rapidly in the liquid phase Friedel Craft alkylation reactions due to the deposition of carbon residue and/or water inside the micropores or the external surfaces. They also report that various poly-alkylated aromatic compounds generated via side reactions, i.e., self-condensation of benzyl alcohol or the benzylation of benzene, and their repetition, block the access of reactants into the active sites [40]. The spent catalyst was regenerated by the calcination method to maintain the catalytic performance. The number of acid sites of the regenerated catalyst given in Table 2 showed that the acidic sites of the spent catalyst were partially recovered. The strong acid sites of the regenerated catalyst recovered to 0.13 mmol/g, which accounted for 46% of the fresh catalyst. Two factors can explain the significant reduction of acidic sites of the catalyst after regeneration. One of them is high-temperature calcination for regeneration, which leads to the steaming of the zeolite, and, thus, the formation of some defects that dehydroxylate at high temperatures [41,42]. The other one is that the calcination temperature in this work was only 520 °C and did not reach 700 °C shown in Figure 7, to remove some organic species' residue. Corroborating the thermal stability of the zeolite samples [25,43], the XRD patterns of the fresh, spent, and regenerated catalyst given in Figure 8 were also investigated.

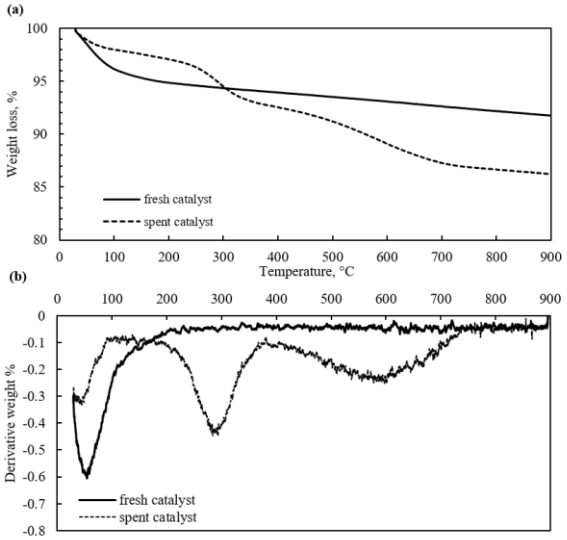

Figure 7. (a) TG and (b) DTG profiles of the fresh and spent catalysts.

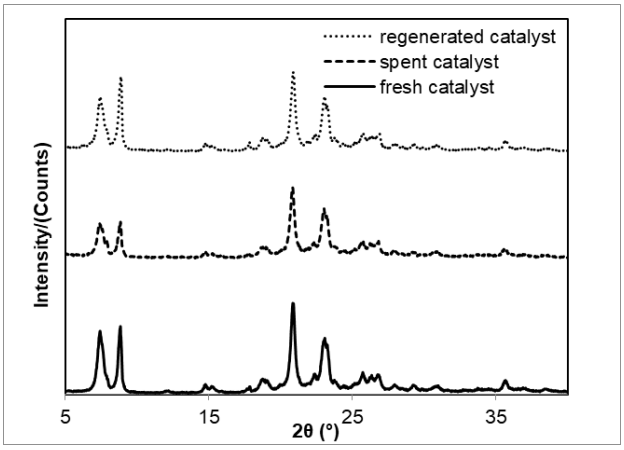

Figure 8. The XRD patterns of the fresh, spent, and regenerated catalysts.

The results indicated that although the spent and regenerated catalyst retains the crystal structure of MTW, the peak intensities of the samples are different. When the relative crystallinity was calculated from the intensities of the peaks at 7.4°, 8.8°, 20.8°, and 23.1° relative to the fresh catalyst, the relative crystallinities

of the spent and regenerated catalysts were found to be 69% and 95%, respectively. After calcinating the spent catalyst, the catalyst almost recovers the original crystallinity.

CONCLUSION

The benzylation reaction of benzene with benzyl alcohol was performed over HZSM-12 and desilicated HZSM-12. The increased mesoporosity of ZSM-12 via alkaline treatment enhanced the catalytic activity of ZSM-12. The effects of reaction parameters on the benzyl alcohol conversion and product selectivities were studied in the presence of desilicated HZSM-12, and selectivity to DPM of 74% for 100% BA conversion was achieved in 4 h of reaction time at 80 °C, 98/1 molar ratio of B to BA, and 2.5 mg/mL of catalyst loading. Under the same reaction conditions, the DPM selectivity was 87% in 8 h reaction time. The catalyst's reusability was investigated after calculating the spent catalyst in static air at 520 °C for four hours. Although the diffractograms of the desilicated HZSM-12 samples (fresh, spent, and regenerated samples) have proven that there were no structural changes, the NH_3-TPD results show that the coverage of the acid sites resulting from organic species produced during the reaction caused deactivation of the catalyst. However, the desilicated HZSM-12 can be regarded as a promising heterogeneous catalyst to improve the selectivity of diphenylmethane by using less reactive benzyl alcohol instead of benzyl chloride as a benzylation agent.

ACKNOWLEDGMENT

This work was supported by Anadolu University, Scientific Research Project Commission under grant number 1410F412, and Eskisehir Technical University, Scientific Research Project Commission under grant number 19ADP079. We thank the METU Central Lab (Ankara/Turkey) for ICP-OES analyses, E. Ayas for SEM analyses, M. Tamer for TGA analyses, and D. Karabulut for helping with laboratory work.

REFERENCES

[1] K. Leng, Y. Wang, C. Hou, C. Lancelot, C. Lamonier, A. Rives, Y. Sun, J. Catal. 306 (2013) 100–108. http://doi.org/10.1016/j.jcat.2013.06.004.

[2] N. Candu, M. Florea, S.M. Coman, V.I. Parvulescu, Appl. Catal., A 393 (2011) 206–214. https://doi.org/10.1016/j.apcata.2010.11.044.

[3] D. Yin, C. Li, L. Tao, N. Yu, S. Hu, D. Yin, J. Mol. Catal. A: Chem. 245 (2006) 260–265. https://doi.org/10.1016/j.molcata.2005.10.010.

[4] N. Candu, S. Wuttke, E. Kemnitz, S.M. Coman, V.I. Parvulescu, Pure Appl. Chem. 84 (2012) 427–437. http://doi.org/10.1351/PAC-CON-11-09-34.

[5] K. Leng, S. Sun, B. Wang, L. Sun, W. Xu, Y. Sun, Catal. Commun. 28 (2012) 64–68. https://doi.org/10.1016/j.catcom.2012.08.016.

[6] Y. Wang, Y. Sun, C. Lancelot, C. Lamonier, J.C. Morin, B. Revel, L. Delevoye, A. Rives, Microporous Mesoporous Mater. 206 (2015) 42–51. http://doi.org/10.1016/j.micromeso.2014.12.017.

[7] V.D. Chaube, Catal. Commun. 5 (2004) 321–326. https://doi.org/10.1016/j.catcom.2004.02.013.

[8] H. Jin, M.B. Ansari, E.Y. Jeong, S.E. Park, J. Catal. 291 (2012) 55–62. https://doi.org/10.1016/j.jcat.2012.04.006.

[9] Y. Sun, R. Prins, Appl. Catal., A 336 (2008) 11–16. https://doi.org/10.1016/j.apcata.2007.08.015.

[10] L. Tosheva, V.P. Valtchev, Chem. Mater. 17 (2005) 2494–2513. https://doi.org/10.1021/cm047908z.

[11] J.C. Groen, J.A. Moulijn, J. Pérez-Ramírez, J. Mater. Chem. 16 (2006) 2121–2131. https://doi.org/10.1039/B517510K.

[12] D. Verboekend, J. Pérez-Ramírez, Catal. Sci. Technol. 1 (2011) 879–890. https://doi.org/10.1039/C1CY00150G.

[13] L. Wang, Y. Wang, A. Wang, X. Li, F. Zhou, Y. Hu, Microporous Mesoporous Mater. 180 (2013) 242–249. http://doi.org/10.1016/j.micromeso.2013.06.029.

[14] C. Perego, S. Amarilli, R. Millini, G. Bellussi, G. Girotti, G. Terzoni, Microporous Mater. 6 (1996) 395–404. https://doi.org/10.1016/0927-6513(96)00037-5.

[15] R. Millini, F. Frigerio, G. Bellussi, G. Pazzucconi, C. Perego, P. Pollesel, U. Romano, J. Catal. 217 (2003) 298–309. https://doi.org/10.1016/S0021-9517(03)00071-X.

[16] E.R. Rosinski, M.K. Rubin, US 3832449 (1974).

[17] L.T. Nemeth, G.F. Maher, US 6872866B1 (2005).

[18] B.H. Chiche, R. Dutartre, F. Di Renzo, F. Fajula, A. Katovic, A. Regina, G. Giordano, Catal. Lett. 31 (1995) 359–366. https://doi.org/10.1007/BF00808600.

[19] S. Akyalcin, L. Akyalcin, M. Bjørgen, Microporous Mesoporous Mater. 273 (2019) 256–264. https://doi.org/10.1016/j.micromeso.2018.07.014.

[20] S. Gopal, K. Yoo, P.G. Smirniotis, Microporous Mesoporous Mater. 49 (2001) 149–156. https://doi.org/10.1016/S1387-1811(01)00412-7.

[21] Y. Hou, N. Wang, J. Zhang, W. Qian, RSC Adv. 7 (2017) 14309–14313. https://doi.org/10.1039/C6RA28844H.

[22] D. Karabulut, S. Akyalcin, Int. J. Chem. React. Eng. 19 (2021) 541–551. https://doi.org/10.1515/ijcre-2020-0175.

[23] X. Wei, P.G. Smirniotis, Microporous Mesoporous Mater. 97 (2006) 97–106. https://doi.org/10.1016/j.micromeso.2006.01.024.

[24] A.L. Patterson, Phys. Rev. 56 (1939) 978. https://doi.org/10.1103/PhysRev.56.978.

[25] K.T.G. Carvalho, E.A. Urquieta-Gonzalez, Catal. Today 243 (2015) 92–102. http://doi.org/10.1016/j.cattod.2014.09.025.

[26] K.S.W. Sing, D.H. Everett, R.A.W. Haul, L. Moscou, R.A. Pierotti, J. Rouquerol, T. Siemieniewska, Pure Appl. Chem. 57 (1985) 603–619.

http://doi.org/10.1351/pac198557040603.

[27] J.C. Groen, L.A.A. Peffer, J.A. Moulijn, J. Pérez-Ramírez, Colloids Surf., A 241 (2004) 53–58. https://doi.org/10.1016/j.colsurfa.2004.04.012.

[28] J.C. Groen, J.C. Jansen, J.A. Moulijn, J. Pérez-Ramírez, J. Phys. Chem. B 108 (2004) 13062–13065. https://doi.org/10.1021/jp047194f.

[29] Q. Wang, Z.M. Cui, C.Y. Cao, W.G. Song, J. Phys. Chem. C 115 (2011) 24987–24992. https://doi.org/10.1021/jp209182u.

[30] U.V. Mentzel, K.T. Højholt, M.S. Holm, R. Fehrmann, P. Beato, Appl. Catal., A 417-418 (2012) 290–297. https://doi.org/10.1016/j.apcata.2012.01.003.

[31] M. Bjørgen, F. Joensen, M. Spangsberg Holm, U. Olsbye, K. P. Lillerud, S. Svelle, Appl. Catal., A 345 (2008) 43–50. https://doi.org/10.1016/j.apcata.2008.04.020.

[32] K. Sadowska, A. Wach, Z. Olejniczak, P. Kustrowski, J. Datka, Microporous Mesoporous Mater. 167 (2013) 82–88. https://doi.org/10.1016/j.micromeso.2012.03.045.

[33] S.J. You, E.D. Park, Microporous Mesoporous Mater. 186 (2014) 121–129. http://doi.org/10.1016/j.micromeso.2013.11.042.

[34] S. Svelle, L. Sommer, K. Barbera, P.N.R. Vennestrøm, U. Olsbye, K.P. Lillerud, S. Bordiga, Y.H. Pan, P. Beato, Catal. Today 168 (2011) 38–47. https://doi.org/10.1016/j.cattod.2010.12.013.

[35] X. Zeng, Z. Wang, J. Ding, L. Wang, Y. Jiang, C. Stampfl, M. Hunger, J. Huang, J. Catal. 380 (2019) 9–20. https://doi.org/10.1016/j.jcat.2019.09.035.

[36] M. Milina, S. Mitchell, Z.D. Trinidad, D. Verboekend, J. Pérez-Ramírez, Catal. Sci. Technol. 2 (2012) 759–766. https://doi.org/10.1039/C2CY00456A.

[37] H.S. Fogler, Elements of Chemical Reaction Engineering, Prentice Hall, Englewood Cliffs, NJ, USA (1999). ISBN 0-13-531708-8.

[38] N. Narender, K.V.V. Krishna Mohan, S.J. Kulkarni, I. Ajit Kumar Reddy, Catal. Commun. 7 (2006) 583–588. https://doi.org/10.1016/j.catcom.2006.01.013.

[39] K. Yoo, P.G. Smirniotis, Appl. Catal., A 246 (2003) 243–251. https://doi.org/10.1016/S0926-860X(03)00026-7.

[40] J.C. Kim, K. Cho, R. Ryoo, Appl. Catal., A 470 (2014) 420–426. https://doi.org/10.1016/j.apcata.2013.11.019.

[41] D.S.A. Silva, W.N. Castelblanco, D.H. Piva, V. Macedo, K.T.G. Carvalho, E.A. Urquieta-González, Mol. Catal. 492 (2020) 111026. https://doi.org/10.1016/j.mcat.2020.111026.

[42] J. Shao, T. Fu, Z. Ma, C. Zhang, H. Li, L. Cui, Z. Li, Catal. Sci. Technol. 9 (2019) 6647–6658. https://doi.org/10.1039/C9CY01053J.

[43] G. Cruciani, J. Phys. Chem. Solids 67 (2006) 1973–1994. https://doi.org/10.1016/j.jpcs.2006.05.057.

SEMA AKYALCIN[1]
LEVENT AKYALCIN[1]
MORTEN BJØRGEN[2]

[1]Department of Chemical Engineering, Faculty of Engineering, Eskisehir Technical University, Eskisehir, Turkey

[2]Department of Life Sciences and Health, Faculty of Health Sciences, Oslo Metropolitan University, Oslo, Norway

NAUČNI RAD

KATALITIČKA SVOJSTVA DESILIKOVANOG ZEOLITA HZSM-12 ZA REAKCIJU BENZILOVANJA BENZENA SA BENZIL ALKOHOLOM

Katalitička proizvodnja difenilmetana u reakciji benzena sa benzil alkoholom je istraživana korišćenjem HZSM-12 i desilikovanog HZSM-12 koji je dobijen tretiranjem ZSM-12 sa 0,2M NaOH na 85 °C tokom 60 min. Netretirani i alkalno tretirani zeoliti ZSM-12 su okarakterisani rendgenskom difrakcijom, izotermama adsorpcije/desorpcije azota, skenirajućom elektronskom mikroskopom, optičkom emisionom spektrometrijom induktivno spregnute plazme i temperaturno programiranom desorpcijom amonijaka. Desilikovani HZSM-12 ima dobra katalitička svojstva za konverziju benzil-alkohola od 100% i selektivnost prema difenilmetanu od 74% i 87% (za 4 h i 8 h reakcionog vremena, redom). Prikazani su, takođe, reakcioni parametri koji utiču na konverziju benzil-alkohola i distribuciju proizvoda. Upoređene su aktivnosti svežeg i regenerisanog katalizatora, a rezultati karakterizacije su pokazali da okludirani organski molekuli smanjuju broj kiselih mesta katalizatora nakon reakcije i regeneracije.

Ključne reči: benzil-alkohol, benzilovanje, deaktivacija katalizatora, desilikacija, difenilmetan, ZSM-12.

CI&CEQ
Chemical Industry & Chemical Engineering Quarterly

Available online at
Association of the Chemical Engineers of Serbia AChE
www.ache.org.rs/CICEQ

Chem. Ind. Chem. Eng. Q. 30 (1) 11–24 (2024) CI&CEQ

LALGUDI SRINIVAS BHADRINARAYANAN
CHINTHALACHERUVU ANAND BABU

Department of Chemical Engineering, Sri Venkateswara College of Engineering, Tamil Nadu, India

A RESINS-NEUTRALIZATION COUPLED ROUTE FOR THE TREATMENT OF STAINLESS-STEEL PICKLING EFFLUENT: A RESEARCH STUDY

Article Highlights

- A cost-effective method for the conversion of Cr^{6+} into $Na_2Cr_2O_7$ using ion exchange resin
- Innocuous solids CaF_2, ZrF_4, $Zr(OH)_4$, $Fe(OH)_3$, $Cr(OH)_3$, and $Ni(OH)_3$ are safely discarded
- Nitrates are converted into $NaNO_3$ as the end product that can be recycled
- The presented strategy enhances the option of recycling pickling wastewater

Abstract

One of the major environmental problems caused by stainless-steel industries is the liquid effluents generated during the production processes. It contains a high concentration of metal ions such as Fe (III), Cr (III), Cr (VI), and Ni (II) in HF and HNO_3 mixture, oil, and rinse wastewater. The used pickling waste stream has a pH of 0.5 and Total Dissolved Salts (TDS) of 520g/L with a density of 1.20g/CC. The present work focused on recycling pickling effluent by combining filtration, resins, and neutralization to remove metal ions efficiently and F^- greater than 99.5%. To remove TDS, laboratory experiments were performed using micro and ultra-filters with a membrane area 0.2m2. Cr (VI) was removed using TulsionFSMP 6301 resin and desorption using $NaNO_3$ and subsequent conversion into $Na_2Cr_2O_7$ as a by-product. For neutralization, $Ca(OH)_2$ and NaOH were used to precipitate metal ions, and the resulting filtrate was polished using $ZrOCl_2$ to remove F- to 0.12 mg/L effectively. The nitrate was recovered as $NaNO_3$. Adsorption isotherm and kinetic studies were utilized for Cr (VI) from experimental data, and a process flow diagram was developed, which can eventually be tested on a larger scale.

Keywords: Spent pickling solution, ion exchange, ultrafiltration, precipitation, industrial recycling, process flow sheet.

SCIENTIFIC PAPER

UDC 502:628.4:669.14

Metallurgical Industries of India (MII) use large quantities of aqueous acidic solution to treat stainless steel materials chemically. The treatment process primarily removes impurities such as stains, rust, scale, and other contaminants left on the steel surface. This process is referred to as acid pickling. The acidic bath is a mixture of hydrofluoric acid and nitric acid in demineralized (DM) water with 1:3:20 (v/v) proportions for the pickling of highly alloyed steels. The acids dissolve the metal oxide, forming a passivation chromium film layer on the steel surface. Lochyński *et al.* (2017) reported the XPS results on the surface morphology of passive film formation after pickling, resulting from increased chromium oxides and hydroxides in the passive layer [1]. After pickling, the steel surface is washed using water to remove the residual acid from the surface of the steel. Hydrofluoric acid reacts with the metal during pickling to form a fluoride complex. As the reaction proceeds, the acid concentration decreases with increased metal ion

Correspondence: C.A. Babu, Department of Chemical Engineering, Sri Venkateswara College of Engineering (Autonomous), Post Bag No.1, Pennalur Village, Chennai - Bengaluru High Road, Sriperumbudur Tk., Kancheepuram District, Tamil Nadu 602117, India.
E-mail: canandbabu@gmail.com
Paper received: 23 October, 2022
Paper revised: 10 April, 2023
Paper accepted: 24 March, 2023

https://doi.org/10.2298/CICEQ221023007B

concentration in the pickling bath. Once the bath gets saturated with the metal, it cannot be used for further pickling operation, and the used pickling solution (UPS) is stored in tanks for disposal or treatment. Exhausted pickling lines and rinse water liquor contain soluble and insoluble metal salts of Fe^{3+}, Ni^{2+}, Cr^{3+}, and Cr^{6+} (with oxygen, it forms chromate [$Cr_2O_4^{2-}$] and dichromate [$Cr_2O_7^{2-}$], fluoride [F^-], and nitrate [NO_3^-]) as contaminants. Metallurgical industries using this route generate large quantities of UPS. Conventionally, the problem is addressed by neutralizing the UPS with calcium hydroxide. The lime reacts with hydrofluoric acid and nitric acid and forms calcium fluoride and calcium nitrate in an aqueous solution along with ferric, chromium, and nickel hydroxides, respectively, and the slurry mixture is filtered to separate the cake. The solid cake is dried and disposed of at a solid waste management facility for further disposal. If left untreated, the pickling wastewater containing toxic Cr^{6+}, F^-, and NO_3^-may leach into the ground and possibly contaminate groundwater [2–4]. According to Central Pollution Control Board (CPCB), pickling sludge and wastewater in India have been regarded as toxic waste and included in the hazardous waste list [5].

Over the last few decades, several processes were developed to treat these types of wastewater mixtures arising from pickling operations, such as acid recovery, recycling, and reduction of heavy metal concentration to an environmentally acceptable level. The methods include ion exchange [6–9], solvent extraction [10], evaporation and crystallization [11], distillation [12], diffusion dialysis, and electro membrane process [13,14]. Tang *et al.* (2018) reported the recovery of iron, chromium, and nickel from pickling sludge using a novel smelting reduction method [15]. The neutralization of UPS with calcium hydroxide produces calcium fluoride as solid waste, and the residual acid is neutralized. It hence cannot be recycled or used as by-products. Several studies have been carried out to solve this problem and reduce the toxic hexavalent chromium content in waste pickle liquor [16]. Relatively little attention was paid to converting mixed acid-metal pickle liquor into useful by-products. The use of membrane-based filtration and ion exchange resins plays a vital role in treating liquid effluents. In 1961, chelating ion-exchange resins were proposed to recover acids from metallurgical waste solutions [6]. Kobuchi *et al.* (1986) investigated the optimum operating conditions using diffusion dialysis and anion exchange membrane technology to recover hydrofluoric and nitric acids. The study outcome reported 100% recovery for nitric acid, 50%–60% recovery for hydrofluoric acid, and removal of more than 85% of ferric ions in mixed solutions [17]. Then, a continuous method for spent pickled liquor using an ion-exchange bipolar membrane and integration of dialysis allows the separation of acid and alkali, resulting in a recovery rate of 90% mixed acid (HF & HNO_3) [13]. A commercially developed ion-exchange technology named Recoflo® claimed improved exchange kinetics in separating mixed acid from metal salts [18]. Experimental investigation on the separation of iron from used pickling baths containing a very high concentration of hydrochloric acid using commercial ion-exchange cation, anion, and chelating resins was reported two decades back [7]. Marañón *et al.* (2000) established experimental assays using anionic resins for pickling water arising from the galvanizing process [19]. The ion exchange process was also used to recover chromic acid from mixed acid solutions [8]. Alguacil *et al.* (2004) examined and reported the removal of chromium (III) ions using ion-exchange resin from acidic waste solutions [9]. An investigation on the close loop circulation of rinse water after acid pickling in stainless steel was achieved using reverse osmosis, electrodialysis, and ion exchange [20]. Ultrafilter (UF) with a very low molecular weight cut-off (MCWO) was tested for retaining metal ions in the filter [21]. Ghare *et al.* (2014) employed commercially available anionic resin to remove iron from the UPS of hydrochloric and sulfuric acids [22]. An original contribution was established by Babu *et al.* (1993) for the removal of fluoride from pickling effluent in two stages using lime and zirconium [23]. A similar recent study also indicated fluoride removal by coagulation using zirconium tetrachloride as a complexing agent [24].

The main goal of this research was to study the application of ion exchange, membrane filtration techniques, and traditional neutralization to treat the mixed effluent generated from the pickling of stainless-steel production on a laboratory and bench scale. A thorough examination of the pickling effluent from an industrial site that produces nuclear-grade stainless steel materials with various compositions and different initial compositions was tested.

The use of ultra and microfilter, anionic ion exchange resin, calcium hydroxide, sodium hydroxide, and zirconium chloride was studied to treat effluent generated from the pickling process. The proposed research is of vital importance for industries handling mixed pickling effluents. The developed process eliminates Cr (VI) and subsequent conversion to sodium dichromate, compared to the current practice of neutralizing the effluents with lime and disposing of them as landfill, but for which the literature is not up to date. The end by-products from the process result in sodium nitrate, which is to be recycled for regeneration of ion exchange resin or sold, and the remaining by-products generated are safely disposed of as per the

allowable limit under the pollution control board [5].

MATERIAL AND METHODS

In this study, laboratory and bench-scale studies were carried out using synthetic and real effluents from the industry, the process parameters have been fixed, and a flow sheet has been developed to recover nitrate as sodium nitrate. Sodium nitrate that is produced can be recycled back into the industry. The experimental protocol involves using a microfilter to remove suspended solids, anion exchange resin to remove Cr (VI), and recovery as sodium dichromate. Metal ions present in the effluent, such as Cr (III), Ni (II), and Fe (III), were precipitated as hydroxides using sodium hydroxide in the second stage. Simultaneously, calcium hydroxide was added to precipitate fluoride as calcium fluoride in the same solution. Polishing of fluoride using zirconium oxychloride was carried out in the final stage. The materials and techniques involved and the outcome of the results for the treatment mentioned above protocol are reported and discussed in this article. In addition, a detailed process flow sheet is provided for possible implementation in the industry.

Chemicals and experimental solutions

All the chemicals used in this study are analytical grade (AR) and directly used in the experiment as supplied by the manufacturer. The list of chemicals used, the supplier, and their purity are described in the following.

Synthetic effluent: Chromium nitrate nonahydrate (≥99.99%, SRL, India), Ferric nitrate (≥99.99%, SRL, India), Potassium dichromate (≥99%, Sigma Aldrich, USA), Nickel nitrate nonahydrate (≥99.99%, SRL, India), Nitric acid (Fisher Scientific, USA), Hydrofluoric acid (Fisher Scientific, USA).

Nitrate analysis: Orthophosphoric acid (Sigma-Aldrich, USA), Sulfanilic acid (≥99%, HiMedia, India), N-(1-Naphthyl) ethylenediamine dihydrochloride, NEDA (98%, SRL, India), Copper sulfate (99.9%, Sigma Aldrich, USA), Hydrazine sulfate (≥99%, Sigma Aldrich, USA), Sodium hydroxide (97%, Sigma Aldrich, USA), Sodium nitrate (99%, SRL, India).

Fluoride analysis: Sodium fluoride (≥99%, SRL, India), Zirconium oxychloride (≥99.5%, Sigma Aldrich, USA), Xylenol orange tetrasodium salt (≥99%, Loba Chemie, India), Potassium chloride (≥99.5%, SRL, India).

Hexavalent chromium analysis: Potassium dichromate (≥99%, Sigma Aldrich, USA), 1,5- diphenylcarbazide (DPC) (SRL, India ≥99% purity).

Neutralization chemicals: Calcium hydroxide (≥98%, SRIL, India), Sodium hydroxide (97%, Sigma Aldrich, USA).

The glassware used in the study was decontaminated by soaking it in a 5% (v/v) hydrochloric acid solution for 24 hours and rinsed with DM water.

Ion-exchange resin

The ion-exchange resins used in this study and their properties are enlisted in Table 1. The resin was washed with demineralized water to remove all impurities. The pretreatment of resin is performed with 4-bed volumes (BV) of 4% sodium hydroxide and washed with 7-BV of DM water, followed by 4-BV of 5% hydrochloric acid and washed with 7-BV of DM water to ensure complete pretreatment of the resin. The resin was dried at 60°C in an oven for 24 hours. The ion exchange capacity and the volume of resin required to treat per 100 mL of effluent are provided in Eq. (1) and Eq. (2), respectively. The anionic resins were eluted by using a desorbing agent (2N $NaNO_3$ and DM water) to evaluate the reusability of the ion-exchange resins and for the conversion of adsorbed dichromate into useful sodium dichromate as a by-product. About 0.5 g of adsorbent was stirred with 50 mg/L of the effluent for 3 hours using an orbital shaker for the desorption of hexavalent chromium. After equilibrium, the effluent concentration was determined. The effluent was then agitated with the eluent for the same duration as the reaction time of 3 hours [25]. After each treatment, the adsorbent material was separated from the reaction mixture and washed with DM water. Desorption experiments for Cr^{6+} ions were performed in the anionic (NO^{3-}) resin column. For equilibrium, adsorption experimental tests, 50 mL of stock solution was put in a flask, and 0.1 g of pretreated resin was added and loaded in an orbital shaker at 250 rpm for 60 minutes to ensure adsorption equilibrium [25,26]. The above-mentioned experimental tests were repeated for accuracy.

$$Ion-exchange\ capacity\left(\frac{meq}{g}\right)=\frac{NaOH_{ml}\times NaOH_{eq/L}}{Mass\ of\ resin} \quad (1)$$

$$\begin{aligned}&The\ volume\ of\ resin\ required\ per\ 100mL\ of\ effluent=\frac{4g}{100g}HF+\frac{10g}{100g}HNO_3=\frac{4}{20}\frac{1000geq}{100g/eq}+\frac{10geq}{63g/eq}\frac{1000meq}{100g}=\\&200+158=358meq\ per\ 100g\ of\ effluent\\&The\ volume\ of\ resin\ required=\frac{358}{IX\ capacity}=(x.)g\ for\ 100mL\ of\ effluent\end{aligned} \quad (2)$$

Table 1. Characteristics of the ion-exchange resin

Resin type/design	SPL, macroporous, SBA	SPL, macroporous, SBA	Powder, SBA
Resin matrix type	Styrene DVB	Styrene DVB	Polystyrene, copolymer
Resin functional group	$-N^+R_3$	Quaternary amine	Quaternary ammonium type II
Standard ionic form	Freebase	Cl^- to OH^-	$Cl^-$to OH^-
Particle size, mm	0.3–1.2	0.55 ± 0.05	50 µm–75 µm
Moisture content, %	52–56	42–48	50 ± 3
Maximum operating temperature, °C	60	60	80
Total capacity, meq/mL	1.4	1.4	3.0
Resin name/Manufacturer	INDION, Ion exchange, India	Amberlite™ 4500CL, USA	Tulsion, FSMP 6301, Thermax, India

Instrumentation

To determine the concentration of iron, nickel, and chromium in the UPS and the treated solution, a flame Atomic Absorption Spectrophotometer (AAS), AA-301 (Thermo Fisher Scientific, USA) equipped with two hollow cathode lamps with individual power supplies was used. The AAS standards of Fe, Cr, and Ni were separately prepared from 1000 mg/L dissolved in 0.5N nitric acid (≥99.99%, SRL, India). The system control and output for recorded data were controlled by Thermo Scientific AA 301 software v.5.1. The AAS measurements were performed with the following conditions: Sample uptake rate: 7 mL/min; Air/acetylene pressure: 5 bar/2.6 bar controlled by rotameter and needle valve; Flame ignition: software-controlled; Fuel (acetylene): 7.66 L/min; Nebulizer: iridium; Spray chamber: nozzle inert; Wavelength range: Cr-357.9 nm, Fe-248.30 nm, Ni-232 nm; Detector: high-performance photomultiplier. A Shimadzu 160A UV-Visible spectroscopy with two quartz cells was used for measuring the concentration of hexavalent chromium at λ=540 nm, fluoride at λ=557 nm, and nitrate at wavelength, λ=220/275 nm in the synthetic, UPS, and treated solutions.

List of equipment used for bench-scale experiments

To prepare synthetic effluent and associated reagents, a 50-LPH reverse osmosis (RO) water plant coupled with a DM unit (Pervel Water Solutions, India) was set up for experimental studies. The DM water was produced upon pumping RO water (AJm75S 4 HP; Leo 3.0 Innovation, India) into two-separate poly-glass pressure vessels (1054 PENTAIR Structural™, India) loaded with 50 kg of cationic and 50 kg anionic ion exchange resins (Ion Exchange, India). The TDS of DM water was maintained between 3 and 6 mg/L, and the conductivity of the DM water (10-11.00 µS/ppm) was continuously monitored using an online controller (MS 623-HMD; Micro set Instrumentation & Controls Ltd, India). The ion exchange column was regenerated using a 5% hydrochloric acid solution for the cation exchanger and a 1% sodium hydroxide solution for the anion exchanger. The spent pickling solution was pumped from the storage tank to the membrane filter using a polytetrafluoroethylene diaphragm pump with a maximum dosing rate of 6 L/h at 4 kg/cm^2 pressure (Pro Aqua Chemical RO dosing pump Ltd, India). RO and UF technology was utilized in the removal of suspended solids. RO spun filters with 5 µm pore size, 25.4 mm length, and 60 mm diameter with the material of constructions [polypropylene (PP), polysulfone (PS), and polyethersulfone (PES)] inbuilt with cartridge, hollow fiber membrane module UF with 10 KD MCWO. The inlet feed and permeate flow rate were set at 6 L/m^{2}h and 3.5 L/m^{2}h. The area of the UF membrane is 0.2m^2, 1.4 mm OD, and 0.8 mm ID, which is packed with PES membranes inside the acrylic shell (TECH INC Incubating Technologies, India) and utilized for removing TSS in the UPS.

An ion exchange column was utilized in the adsorption of Cr (VI) in pickling wastewater [27]. The crystallization process for the formation of sodium dichromate solution in ion exchange regenerated liquid was performed in a high-temperature oven at 107 °C (Bio-Technics, India). The precipitation of iron, nickel, and total chromium in the form of hydroxides was achieved by mixing 5 eq/L caustic soda with 5 eq/L calcium oxide solution and adjusting the pH at 0.3 to 9.0. The hexavalent chromium-free pickle liquor precipitation was carried out in a volumetric flask using a magnetic stirrer (RSW 127; Royal Scientific, India) with various magnetic pellets. The pH in the precipitation process is carefully monitored using a pH meter (ECOTestrpH2; Thermo Fisher Scientific, USA) (0–14 pH) with ±0.1 accuracy, auto-calibration, and auto-buffer recognition. The filtration of the sludge precipitated with hydroxide was performed using a vacuum filter. The filtration of zirconium oxychloride treated liquid for fluoride removal was filtered using a Whatman paper (Grade 1).

Process steps involved in the recycling pickling waste

UFs were used to capture total suspended solids. Followed by an ion-exchange column [27] where the target Cr^{6+} ion was adsorbed by solid anionic resin, and the $Cr_2O_7^{2-}$ ion was combined with Na^+ ions in the aqueous solution resulting in sodium dichromate through partial crystallization. The steps involved in the ion exchange process can be represented as follows given by equations 3 and 4:

$$Adsorption: 2R^+ + Cr_2O_7^{2-} \rightarrow R_2Cr_2O_7 \quad (3)$$

$$Regeneration: R_2Cr_2O_7 + 2Na^+ \rightarrow 2R^+ + Na_2Cr_2O_7 \quad (4)$$

The exhausted ion-exchange resin column was regenerated using sodium nitrate solutions. A five-step process utilized in this study for treating the UPS is devised as provided in Figure.1

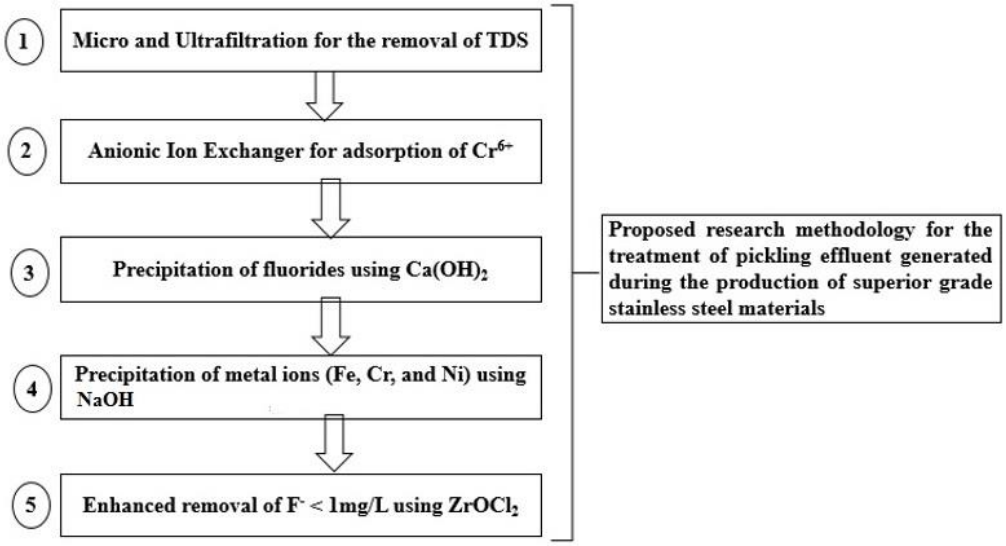

Figure 1. Experimental steps involved in the proposed research.

Bench-scale experiments

An experimental setup for verifying the process mentioned above steps was performed in this study, as shown in Figure 2. The pickling effluent contained suspended solids; hence, the liquid was filtered using a 5 µm micro filter and 10 kDa UF. The Microfilter and UF were fitted upstream to remove all the total suspended solids. A diaphragm pump controlled the UF flow rate. The selection of pump material was critical as the acidic medium passed through the pump, which was notoriously corrosive. In this study, the pump material is made from high-density polyethylene, which is non-corrodible and acid-resistant. The ion-exchange column loaded with resin was measured accurately using a weighing balance.

The permeate from the filtration process was collected and neutralized with mixed 5N NaOH and 5N $Ca(OH)_2$ solution in a conical flask using a magnetic pellet as a stirrer. The mixing has to be perfectly controlled so that all the metal ions, such as iron, nickel, and chromium in the permeate, get precipitated. Fluoride reduction was carried out separately using 100 mg/L zirconyl oxychloride solution in another conical flask using a magnetic pellet as a stirrer. The solution was added to the treated filtrate, the diluted 1 eq/L sodium hydroxide was added and stirred for 45 minutes, and the solution was left to settle for 24 hours. The clear supernatant solution was separated and analyzed for fluoride concentration, and the optimum pH was determined. This bench-scale process was repeated several times to collect sufficient data to generate the results for demonstration in the pilot scale.

Kinetic batch experiments were carried out using 50 mL of the stock solution put in a flask, and 0.1 g of pre-treated resin (Tulsion FSMP 6301, Thermax, India) was added and loaded in an orbital shaker (Scientech Technologies; SE-140, India) at 250 rpm at 26 °C. The solution was filtered, and the equilibrium concentration was determined using the 1,5-diphenylcarbazide (DPC) test [29]. The batch experimental tests were repeated several times for solutions of different initial concentrations to ensure sufficient data were collected for isothermal identification of hexavalent chromium adsorption by the NO_3^- resin.

Figure 2. Bench-scale experimental setup.

Working method for UV-Visible spectroscopic analysis

Determination of hexavalent chromium

The hexavalent chromium concentration in the UPS was determined by the DPC test [28,29]. The UPS and ion exchange treated samples were made up by adding an 8 mL solution with 2 mL DPC. The solution was kept still for 20 minutes to develop violet coloration and analyzed for hexavalent chromium. The calibration curve for concentration versus absorbance was plotted with a correlation coefficient, r^2, close to unity UFs.

Determination of nitrate

The nitrate concentration in the UPS was ascertained by N-(1-naphthyl) ethylenediamine dihydrochloride (NEDA) method [30,31]. Few modifications have been made in the experimental procedure for the accuracy of results. The experimental procedure is as follows: 1 mL of the sample to be analyzed was diluted to the 20 mg/L, 40 mg/L, 60 mg/L, 80 mg/L, and 100 mg/L from the prepared 1000 mg/L sodium nitrate solution. Secondly, 2 mL of diluted sample was added with 1 mL of copper sulfate and hydrazine sulfate (reducing agent), 1 mL of sodium hydroxide solution, and 0.5 mL of coupling agent, which a heated and cooled to form pink solution, which is a mixture of orthophosphoric acid, sulfanilic acid, and NEDA. The reagents were mixed thoroughly and diluted with DM water, 5.5 mL making up a 10 mL solution. The solutions were mixed thoroughly and filtered using Whatman paper (Grade 1). The absorbance was measured at room temperature, and a calibration graph was plotted to obtain the concentration of the unknown sample using standard solutions with a correlation coefficient, r^2, close to unity.

Determination of fluoride

The fluoride concentration in UPS was examined by the xylenol orange test [32]. The experimental procedure was as follows: 15 mL of working standard and treated effluent, 5 mL zirconium oxychloride solution, and 2.5 mL of potassium chloride solution were mixed thoroughly. About 5 mL of xylenol orange solution was added by swirling the flask for 15 seconds. After 30 seconds, 25 mL of DM water was added, and the delivery break time should be approximately 7 seconds and repeatable. The contents were filtered using Whatman paper (Grade 1). The liquid was analyzed for fluoride concentration by constructing a calibration curve for concentration versus absorbance and plotted with a correlation coefficient, r^2, close to unity.

Equilibrium ion-exchange isotherms

The equilibrium isotherms describe how the adsorbent interacts with the adsorbate. The correlation of experimental results to the adsorption model can help to understand the adsorption mechanisms, the adsorbent surface heterogeneity, and its importance in the design and operation of adsorption [9]. A practical approach to the two and three-parameter adsorption isotherm models was chosen in this study. Two commonly used isotherm models, namely, Langmuir and Freundlich, were employed to describe the adsorption of chromium present in the effluent [8,14,33–35]. Sufficient data were collected for isothermal identification of Cr^{6+} adsorption by using NO^{3-}resin. The adsorption isotherm was executed from the bench-scale experiments. However, the results may be vital for performing adsorption and regeneration to evaluate pilot plant operations.

Langmuir isotherm

Langmuir suggested a theory to describe the monolayer coverage of adsorbate over a homogeneous adsorbent surface [8,33]. The adsorption isotherm is based on the assumption that sorption takes place at specific homogeneous sites within the adsorbent. Once an adsorbate molecule occupies a site, no further adsorption can take place at that site. Thus, an

equilibrium value can be reached by using a linear Eq. (5).

$$\frac{C_e}{q_e} = \left(\frac{1}{q_m L}\right) + \left(\frac{C_e}{q_m}\right) \quad (5)$$

where C_e is the equilibrium concentration (mg/L), q_e is the equilibrium adsorption capacity, i.e., the amount of chromium adsorbed on anionic resin beads (mg/g), and n is the isotherm constant.

The slope and intercept were determined by plotting C_e versus C_e/q_e, and the essential characteristics of the Langmuir equation can be expressed in terms of dimensionless separation factor Eq (6).

$$RL = \frac{1}{(1 + LC_0)} \quad (6)$$

where RL is the dimensionless separation factor indicating the shape of the isotherm. L is the Langmuir constant related to adsorption energy, and C_o is the highest initial solute concentration.

By plotting the graph for C_e versus C_e/q_e, it was found that the R^2 value was in the range and approximately equaled 0.998. It was found the shape is linear. Therefore, the Langmuir isotherm fits the adsorption process as provided in Figure 3a. As the values of the synthetic effluent approximate that of the original effluent, the kinetics and isotherms were plotted only for the original effluent.

Freundlich isotherm

Freundlich suggested a model that describes the properties of heterogeneous adsorption systems, especially for organic compounds and highly interactive species on solid materials [8,33,34]. The studies from Freundlich showed that the ratio of the amount of solute adsorbed onto a given mass of adsorbent to the concentration of the solute in the solution was not a constant value at different concentrations. A multisite adsorption isotherm for heterogeneous surfaces is expressed as Eq. (7):

$$\log q_e = \log k_e + \frac{1}{n} \log C_e \quad (7)$$

where k_e and n are the Freundlich constants, Q_e is the ratio of the mass of adsorbate and mass of adsorbent, and C_e is the equilibrium concentration of the adsorbate.

The higher the n value, the stronger the adsorption intensity. The Freundlich constants were determined from the slope and intercept by plotting log q_e versus log C_e. The Freundlich isotherm model fit reveals that the adsorption of Cr^{6+} has a negative slope, as seen in Figure 3b, and the R^2 value is higher for the Langmuir isotherm model when compared to the Freundlich isotherm model. Therefore, Langmuir isotherm best suits the adsorption process. The isotherm parameters using the model fit are listed in Table 2. It can be inferred that those values of R^2 are greater than 0.985. These adsorption isotherm parameters allow easy identification of equilibrium ion exchange of anionic-based resin for different initial conditions.

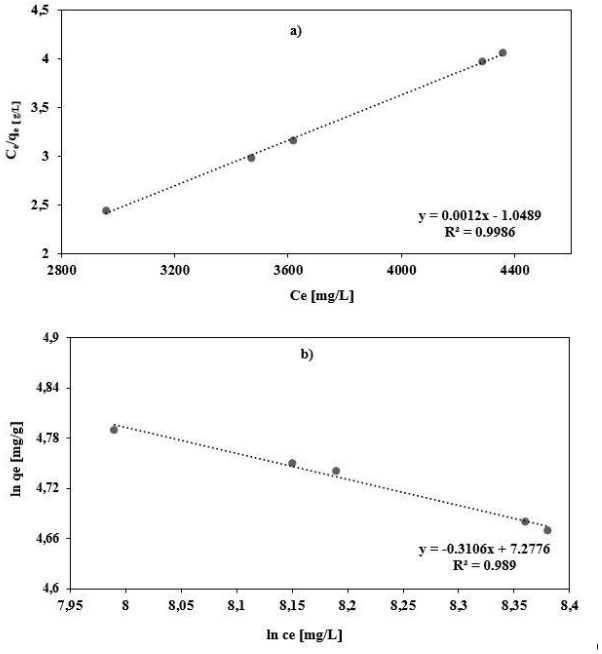

Figure 3. Langmuir (a) and Freundlich (b) isotherm for adsorption of chromium (VI) by anionic ion exchange (NO_3^-) resin.

Table 2. Adsorption isotherm parameters and linear regression coefficient, R^2.

	Langmuir			Freundlich		
	Q_m (mg/g)	R_L	R^2	K	n	R^2
Pore size (ϕ)	833.33	0	0.998	19.79	3	0.989

Kinetic studies

Kinetic models such as the Lagergren first-order, pseudo-second-order kinetic, Elovich, and intra-particle diffusion models were used to evaluate adsorption kinetics and rate-limiting steps. To investigate the suitability of pseudo-first-order Eq. (8) and second-order Eq. (9) kinetic models for the adsorption of hexavalent chromium, the Lagergren equation was utilized in this study [8,34,35].

Pseudo-first-order equation is given as:

$$\ln(q_e - q_t) = \ln q_e - k_1 t \quad (8)$$

where k_1 is the pseudo-first-order rate constants (min^{-1}), q_e and q_t are the amount of hexavalent chromium adsorbed (mg/g) at equilibrium, and time, t (min), respectively.

From the numerical analysis, the value q_e of 56.13 mg/g does not match the theoretical value of 43.584 mg/g. Therefore, it was observed that this process does not follow a pseudo-first-order reaction, as shown in Figure 4a.

Pseudo-second-order equation is given as:

$$\frac{t}{q_t} = \frac{1}{k_2 q_e^2} + \frac{t}{q_e} \quad (9)$$

where k_2 is the pseudo-second-order rate constant (g/mg·min), q_e and q_t are the amounts of hexavalent chromium adsorbed (mg/g) at equilibrium and at the time, t (min), respectively.

From the numerical calculations, the value of q_e= 49.75 mg/g and k_2=0.0122 g/mg min, which almost approximates the theoretical value of q_e= 43.584mg/g, and R^2 value is close to unity in second-order kinetics as provided in Figure 6. Therefore, it can be suggested that the experimental data accurately support the best fit from the pseudo-second-order kinetic model for the adsorption of hexavalent chromium on anionic resin beads.

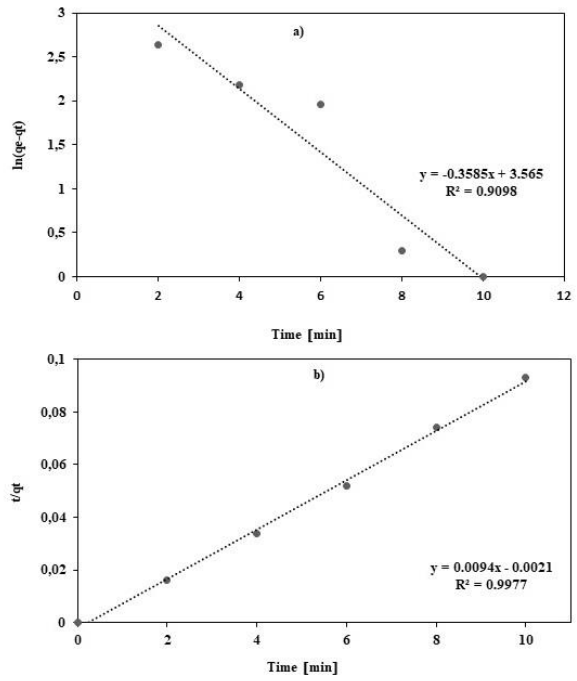

Figure 4. Pseudo first-order (a) and second-order (b) kinetics for adsorption of chromium (VI) by anionic ion exchange (NO_3^-) resin.

RESULTS AND DISCUSSION

The results obtained from the bench-scale experiments are discussed to understand the behavior of synthetic and actual pickling effluent for the treatment methods discussed above. The chemical composition of pickling effluent, prefiltering of pickling waste, hexavalent chromium removal by anionic ion exchange, desorption of hexavalent chromium, hydroxide precipitation of fluorides and metal ions (Fe (III), Cr (III), Cr (VI), and Ni (II)), secondary removal of fluoride using zirconium oxychloride and treatment process flow sheet for pilot scale demonstration is discussed in this section.

Characterization of pickling effluent

Pickling effluent of various lines from a metallurgical site in India was characterized and observed over time. Experimental investigations were performed to characterize the pickling effluent concerning its chemical composition: metal content (total Fe, Cr, and Ni), NO_3^-, F^-, pH, total dissolved salts, and total suspended solids.

Prefiltering of pickling waste

Two types of microporous membrane filters made from 5 µm pore size polypropylene (PP) and 5 µm polysulfone (PS) and a UF with 10 kDa pore size made of polyethersulfone (PES) were tested in the filtering of suspended particles removal in the effluent. The primary filtration was carried out using microporous membrane filters (a,b) and secondary filtration using UF (c) filter for further removal of finer particles that escaped the first microfilter. After experimentation, it was found that it is possible to remove 50% of primary suspended particles by employing a PS-based micro filter and up to 99.95% of suspended solids using PES UF. The prefiltration experimental trials were conducted using actual effluent from a pickling bath. A 20% reduction in solid content was observed using a polypropylene (PP) micro filter and a 50% reduction using a polysulfone micro filter. The addition of polyethersulfone (PES) based ultra-filter in this study achieved 99.95% removal of total suspended solids. Schmidt *et al.* (2007) [20] experimented with microfiltration as a prefilter to separate contaminated rinse water regeneration in steel pickling. Our study utilized the enhancement of microfiltration with ultrafiltration gave better efficacy for removing total suspended solids. It was found that 5 µm polyether sulfone has higher efficiency compared to 5 µm polypropylene.

Removal of Cr^{6+} using anion exchange process

An ion-exchange technology was used for the removal of hexavalent chromium. The decrease in Cr^{6+} concentration to permissible limits was achieved after passing the effluent for four cycles in the ion exchange resin. Exactly 1.0 mL of effluent was collected after

every cycle and analyzed for Cr^{6+} concentration. This process was repeated several times to verify the ion exchange-resin efficacy. The resin in the form of anionic resin was utilized to adsorb the anionic chromium in the form of dichromate and thus exiting only the remaining metal ions. The retained Cr^{6+} in the ion-exchange bed was eluted using sodium nitrate and sodium hydroxide to convert into sodium dichromate using partial crystallization. The ion exchange process was carried out for four cycles in three columns with three different resin materials equally distributed. Among the three resins utilized in this study, the highest efficiency was observed in Tulsion, FSMP 6301 Thermax resin, as provided in Table.1. After experimentation, it was found that Thermax resin had the lowest Cr^{6+} exit concentration of 0.14 mg/L. The other two Amberlite™4500CL, USA, and the INDION, Ion exchange, India resin materials had Cr^{6+} exit concentrations of 3.79 mg/L and 6.79 mg/L, respectively. It occurred due to the low porosity and high resin affinity with a smaller surface area to adsorb the dichromate ions. Earlier studies revealed the use of anionic resin (OH-type, Ambersep 900) for the adsorption of dichromate ions and converting it into chromic acid using strong base cationic (H-type, Ambersep 132) resin. The effective ion-exchange adsorption of Cr^{6+} using ion exchange for Na^{+} was reported in their study. The study illustrates that the complete desorption of Cr^{6+} in ion exchange is strongly dependent on a high feed flow rate and regeneration with a low flow rate [8].

Similar ion exchange resins were used to remove iron ions (Fe^{3+}) from pickling wastewater with hydrochloric acid. It is reported that Fe^{3+} ions were removed by anionic complexes using chloride anion. It is to be noted that anionic resins with complexing agents are highly efficient in the removal of iron, using Lewatit MP-500 resin up to 6 mg/L. Also, the exchange capacity increased with metal concentration. A low flow rate of 10 mL/min with elution carried out using 2.5-BV of water was observed from the earlier study. Marañón *et al.* (2000) [19] extended the above study using two different anionic resins, namely Lewatit MP-500 and Lewatit M-504, to remove Fe^{3+} and Zn^{2+} from HCl pickling bath. The test results demonstrated a very high capacity for removing Zn ions. The retained metals in the resin were eluted with DM water with 3-BV for iron and 6-BV for zinc. For both cases, it was reported that the decomposition of the metals retained chloro complexes releasing $ZnCl_2$ and $FeCl_3$. The resins were dissociated to chloride form to be reused again.

Desorption of hexavalent chromium

The economic feasibility of the adsorption process deals with the regeneration of the spent adsorbents in pilot plant operation. The study was performed in a strong base anionic resin Tulsion, FSMP 6301, as it had a higher affinity for the adsorption of hexavalent chromium than the other two resins employed in this research work. The percentage adsorption in each case was computed by using the following relation (10):

$$\%\ adsorption = \frac{Concentration\ of\ desorption, C_{des}}{Concentration\ of\ adsorption, C_{ads}} \qquad (10)$$

C_{des} and C_{ads} (mg/L) represent the effluent concentration in desorbed and adsorbed phases, respectively. Three experiments were employed to study the desorption of Cr (VI) resin using sodium nitrate and rinse water. All the experimental trials exhibited similar characteristics. From the mass balance of desorption studies, it was evident that 97.78±0.1% of hexavalent chromium accumulated inside the column was effectively removed using sodium nitrate.

The formation of sodium dichromate after passing the 5 eq/L sodium nitrate solution through the column was observed in this study. The resulting liquid was collected and evaporated at 107 °C in an oven. The evaporation of dichromate liquid was continued till the liquid reached the supersaturation state. The formation of dichromate began when the liquid reached the supersaturation stage. Hence the liquid was heated to reach its supersaturation stage. The initiation of crystal formation was detected as sodium dichromate crystals. The crystals grew when evaporation was further continued. This process was repeated for several days in the oven to obtain a few grams of sodium dichromate crystals. The presence of sodium in the desorbed liquid was verified using a flame photometer. It is noted that this is a cyclic process, and adsorption regeneration takes an enormous time to produce a bulk of sodium dichromate materials. It was consistent with the theoretical prediction for converting hexavalent chromium into sodium dichromate.

Hydroxide precipitation of fluoride and metal ions

The effect of pH is an important parameter controlling the uptake of fluoride and heavy metals from an aqueous solution. The Atomic Absorption Spectrophotometer (AAS) results of neutralization in the filtrate were studied in the pH range of 6.0–9.0. The precipitation of fluoride in the form of calcium fluoride is achieved by first adding 5 eq/L slaked lime solution from pH 0.3 to 2.0–2.5. Simultaneously, a 5 eq/L lye solution was utilized from pH 2.0–2.5 to 7.0–9.0 to achieve hydroxide precipitation of metal ions (Fe, Cr, and Ni). The effect of pH on the F^{-}, Fe, Cr, and Ni ions was tested at pH values ranging from 0.3 to 9.0 in this study. It was found that the optimum pH for removing

metal ions lies between 6.0 to 8.0.

Results showed that the addition of lime and lye to effluent influenced the reduction of calcium fluoride at pH 2.0–2.5 and hydroxide precipitation of metal ions (Fe, Cr, and Ni) at pH 7.0–9.0. From experimental results, it was observed between pH 0.3 and 2.0, the precipitation of calcium fluoride tends to be slower with excessive slaked lime addition, and from pH 2.0 to 9.0, the hydroxide precipitation of metal ions (Fe, Cr, and Ni) tends to be faster with less lye addition. The initial pH value from 0.6 to reaching pH 2.0 took 45 minutes using slaked lime. It was observed the pH quickly increased in less than 15 minutes retention time from pH 2.0 to 7.0 under lye addition. The time duration was averaged from several experimental trials. When the absolute value of the pH is at its highest, the precipitation retention time is lowered with a faster neutralization reaction. The results of pH balance versus time from the addition of slaked lime and caustic soda are provided in Figure 5.

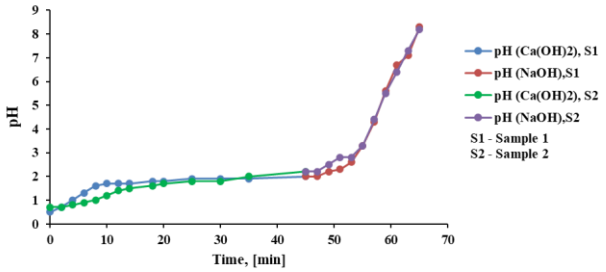

Figure 5. Addition of slaked lime and caustic in the effluent for pH balance after filtration and ion exchange process.

The neutralization of pickling wastewater has been vastly investigated by several investigators ever since the stainless-steel pickling process was implemented. The most common and traditional method for treating pickling wastewater is neutralization. The pH was increased, and most of the metal ions were precipitated, forming metal hydroxide sludge. The sludge can be safely discarded, but not the filtrate, since they contain a high nitrate concentration above the allowable limits. In the current environmental problems, wastewater treatment generated from the pickling process has become an area of interest. The disadvantage of only using the neutralization technique for pickling effluent is that the nitrate content in water is not reduced. It has led to further development and treatment methods for nitrate reduction [36]. In this study, neutralization treatment is used partly to remove metal ions (Fe, Cr, and Ni), and fluorides and nitrates were recovered.

Removal of fluoride using zirconium oxychloride

Zirconium oxychloride was employed to remove the fluoride in the separated filtrate. The primary filtrate from the neutralization process was polished using a zirconium chloride solution. The concentration of the polishing $ZrOCl_2$ solution, in addition to the separated filtrate, is dependent on the fluoride concentration from the previous neutralization process. It was tested to reduce the fluoride content from <10 mg/L to <0.2 mg/L in the treated filtrate using 100 ppm $ZrOCl_2$ solution from the actual effluent. The results were in concordance with Babu *et al.* (1993) [23], indicating the potential removal of fluoride in pickling wastewater with <100 mg/L, and F^- concentration drastically reduced to 0.12 mg/L using zirconium. The earlier study indicates that the zirconium hydroxide precipitate formed can be quantitatively removed using dilute sodium hydroxide. The present study reports an optimum pH level of 8.3 and 8.2 in the actual and synthetic polished filtrate. The final treated liquid contains sodium nitrate, which is used to regenerate the ion exchange column or can be sold for industrial use (e.g., bleaching agent). Also, a recent study by Gan *et al.* (2019) [24] experimented with the mechanism and performance of zirconium tetrachloride to remove fluoride using aluminum sulfate as a coagulant. The optimum pH was between 4.0 and 6.0 for the zirconium tetrachloride complex and between 8.0 and 10.0 for the zirconium aluminum sulfate complex. Their results also highlighted the use of the Zr-F complex as a superior material considering the Al-F complex as the resulting solution also showed a lower residual concentration of metal ions. The summary of results from this novel treatment process for treating the effluent generated during the pickling of stainless steel products is provided in Table 3.

Limitations of the proposed system for pilot scale demonstration

While scaling up the proposed process, the following limitations are to be considered. The condition of the micro and ultra-filters, ion exchange resin, and the best time to clean it. The replacement of poly sulfone micro-filter and polyether sulfone-based ultra-filter. The resin samples employed in the process shall be periodically checked for their physical and chemical stability, resin fouling, and clogging leading to channeling. Maintaining the concentration levels of metal ions in the pickling effluent. New ion exchange efficiency versus used ion exchange capacity may lead to inconsistent results.

Theoretical pilot plant calculations and economic benefit analysis

The volume of pickled waste per year at SSTP = 100 kL. The volume of pickled waste per month at SSTP = (100000 L)/12=8333.33 liters of pickled liquor. Commercial pilot plant operational days in a month = 20.

Number of liters to be treated per day= 8333.33/20 = 416.66 L/day. Approximately 70 L per hour for 6 hours of operation in a day. Pilot plant operation for techno commercial viability = 20 x 12 = 240 days/year = 240 x 24 = 5760 hours of operation per year. Demonstration pilot plant is 1/5 th of original plant = 70 L/hr = 14 to15 L/hr, operation per day = 84 L/day. Ion exchange capacity = 3 meq/g. Cr^{6+} concentration = 4.3 g/l = 4.3/51.99 = 0.082 meq/l × 150 = 12,450(meq/1000) = 12.5/3 = 4.13 = 5 kg. One week operation = 5 kg × 5 batches = 25 kg. At 60% utilization of anionic bed = 25/0.6 = 41 kg = 40 to 50 L resin column. Five batches of pickled waste to be treated 5 × 132 L = 660 L. After five batches of regeneration using 3 N $NaNO_3$, 12.5 eq Cr^{6+} to $NaNO_3$ = 12.5/3N = 4.2 L of theoretical regeneration. 20 L of 3N $NaNO_3$ to be used for regeneration after five operation cycles. 20 L of DM water, 50 L evaporator, and crystallizer (once in-week operational). The concentration of metal ions, fluoride, and nitrate on an industrial scale is provided from experiments. 70 g/l of F^- for CaF_2 = 78/(19 × 2) × 70 = 140. 11.7 g/l of Cr^{3+} for $Cr(OH)_3$ = 105/51.99 × 11.7 = 24 g. 70 g/l of Fe^{2+} for Fe $(OH)_3$ = 107/55.84 × 70 = 134 g. 25 g/l of Ni^{2+} for $Ni(OH)_2$ = 93/58.69 ×25 = 40 g. Total hydroxides = 140 + 24 + 134 + 40 = 338 g/L. Effluent treatment per batch = 84 L/day. Total hydroxides = 84 L/day × 338 g/L = 28,392~30 kg solids. Fluoride conversion to ZrF_4 = 100/1000 g/L × 132 × 167/(19 × 4) = 29 g/batch = 0.03 kg/batch. Total nitrate = 120 g/L. Per batch about 14 L = 120 x 14 = 1680 g. 90% recovery = 1680 x 0.9 = 1512 g. $NaNO_3$ in the treated effluent =1512/30 g/L = 50.5 g/L = 50.5 x 84/62 = 70 g/L as $NaNO_3$. To find out the amount of sludge produced in the precipitation/clarifier tank, we consider the following chemical reaction taking place inside the effluent bath for neutralization:

$$2HF + Ca(OH)_2 \rightarrow CaF_2 + 2H_2O$$
$$Fe(NO_3)_3 + 3NaOH \rightarrow Fe(OH)_3 + 3NaNO_3$$
$$Cr(NO_3)_3 + 3NaOH \rightarrow Cr(OH)_3 + 3NaNO_3$$
$$Ni(NO_3)_2 + 2NaOH \rightarrow Ni(OH)_2 + 2NaNO_3$$

A stoichiometry balance was calculated to determine the total sludge produced for neutralization consideration. Total sludge produced for 1 L of the effluent = 381 g. For 22 L of effluent per day (pilot plant), 7.2 L of NaOH and 1.7 L of $Ca(OH)_2$ are required to neutralize the effluent. The total volume of neutralizing agent is ~16 L.

From the above calculations, the initial cost in establishing the pilot plant cost, i.e., the present value of the future benefit, is between ₹.10 Lakhs to 20 Lakhs, i.e., $12,500–$18,500, on average, $15,500. The present value of the future costs will be approximately $10,500 by selling bulk chemicals from recycling.

The net present value (NPV) = Σ Present value of future benefits - Σ Present value of future costs = $15,500–$10,500 = $5000. Since the NPV is positive, the project shall be executed.

Table 1. Pickling effluent concentration before and after treatment with discharge limits [4].

Pollutant species	Concentration before treatment	Concentration after treatment	Concentration before treatment	Concentration after treatment	Permissible limit
	Original effluent		Synthetic effluent		
Iron, mg/L	179074	1.55	133500	0.58	3.0
Chromium, mg/L	27285	1.78	27252	0.14	2.0
Hexavalent chromium, mg/L	100	0.14	66	0.06	0.1
Nickel, mg/L	24070	1.29	15007	1.83	3.0
Fluoride, mg/L	69540	-	65500		15
Fluoride (Stage I, neutralization)	-	9.37	-	10.86	-
F^-, pH	-	5.3	-	5.1	-
Fluoride (Stage II, $ZrOCl_2$ polishing)	-	0.12	-	0.19	-
F^-, pH	-	8.3	-	8.2	6.0–9.0
Nitrate, mg/L	81450	52333	79950	46650	10
pH	0.50	8.3	0.30	8.2	6.0–9.0
Density, g/CC	1.20	1.10	1.10	1.09	
TDS, mg/L	520000	-	-	-	-
TSS, mg/L	72000	-	-	-	-

Flowchart for treatment of pickling waste

Based on the process mechanism for treating the UPS, a process-flow sheet was developed and schematically represented in Figure 6. A single-packed column of (NO^{3-}) type resin (50 kg) will be employed in the ion exchange column. The metallurgical plant at the site generated about 100 kL of spent pickling effluent per year. The volume of spent liquor per month was about 8340 L. A plant with 20 days per month of operation was envisaged. About 416 L of spent waste was treated daily with 70 L per hour for 6 hours of batch operation a day. The techno-commercial viability of plant operation was about 5760 hours per year, an operation of 240 days per year. The remaining 125 days were left for plant maintenance. The process started with pickling waste solution entering the micro-filter and UFs, where the total dissolved salts were captured. Second, the filtered liquid was passed through the resin column, where the dichromate was adsorbed onto the solid phase by NO^{3-}ions. The ion-exchange operation continued until the Cr^{6+} concentration in the exit aqueous solution exceeded the direct discharge limit of 0.1 mg/L [5].

As the resin was in nitrate form, hexavalent chromium adsorbed onto the resin was converted to sodium dichromate solids using a partial crystallization process at 60 °C. The remaining liquid entered the precipitation tank where much of Cr^{3+}, Fe^{3+}, $Ni^{2+,}$ and the bulk of F^- was precipitated to metal hydroxides by mixed addition of $Ca(OH)_2$ and NaOH and by adjusting the pH from acidic pH < 1.0 to base pH <9.0. The precipitated sludge was passed through a rotary filter to separate solid-liquid and toxic-free solids and was sent to disposal. $ZrOCl_2$ solution was prepared and added to the treated filtrate; dilute sodium hydroxide was added and stirred, and the solution was left to settle for 24 hours. The clear supernatant solution was drawn for fluoride analysis, and the optimum pH was determined. It was done to reduce the fluoride discharge levels to <1 mg/L in the treated effluent [22]. The solids zirconium fluoride and zirconium hydroxide formed in this process were removed. The final treated liquid contained only $NaNO_3$ solutions which were to be recycled.

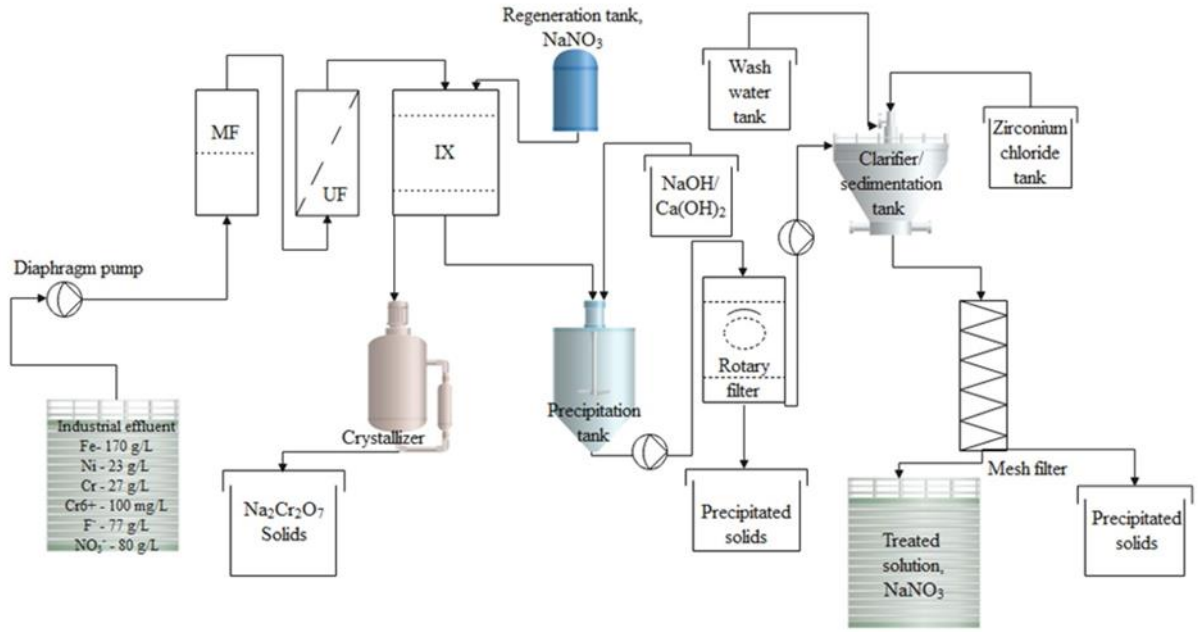

Figure 6. Developed process flow sheet for recycling used pickling wastewater.

CONCLUSION

Bench-scale experiments combining filtration, ion exchange process, and neutralization were utilized to treat pickling effluent. In step I, micro and ultrafiltration indicate a 99.95% removal of TSS/TDS. In step II, the ion exchange resin efficiently adsorbed Cr^{6+} and desorbed as $Na_2Cr_2O_7$ using $NaNO_3$ solution by partial crystallization. However, the process was time-consuming to lower the Cr^{6+} concentration. It is suggested to use sulfate-based agents to reduce Cr^{6+} to Cr^{3+}. In step III, neutralization treatment for the bulk of F^- using Ca $(OH)_2$, followed by hydroxide precipitation of metal ions (Fe, Ni, and Cr) using NaOH. The resulting filtrate was polished using $ZrOCl_2$ reagent to reduce F^- concentration to 0.12 mg/L. The resultant filtrate was recycled as $NaNO_3$. The adsorption isotherm of the toxic Cr^{6+} ion exchange resin followed the Langmuir model and pseudo-second-order kinetics up to 100 mg/L Cr^{6+} concentration. The presented characteristics of the pickling sludge composition may be useful in overcoming the traditional neutralization

problem by removing toxic Cr^{6+}, conversion of nitrate and allowable fluoride discharge, economic aspects of stainless-steel production, and general issues related to environmental pollution and sustainability. This indigenously developed technology can ultimately be tested on a pilot scale basis in batch mode.

ACKNOWLEDGMENT

This work was supported by Anadolu University, Scientific Research Project Commission under grant number 1410F412, and Eskisehir Technical University, This R&D project was supported by the Board of Research in Nuclear Sciences (BRNS), Department of Atomic Energy (DAE), Government of India, for sanction number 36(1)/14/53/2016-BRNS. The authors would like to extend their gratitude to Dr. S. Ganesh Vaidyanathan, Principal, Sri Venkateswara College of Engineering (SVCE), Sriperumbudur, Dr. N. Meyyappan (Head of the Department, Chemical Engineering, SVCE), and Shri. R.V.R.L. Visweswara Rao, Nuclear Fuel Complex, Hyderabad, for the collaborative research work.

ABBREVIATIONS

AAS	Atomic Absorption Spectrometry
CPCB	Central Pollution Control Board (India)
Cr^{3+}	Trivalent chromium
Cr^{6+}	Hexavalent chromium
DM water	Demineralized water
F^-	Total Fluorides
FM	Flame Photometry
MII	Metallurgical Industries of India
$NaNO_3$	Sodium itrate
$Na_2Cr_2O_7$	Sodium dichromate
NO^{3-}	Nitrates
Na^+	Sodium ions
PE	Process Flow Sheet
SBA	Strong Base Anion
SE	Synthetic Effluent
TDS	Total dissolved salts
TE	Treated effluent
TSS	Total suspended solids
UF	Ultrafilter
UPS	Used Pickling Solution
UV/VIS	Ultraviolet-Visible Spectrophotometer
$ZrOCl_2$	Zirconyl chloride

REFERENCES

[1] P. Lochynski, A. Sikora, B. Szczygiel, Surf. Eng. 33 (5) (2017) 395–403.http://doi.org/10.24425/aep.2021.139499.

[2] F.C. Richard, Alain C. M. Bourg, Water Res. 25 (1991) 807–816. https://doi.org/10.1016/0043-1354(91)90160-R.

[3] C. Cervantes, J. Campos-García, S. Devars, F. Gutiérrez-Corona, H. Loza-Tavera, J.C. Torres-Guzmán, R. Moreno-Sánchez, FEMS Microbiol. Rev. 25 (2001) 335–347. https://doi.org/10.1111/j.1574-6976.2001.tb00581.x.

[4] A. Banchhor, M. Pandey, P.K. Pandey, Res. J. Chem. Sci. 7 (7) (2017) 39–44. http://www.isca.in/rjcs/Archives/v7/i7/7.%20ISCA-RJCS-2017-024.pdf.

[5] Central Pollution Control Board, Government of India, The Environment (Protection) Rules, 1986 [Schedule-VI], General standards for discharge of environmental pollutants Part-a: Effluents, https://www.cpcb.nic.in/GeneralStandards.pdf [accessed 14 April 2018].

[6] R. David Szidon, J.S. Fritz, Separation of metal ions on chelating resin, https://dr.lib.iastate.edu/handle/20.500.12876/6951 [accessed 2 September 2018].

[7] E. Marañón, F. Suárez, F. Alonso, Y. Fernández, H. Sastre, Ind. Eng. Chem. Res. 38 (1999) 2782–2786. http://doi.org/10.1021/ie9806895.

[8] S.H. Lin, C.D. Kiang, Chem. Eng. J. 92 (2003) 193–199. https://doi.org/10.1016/S1385-8947(02)00140-7.

[9] F.J. Alguacil, M. Alonso, L.J. Lozano, Chemosphere 57 (2004) 789–793. http://doi.org/10.1016/j.chemosphere.2004.08.085.

[10] J. Laso, V. García, E. Bringas, A.M. Urtiaga, I. Ortiz, Ind. Eng. Chem. Res. 54 (2015) 3218–3224. https://doi.org/10.1021/acs.iecr.5b00099.

[11] A. Krepler (Ruthner Industrieanlagen-Aktiengesellschaft, Vienna, Austria), US4144092A (1978).

[12] C.J. Brown, M. Sheedy, Iron control and disposal: Proceedings of the second International Symposium on Iron Control in Hydrometallurgy, Canadian Institute of Mining, Metallurgy and Petroleum, Ottawa, Canada (1996), p.457-470. ISBN:9780919086715, 0919086713.

[13] M. Sugisawa, T. Sasaki, Y. Nishimoto, (Shinco Pantec Company Limited, Kobe, Japan), US4943360A (1988).

[14] C. Negro, M.A. Blanco, F. López-Mateos, A.M.C.P. DeJong, G. LaCalle, J. Van Erkel, D. Schmal, Sep. Sci. Technol. 36 (2001) 1543–1556. https://doi.org/10.1081/SS-100103887.

[15] Z. Tang, X. Ding, X. Yan, Y. Dong, C. Liu, Metals 8 (2018) 1–11. https://doi.org/10.3390/met8110936.

[16] T. Forsido, R. McCrindle, J. Maree, L. Mpenyana-Monyatsi, SN Appl. Sci. (2019) 1:1605. https://doi.org/10.1007/s42452-019-1649-z.

[17] Y. Kobuchi, H. Motomura, Y. Noma, F. Hanada, J. Membr. Sci. 27 (1986) 173–179. https://doi.org/10.1016/S0376-7388(00)82054-2.

[18] M. Sheedy, JOM 50 (1998) 66–69. https://doi.org/10.1007/s11837-998-0359-6

[19] E. Marañón, Y. Fernández, F.J. Súarez, F.J. Alonso, H.

Sastre, Ind. Eng. Chem. Res. 39 (2000) 3370–3376. https://doi.org/10.1021/ie0000414.

[20] B. Schmidt, R. Wolters, J. Kaplin, T. Schneiker, M. de los A. Lobo-Recio, F. López, A. López-Delgado, F.J. Alguacil, Desalination 211 (2007) 64–71. https://doi.org/10.1016/j.desal.2006.03.591.

[21] X. Bernata, A. Fortuny, F. Stüber, C. Bengoa, A. Fabregat, J. Font, Desalination 221 (2008) 413–418. https://doi.org/10.1016/j.desal.2007.01.100

[22] N.Y. Ghare, K.S. Wani, V.S. Patil, Int. J. Emerg. Trends Eng. Dev. 1 (2014) 318–326. https://rspublication.com/ijeted/2014/jan14/33.pdf.

[23] C. Anand Babu, B. Ayengar, K.B. Lal, R.V Amalraj, Waste Manage. 13 (1993) 279–283. https://doi.org/10.1016/0956-053X(93)90052-X.

[24] Y. Gan, X. Wang, L. Zhang, B. Wu, G. Zhang, S. Zhang, Chemosphere 218 (2019) 860–868. https://doi.org/10.1016/j.chemosphere.2018.11.192.

[25] X. Li, W. Li, S. Wang, Y. Cui, J. Zhao, Y. Zeng, F. Li, Adv. Mat. Res. 518-523 (2012) 2956–2960. http://doi.org/10.4028/www.scientific.net/AMR.518-523.2956.

[26] N.S. Yousef, R. Farouq, R. Hazzaa, Desalin. Water Treat. 57 (2016) 21925–21938. https://doi.org/10.1080/19443994.2015.1132474.

[27] C. Anand Babu, S. Swathi, L.S. Bhadrinarayanan, N. Meyyappan (Sri Venkateswara College of Engineering, Sriperumbudur, TamilNadu, India), 396960IN (2018). https://ipindiaservices.gov.in/PatentSearch/PatentSearch/ViewApplicationStatus.

[28] K.K. Onchoke, S.A. Sasu, Adv. Environ. Chem. 2016 (2016) 1–10. https://doi.org/10.1155/2016/3468635.

[29] M. Petrescu, E. Bucur, V. Danciulescu, A. Cozea, C.M. Borcescu, M. Bratu, G. Tanase, Rom. J. Ecol. Environ. Chem. 2 (2020) 185–192. https://doi.org/10.21698/rjeec.2020.223.

[30] N. Gayathri, N. Balasubramanian, Indian J. Chem. 40 (2001) 656–658. http://nopr.niscpr.res.in/bitstream/123456789/21062/1/IJCA%2040A%286%29%20656-658.pdf.

[31] V. Guimarães, H. Durão, M. Azenha, J. AOAC Int. 2014 (2014) 1–8. http://doi.org/10.5740/jaoacint.12-007.

[32] A.G. Macejunas, J. AWWA 61(1969) 311–313. https://doi.org/10.1002/j.15518833.1969.tb03762.x.

[33] P. Manikandan, K. Manjula Rani, S.V. Priya, V.N. Kowshalya, Nat., Environ. Pollut. Technol. 10 (1) (2011) 1–6. https://neptjournal.com/upload-images/NL-21-1-(1)-B-1641.pdf.

[34] N.K. Hamadia, X.D. Chena, M.M. Farid, M.G.Q. Lub, Chem. Eng. J. 84(2) (2001) 95–105. https://doi.org/10.1016/S1385-8947(01)00194-2.

[35] C. Marcu, C. Varodi, A. Balla, Anal. Lett. 54 (1–2) (2021) 140–149. https://doi.org/10.1080/00032719.2020.1731523.

[36] L. Dahlgren, Treatment of spent pickling acid from Stainless Steel Production: A review of regeneration technologies with focus on neutralization process for implementation in Chinese industry, http://www.diva-portal.org/smash/record.jsf?pid=diva2%3A473369&dswid=-3065 [accessed 14 January 2019].

LALGUDI SRINIVAS BHADRINARAYANAN

CHINTHALACHERUVU ANAND BABU

Department of Chemical Engineering, Sri Venkateswara College of Engineering, Tamil Nadu, India

NAUČNI RAD

OBRADA LUŽINE IZ PROCESA DEKAPIRANJA NERĐJAJUĆEG ČELIKA KUPLOVANE SA NEUTRALIZACIJOM SMOLOM: ISTRAŽIVAČKA STUDIJA

Jedan od najvećih ekoloških problema izazvanih industrijom nerđajućeg čelika su tečni efluenti koji nastaju tokom proizvodnih procesa. Oni sadrže visoku koncentraciju metalnih jona, kao što su Fe(III), Cr(III), Cr(VI) i Ni(II), u smeši HF i HNO_3, ulja i otpadne vode od ispiranja. Korišćena otpadna lužina iz procesa dekapiranja ima pH od 0,5 i koncentraciju ukupnih rastvorenih soli (TDS) od 520 g/l sa gustinom od 1,20 g/mL. Ovaj rad se fokusirao na reciklažu efluenta za dekapiranje kombinovanjem filtracije, smola i neutralizacije kako bi se efikasno uklonili metalni i fluoridni joni više od 99,5%. Da bi se uklonio TDS, laboratorijski eksperimenti su izvedeni korišćenjem mikro i ultrafiltera sa površinom membrane 0,2 m^2. Cr(VI) je uklonjen upotrebom TulsionFSMP 6301 smole i desorpcijom korišćenjem $NaNO_3$ i naknadnom konverzijom u $Na_2Cr_2O_7$ kao nusproizvoda. $Ca(OH)_2$ i NaOH korišćeni su za neutralizaciju i taloženje metalnih jona, a dobijeni filtrat je poliran korišćenjem $ZrOCl_2$ da bi se efektivno uklonili fluoridni joni do 0,12 mg/l. Nitrat je dobijen kao $NaNO_3$. Iz eksperimentalnih podataka za Cr(VI) korišćene su izotermne i kinetičke studije adsorpcije i razvijen je dijagram toka procesa koji se eventualno može testirati na većoj razmeri.

Ključne reči: otpadni rastvor za dekapiranje, jonska razmena, ultrafiltracija, precipitacija, industrijska reciklaža, tok procesa.

CI&CEQ
Chemical Industry & Chemical Engineering Quarterly

Available online at
Association of the Chemical Engineers of Serbia AChE
www.ache.org.rs/CICEQ

Chem. Ind. Chem. Eng. Q. 30 (1) 25–34 (2024) CI&CEQ

PUJI WAHYUNINGSIH[1]
MUSLIMAH MUSLIMAH[1]
YUSNAWATI YUSNAWATI[2]

LOCAL SALT PURIFICATION IN ACEH TIMUR REGENCY USING ALKALINE (KOH AND NAOH) ACTIVATED BENTONITE

Article Highlights

- The purification methods used to obtain a good quality salt
- Alkaline activation increase the characters of bentonite
- The activation process in bentonite increase in NaCl levels in local salts
- The alkaline activated-bentonite has binded Ca and Mg metals in local salts
- KOH-activated bentonite has a higher NaCl level than NaOH-activated bentonite

Abstract

Various purification methods have been developed to improve local salt quality, with the NaCl content above 94%. Bentonite is one of the materials used as binder impurities in purification. The purpose of the study was to synthesize a modified bentonite using an alkaline solution, which includes sodium hydroxide (NaOH) and potassium hydroxide (KOH) with various concentrations (1 M, 1.5 M, 2 M, and 2.5 M) and determined levels of Na^+, Ca^{2+} and Mg^{2+} metals using AAS. The bentonite and activating agent 1 M (1:10) were stirred for three hours. Then, the bentonite was dried for two hours in an oven at 110 °C. The activated bentonite was dried for four hours at 170 °C. The activated bentonite was characterized using XRD, FTIR, and SEM. The basal spacing d_{001} on the diffractogram bentonite was significantly unaffected by alkaline activation. FTIR analysis represents the stretching vibration of -OH shifts towards a lower wavenumber. Alkaline activation reduced impurities from bentonite and increased the pore surface's porosity. NaCl levels in people's salt increased after being activated using alkaline. The increase in Na^+ levels was followed by a decrease in Ca^{2+} and Mg^{2+} contents. KOH-activated bentonite had a higher NaCl level than NaOH-activated bentonite.

Keywords: bentonite, activation, alkaline, salt purification.

[1]Departemen of Chemistry, Faculty of Engineering, Universitas Samudra, Aceh, Indonesian

[2]Faculty of Engineering, Universitas Samudra, Aceh, Indonesian

SCIENTIFIC PAPER

UDC 666.322:66

Salt, one of Indonesia's primary commodities, strategically staples consumption and industrial needs [1]. East Aceh Regency is one of the salt-producing areas in Aceh, with a total production of 433.85 tons/year. However, the amount only meets 26% of the people's salt needs (approximately 1,350 tons/year) [2]. Therefore, efforts are necessary to increase production and improve salt quality according to the Indonesian National Standard (SNI). The salt produced also contains impurities such as $MgSO_4$, $CaSO_4$, $MgCl_2$, KCl, and soil impurities [1].

Salt in East Aceh Regency is still processed conventionally using the evaporation method. This process results in low-quality salt that does not meet the quality standard of SNI 3556: 2010, requiring NaCl content above 94% and the part not soluble in water less than 0.5% w/w. This local salt could not be consumed directly both for consumption and industrial needs since its NaCl content is still under Indonesian National Standard (SNI) Number. The results showed that the NaCl content was 10.98%, the water content was 7%, the insoluble part in water was 4% w/w, and

Correspondence: P. Wahyuningsih, Departemen of Chemistry, Faculty of Engineering, Universitas Samudra, Aceh, Indonesian, 24416.
E-mail: puji_wahyuningsih@unsam.ac.id
Paper received: 22 September, 2022
Paper revised: 15 February, 2023
Paper accepted: 12 May, 2023

https://doi.org/10.2298/CICEQ220922008W

the iodine content was 42.49 mg/kg. Impurities, such as metals Ca and Mg, cause the NaCl low level. The impurities should be precipitated to obtain a good quality salt using purification methods.

Several purification methods have been developed to increase the level of NaCl in salt to fulfill requirements, including the hydro extraction method [3,4], recrystallization with the addition of $Ca(OH)_2$, NaOH, and $CaCO_3$ [5,6], precipitation and evaporation methods [7,8], purification using sodium hydroxide (NaOH) [9], ion exchange method [10], and iodization method using a spray mixer [1]. A binder can minimize these impurities, such as NaOH, CaO, $Ba(OH)_2$, and $(NH_4)_2CO_3$ [7]. Another usable binder to remove impurities in salt is bentonite. There has not been a thorough investigation on bentonite as a salt binder yet, even though bentonite is widely used for the removal of metal ions and other impurities from water [11], as well as the removal of both anionic [12] and cationic [13] pollutants.

Bentonite is a low-cost material because it is abundantly available in nature [14,15]. Bentonite is a type of clay mineral with layered structures of the 2:1 type, including mostly montmorillonite. Two silica (Si^{4+}) tetrahedral sheets and one alumina (Al^{3+}) octahedral sheet make up the fundamental structure of bentonite [16]. A net negative electric is produced by replacing some trivalent ions, like Al^{3+}, with some divalent ions, such as Fe^{2+} or Mg^{2+} in the octahedral layer, or by replacing Si^{4+} with Al^{3+} in the tetrahedral layer [17,18]. Various exchangeable hydrated alkali and alkaline earth metal cations occupy the bentonite's interlayer space to compensate for the charge deficiency [19]. Bentonite has unique physicochemical characteristics that transform it into an efficient adsorbent for different types of pollutants, such as low permeability, low cost, strong absorptive affinity with inorganic and organic substances, large specific surface, high porosity, high cation exchange capacity [18,20–23], good adsorption capacity, expansible interlayer space, flexible, and tunable acidity [18], micro and mesoporous particles [21].

In other words, the quality of bentonite needs improvement through activation or treatment prior to being used effectively in the industry. Bentonite may be activated in four main methods to enhance many features. The procedures are: (i) chemical, (ii) physical, (iii) pillaring, and (iv) thermal. Inorganic acids (such as H_2SO_4 or HCl) activate bentonite to replace the exchangeable ions of bentonite during chemical processes [17]. The activators used are strong acids and bases, such as chloric acid (HCl), nitric acid (HNO_3), sulphuric (H_2SO_4), phosphoric acid (H_3PO_4), calcium chloride ($CaCl_2$), magnesium chloride ($MgCl_2$), zinc chloride ($ZnCl_2$), sodium hydroxide (NaOH), potassium hydroxide (KOH), sodium carbonate (Na_2CO_3), and sodium chloride (NaCl). The activation of bentonite by acids and bases makes the exchangeable cations in its structure more effective [24]. Bentonites and other clays' mineralogical and physicochemical properties substantially change with acid and alkali treatments [25]. The activation can increase the pore size and surface area to increase the adsorption performance of metal impurities (Ca and Mg) in the recrystallization process and improve the quality of salt.

A promising way of activating bentonite-like clays is alkaline activation. This technique is more versatile than acidic activation in obtaining more active sorbents and having lower requirements for the initial feedstock. Alkaline metal hydroxides and mixtures of calcium hydroxide with salts of mineral acids (e.g., NaCl, Na_2SO_4, Na_3PO_4, Na_2CO_3, etc.) are commonly used as alkaline agents. Alkaline treatment with sodium and calcium hydroxides using the salts mentioned above in the activating solutions will transform them into oxides of aluminum, iron, magnesium, and other metals, along with silica [24]. It may form an aluminosilicate component, calcium, aluminium hydrosilicates, and compounds with an intrinsically developed porous structure and acidic surfaces upon subsequent precipitation of the hydroxides and the activated clay.

The study aimed to synthesize and characterize bentonite from Aceh Tamiang and modified bentonite preheated with acid and alkaline solution. The acid and alkaline activation technique was applied for bentonite modification. Acid and alkaline were selected because of their activated bentonite with a high specific area, porosity, and adsorption capacity. The modified bentonite was studied to remove calcium and magnesium in salt water to increase the content of NaCl. Additionally, bentonite structure characteristics (raw and modified form) were investigated.

MATERIAL AND METHODS

Materials

The materials used were distilled water, aquabidest, a pH meter, Whatman 42 filter paper, sodium hydroxide (NaOH), and potassium hydroxide (KOH). They were obtained from E. Merck (Germany) in pro-analytical grade and used without further purification. Bentonite samples were collected from Aceh Tamiang Regency, Aceh Province, and salt samples from Aceh Timur Regency, Aceh Province.

Sample preparation

Sample preparation refers to the procedure

described elsewhere [26]. The bentonite was crushed and sieved using a 250-mesh sieve. Powder of bentonite (50 g) was put into the ultrasonic batch for 15 minutes with a power of 750 watts. Bentonite has been distributed at room temperature for equilibrium (about three days) to swell all the clay minerals. A filtration tank was filled with the bentonite solution and then agitated at a speed of 60 rpm. The solution was filtered, and the resulting sludge was called fraction 1. The filtrate resulting from stage I was stirred three times, left for three days, and filtered to produce a precipitate called fraction 2. Furthermore, the filtrate produced in stage II was stirred three times, let stand for seven days, and filtered until the sediment or fraction three was obtained. The filtrate in the final stage evaporated to produce fraction 4 [27,28].

Synthesis of activated-bentonite

Bentonite was crushed and repeatedly rinsed for three hours with distilled water. The solution was filtered using a centrifuge at 5000 rpm for 30 minutes. Then, the precipitate was dried for six hours at 110 ˚C, smoothed out, and sieved through a 270 mesh sieve. Additionally, sodium and potassium hydroxide at various concentrations (1 M, 1.5 M, 2 M, and 2.5 M) activated the bentonite. The bentonite and activating agent 1 M (1:10) mixture was agitated for three hours, and the filtrate was separated from the original mixture. The bentonite was neutralized by distilled water washing before being dried in a 110 °C oven for 2 hours. The activated bentonite was dried at 170 °C for 4 hours.

Samples characterization

Fourier transform infrared (FTIR) spectra of the materials (raw bentonite and modified bentonite) were recorded on a Shimadzu Prestige-21 FT-IR spectrophotometer. The X-ray diffractogram of the materials was recorded on an X-Ray Diffraction (XRD) Shimadzu S-6000. The X-Ray Diffraction data were obtained by XRD Multifex Rigaku with Ni-filtered Copper Kα radiation of wavelength 1.5406 Å operated at 40 kV and 30 mA. The surface morphology of the materials was measured by a scanning electron microscope (SEM) on JEOL JSM-6510.

The process of salt purification

Before crystallization, the salt product was purified using alkaline-activated bentonite as a binder for impurities. The salt sample was first dissolved to create a saturated salt solution. The alkaline-activated bentonite was added to the salt solution in a 1:10 ratio. The mixture was then stirred for three hours. Filtration was used to separate the solid phase from the filtrate in the mixture. The obtained filtrate was then evaporated to crystallize it. After obtaining the NaCl crystal product, it was dried for two hours at 110 °C. Atomic Absorption Spectroscopy (AAS) measured the concentration of Na^+ Ca^{2+}, and Mg^{2+} metals released from the bentonite into a solution mixture. The predicted values for Na, Ca, and Mg yields were obtained using the quadratic model [29].

RESULTS AND DISCUSSION

The characteristics of NaOH activated-bentonite

X-ray diffraction analysis (XRD) is measured to confirm the structural changes of bentonite after activation using NaOH. According to the standard pattern COD Card Number 96-901-0958, the diffraction peaks of raw bentonite are observed at 2θ = 19.7°, 26.5°, 34.91°, 54.34°, and 61.80°, which characterizes the bentonite structure with the montmorillonite type [30]. The diffraction peaks d_{001} of the raw bentonite at a low angle of 2θ = 2°–10° is a characteristic peak of smectites, which is the main clay mineral of bentonite. Unfortunately, this study did not detect the diffraction peaks d_{001} of the raw bentonite at 2θ<10° position.

The diffraction peaks d_{001} for NaOH activated-bentonite shifted to the left with increasing concentration of NaOH used in the activation process (Figure 1). It was confirmed that the smectite phase was present when a typical characteristic peak of the bentonite d_{001}, activated using 1 M NaOH, was at a 2θ value of 5.56° (d spacing 15.87 Å). With increasing NaOH activation concentration, the d_{001} peak shifted to the right and decreased the basal spacing value. After activation with NaOH 1.5 M, 2 M, and 2.5 M, the diffraction peaks of bentonite are 5.73° (d spacing 15.38 Å), 5.34° (d spacing 16.50 Å), and 5.48° (d spacing 16.09 Å), respectively. The cation exchange capacity was preferable in the presence of sodium cations between layers because sodium cations (Na^+) are more easily exchanged (except Li^+), and sodium has the greatest hydration strength and lower valence, reducing the bond strength with the bentonite mineral surface. The reaction was an exchange reaction between Ca^{2+} ions in the interlayer of the mineral bentonite with Na^+ ions in an alkaline solution.

The FTIR spectra of NaOH-activated bentonite and bentonite are represented in Figure 2. The absorption peaks of bentonite without activation appear at wave numbers, namely 466.77 cm^{-1}; 632.65 cm^{-1}; 979.84 cm^{-1}; 1103.28 cm^{-1}; 1654.92 cm^{-1}; 2040.69 cm^{-1}; 2441.88 cm^{-1}; 2781.35 cm^{-1}; 3402.43 cm^{-1}; 3606.89 cm^{-1}; and 3645.46 cm^{-1}.

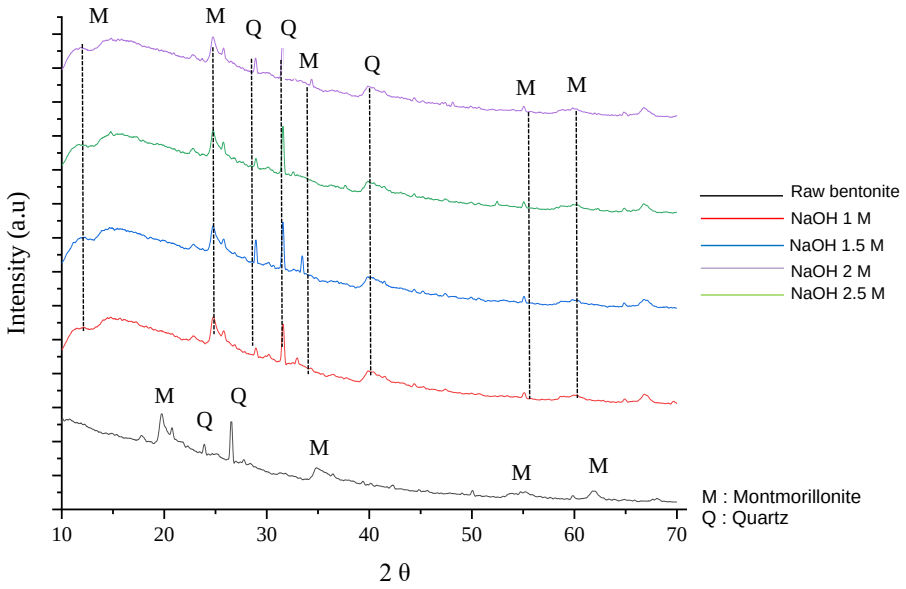

Figure 1. Difractogram XRD NaOH-activated bentonite.

The absorption peaks at 3606.89 cm^{-1} and 3402.43 cm^{-1} were caused by stretching vibrations of the -OH group from the bentonite structure and water molecules. The absorption band at 1654.92 cm^{-1} was the deformation of the OH group on the water molecule, while the absorption band at 1103.28 cm^{-1} was the stretching vibration of Si-O-Si. The peak in the lower wavenumber region (1200 cm^{-1}–400 cm^{-1}) indicated that bentonite is dominated by bentonite groups. The absorption bands at 979.84 cm^{-1}, 632.65 cm^{-1}, and 632.65 cm^{-1} were Al-Al-OH stretching, Si-O-Si stretching, and Si-O-Si bending, respectively [31,32]. Activation of NaOH did not produce a significant change in the absorption of bentonite. Instead, the absorption shifted to a lower wavenumber region than bentonite without activation. In NaOH-activated bentonite, absorption appears at 931 cm^{-1} due to the OH bending vibration in octahedral Al-Al-OH [31].

The wavenumber of 3448 cm^{-1} in the unactivated bentonite (Figure 1) shows the stretching vibration of the -OH group being hydrated by the adsorbed water molecules. There was an absorption band at 1635.26 cm^{-1}, representing the H-O-H bending vibration of the water in the bentonite interlayer [27]. The appearance of a strong absorption band with high intensity at 1036.98 cm^{-1} showed the asymmetric stretching vibration of Si-O. The -OH stretching vibration shifts towards a lower wavenumber with increasing NaOH concentration. The interaction of octahedral -OH with Na^+ cations in NaOH activator solution causes the interaction of the O and H bonds in the -OH group to weaken, resulting in a decrease in wavenumber and intensity of adsorption peak -OH groups.

Raw bentonite has a smooth aggregate surface and more densely packed flakes (Figure 3a). However, when activated with NaOH, the aggregate looks foggy and ragged (Figure 3 (b–e)). It is consistent with the specific surface areas of the NaOH-activated bentonite. The clay surface has become more porous due to the leaching of cations and impurities. The leaching increased the pore surface area and caused the creation of new pores [33]. The surface of the raw bentonite sample (Figure 3a) had larger pores between the particles than the NaOH-activated bentonite [34].

The characteristics of KOH activated-bentonite

The structural changes in the bentonite to the alkaline treatment were studied using the X-ray diffraction technique. Figure 4 depicts the XRD profile of the raw bentonite and KOH-activated bentonite at various concentrations. A typical characteristic peak of the d_{001} of bentonite activated using 1 M KOH was at a 2θ value of 5.48° (d spacing 16.09 Å), confirming the smectite phase's presence. The d_{001} peak shifted to the left and caused an increase in the basal spacing value with increasing KOH activation concentration. The diffraction peaks d_{001} of bentonite after activation using KOH 1.5 M, 2 M, and 2.5 M are 5.46° (d spacing 16.15 Å); 5.40° (d spacing 16.32 Å), and 5.36° (d spacing 16.44 Å), respectively. The displacement of the diffraction peaks at a low angle was followed by a decrease in the intensity of the peaks, indicating a decrease in crystallinity in the presence of activated bentonite using KOH solution.

The wavenumber 3448 cm^{-1} in unactivated bentonite, as shown in Figure 5 (a–e), shows the stretching vibration of the OH group of the silanol group

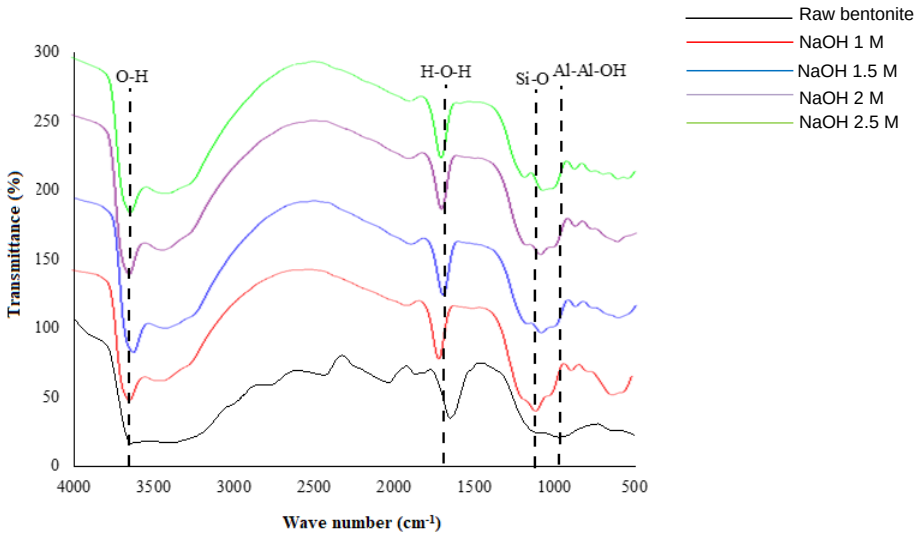

Figure 2. FTIR Spectrum NaOH-activated bentonite.

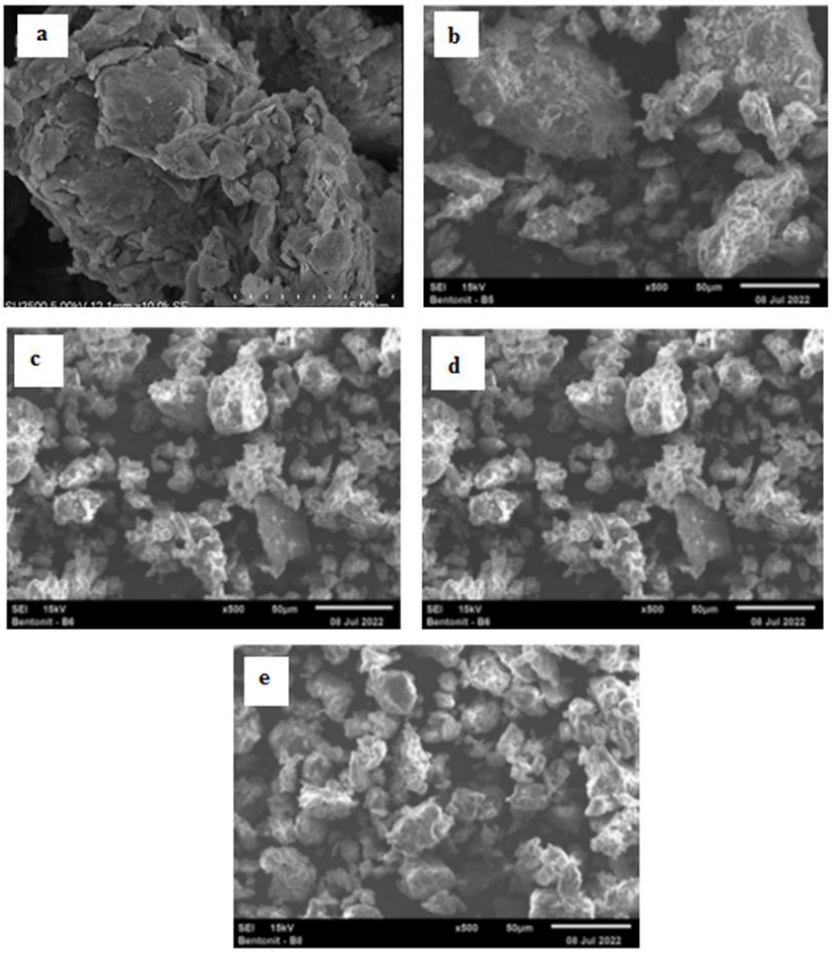

Figure 3. Micrograph SEM NaOH-activated bentonite.

(Si-OH) coordinated to the octahedral Al^{+3} cation [31]. The -OH stretching vibration shifts towards a lower wavenumber with increasing KOH concentration. The interaction of the -OH octahedral with the K^{+} cation in the KOH activator solution causes the interaction of the O and H bonds in the -OH group to weaken, decreasing

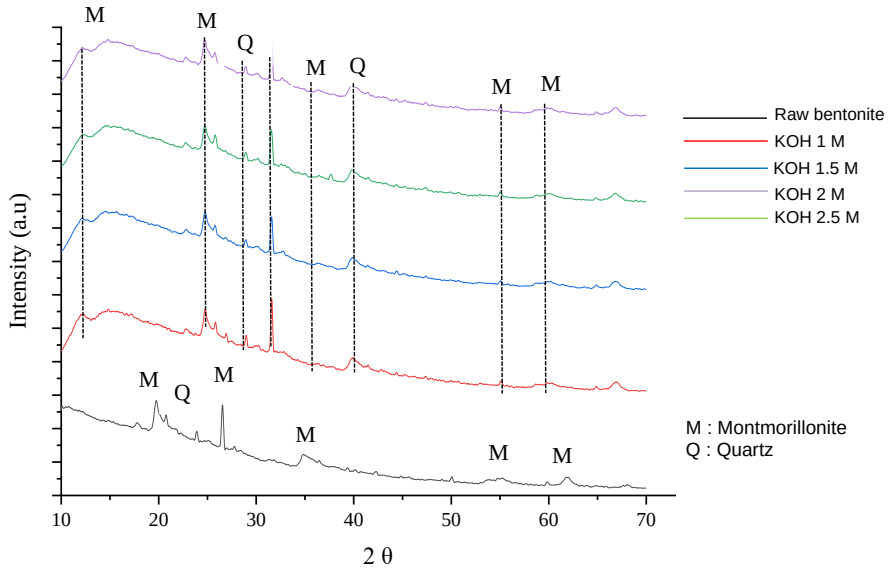

Figure 4. Difractogram XRD KOH-activated bentonite.

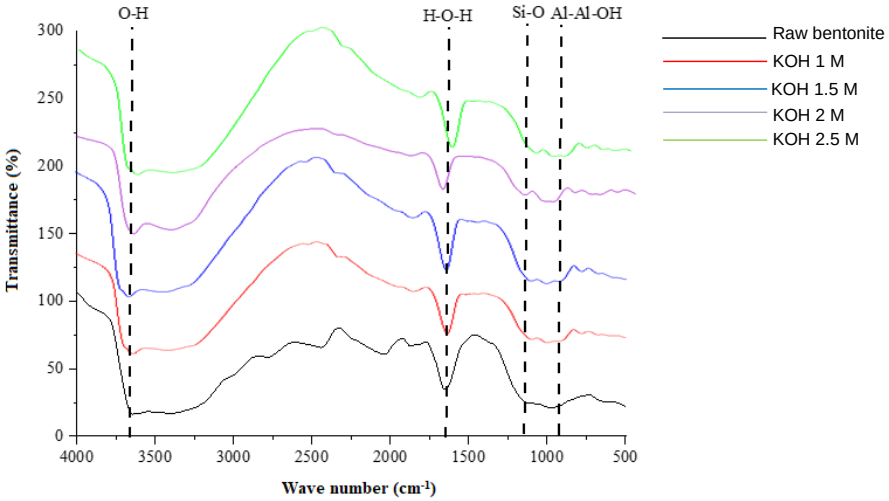

Figure 5. FTIR Spectrum KOH-activated bentonite.

the wavenumber. There was an absorption band at 1635.26 cm^{-1}, which represents the H-O-H bending vibration of water, and an absorption band at 1036.98 cm^{-1} for the asymmetric stretching vibration of Si-O-Si [31].

The SEM micrograph in Figure 6(a–e) shows that the bentonite microstructure has a smaller pore, a more uniform distribution, and a prism type [32]. The surface of natural bentonite seems to be a smooth aggregate and contains more densely packed flakes (Figure 6a). The surface of bentonite activated with KOH forms coarser aggregates than bentonite without activation (Figure 6b–e). After alkaline treatment, the particles became smaller and thinner [33]. The surface of bentonite becomes more porous due to the leaching of cations and impurities after treatment with KOH. KOH activation in bentonite results in more open pores. The higher the concentration of KOH, the smaller the particle size and the more uniform the pore size distribution, and vice versa. Smaller pore size indicates a larger pore surface area, thereby increasing the adsorption capacity of heavy metals.

The effect of alkaline concentration of activated-bentonite on NaCl level

The activator used was a strong base, namely NaOH and KOH. The performance of alkaline-activated bentonite and bentonite as activators in the purification process of people's salt produced by salt farmers in East Aceh Regency was conducted by determining the levels of Na^+, Ca^{2+}, and Mg^{2+} metals using Atomic Absorption Spectrophotometer (AAS). The results of AAS analysis of Na^+, Ca^{2+}, and Mg^{2+} metals before and

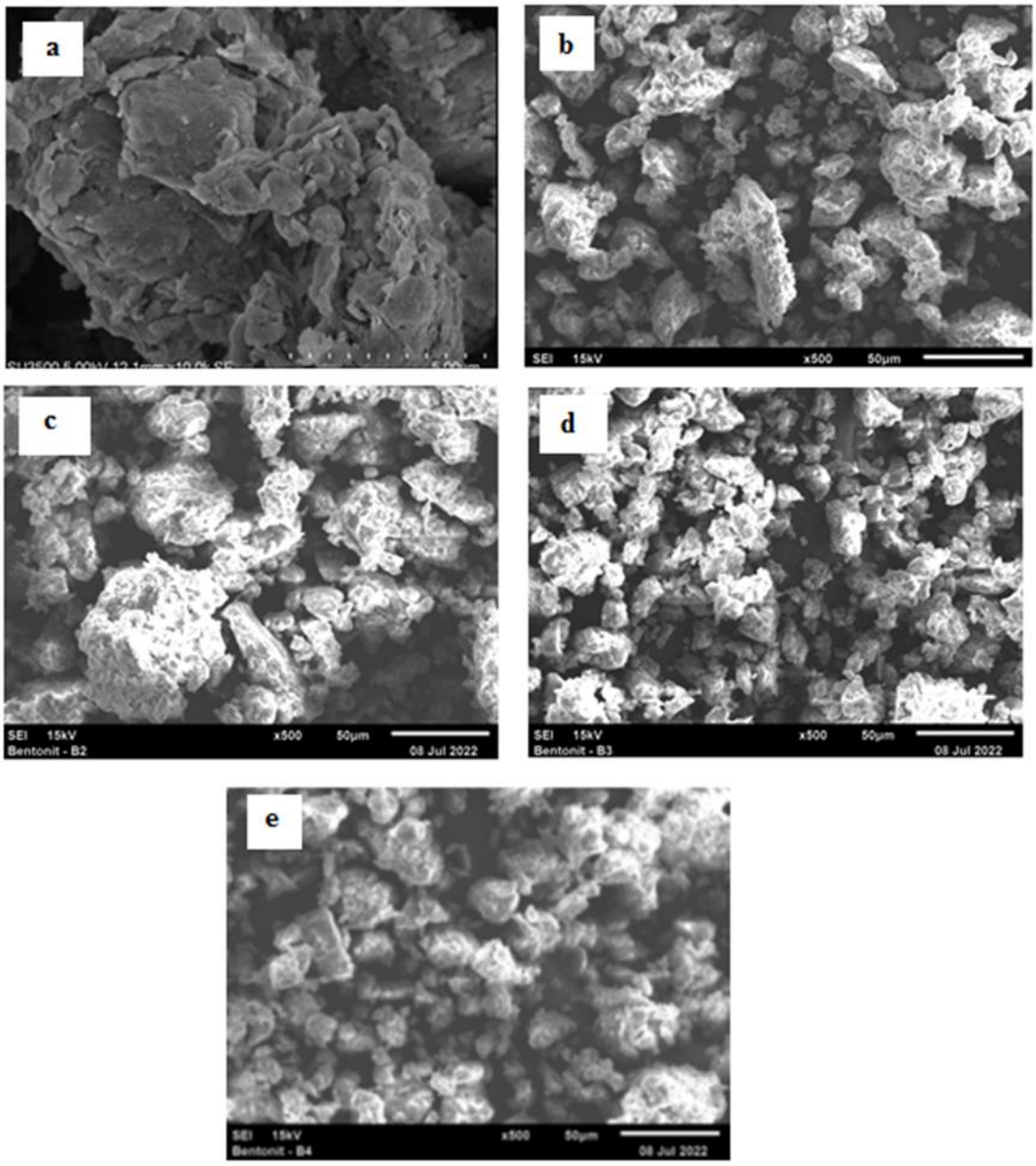

Figure 6. Micrograph SEM KOH-activated bentonite.

after recrystallization using KOH and NaOH are shown in Figure 7 and Figure 8.

Figure 7 and Figure 8 represent the levels of Na^+, Ca^{2+}, and Mg^{2+} metals before and after recrystallization using strong bases (NaOH and KOH). Na^+, Ca^{2+}, and Mg^{2+} values in people's salt before leaching using NaOH and KOH are 3032.50 ppm, 48.89 ppm, and 533.03 ppm, respectively. Figure 7 displays Na^+ levels in people's salt increased after being activated using 1 M KOH is 4004.50 ppm and decreased with increasing KOH concentration are 3796.05 ppm (1.5 M), 3829.05 ppm (2 M), and 3755.60 ppm (2.5 M). The increase in NaCl levels was followed by a decrease in the levels of Ca^{2+} and Mg^{2+} metals because the activation process can increase the pore size and surface area to increase the adsorption performance of activated bentonite against metal impurities, such as Ca^{2+} and Mg^{2+} in the crystallization process and improve the quality of the recrystallization results. The activation increases the surface area and porosity. In addition, bentonite also has a lot of negative charges (O-) contained in the tetrahedral and octahedral layers, which can bind metals such as Ca and Mg.

The Na^+ level in KOH-activated bentonite is greater than that of NaOH-activated bentonite. The Na^+ levels in people's salt increased after being activated using NaOH 1 M is 3704.10 ppm and increased with increasing KOH concentration are 3794.90 ppm (1.5 M), 3953.55 ppm (2 M), and 3846.25 ppm (2.5 M). The high Na^+ level was due to the presence of Na^+

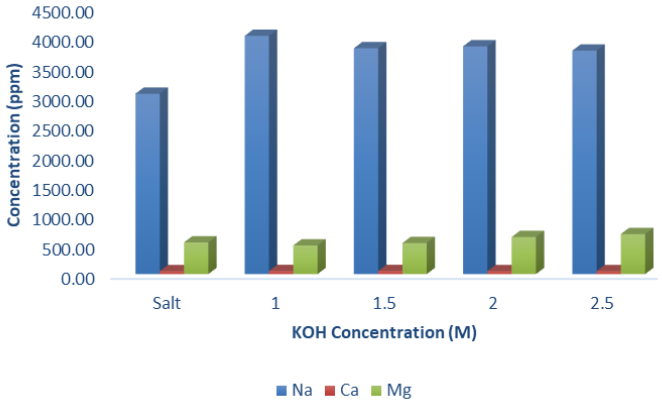

Figure 7. The results of AAS analysis of NaCl, and Ca and Mg metals before and after recrystallization using KOH-activated bentonite.

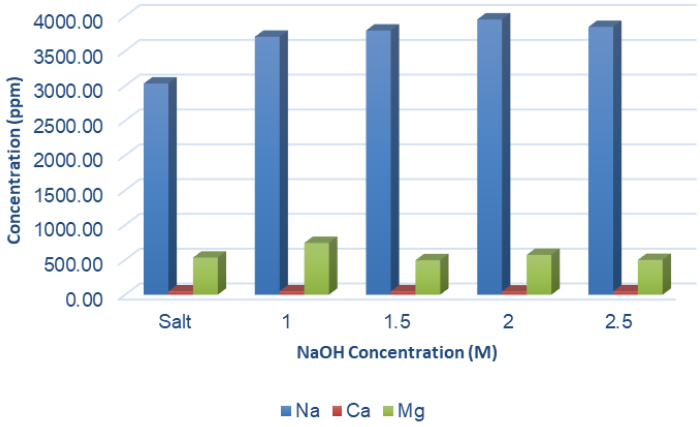

Figure 8. The results of AAS analysis of NaCl, and Ca and Mg metals before and after recrystallization using NaOH-activated bentonite.

cations unexchanged between bentonite layers, while in KOH activation, Na^+ cations will be exchanged with K^+ from the KOH activator. The concentration of NaOH producing the highest level of Na^+ is 2 M. At a concentration of 2 M, Ca^{2+} and Mg^{2+} metals will precipitate to form $Ca(OH)_2$ and $Mg(OH)_2$ during the filtration process before recrystallization [9]. It follows the research by [10], stating that a concentration of 2 M is very effective in increasing Na^+ levels. The overly high concentration of NaOH makes the bentonite structure unstable due to the dealumination process, so the NaCl content decreases at 2.5 M NaOH concentration.

CONCLUSION

Significantly, the activation of bentonite using alkaline activation (NaOH and KOH) have not resulted in changes to the physicochemical properties of bentonite. However, it can remove impurities contained in bentonite. Therefore, it can increase pore size and porous in surface materials. According to XRD analysis data, alkaline activation to bentonite causes a minor shift toward a higher angle and does not alter the basal spacing d_{001} on the diffractogram. The FTIR analysis indicated that the stretching vibration of -OH shifts towards a lower wavenumber as alkaline concentration increases. The wavenumber is reduced because the -OH of the octahedral becomes weak due to contact cations in the layer with the activator solution. The NaCl level in KOH-activated bentonite was greater than that of NaOH-activated bentonite. The increase in Na^+ levels was followed by a decrease in the levels of Ca^{2+} and Mg^{2+} metals because the activation process can increase the pore size and surface area to increase the adsorption performance of activated bentonite against metal impurities, such as Ca^{2+} and Mg^{2+} in the crystallization process, and improve the quality of the recrystallization results.

ACKNOWLEDGMENT

We would like to thank Kemendikbud for funding the research through the grant of Penelitian Dasar Kompetitif Nasional (PDKN) Tahun 2022 with contract

number 323/UN54.6/PG/2022. We also thank UPT. Laboratorium Dasar Universitas Samudra and Laboratorium Politeknik Lhokseumawe for supporting facilities in the research.

REFERENCES

[1] T. Widjaja, A. Altway, I. Gunardi, L. Pudjiastuti, D. Nury, A. Nabila, N. Prasetyawati, M. Saifulloh, Noviyanto, IOP Conf. Ser. Mater. Sci. Eng. 543 (2019) 012024. https://iopscience.iop.org/article/10.1088/1757-899X/543/1/012024.

[2] Aceh Province Regional Statistic. 2021. https://datadpmptsp.acehprov.go.id.

[3] R. Astuti, C. Yulianti, R. Prasetya, J. Pharm. Sci. 1 (2016) 9–14. https://doi.org/10.53342/pharmasci.v1i1.46.

[4] W. Nurhikmah, R. Irawati, J. Ilm. Techno. Enterp. Acta 5 (2020) 10–11. http://journal.unifa.ac.id/index.php/tea/article/view/189.

[5] I. Ihsannudin, S. Pinujib, S. Subejo, B.Bangko, Water. Pract. Technol. 5 (2016) 395–409. https://doi.org/10.15294/edaj.v5i4.22177.

[6] A. Lukum, E. Mohamad, A. Tangahu, S. Ohi, J. Phys. Conf. Ser. 1968 (2021) 012013. https://iopscience.iop.org/article/10.1088/1742-6596/1968/1/012013.

[7] Jumaeri, T. Sulistyaningsih, D. Alighiri. J. Phys. Conf. Ser. 1918 (2018) 032023. https://iopscience.iop.org/article/10.1088/1742-6596/1918/3/032023.

[8] E. Tarmizi, K. Sunandar, A. Wibowo, J. Pangan Agroind. 9 (2021) 165–172. https://jpa.ub.ac.id/index.php/jpa/article/view/774/552.

[9] M. Rahem, A. Kartika, Juvenil 1 (2020) 461–467. https://journal.trunojoyo.ac.id/juvenil/article/view/8935.

[10] C. Pujiastuti, K. Sumada, Y. Ngatilah, J Phys. Conf. Ser. 953 (2018) 012215. https://iopscience.iop.org/article/10.1088/1742-6596/953/1/012215.

[11] W. Musie, G. Gonfa, Results Eng. 14 (2022) 100440. https://doi.org/10.1016/j.rineng.2022.100440.

[12] X. Chen, L. Wu, F. Liu, P. Luo, X. Zhuang, J. Wu, Z. Zhu, S. Xu, G. Environ. Sci. Pollut. Sci. Res. 25 (2018) 15980–15989. https://link.springer.com/article/10.1007/s11356-018-1794-8.

[13] S.S. Gupta, K. Bhattacharyya, RSC. Adv. 4 (2014) 28537–28586. https://doi.org/10.1039/C4RA03673E.

[14] R. Elmorsi, G. Mostafa, K. El-Sherbini, J. Environ. Chem. Eng. 9 (2021) 104606. https://doi.org/10.1016/j.jece.2020.104606.

[15] S. Baloyi, J. Moma, J. Environ. Chem. Eng. 8 (2020) 104186. https://doi.org/10.1016/j.jece.2020.104186.

[16] A. Maged, J. Iqbal, S. Kharbish, I. Ismael, A. Bhatnagar, J. Hazard. Mater. 384 (2020) 121320. https://doi.org/10.1016/j.jhazmat.2019.121320.

[17] H. Rahimzadeh, M. Tabatabaei, M. Aghbashlo, H. Panahi, A. Rashidi, S. Goli, M. Mostafaei, M. Ardjmand, A. Nizami, Front. Energy Res. 6 (2018) 1–10. https://www.frontiersin.org/articles/10.3389/fenrg.2018.00137/full.

[18] J. Liu, X.Q, Wang, B.B, Yang, C.L, Liu, C. L, Xu, W.S, Dong, Renewable Energy 120 (2019) 231–240. https://doi.org/10.1016/j.renene.2017.12.104.

[19] B.S. Kumar, A. Dhakshinamoorthy, K. Pitchumani, Catal. Sci. Technol. 4 (2014) 2378–2396. https://doi.org/10.1039/C4CY00112E.

[20] M.K. Uddin, Chem. Eng. J. 308 (2017) 438–462. https://doi.org/10.1016/j.cej.2016.09.029.

[21] N. Ayub, M.N, Chaudhry, Pol. J. Environ. Stud. 30 (2022) 1039–1050. https://doi.org/10.15244/pjoes/124739.

[22] S. Barakan, V. Aghazadeh, Environ. Sci. Pollut. Res. 28 (2021) 2572–2599. https://doi.org/10.1007/s11356-020-10985-9.

[23] P. Belousov, A. Semenkova, T. Egorova, A. Romanchuk, S. Zakusin, O. Dorzhieva, E. Tyupina, Y Izosima, I. Tolpeshta, M. Cherno, V. Krupskaya, Minerals 9 (2019) 625. https://doi.org/10.3390/min9100625.

[24] A. Vezentsev, N. Volovicheva, S. Korol'kova, P. Sokolovskiy. Russ. J. Phys. Chem. 96 (2022) 381–386. https://doi.org/10.1134/S0036024422010265.

[25] H. Bayram, G. Ustunisik, M. Önal, Y. Sarıkaya, Clay Miner. 56 (2021) 148–155. https://doi.org/10.1180/clm.2021.28.

[26] H. Tisna, Y. Amri, T.A. Fadly, Orient. J. Chem. 35 (2019) 1535–1538. http://dx.doi.org/10.13005/ojc/350509.

[27] B. Tyagi, C.D, Chudasama, R.V, Jasra, Spectrochim. Acta 64 (2006) 273–278. https://doi.org/10.1016/j.saa.2005.07.018.

[28] S. Gea, F. Meikhal, T. Hidayat, Marpongahtun,. J. Phys.: Conf. Ser. 1116 (2018) 042011. https://iopscience.iop.org/article/10.1088/1742-6596/1116/4/042011.

[29] A. Imessaoudene, S. Cheikh, J. Bollinger, L. Belkhiri, A. Tiri, A. Bouzaza, A. El Jery, A. Assadi, A. Amrane, L. Mouni, Appl. Sci. 12 (2022) 7587. https://doi.org/10.3390/app12157587.

[30] R. Nino, N.D.E. Purba, A. Kristiani, E. Agustian, R.R. Widjaya, A.A. Dwiatmoko, Catal. Commun. 174 (2023) 106598. https://doi.org/10.1016/j.catcom.2022.106598.

[31] T. Ibigbami, A. Adeola, D. Olawade, O. Ore, B. Isaac, A. Sunkanmi, Water. Pract. Technol. 17 (2022) 784–797. https://doi.org/10.2166/wpt.2022.018.

[32] Ruslan, Khairuddin, J. Hardi, M. Mirzan, AIP Conf. Proc. 2243 (2020) 030022. https://doi.org/10.1063/5.0001508.

[33] P. Rout, L. Garanayak. IOP Conf. Ser. Mater. Sci. Eng. 970 (2020) 012012. https://iopscience.iop.org/article/10.1088/1757-899X/970/1/012012.

[34] W. Musie, G. Gonfa. Results in Engineering. 14 (2022) 100440. https://doi.org/10.1016/j.rineng.2022.100440.

PUJI WAHYUNINGSIH[1]
MUSLIMAH MUSLIMAH[1]
YUSNAWATI YUSNAWATI[2]

[1]Departemen of Chemistry, Faculty of Engineering, Universitas Samudra, Aceh, Indonesian

[2]Faculty of Engineering, Universitas Samudra, Aceh, Indonesian

PROČIŠĆAVANJE LOKALNE SOLI U REGIONU ACEH TIMUR KORIŠĆENJEM ALKALNOG (KOH i NAOH) AKTIVISANOG BENTONITA

Razvijene su različite metode prečišćavanja za poboljšanje kvaliteta lokalne soli, sa sadržajem NaCl iznad 94%. Bentonit je jedan od materijala koji se koristi za vezivanje nečistoća u postupku prečišćavanju. Cilj istraživanja je bioa da se sintetiše modifikovani bentonit korišćenjem alkalnog rastvora, koji uključuje natrijum hidroksid (NaOH) i kalijum hidroksid (KOH) različitih koncentracija (1 M, 1,5 M, 2 M i 2,5 M) i utvrđenih nivoa Na, Ca. i Mg pomoću AAS. Bentonit i sredstvo za aktiviranje 1 M (1:10) su mešani tri sata. Zatim je bentonit sušen dva sata u pećnici na 110 °C. Aktivirani bentonit je sušen četiri sata na 170 °C i karakterisan metodama KSRD, FTIR i SEM. Bazalni razmak d_{001} na difraktogramu bentonita nije značajno pod uticajem alkalne aktivacije. FTIR analiza je ukazala na pomeranje vibracije istezanja -OH ka nižem talasnom broju. Alkalna aktivacija je smanjila nečistoće u bentonitu i povećala poroznost površine pora. Nivoi NaCl u soli za ishranu se povećavaju nakon alkalne aktiviranje. Povećanje nivoa Na^+ praćeno je smanjenjem sadržaja Ca^{2+} i Mg^{2+}. Bentonit aktiviran KOH imao je viši nivo NaCl od bentonita aktiviranog NaOH.

Ključne reči: bentonit, aktivacija, alkalna, prečišćavanje soli.

NAUČNI RAD

CI&CEQ
Chemical Industry & Chemical Engineering Quarterly

Available online at
Association of the Chemical Engineers of Serbia AChE
www.ache.org.rs/CICEQ

Chem. Ind. Chem. Eng. Q. 30 (1) 35–46 (2024) CI&CEQ

CEMRE AVŞAR[1,2]
SUNA ERTUNÇ[2]

FLUORIDE REMOVAL FROM PHOSPHOGYPSUM: A STUDY ON A PRE-INDUSTRIAL SCALE AND ITS MATHEMATICAL ANALYSIS

[1]Toros AGRI Industry and Trade Co. Inc. R&D Center, Mersin / Turkey

[2]Ankara University, Department of Chemical Engineering, Ankara/ Turkey

Article Highlights

- A cost-effective route for fluoride removal from phopshogypsum on pre-industrial scale is proposed
- Statistical analysis and mathematical modeling were applied to the purification process
- Optimum conditions for high-performance and cost-effective industrial treatment determination

Abstract

This study discusses fluoride removal efficiency from phosphogypsum (PG) on a lab-scale experiment matrix designed by the Box-Behnken method. Temperature, solid/liquid ratio, and time were supposed to influence fluoride removal efficiency from PG by various salt solution media. Experiment matrices were designed according to salt solution types: seawater, 5% NaCl, and 10% NaCl solutions. The factor-response analysis showed a direct proportionality between fluoride removal efficiency and temperature. The optimum fluoride removal conditions based on the experimental data obtained by the multi-variable design matrix were determined by the Design Expert v.12 software. The optimum temperature, time, and solid/liquid ratio were 80 °C, 3 h, and 0,174 for seawater. The software predicted a 73,31% fluoride removal efficiency at the optimum conditions, whereas the experimental value was 74,99%. Since the actual vs. predicted data show high consistency, results might also be useful when industrial-scale fluoride removal to a predetermined level is required prior to a particular use of PG. PG has a high potential as an alternative raw material, and fluoride removal might be important in recycling applications. This study provides a novel pre-industrial scale fluoride removal inventory, especially for the fertilizer and cement industry.

Keywords: phosphogypsum, fluoride removal, Box-Behnken design, response surface methodology.

SCIENTIFIC PAPER

UDC 666.13:66:004

Phosphogypsum (PG), a by-product of the manufacturing of phosphoric acid using the wet process route, can be chemically defined as impure gypsum in dihydrate form (>95 wt% $CaSO_4 \cdot 2H_2O$). Due to the reaction stoichiometry, PG (by-product) is generated five folds than H_3PO_4 (desired product) by mass. PG is discharged from the process followed by the reaction and stored as piles along coastal areas. In most cases, PG piles are left untreated, which poses a risk of impurity leakage into the groundwater during long-term storage periods. It is challenging to categorize PG using a single formulation since numerous process variables influence the chemical structure of the substance. Fluorides, heavy metals, and radionuclides originated from phosphate rocks used as the raw material in the wet process, and P_2O_5, the process residue, can all be categorized as impurities in the PG structure. One of the key elements influencing the retention of the utilization rate is the type and quantity of impurities in the chemical composition of PG. However, since PG has a chemical composition

Correspondence: C. Avşar, Toros AGRI Industry and Trade Co. Inc. R&D Center, 33020, Mersin / Turkey.
E-mail: cemre.avsar@toros.com.tr
Paper received: 3 February, 2023
Paper revised: 3 May, 2023
Paper accepted: 4 June, 2023

https://doi.org/10.2298/CICEQ230203009A

containing more than 95% $CaSO_4 \cdot 2H_2O$, it can efficiently serve as an alternative to gypsum. The fluoride content in PG must meet the requirement of 0.18 wt% for probable future utilization in the cement industry, even though recycling applications of PG are typically conducted in this sector. Since the average amount of fluoride in PG samples from different parts of the world is 0.9 weight percent, investigations on fluoride removal are crucial to ensure the recycling of PG [1,2]. This study provides potential environmental and industrial prospects. Concentration prediction of a specific impurity and establishing a correlation between a predetermined factor and the impurity concentration might be necessary to take action in the case of potential environmental risks. In this manner, this study provides a practical approach to the relationship between fluoride concentration and temperature. It helps to predict the possible fluoride leakages from PG piles to groundwater according to temperature variations during storage periods. From a circular economy perspective, using industrial wastes by enabling continuous circularity in production chains is important to provide sustainable resources. However, the chemical content of industrial wastes might not be appropriate for direct recycling, and purification studies might be required. PG is a potential and promising input for the cement industry, and initial fluoride concentration affects its performance in cement industry-related applications. The practical relationship between temperature and fluoride removal from PG provided by this study is a strategical highlight since the output can be industrially applicable in the case where the fluoride concentration of PG is higher than the limit levels, and fluoride removal is of importance for the utilization of PG sample in the cement industry.

Different methodologies, such as pre-treatment with different salt solutions, have been developed on the industrial recovery of PG material, whose use as a raw material is very limited due to the impurities such as heavy metals, and it has been presented to the manufacturer as an alternative to provide waste management control. Due to the optimum conditions provided by this study, the ease of application of the proposed method of pre-treatment with seawater benefits the industry by providing cost advantages to fertilizer producers.

PG recycling

The conventional economy's linear flow-based strategy makes it possible to use finite resources continuously. Additionally, the ecology is negatively affected by ineffective waste management. However, the circular economy's design principles are based on the cyclic flow of raw materials utilized in industrial applications along with efficient energy utilization. The circular flow of raw materials for effective and sustainable consumption is enabled by sustainable development goals, which internalize the circular economy strategy. Utilizing industrial wastes as process input and incorporating renewable resources into current manufacturing processes would fit under the sustainable development goals concept [3,4]. Through recycling procedures, waste management solutions in a circular economy encourage the cyclic flow of materials. Therefore, there should be a greater variety of waste management applications [5]. The phosphate fertilizer industry is one of the industries facing the challenge of generating vast waste products from wet-process phosphoric acid production.

The main input in the phosphate-based fertilizer production process is phosphoric acid. When considering the economic viability of producing phosphoric acid on an industrial scale, the wet process, which involves dissolving natural phosphate rock in sulfuric acid, is the most desirable method [6,7]. The process outputs are about 26%–32% P_2O_5-involving phosphoric acid and impure gypsum precipitate. This precipitate is known as PG, and its chemical composition includes radionuclides derived from phosphate rocks, fluorine, heavy metals, and P_2O_5 as the by-product of wet processing. According to recent figures, 300 Mtons of PG are produced annually [8–10].

The European Union (EU) categorizes PG as hazardous waste, although it can be used as a high-quality gypsum alternative. But PG may be categorized as non-hazardous waste if it satisfies the requirements of the hazard property codes for a particular application area [4,11,12]. The usage rate is hampered by the PG's classification as hazardous waste. Huge amounts of PG remain untreated due to its 15% recycling rate [13]. Basic issues with the management PG include the land cost of the piles and remediation expenditures related to reducing environmental degradation [14–16]. Recent research on using PG for various industrial applications highlights the need to create an environmentally friendly recycling system that permits the widespread use of PG.

PG and fluoride removal

The primary component impacting the chemical structure of PG is phosphate rock, utilized as the input of the wet process. Besides, other operational process variables, like process effectiveness, post-production disposal strategies, and the PG stack's physical state, also impact the PG structure [17]. PG is challenging to specify in a single formulation due to its variable chemical structure, although the amount of impurities is considered within a predetermined range.

Fluoride is one of the impurities in PG composition, and the approximate amount of fluoride is 0.9% wt among PG samples found worldwide. Fluoride is an important trace element for living bodies; however, excess fluoride input might affect various organs and systems. Developments in agricultural and industrial applications have triggered the irrepressible fluoride release to the environment, and today fluoride pollution in any form of environment, aquatic or human life, has become a serious problem [18]. Fluoride release from various minerals, such as fluorite, tourmaline, biotite, quartz, kyanite, etc., is commonly encountered. Among these minerals, gypsum is another fluoride source, and release mechanisms are noted to actualize in a wide range of pH values [19]. The average fluoride content in worldwide PG samples is mostly below 0.9 wt%, except for the Tunisian and Algerian samples. These samples have higher fluoride concentrations than the other PG samples.

In contrast, the rest samples have similar fluoride amounts, being approximately below 0.9 wt%, being independent of the year and location of the sample. Fluoride concentrations of PG samples might be relevant to the age of the PG piles. Fluorite and fluorapatite are the dominant mineral phases affecting the fluoride concentration in PG. During the long-term storage period, approximately 0.1 wt% fluoride in PG is released into the gaseous phase, whereas the accumulation of precipitated fluoride complexes in soils as in the form of CaF_2 and $Ca_5(PO_4)_3F$ might also occur [20,21]. Natural fluoride minerals like fluorspar (CaF_2), fluorapatite ($Ca_3(PO_4)_2Ca(FCl_2)$), cryolite (Na_3AlF_6), and sellaite (MgF_2) have very low solubility in water. Still, because PG stacks are frequently deposited along marine coastlines like many other industrial by-products, fluoride leakage may occur over an extended time under favorable conditions. During long-term storage periods, the leakage of water-soluble pollutants negatively influence the residential area by changing the chemical composition of groundwater and having a hydrodynamic impact on the environment [20,21]. Hence, industrial effluents are more dominant as fluoride sources in aqueous media. The fluoride concentration in the effluent streams should be periodically controlled within the regulatory orientations [22,23].

Although the effect mechanism of fluoride cannot be systematically described, kinetic, thermodynamic, and molecular modeling simulations can be applied for fluoride leachability [24]. Fluoride naturally occurs in groundwater; however, many the industries, such as metallurgy, iron-steel, copper, battery, and cement, discharge effluents containing fluoride about 250 ppm–1500 ppm and might reach up to 10.000 ppm in extreme cases [25,26]. PG is a different case since it is not an industrial effluent but a solid waste stacked and formed sediments in long-term storage periods. PG stacks are generally located near coastal areas, and fluoride leakage into groundwater might occur during storage. This phenomenon reduces the initial fluoride content in PG, transferring fluoride into groundwater; thus, this naturally occurring process can also be termed as fluoride removal. PG contains some impurities depending on the phosphate rock used in the wet process and process residues in its chemical structure. The removal of these impurities in the experimental studies indicates that PG does not contain more than any industrial pollutants depending on its solubility ratio. It has been determined that no contamination or toxicity has been found in the samples taken from the environment where PG is discharged. However, after the production of H_3PO_4, an important development has been achieved regarding heavy metal removal by chemical precipitation method and minimizing environmental problems.

Chemical, physical, and thermal processes are used to remove impurities from PG. Combinations of these techniques are also used in some situations. For purification, PG is typically treated with ammonium hydroxide, citric acid, sulfuric acid, or dissolved lime; flotation or calcination is also used to remove impurities [27–29,12]. The crystalline gypsum structure is degraded during chemical impurity removal processes that involve sulfate ion replacement [30]. In this way, impurity removal from salt solution can be successful without causing crystalline structure degradation. Results for the use of seawater could help forecast PG-stack-based leaks over long-term storage periods [31,32].

Box Behnken design of the response surface methodology

Traditional optimization studies rely on experiment conduction as one factor at a time (OFAT). This strategy relies on the variation of one variable or factor at a time, keeping other variables constant. This approach is generally impractical when conducting all necessary experiments with each possible factorial combination. The time-consuming disadvantage of the conventional method can be turned off by the optimization of all the variables simultaneously by statistical experimental design. Response surface methodology, which analyzes an empirical model using a combination of statistical and mathematical techniques, is particularly appropriate for studies involving particular experiment designs because it allows for the minimization of the number of runs that an experiment set must undergo for a given set of

factors and factor levels [33,34].

RSM is a highly effective approach when determining the optimum operational conditions in a specific experimental setup or a region within the limits of specified optimum experimental conditions [35]. One of the design matrices in RSM is the Box-Behnken design (BBD), which includes multivariable, 2^{nd} order, rotatable, or nearly rotatable designs. Application of BBD can be conducted in two different forms, one of which is a central point and the middle points of the edges, and the other is a 2^2 factorial design and a central point. When an evaluation is required under challenging experimental settings and to ascertain the reaction of the function on its maxima or minima, this form of experimental design can be beneficial [36].

Tetteh and Rathilal studied the biogas and decontamination removal efficiency of bio photocatalytic degradation of municipality wastewater by using RSM based on a modified BBD experiment to optimize and maximize the desirability of the bio photocatalytic system. The modified RSM-BBD model was studied to determine the optimum catalyst load, hydraulic retention time, and temperature. Experimental verification results showed a high agreement with the predicted results in the RSM-BBD model at a high regression (R^2 > 0.98) and within the range of 95% confidence level [37]. Another modeling and optimization study using RSM on industrial wastewater treatment with 17 experimental runs was conducted by introducing coagulant dosage, settling time, and mixing rate as the variables in the design matrix. The predictability of the RSM model was validated using an artificial neural network (ANN). The results were in agreement with the RSM model, where the coefficient of determination (R^2) was 0.994 for the ANN model and 0.97 for the RSM model, within the range of 95% confidence level (p<0.05) [38]. Apart from these model prediction and optimization studies using RSM for industrial wastewater treatment applications, some studies regarding fluoride removal are also available in the literature.

Mourabet *et al*. employed a BBD by introducing starting concentration, temperature, adsorbent dosage, and pH as the input parameters in an aqueous solution [35]. The RSM was used to optimize fluoride removal with apatitic tricalcium phosphate. Results indicated that a second-order polynomial model, with an R^2 value of 0.966, provided a good fit for the regression analysis and experimental results [35]. El-Din Mohamed *et al*. conducted a study to compare the outcomes of OFAT and BBD, and a fluoride biosorption optimization study using *Padina sp*. algae as the biosorbent was carried out [39]. The maximum amount of fluoride removed, according to OFAT data, was 85.95%; however, according to the BBD results, the maximum amount of fluoride removed was 94.57%. ANOVA analysis was used to determine the statistical significance of the constructed model, and RSM was found to be more useful for efficient optimization [39].

This study gives a novel approach and a brief demonstration of fluoride removal efficiency upon salt solution treatment of PG according to a multi-variable BBD with time, solid/liquid (w/v) ratio and temperature as the parameters in various salt solution media. Seawater and 5% NaCl and 10% NaCl solutions were studied to investigate the fluoride removal efficiency from PG, and lab-scale experiment results were simulated in Design Expert v.12 software. Since PG piles are located near coastal regions and seawater is investigated as a salt solution media, this study might be useful to predict the quantity of real-time fluoride leakage to the sea ecosystem. Another study highlight is the computational approach to fluoride removal from PG, enabling a straightforward prediction when fluoride impurity is important. PG-related industries might favor the outputs of this study for particular reasons. For example, the fertilizer industry might benefit from periodic regulatory controls of groundwater fluoride concentrations near PG piles. The outputs of this study might be effective in setting up a correlation between fluoride leakage and seasonal temperature variations, and precautions can be taken before regulatory controls do not cause abnormal fluoride concentrations in the groundwater near PG piles. The cement industry also utilizes PG recycling strategies; however, the changeable chemical of PG might not always be appropriate in terms of fluoride concentration, and there would be some cases for prior purification. The study outputs might benefit the cement industry for a practical fluoride content analysis in the PG before its process applications.

MATERIAL AND METHODS

Experimental

PG samples used in the study were provided by Toros Agri Industry anf Trade Co. Inc. (Mersin/Turkey). The initial PG sample has a free water content of 13%, a slightly acidic pH of 4.8 to 6, and conductivity of 2230 μmhos/cm to 2320 μmhos/cm. Mineralogy characterization showed a 99.4% dihydrate gypsum with trace amounts of quartz, anhydrite, and bassanite. PG samples showed a variable morphology from stubby, lath-shaped crystals to irregularly-shaped crystals and brown to light brown appearance in color. Particle size distribution showed 97% silt-size particles and 3% fine sand-size particles, with a mean particle diameter of 25 μm to 32 μm.

Besides seawater (sampled near PG stack, a

region near Mersin Port, Mediterranean Sea), 5% and 10% (wt%) NaCl solutions were used to remove fluoride from PG and to determine the appropriate salt solution.

Evaporation yielded a 5% (wt%) salt concentration for seawater, and NaCl solutions with 5% and 10% (wt%) were prepared compared to seawater in terms of concentration and salt type. The salt solutions of 5% and 10% NaCl were determined to be a single type of salt with the same concentration and concentrated salt amount, respectively. Seawater is assumed to be a mixture of different salt types. The BBD matrix for three factors is shown in Table 1, with five replicates at the center points and both coded and real values. In accordance with the design matrix shown in Table 1, experiment runs were carried out to examine the impacts of multivariable parameters and identify the ideal conditions for the removal of fluoride from PG into aqueous salt solutions. The three independent variables were temperature (20-80 °C), time (3 h–6 h), and the solid/liquid ratio (0.1 w/v–0.2, w/v). The efficacy of fluoride removal was examined according to the interactions and quadratic effects of the various parameters. The salt solution type is regarded as a variable because the experiments shown in Table 1 were carried out with the abovementioned salt solution systems. All the experiments were carried out randomly and in triplicates to minimize the unexplained variation in responses owing to systematic errors.

Table 1. Box-Behnken design matrix for three factors, both coded and actual values.

Run #	A: Temperature (°C)	B: Time (h)	C: Solid/Liquid Ratio (w/v)
1	50 (0)	3 (-1)	0.2 (+1)
2	80 (+1)	4.5 (0)	0.1(-1)
3	50 (0)	4.5 (0)	0.15 (0)
4	20 (-1)	6 (+1)	0.15 (0)
5	50 (0)	3 (-1)	0.1 (-1)
6	50 (0)	4.5 (0)	0.15 (0)
7	20 (-1)	4.5 (0)	0.2 (+1)
8	20 (-1)	3 (-1)	0.15 (0)
9	80 (+1)	4.5 (0)	0.2 (+1)
10	50 (0)	4.5 (0)	0.15 (0)
11	50 (0)	6 (+1)	0.2 (+1)
12	80 (+1)	3 (-1)	0.15 (0)
13	50 (0)	4.5 (0)	0.15 (0)
14	50 (0)	4.5 (0)	0.15 (0)
15	20 (-1)	4.5 (0)	0.1 (-1)
16	80 (+1)	6 (+1)	0.15 (0)
17	50 (0)	6 (+1)	0.1 (-1)

10 g of sieved PG samples with particle sizes of less than 125 μm were weighed, and the experiment runs listed in Table 1 were carried out in solutions of 5% and 10% NaCl and seawater. After each experiment, a filter was applied to the PG/salt solution system. UV-Spectrophotometry was used to measure the fluoride concentration in experiment supernatants (HACH Lange DR 3900 UV Spectrophotometer).

The degree of fluoride removal efficiency was calculated according to Eq. (1), where $F_{supernatant}$ is the fluoride concentration of the supernatant of PG/salt solution samples stirred after specified time according to BBD matrix, and $F_{salt\ solution,\ initial}$ and $F_{initial,PG}$ are the initial fluoride content of the salt solution and PG sample, respectively. $F_{salt\ solution,\ initial}$ and $F_{initial,PG}$ values are given in Table 2.

$$Fluoride\ removal\ efficiency\,(\%) = \frac{F_{\text{supernatant}} - F_{\text{salt solution, initial}}}{F_{initial,PG}} \cdot 100 \quad (1)$$

The fluoride removal performance of seawater and 5% and 10% NaCl solutions were compared. The most suitable among them were selected, and the factor levels were optimized for maximum fluoride removal efficiency defined with Eq. (1). The resulting data were fitted to a second-order polynomial model including main, interaction, and quadratic effects of the variables (factors) on the response variable. The statistical significance of the variables was determined using Analysis of Variance (ANOVA) with a confidence level of 95%. Moreover, the developed model's adequacy was estimated by evaluating the lack of fit test and determination coefficient (R^2) obtained from ANOVA.

Predicted values were plotted against the actual responses for each salt solution treatment to show the explanation performance of the model in the experimental data.

A detailed schematic illustration of the sampling, model design, experimental study, and data analysis throughout the study is given in Figure 1.

RESULTS AND DISCUSSION

The initial fluoride concentrations of each salt solution are listed in Table 2, which serves as a starting point for the computation of the fluoride removal efficiency shown in Eq.(1). Removal efficiency values for each of the experiment sets were calculated from the fluoride concentrations of all the supernatant samples measurements obtained by three replications, were given in Table 3.

Fluoride removal was estimated in each salt solution system, and the removal rates in each system

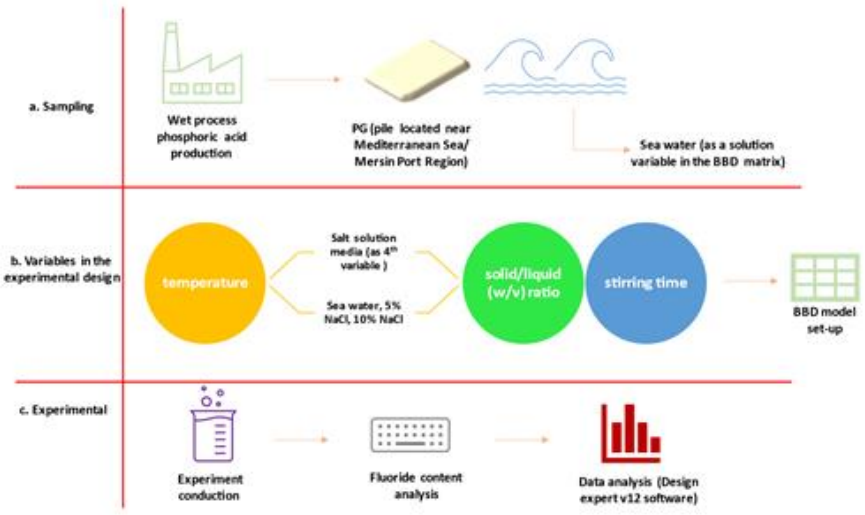

Figure 1. Schematic illustration of the study.

Eq.(1) revealed a continuous variation strongly influenced by temperature. Thus, Table 3 shows the reorganized version of the BBD matrix according to temperature to observe the fluoride removal efficiency upon the change in the temperature of the salt solution systems.

Table 2. Initial fluoride concentrations (ppm).

Sample	Fluoride (ppm)
PG	96
Seawater	7.6
5% NaCl solution	3.6
10% NaCl solution	5.6

Table 3 shows that the efficiency of removing fluoride from all solutions is exactly proportional to temperature. Figure 2 displays the average fluoride removal efficiency in several solutions according to temperature.

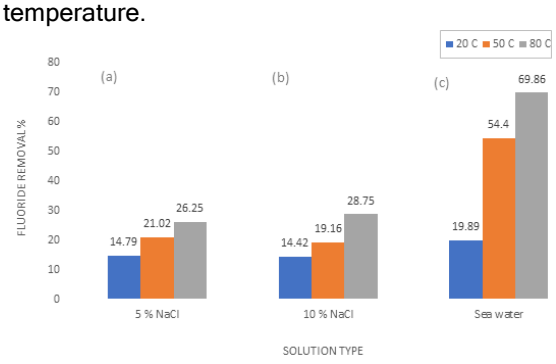

Figure 2. Fluoride removal efficiency according to temperature in (a) 5% NaCl, (b) 10% NaCl and (c) seawater.

Table 3. Box-Behnken design matrix for fluoride removal efficiencies from PG.

Run #	Temperature (°C)	Seawater	5% NaCl	10% NaCl
4	20	22.08	14.58	15.00
7	20	22.29	13.33	14.38
8	20	18.33	14.17	13.73
15	20	16.88	17.08	14.58
1	50	55.00	16.67	20.42
3	50	54.17	19.17	17.92
5	50	50.83	17.92	18.33
6	50	57.08	20.00	17.50
10	50	NA*	23.75	16.25
11	50	57.08	22.92	24.17
13	50	NA*	21.67	20.83
14	50	55.42	23.33	18.33
17	50	51.25	23.75	18.75
2	80	65.42	25.42	28.33
9	80	70.00	27.50	29.17
12	80	74.17	26.25	30.42
16	80	NA*	25.83	27.08

NA*: Not Applicable

The lowest fluoride removal efficiency was demonstrated by a 5% NaCl solution followed by a 10% NaCl solution. Seawater displayed the best fluoride removal efficiency. Similarly, average fluoride removal efficiencies at different temperatures according to salt solutions are given in Figure 3.

Seawater is a complex salt solution system,

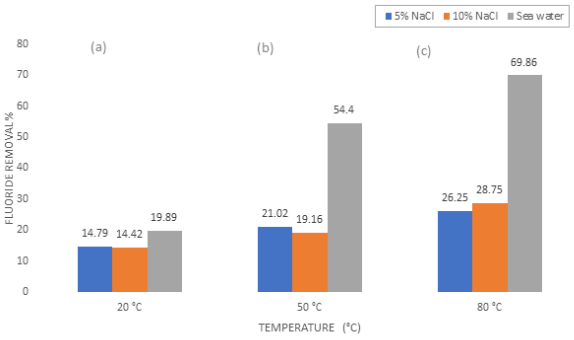

Figure 3. Fluoride removal efficiency according to salt solution type at (a) 20 °C, (b) 50 °C, and (c) 80 °C.

whereas 5% and 10% NaCl are single-salt solutions. Fluoride removal efficiency in complicated salt solution systems exhibits a greater rate, according to the removal efficiency values shown in Table 3. Temperature is a calculated multivariable included in the BBD matrix that significantly affects fluoride removal efficiency. There was a direct correlation between temperature and fluoride removal efficiency in earlier research published in the literature [40–42]. Seawater demonstrated the greatest fluoride removal efficiency regarding both solution type and temperature. The initial fluoride level of the 20-year-old PG stack was measured at 96 ppm, and the low fluoride concentration may be due to fluoride leakages during long-term storage. The first burst release was used to depict long-term fluoride release because it displays a time-decreasing pattern, and the low fluoride content of the PG stack is consistent with the data from the literature [43]. Although the sampled PG stack does not concern the environment, its purity may be problematic if the material is used as a resource.

Fluoride removal results were evaluated by Design Expert v.12 software. ANOVA analyses for each salt solution are given in Table 4 for seawater, 5% NaCl, and 10% NaCl, respectively.

Model *F*-values (199.56, 25.19, and 27.34) of each salt solution treatment result show that all models are significant. The probability that such a large *F*-value will occur due to noise is only 0.01%. *p*-values less than 0.0500 indicate that the model terms are significant. In this case, A, C, and A^2 are the important model terms for the seawater treatment. On the other hand, for the 5% and 10% NaCl purifications, the meaningful model term is only A. While the seawater treatment results are modeled with a quadratic model, 5% and 10% NaCl treatment results are modeled with the linear model, only including the main effects of the factors. Values greater than 0.1000 indicate the model terms are not significant. If there are many insignificant model terms (not counting those required to support hierarchy), model reduction may improve the model. But in this study, regression models with all the model terms, whether the model term was significant or not, were considered to predict the response variable, so the model reduction was not made. The lack of fit *F*-value of each salt solution treatment (1.58, 0.90, and 2.17) implies it is insignificant relative to the pure error. Non-significant lack of fit is good for all three models.

Regression models with coded factor values for fluoride removal efficiencies for all salt solutions were obtained as given the Eq.(2–4) below:

$$\begin{aligned}&\textit{Fluoride removal efficiency} - \textit{Sea water}\,(\%) = \\ &55.56 + 24.71A - 0.0260B + 2.50C - 2.55AB - 0.2083AC \\ &+0.4167BC - 9.94A^2 - 0.0434B^2 - 1.97C^2\end{aligned} \quad (2)$$

$$\textit{Fluoride removal efficiency} - 5\%\ \textit{NaCl}\,(\%) = 20.78 + 5.73A + 1.51B - 0.4688C \quad (3)$$

$$\textit{Fluoride removal efficiency} - 10\%\ \textit{NaCl}\,(\%) = 20.31 + 7.16A + 0.2630B + 1.02C \quad (4)$$

Predicted response versus actual response plots are given in Figure 4. The best model prediction was obtained for the seawater treatment with the determination coefficient value (R^2) of 0.9978. In contrast, model predictions for the 5% and 10% NaCl treatments were not good enough, with R^2-values of 0.853 and 0.863, respectively.

Since seawater was the best salt solution for fluoride removal from PG, considering both the resulted percent yields and the ANOVA analysis, 3D response surface plots were drawn to analyze the factor effects on the seawater treatment, as given in Figure 5.

Figure 5 shows no significant relationship between fluoride removal efficiency and time at lower temperatures. But, increasing temperature changes the trend, and higher fluoride efficiency can be observed in shorter periods at higher temperature ranges. The solid/liquid ratio also shows higher fluoride removal efficiency at higher temperatures. Upon the multivariable in the BBD matrix, consistent relation was observed according to temperature, and it can be said that fluoride removal efficiency is a temperature-dependent phenomenon.

The optimum temperature, time, and solid/liquid ratio were obtained to be 80 °C, 3 h, and 0.174 solid/liquid (PG/seawater, w/v) ratio, respectively, in Design Expert v.12 software, predicting a fluoride removal of 73.31% with the optimum combination of experimental parameters. Experimental verification of optimum conditions obtained by Design Expert v.12 software was also performed with a basis of 10 g PG sample, having a solid/liquid ratio of 0.174 (PG/seawater, w/v) treated at 80 °C and 3 h. Results showed 74.99% fluoride removal efficiency, which is

Table 4. ANOVA results of fluoride removal efficiencies for seawater, 5% NaCl solution, and 10% NaCl solution.

Source	Sum of squares			df			Mean square			*F*- value			*p*-value		
	NaCl (%)														
	SW[a]	5	10	SW	5	10	SW	5	10	SW	5	10	SW	5	10
Model	4967.7	282.60	419.40	9	3	3	551.98	94.20	139.80	199.56	25.19	27.34	<0.0001	<0.0001	<0.0001
A[b]	3257.38	262.59	410.59	1	1	1	3257.38	262.59	410.59	1177.64	70.22	80.29	<0.0001	<0.0001	<0.0001
B[c]	0.0036	18.25	0.5534	1	1	1	0.0036	18.25	0.5534	0.0013	4.88	0.1082	0.9729	0.0457	0.7474
C[d]	50.00	1.76	8.25	1	1	1	50.00	1.76	8.25	18.08	0.4701	1.61	0.0131	0.5050	0.2262
AB	13.03			1			13.03						0.0958		
AC	0.1736			1			0.1736			0.0628			0.8145		
BC	0.6944			1			0.6944			0.2511			0.6426		
A^2	296.37			1			296.37			107.14			0.0005		
B^2	0.0057			1			0.0057			0.0020			0.9661		
C^2	11.65			1									0.1094		
Residual	11.06	48.61	66.48	4	13	13		3.74	5.11						
Lack of fit	6.78	32.50	55.16	2	9	9		3.61	6.13		0.8966	2.17	0.3871	0.5929	0.2375
Pure error	4.28	16.11	11.32	2	4	4		4.03	2.83						
Cor total	4978.86	331.21	485.87	13	16	16									

[a] - Seawater; [b] - Temperature; [c] - Time; [d] - Solid/Liquid ratio.

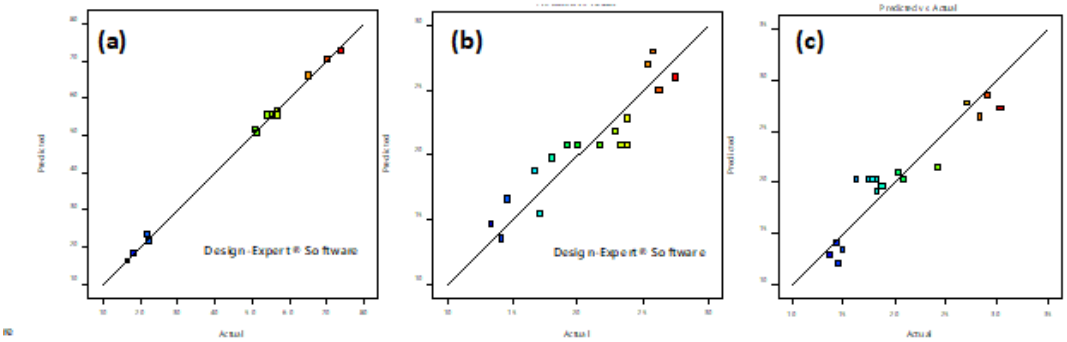

Figure 4. Predicted response versus actual response in fluoride removal efficiencies for salt solution treatments (a) seawater, (b) 5% NaCl, and (c) 10% NaCl.

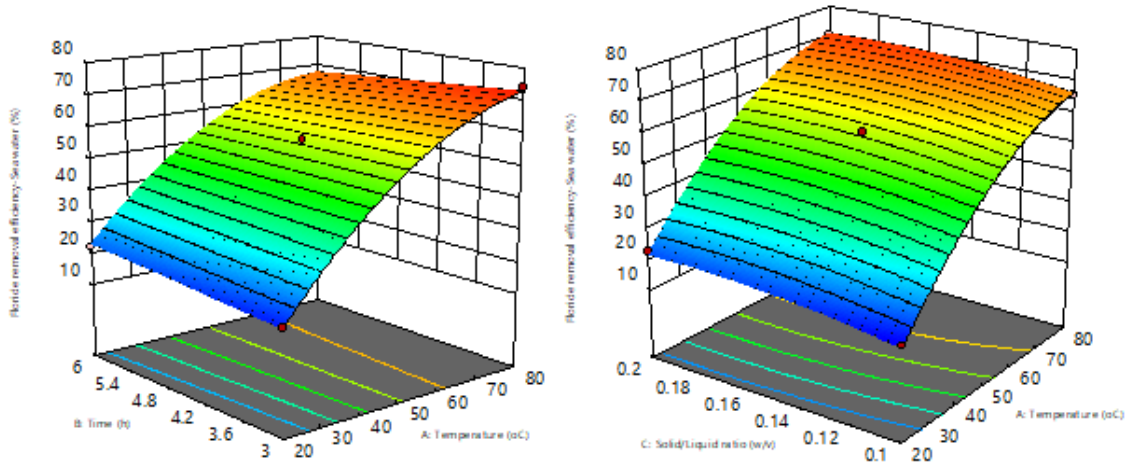

Figure 5. Response surface plots showing the interactions between process parameters for fluoride removal efficiency from PG (a) temperature and time, (b) temperature and solid/liquid ratio.

statistically within the 95% confidence range.

The use of PG material as raw material is paved with the fluoride removal method by washing with salt solutions, which is offered as an alternative to the problem of PG being formed as a by-product in large piles in phosphoric acid production and keeping them as piles without being used as raw material for any industry due to impurity content. It provides an important cost advantage for raw materials to the manufacturer.

Although the damage mechanism of fluoride in terms of leakage to groundwater or impact on the nearby marine or soil ecosystem has not been extensively defined, the study's results might be directive to predict the quantitative fluoride leakage from the PG stacks into groundwater upon seasonal temperature variations. Optimum conditions determined by the experimental data indicated that pre-treatment of PG with seawater was the most effective method for fluoride removal. The effect of seawater on fluoride removal provides a cost advantage to the industrial manufacturer, and the pollution removal with recommended seawater is ground. One of the important details of this study is that PG can be discharged without any environmental threat due to the treatment of phosphate rock or uncontrolled PG with seawater. Because a pre- or post-treatment process to be applied to the raw material or by-product with seawater can be accepted as an easy and simple method that today's fertilizer manufacturers can apply, in which phosphoric acid production is conducted.

Fluoride removal from PG is a contamination problem that has been prominent in the literature until today. However, environmental problems have been partially minimized in the proposed pollution removal methods and directed the manufacturer to alternative studies. As the focus of this article, an economical solution method that can be applied in existing phosphoric acid production facilities is presented to the producer with the pollution removal method.

CONCLUSION

The salt solution media used in this study included seawater, 5% NaCl, and 10% NaCl solutions. The results of the experimental study showed a consistent relationship based on temperature. The efficacy of fluoride elimination is, therefore, a temperature-dependent phenomenon. Optimization of the multi-response system was performed by Design Expert v.12 software, and the simulation indicated a 73,31% fluoride removal with seawater when the experiment was performed at 80 °C, 3 h, and 0,174 solid/liquid (PG/seawater, w/v) ratio, respectively. The study's results may help estimate how much fluoride will leak from PG stacks into groundwater due to temperature changes or guide fluoride removal under predetermined ideal conditions when PG purification is crucial before recycling for a particular use. The former case is in accordance with the circular economy, investigating a fluoride removal and purification study to use PG in further recycling processes. The latter case gives a brief simulation for predicting the deviations in fluoride concentrations in the groundwater related to the leakages from PG piles in different seasonal conditions.

ACKNOWLEDGMENT

This study is financially supported by The Scientific and Technological Research Council of Turkey (TÜBİTAK, Project No: 118C085) and conducted between the cooperation of Ankara University and Toros AGRI Industry and Trade Co. Inc. R&D Center within the scope of TÜBİTAK 2244 Industrial Ph.D. Fellowship Program.

NOMENCLATURE

PG	Phosphogypsum
BBD	Box-Behnken Design
RSM	Response Surface Methodology
EU	European Union
OFAT	One Factor at a Time
ANN	Artificial Neural Network
ANOVA	Analysis of Variance

REFERENCES

[1] M. Abdelhadi, N. Abdelhadi, T. El-Hasan, Earth Sci. Res. 7(2) (2018) 28–41. https://doi.org/10.3176/oil.2019.2S.12.

[2] M. Singh, M. Garg, S.S. Rehsi, Const. Build. Mater. 7(1) (1993) 3–7. https://doi.org/10.1016/0950-0618(93)90018-8.

[3] K. Chojnacka, D. Skrzypczak, K. Mikula, A. Witek-Krowiak, G. Izydorczyk, K. Kuligowski, P. Bandrow, M. Kulazynski, J. Clean. Prod. 313 (2021) 1–12. https://doi.org/10.1016/j.jclepro.2021.127902.

[4] L.F.O. Silva, M. L. S. Oliveira, T.J. Crissien, M. Santosh, J. Bolivar, L. Shao, G.L. Dotto, J. Gasparotto, M. Schindler, Chemosphere 286(1) (2022) 1–14. https://doi.org/10.1016/j.chemosphere.2021.131513.

[5] H. Salmenpera, K. Pitkänen, P. Kautto, L. Saikku, J. Clean. Prod. 280(1) (2021) 1–19. https://doi.org/10.1016/j.jclepro.2020.124339.

[6] B. Karshiev, A. Seytnazarov, U. Alimov, S. Namazov, A. Reymov, A. Rasulov, Vopr. Khim. Khim. Tekhnol. 1 (2021) 24–34. https://doi.org/10.32434/0321-4095-2021-134-1-24-34.

[7] Q. Chen, S. Sun, Y. Liu, C. Qi, H. Zhou, Q. Zhang, Int. J. Miner. Metall. 28 (2021) 1440–1452. https://doi.org/10.1007/s12613-021-2274-6.

[8] L. Feng, K. Jin, H. Wang, Coatings 11(7) (2021) 1–12. https://doi.org/10.3390/coatings11070802.

[9] L. Yang, Y. Zhang, Y. Yan, J. Clean. Prod. 127 (2016) 204–213. https://doi.org/10.1016/j.jclepro.2016.04.054.

[10] H. Wang, X. You, J. Tian, X. Cheng, J. Wang, IOP Conf. Ser.: Earth Environ. Sci. 668 (2021) 1–7. https://doi.org/10.1088/1755-1315/668/1/012076.

[11] J. Rosales, M. Gazquez, M. Cabrera, J.P. Bolivar, F. Agrela, in Waste and Bypoducts in Cement-Based Materials- Innovative Sustainable Materials for a Circular Economy, J. de Brito, C. Thomas, C. Medina, F. Agrela Ed., Woodhead Publishing, (2021) 153–189. ISBN: 9780128208953.

[12] W. Cao, W. Yi, J. Li, J. Peng, S. Yin, Const. Build. Mater. 309 (2021) 125190. https://doi.org/10.1016/j.conbuildmat.2021.125190.

[13] C.R. Canovas, R. Perez-Lopez, F. Macias, S. Chapron, J.M. Nieto, S. Pellet-Rostaing, J. Clean. Prod. 143 (2017) 497–505. https://doi.org/10.1016/j.jclepro.2016.12.083.

[14] F. Wu, S. Liu, G. Qu, B. Chen, C. Zhao, L. Liu, J. Li, Y. Ren, J. Adv. Chem. Eng. 9 (2022) 1–11. https://doi.org/10.1016/j.ceja.2021.100227.

[15] K. Ren, N. Cui, S. Zhao, K. Zheng, X. Ji, L. Feng, X. Cheng, N. Xie, Crystals 11(7) (2021) 1–20. https://doi.org/10.3390/cryst11070719.

[16] Z. Wei, Z. Deng, J. Environ. Radioact. 242 (2022) 106778. https://doi.org/10.1016/j.jenvrad.2021.106778.

[17] H. Tayibi, M. Choura, F.A. Lopez, F.J. Alguacil, A. Lopez-Delgado, J. Environ. Manage. 90(8) (2009) 2377–2386.

https://doi.org/10.1016/j.jenvman.2009.03.007.

[18] S. Wu, Y. Wang, M. Iqbal, K. Mehmood, Y. Li, Z. Tang, H. Zhang, Environ. Pollut. 304 (2022) 119241. https://doi.org/10.1016/j.envpol.2022.119241.

[19] P. Singh, A. Saxena, J. Geol. Soc. India 98 (2022) 133–138. https://doi.org/10.1007/s12594-022-1939-8.

[20] Y. Chernysh, O. Yakhnenko, V. Chubur, H. Roubik, Appl. Sci. 11 (4) (2021) 1–20. https://doi.org/10.3390/app11041575.

[21] P.M. Rutherford, M.J. Dudas, J.M. Arocena, Environ. Technol. 16(4) (1995) 343–354. https://doi.org/10.1080/09593331608616276.

[22] A. Jeyaseelan, A.A. Ghfar, M. Naushad, N. Viswanathan, J. Environ. Chem. Eng. 9(1) (2021) 1–12. https://doi.org/10.1016/j.jece.2021.105384.

[23] L. Lahlmunsiama, N. Ngainunsiami, D. Kim, D. Tiwari, Chem. Eng. Process. 165 (2021) 1–14. https://doi.org/10.1016/j.cep.2021.108428.

[24] S. Ghosh, A. Malloum, C.A. Igwegbe, J.O. Ighalo, S. Ahmadi, M.H. Dehghani, A. Othmani, Ö. Gökkuş, N.M. Mubarak, J. Mol. Liq. 346 (2022) 118257. https://doi.org/10.1016/j.molliq.2021.118257.

[25] C.F.Z. Lacson, M. Lu, Y. Huang, J. Clean. Prod. 280(1) (2021) 1–20. https://doi.org/10.1016/j.jclepro.2020.124236.

[26] K. Wan, L. Huang, J. Yan, B. Ma, X. Huang, Z. Luo, H. Zhang, T. Xiao, Sci. Total Environ. 773 (2021) 1–20. https://doi.org/10.1016/j.scitotenv.2021.145535.

[27] R. Moalla, M. Gargouri, F. Khmiri, L. Kamoun, M. Zairi, Environ. Eng. Res. 23(1) (2018) 36–45. https://doi.org/10.4491/eer.2017.055.

[28] X. Chen, J. Gao, Y., Zhao, Constr. Build. Mater. 229 (2019) 1–9. https://doi.org/10.1016/j.conbuildmat.2019.116864.

[29] M. Du, J. Wang, F. Dong, Z. Wang, F. Yang, H. Tan, K. Fu, W. Wang, Research Square, preprint 1(1) (2021) 1–19. https://doi.org/10.21203/rs.3.rs-888156/v1.

[30] J.S.A. Neto, J.D. Bersch, T.S.M. Silva, E.D. Rodriguez, S. Suziki, A.P. Kirchheim, Constr. Build. Mater. 299 (2021) 1–11. https://doi.org/10.1016/j.conbuildmat.2021.123935.

[31] B. Guan, L. Yang, H. Fu, B. Kong, T. Li, L. Yang. Chem. Eng. J. 174 (1) (2011) 296–303. https://doi.org/10.1016/j.cej.2011.09.033.

[32] Q. Guan, Y. Sui, F. Zhang, W. Yu, Y. Bo, P. Wang, W. Peng, J. Jin, Physicochem. Probl. Miner. Process. 57(1) (2021) 168–181. https://doi.org/10.37190/ppmp/130795.

[33] S.J.S. Chelladuri, K. Murugan, A.P. Ray, M. Upadhyaya, V. Narasimharaj, S. Gnanasekaran, Mater. Today: Proc. 37(2) (2021) 1301–1304. https://doi.org/10.1016/j.matpr.2020.06.466.

[34] N. Manmai, Y. Unpaprom, R. Ramaraj. Biomass Convers. Biorefin. 11 (2021) 1759–1773. https://doi.org/10.1007/s13399-020-00602-7.

[35] M. Mourabet, A. El Rhilassi, H. El Boujaady, M. Bennani-Ziatni, R. El Hamri, A. Taitai, Appl. Surf. Sci. 258(10) (2012) 4402–4410. https://doi.org/10.1016/j.apsusc.2011.12.125.

[36] S.L.C. Ferreira, R.E. Bruns, H.S. Ferreira, G.D. Matos, J.M. David, G.C. Brandao, E.G.P. da Silva, L.A. Portugal, P.S. dos Reis, A.S. Souza, W.N.L. dos Santos, Anal. Chim. Acta 597(2) (2007) 179–186. https://doi.org/10.1016/j.aca.2007.07.011.

[37] E.K. Tetteh, S. Rathilal, Bioengineering 9(3) (2022) 95. https://doi.org/10.3390/bioengineering9030095.

[38] N.P. Sibiya, G. Amo-Duodu, E.K. Tetteh, S. Rathilal, Sci. Afr. 17 (2022) e01282. https://doi.org/10.1016/j.sciaf.2022.e01282.

[39] W. Salah El-Din Mohamed, M.T.M.H. Hamad, M.Z. Kamel, Water Environ. Res. 92(7) (2020) 1080–1088. https://doi.org/10.1002/wer.1305.

[40] A. Masmoudi-Soussi, I. Hammas-Nasri, K. Horchani-Naifer, M. Ferid, Int. J. Miner. Process. 123 (2013) 87–93. https://doi.org/10.1016/j.hydromet.2020.105253.

[41] Z. Li, G.P. Demopoulos, J. Chem. Eng. Data 50(6) (2005) 1971–1982. https://doi.org/10.1021/je050217e.

[42] Z. Li, G.P. Demopoulos, J. Chem. Eng. Data 51(2) (2006) 569–576. https://doi.org/10.1021/je0504055.

[43] L. Fornsten, Biomaterials 19(6) (1998) 503–508. https://doi.org/10.1002/tqem.21929.

CEMRE AVŞAR[1,2]
SUNA ERTUNÇ[2]

[1]Toros AGRI Industry and Trade Co. Inc. R&D Center, Mersin / Turkey

[2]Ankara University, Department of Chemical Engineering, Ankara/ Turkey

NAUČNI RAD

UKLANJANJE FLUORIDA IZ FOSFOGIPSA: PREDINDUSTRIJSKA STUDIJA I NJENA MATEMATIČKA ANALIZA

Ova studija govori o efikasnosti uklanjanja fluorida iz fosfogipsa na matrici eksperimenta u laboratoriji dizajniranoj Boks-Benkenovim planom. Temperatura, odnos čvrsta/tečnost i vreme utiču na efikasnost uklanjanja fluorida iz fosfogipsa pomoću rastvora različitih soli. Eksperimentalne matrice su dizajnirane prema tipovima rastvora soli: morska voda, 5% NaCl i 10% rastvori NaCl. Analiza faktor-odgovor je pokazala direktnu proporcionalnost između efikasnosti uklanjanja fluorida i temperature. Optimalni uslovi uklanjanja fluorida su određeni softverom Design Expert v.12. Optimalna temperatura, vreme i odnos čvrsta/tečnost bili su 80 °C, 3 h i 0,174 za morsku vodu. Softver je predvideo efikasnost uklanjanja fluorida od 73,31% pri optimalnim uslovima, dok je eksperimentalna vrednost bila 74,99%. Pošto se stvarna i predviđena efiksanost uklanjanja dobro slažu, postupak bi moga biti korišćen kada je potrebno uklanjanje fluorida na industrijskom nivou do unapred određenog nivoa pre određene upotrebe fosfogipsa. Ova studija pruža novi postupak za uklanjanje fluorida na preindustrijskom nivou, posebno za industriju đubriva i cementa. Fosfogips ima veliki potencijal kao alternativna sirovina, a uklanjanje fluorida može biti važno u primenama reciklaže.

Ključne reči: fosfogips, uklanjanje fluorida, Boks-Benkenov dizajn, metodologija odzivne površine.

CI&CEQ
Chemical Industry & Chemical Engineering Quarterly

Available online at
Association of the Chemical Engineers of Serbia AChE
www.ache.org.rs/CICEQ

Chem. Ind. Chem. Eng. Q. 30 (1) 47–58 (2024) CI&CEQ

BENSABER BENSEBIA[1]
FATMA-ZOHRA CHAOUCHE[1]
OUAHIDA BENSEBIA[2]
SOUMIA KOUADRI MOUSTEFAÏ[3]

[1]Laboratory of Plant Chemistry-Water-Energy, Department of Process Engineering, Faculty of Technology, Hassiba Benbouali University, Chlef, Algeria

[2]Industrial Process Engineering Sciences Laboratory, Houari Boumediene University of Sciences and Technology, Bab Ezzouar, Algeria

[3]Department of Process Engineering, Faculty of Technology, Hassiba Benbouali University, Chlef, Algeria

SCIENTIFIC PAPER

UDC 66.096.5:51-7

BED EXPANSION IN TURBULENT BED CONTACTOR: EXPERIMENTS AND PREDICTION

Article Highlights

- Trends in bed expansion (Hd/Hst) evolution with operating variables
- A method for the prediction of bed expansion has been proposed
- The proposed calculation has been tested with experimental data, confirming its reliability
- The study determined the best correlations for predicting the expansion of the bed

Abstract

In this work, turbulent bed contractor (TBC) hydrodynamics have been studied in terms of bed expansion (Hd/Hst) using a particular approach to predict this important property for the design of such equipment. The study is based on 1604 sets of experimental data on the bed expansion, obtained by varying the operating variables (gas velocity, liquid spray, packing characteristics, static bed height, and free opening of the supporting grid). The prediction of the bed expansion necessitates the estimation of gas and liquid holdups. To achieve this, we employed a variety of correlations derived from existing literature, comprising six equations for gas holdup and twenty equations for liquid holdup estimation. Out of a total of 120 cases, bed expansion was estimated, and the accuracy of the model was evaluated by calculating the mean absolute error in percentage (MAPE), root mean square error (RMSE), correlation coefficient (ρ_{XY}), and explained variance (VE_{CV}). This study identified suitable correlations for gas and liquid holdups, leading to predictions with acceptable errors. Furthermore, statistical analysis was employed in a subsequent phase of the study to determine the most appropriate correlations for predicting bed expansion among those proposed by various authors.

Keywords: three-phase fluidization, turbulent bed contactor, bed expansion, gas holdup, liquid holdup.

The Turbulent Bed Contactor (TBC) is a three-phase fluidized bed of low-density spherical particles. The solid is fluidized by an upwardly flowing gas (continuous phase) and irrigated by a downwardly flowing liquid. Non-flooding grids, positioned at a sufficient distance to allow for bed expansion, support the bed. A turbulent and random motion of the packing enhances contact between the gas and liquid phases. This turbulent motion generates rapid interface renewal and a large interfacial area, increasing mass and heat transfer rates. The TBC presents several advantages over conventional contactors, including high capacity, high efficiency, and resistance to clogging.

In physical processing, the TBC is used in air-cooling humidification and dehumidification, particulate removal, and lactose granulation [1–3]. In chemical processing, it is employed in gas desulphurization, absorption, desorption, and distillation [4–7]. In biological processing, it is used for alcohol fermentation. Muroyama and Fan [8] discussed some

Correspondence: B. Bensebia, Laboratory of Plant Chemistry-Water-Energy, Department of Process Engineering, Faculty of Technology, Hassiba Benbouali University, B.P. 151, 02000 Chlef, Algeria.
E-mail: bensebiab@yahoo.fr; b.bensebia@univ-chlef.dz
Paper received: 4 March, 2023
Paper revised: 15 May, 2023
Paper accepted: 6 June, 2023

https://doi.org/10.2298/CICEQ230304010B

specific applications. In recent years, under the double constraint of the imperatives of environmental protection and pollution reduction and the rational use of energy, TBC has offered new opportunities, particularly in air pollution control [9].

Numerous published studies have focused on exploring the hydrodynamic parameters and performance of the Turbulent Bed Contactor (TBC), determining mass and heat transfer rates and associated parameters. Most of these studies have proposed empirical correlations for predicting the diverse hydrodynamic and mass and heat transfer parameters. In recent years, several authors have adopted the Computational Fluid Dynamics (CFD) approach for modeling the flow behavior in three-phase gas-liquid-solid systems, with specific emphasis on TBCs [10–12].

In 1972, O'Neill *et al.* [13] proposed a model for this three-phase fluidized bed based on the hydrodynamic behavior of a conventional packed column. They classified the TBC operation into two regimes: TBC Type 1 - Fluidization without "Incipient Flooding" and TBC Type 2 - Fluidization due to "Incipient Flooding." In Type I, fluidization started before flooding in the column, whereas in Type 2, fluidization started after flooding. All subsequent studies have referenced this model, which clarified several contradictions in previous findings and outcomes, constituting a significant contribution to comprehending the hydrodynamic behavior of the TBC process.

The bed expansion, which determines the fluidized bed height, is one of the key design parameters for the fluidized bed of TBC. Knowledge of this factor would allow calculation of the expanded volume of the bed and provide a basis for determining liquid and gas holdups. The work of Muroyama and Fan [8] comprehensively summarizes the experimental data of different authors on bed expansion in the Turbulent Bed Contactor (TBC).

According to many authors [14–18], the gas-distributing grid strongly affects the bed expansion behavior, resembling a bubble column with a high gas holdup. For grids having a small open area, a liquid layer formed above the grid causes an axial variation of the liquid holdup. Levsh *et al.* [15], which investigated the effects of the geometry of the supporting grid on the pressure drop and bed expansion of TBC, suggested a correlation between the dynamic bed height and the height of the liquid layer.

Chen and Douglas [19] showed that the bed height increased linearly with gas velocity and liquid velocities for low-density particles. Tichy and Douglas [20] reported that the bed expansion (H_d/H_{st}) is independent of both the static bed height (H_{st}) and particle density (ρ_p) for low particle density and that a rapid increase in dynamic bed height (H_d) has been observed for gas velocities approaching the true flooding point. Balabekov *et al.* [21,22], Ushida *et al.* [23], and Handl [24] noted the existence of two regions of bed expansion, while Vunjak-Novakovic *et al.* [14] observed, based on their experimental data, three regions of the curves in the expansion of the bed with the gas velocity.

The objective of this study, based on a large number of experimental data on the expansion of the bed in the turbulent bed contactor (Type II-TBC), is essentially oriented to the analysis of the evolution of the expansion with the operating variables, such as gas and liquid fluxes, static bed height, and opening of the supporting grid. The results of this analysis, as well as the experimental data, were used to develop a correlation allowing the prediction of the expansion of the bed in the turbulent bed contactor (Type II-TBC).

MATERIAL AND METHODS

Experimental procedure and apparatus

The experimental setup shown in Fig. 1 and previously described [25] consists of three main parts (Fig. 1a), including the fluidization column and the liquid (water) and gas (air) supply systems. The column comprises a plexiglass cylinder of 0.12 m internal diameter and 1.60 m height (1). The column is equipped, in its lower part, with a packing support grid with a variable free opening (2) and at the inlet of the gas distributor (3), ensuring a uniform gas flow through the whole section of the column. The top of the column is equipped with a liquid distributor (4) to ensure a uniform flow of liquid through the entire column section, especially at low flow rates. The liquid supplied to the distributor (Fig. 1b) comes from a reservoir (5) fed by tap water using a centrifugal pump (6). The air supplied to the gas distributor comes from the system's compressor tank (7) via a pressure reducer (8). The bed of particles (9) consists of hollow polypropylene spheres and lies in a static state on a supporting grid. The liquid and gas fluxes were controlled by valves (14, 15), and their flows were measured by rotameters (10 and 11). A U-tube water manometer measured the pressure across the column (12). To reduce pressure fluctuations, a particular device (13) has been designed to separate liquid droplets entrained by the gas at parietal connections.

Experimental conditions

Three relative static bed heights ((H_{st}/D_C) = 0.5;

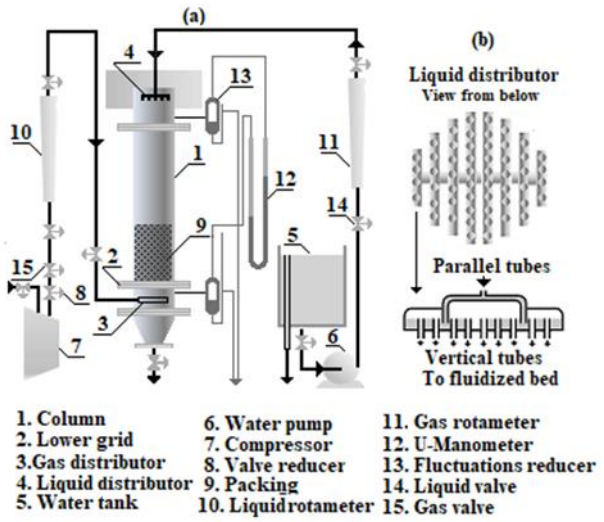

Figure 1. Experimental setup.

0.75 and 1.0)) were considered. For each static bed height, two different sets of packing were considered. For each packing (ρ_{PI}=868 kg m^{-3}, d_{PI}=0.01 m and ρ_{PII}=736 kg m^{-3}, d_{PII}=0.015 m), the opening of the lower grid (φ) was varied as (0.32; 0.56 and 0.82). Each support grid opening used five liquid fluxes (L=4.57; 10.23; 15.84; 20.94, and 27.90 kg m^{-2} s^{-1}). For each series thus defined (ρ_p, d_p, H_{st}, and L), the gas flux (G) was varied from 0 to 10 kg m^{-2} s^{-1}. Thus, for the 13 experimental series considered, 1604 sets of experimental data were measured. The pressure drop and the dynamic bed height were measured simultaneously. The full operating conditions are summarized in Supplementary material (Appendix A, Table A1.).

Methods

The fundamental dynamic bed height (H_d) equation is easy to obtain. Since the total volume of the fluidized bed (V_t) is the sum of the volumes of the different phases (V_s, V_l, and V_g), we can write in terms of fractions for each phase:

$$\varepsilon_S + \varepsilon_l + \varepsilon_g = 1 \tag{1}$$

We define, from the mass balance of the liquid phase and the solid phase, the solid and liquid holdup based on the static bed height ($\varepsilon_{s_{st}}$ and $\varepsilon_{l_{st}}$), as follows:

$$\varepsilon_{l_{st}} = \varepsilon_l \frac{H_d}{H_{st}} \tag{2}$$

$$\varepsilon_{S_{st}} = \varepsilon_S \frac{H_d}{H_{st}} \tag{3}$$

where H_d and H_{st} are the dynamic and static bed heights. If we write that ε_0 is the void fraction of the dry packing, we get:

$$\varepsilon_{S_{st}} = (1-\varepsilon_0) \tag{4}$$

The mass balance for the same amount of solid particles in a static and dynamic state gives:

$$\Omega H_{st}\rho_s(1-\varepsilon_0) = \Omega H_d \rho_s\left(1-(\varepsilon_l+\varepsilon_g)\right) \tag{5}$$

If we call (ε) the sum of liquid (ε_l) and gas holdup (ε_g):

$$\varepsilon = \varepsilon_l + \varepsilon_g \tag{6}$$

and combining Eqs. 1, 5, and 6, we obtain for ε_s :

$$\varepsilon_s = 1-\varepsilon = \frac{H_{st}}{H_d}(1-\varepsilon_0) \tag{7}$$

that becomes:

$$\frac{H_d}{H_{st}} = \frac{(1-\varepsilon_0)}{(1-\varepsilon)} \tag{8}$$

Rewriting Eq. 8, considering Eqs. 2 and 6 gives the fundamental relationship for the ratio H_d/H_{st}, which represents the bed expansion from liquid $(\varepsilon_{l_{st}})$ and gas (ε_g) holdups:

$$\frac{H_d}{H_{st}} = \frac{\varepsilon_{l_{st}} + (1-\varepsilon_0)}{(1-\varepsilon_g)} \tag{9}$$

RESULTS AND DISCUSSION

We have experimentally determined the expansion of the bed and the associated pressure drop. The effects of operating variables (gas and liquid fluxes (G and L), free supporting grid area (φ), static bed height (H_{st}), and packing characteristics (ρ_p, d_p) on bed expansion were determined. The experimental results consisted of 65 curves of the evolution of bed expansion. For brevity, we present only a few examples of experimental data.

Effect of gas and liquid velocities (u_g, u_l)

Fig. 2 shows that the bed expansion (H_d/H_{st}) increases sharply with the increase of the gas and liquid velocities (u_g and u_l), as has been observed earlier [15–17,19,20,26–28].

Effect of grid opening (φ) on bed expansion

Figure 3a clearly shows that a reduction in the opening of the lower supporting grid promoted the bed expansion and that this effect was enhanced by increasing the liquid velocity. It is illustrated in the inset figure in Fig. 3a, which represents the expansion's evolution for various support grid openings and liquid velocities of 0.00457, 0.01023, and 0.02094.m s^{-1}.

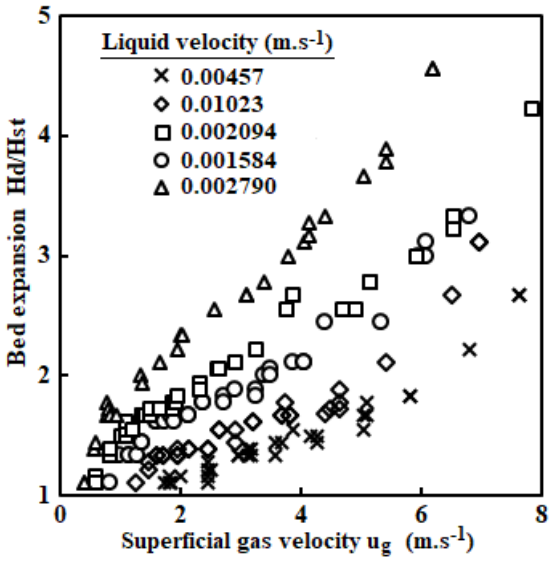

Figure 2. Variation of the bed expansion (H_d/H_{st}) with gas velocity (u_g) and liquid fluxes (L) for series II: (ρ_{PI}=868 kg m^{-3}, d_{PI}=0.010 m, φ=0.56, H_{st}=0.090 m).

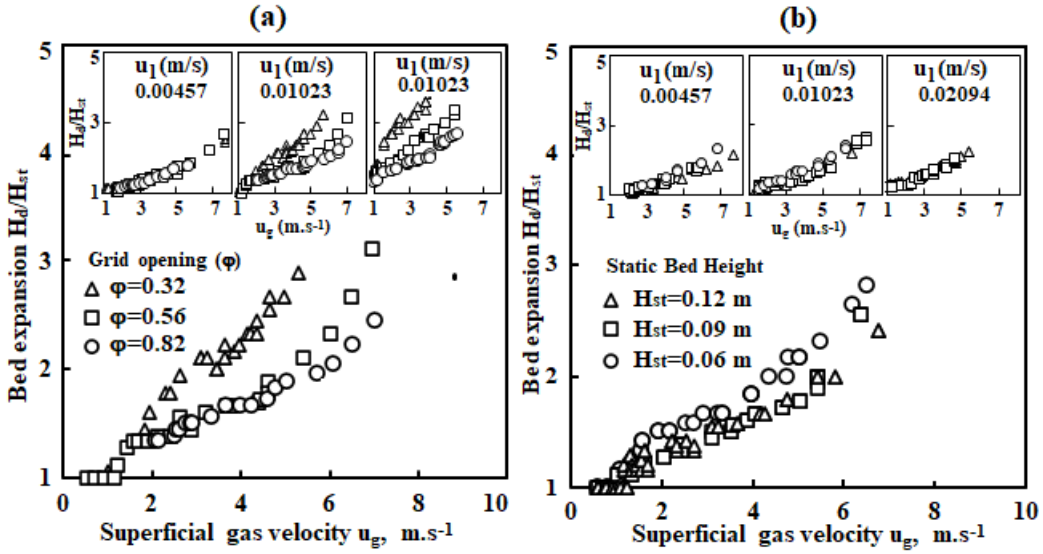

Figure 3. a) Effect of grid opening (φ) on bed expansion (H_d/H_{st}) for series I, II, and III (ρ_{PI}=868 kg m^{-3}, d_{PI}=0.010 m, H_{st}=0.090 m, L=10.23 kg m^{-2} s^{-1}. b) Effect of static bed height on bed expansion (H_d/H_{st}) for series VIII, XI, and XIV (ρ_{PII}=736 kg m^{-3}, d_{PII}=0.015 m, φ=0.56, L=15.84 kg m^{-2} s^{-1}).

Effect of static bed height (H_{st})

The results presented in Figure 3b show that the static head (H_{st}) had no significant effect on bed expansion for the different liquid flows.

Models' development

According to Vunjak-Novakovic *et al.* [14], three models for bed expansion in TBC have been proposed: Levsh *et al.* [15], Tichy and Douglas [29], and O'Neil *et al.* [30]. The first model of Levsh *et al.* [15] was considered incomplete [14] because it included the gas fraction in the bed for which no correlation was given. The second model of Tichy and Douglas [29] is based primarily on the analysis of experimental data [19,29], which shows a linear dependence between the bed expansion (H_d/H_{st}) and the gas flow rate, and the fact that the bed expands as a consequence of the pressure drop increase caused by the increase in the gas flow rate. There is, thus, a mutual relationship between the pressure drop and the expanded bed height. The shortcomings of this approach [14] are the use of an equivalent diameter of gas channels, somewhat fictitious for fluidized beds, and the use of correlations valid for fully fluidized beds at all gas velocities. According to their incipient flooding model [13] and using the Wallis equation for flooding in packed

beds [31], O'Neil *et al.* [30] derived the third model based on Eq. 14 to predict bed expansion in TBC. However, as the expression (Eq. 14) was derived for incipient fluidization due to flooding, it could not be recommended for TBC type II.

In our opinion, adding the model based on Eq. 9 would also be necessary, which is considered the basic relationship to the definition of expansion. However, the implementation of this model requires reliable correlations for estimating gas and liquid holdups.

The study of different correlations for estimating the expansion (Table 1) identifies readily another model based on a relationship between the minimum fluidization velocity and expansion: those of Uysal [32], Khanna [33], and Blyakher *et al.* [28]. Other expressions are mainly based on the attempt to correlate experimental data and based on the operative variables affecting the bed expansion.

Table 1. Correlations for bed expansion (H_d/H_{st}) for TBC.

Authors	Correlations (S.I. Units)	Eq.
Levsh *et al.* [15]	$\frac{H_d}{H_{st}} = 4.4\ {u_l}^{0.43}{u_g}^2 \ \ for\ u_l < 0.0078\ m/s, \quad u_g < 2.5\ m/s$ $\frac{H_d}{H_{st}} = 2.2\ {U_l}^{0.35}{u_g}^2 \ \ for\ u_l > 0.0078\ m/s, \quad u_g > 2.5\ m/s$	(10)
Tichy & Douglas [20]	$\frac{H_d}{H_{st}} = 0.8849 + 0.3166\ G - 18.33\ d_P + 0.5852\ L^{0.6}{d_P}^{0.5}$	(11)
Rama *et al.* [26]	$\frac{H_d}{H_{st}} = 2.132\ {d_P}^{0.12}{u_l}^{0.31} + 1.02\ {d_P}^{-1.7}{\rho_P}^{-1.2}{u_l}^{0.2}U_g$	(12)
Blyakher *et al.* [28]	$\frac{H_d}{H_{st}} = 1.17 + (0.065 + 24.6\ {u_l}^{0.75})(\rho_g u_g - \rho_g u_{mf})$	(13)
O'Neil *et al.* [30]	$\frac{H_d}{H_{st}} = \frac{1-\varepsilon_0}{1-\varepsilon}, \varepsilon = \left[K\left(27+\frac{4K}{108}\right)^{1/2} + \frac{K}{2}\right]^{1/3} - \left[K\left(27+\frac{4K}{108}\right)^{1/2} - \frac{K}{2}\right]^{1/3}$ $K = \left[{u_g}^{1/2} + {u_l}^{1/2}(\rho_l/\rho_g)^{1/4}\right]/\left[0.775(g d_P \rho_l/6\rho_g)^{1/4}\right]$	(14)
Uysal [32]	$\frac{H_d}{H_{st}} = 1 + \frac{0.147(\rho_g u_g - \rho_g u_{mf})}{H_{st}}, \qquad u_{mf} = \frac{10.86\ {d_P}^{0.488}10^{0.01985\,L}}{\rho_g}$	(15)
Khanna [33]	$\frac{H_d}{H_{st}} = 1 + 0.414(\rho_g u_g - \rho_g u_{mf})(\rho_g u_{mf})^{0.2}, u_{mf} = \frac{526.47{d_P}^{1.5}10^{0.0117\,L}}{\rho_g}$	(16)
Lyashuk [34]	$\frac{H_d}{H_{st}} = 0.16{u_g}^{0.44}L^{0.27}{H_{st}}^{-0.71}\varphi^{-1.54}$	(17)
Shackley [35]	$\frac{H_d}{H_{st}} = 0.0833\ (-14.9\varphi^2 + 15.7\varphi - 2.1){H_{st}}^{-0.34}L^{0.26}{\rho_P}^{-0.43}{u_g}^{0.78}{d_P}^{-0.85}$	(18)
Gimenes & Handley [36]	$\frac{H_d}{H_{st}} = 1.862\ {d_P}^{0.306}\left(1-\frac{\varphi}{\psi_v}\right)^{1.37}L^{0.108}(10^3\rho_P v_P)^{-0.107}exp(0.356\ u_g)$	(19)
Aksel'rod & Yakovenko [37]	$\frac{H_d}{H_{st}} = 0.933\ {u_l}^{0.3}{H_{st}}^{-0.4}\left(\frac{U_g}{\varphi}\right)^{0.93} for\ \frac{u_g}{\varphi} \geq 6\ m/s$ $\frac{H_d}{H_{st}} = 2.16\ {u_l}^{0.3}{H_{st}}^{-0.4}\left(\frac{u_g}{\varphi}\right)^{0.43} for\ \frac{u_g}{\varphi} < 6\ m/s$	(20)
Azhar-Ul Haq [38]	$\frac{H_d}{H_{st}} = 1.704\ {u_l}^{0.13}{u_g}^{0.544}\ {H_{st}}^{-0.1055}{\rho_p}^{-0.2426}{d_p}^{-0.38}$	(21)

Proposed model

In this work, we proposed a model based on the basic theoretical equation of the fluidized bed expansion (Eq. 9) derived from the mass balance of the fixed and the fluidized bed. The model has an unquestionable theoretical consistency, and its application for predicting the fluidized bed expansion requires the estimation of the liquid and gas holdups ($\varepsilon_{l,st}$, ε_g). In the end, the prediction of the bed expansion depends only on the choice of the most appropriate correlations for the liquid and gas holdups. From the set of correlations for liquid and gas holdup in the literature, we had chosen those that gave the best predictions. These correlations are presented in Table 2.

The adopted procedure estimates the fluidized bed expansion (H_d/H_{st}) using Eq. 9, which requires the calculation of liquid (ε_{lst}) and gas (ε_g) holdups.

In this work which objective was to propose a prediction model of the fluidized bed expansion for the turbulent bed contactor, and to achieve this, we

employed a variety of correlations derived from existing literature, comprising six equations for gas holdup (Eqs. 42–47) and 20 equations (Eqs. 22–41) for liquid holdup (Table 2). One hundred twenty pairs of correlations were obtained (Table 3) for liquid holdup ($\varepsilon_{l,st}$) and gas holdup (ε_g) that we used to estimate the expansion (H_d/H_{st}).

Table 2. Correlations for liquid and gas holdup ($\varepsilon_{l,st}$ and ε_g) for TBC.

Authors	Correlations for liquid holdup ($\varepsilon_{l,st}$)	Eqs
Vunjak-Novakovic *et al.* [14]	$\varepsilon_{l_{st}} = 7.326\ Re_l^{-0.0591} Fr_l^{0.4354} \left(\frac{H_{st}}{D_C}\right)^{-0.4328} \left(\frac{\rho_p}{\rho_l}\right)^{0.0904} + 0.02\ (Type\ II)$	(22)
Chen & Douglas [19]	$\varepsilon_{l_{st}} = 0.02 + 2.369\ 10^{-3} {U_L}^{0.6} {\rho_l}^{0.6} {d_P}^{-0.5}$	(23)
Balabekov *et al.* [21]	$\varepsilon_{l_{st}} = c\left[\left(0.828\frac{L}{u_g}\right)\frac{\rho_g}{\rho_l}\right]^{k+1}(1-\varepsilon_0)\frac{\rho_P}{\rho_l}$ *For partial fluidization:* $c = 0.05\ \ k = 0.8$ *For developed fluidization:* $c = (0.695/\varphi^3)(0.005/d_p)(\rho_p/\rho_l)^{-0.74}(L/10^2)^2, \quad k = (1.58/\varphi^{-0.16})(0.005/d_p)^{-0.1}$	(24)
Ushida *et al.*[23]	$\varepsilon_{l_{st}} = \frac{9.38\ 10^9}{g\rho_l}\ {\mu_l}^{2.3}\varphi^{-0.42}\left(\frac{d_0}{D_C}\right)^{-0.84} {\rho_P}^{0.18} L$	(25)
Handl [24]	$\varepsilon_{l_{st}} = 26.8\ \varepsilon_0\ {Re_l}^{-0.189}\ {Fr_l}^{0.474}$	(26)
Rama *et al.* [26]	$\varepsilon_{l_{st}} = 11\ {Ga_l}^{0.09}\ {Fr_l}^{1.66}\ {Re_l}^{-0.34}\ {We_l}^{-0.34}\left(\frac{H_{st}}{d_p}\right)^{-0.4}\left(\frac{\varphi d}{D}\right)^{-0.58} + 0.086$	(27)
Lyashuk [34]	$\varepsilon_{l_{st}} = 0.001648\ {U_g}^{0.16} L^{0.95} {H_{st}}^{-1.09} \varphi^{-2.02}$	(28)
Shackley [35]	$\varepsilon_{l_{st}} = 3.5\ 10^{-4}\ {U_g}^{0.75} L^{0.7} {H_{st}}^{-0.92} \varphi^{-2.5}$	(29)
Gimenes & Handley [36]	$\varepsilon_{l_{st}} = 9.75\ 10^3\ {H_{st}}^{-0.357}\left(\frac{d_p}{\psi_v}\right)^{-0.411} L^{0.616} exp(0.237 u_g)\ (Oblate\ spheres)$	(30)
Aksel,rod & Yakovenko [37]	$\varepsilon_{l_{st}} = 3.9\ 10^{-2} L\ \frac{\rho_P}{\rho_l}$	(31)
Kito *et al.* [39]	$\varepsilon_{l_{st}} = 12.8\ {Ga_l}^{0.090}\ {Fr_l}^{1.66}\ {Re_l}^{-0.34}\ {We_l}^{-0.34}\left(\frac{H_{st}}{d_p}\right)^{-0.4}\left(\frac{\varphi d}{D}\right)^{-0.58}$	32)
Paterson & Clift [40]	$\varepsilon_{l_{st}} = 2.29\ {U_g}^{-0.07} {U_L}^{0.71} {H_{st}}^{-0.52} \varphi^{-0.874}$	(33)
Petrov & Tassaev [41]	$\varepsilon_{l_{st}} = 8.9\ 10^{-4} U_g^{0.13} L^{0.4} {H_{st}}^{-0.7} d_p^{-0.6} \varphi^{-0.5} \rho_p^{0.02}$ *for partial fluidization* $\varepsilon_{l_{st}} = 1.9\ 10^{-4} U_g^{1.3} L^{0.5} d_p^{-0.6} \varphi^{-0.6} \rho_p^{0.02}$ *for full fluidization*	(34)
Soundarajan & Krishnaiah [42]	$\varepsilon_{l_{st}} = 7.7\ {Ga_l}^{0.090}\ {Fr_l}^{1.66}\ {Re_l}^{-0.34}\ {We_l}^{-0.34}\left(\frac{H_{st}}{d_p}\right)^{-0.4}\left(\frac{\varphi d}{D}\right)^{-0.58} {U_g}^{0.57}\ Type\ II$	(35)
Gel'perin *et al.* [43]	$\varepsilon_{l_{st}} = 0.001369\ {U_L}^{0.5} {\rho_l}^{0.6} {d_P}^{-0.5}$	(36)
	$\varepsilon_{l_{st}} = 4.36\ 10^{-3}\ L^{0.5} {H_{st}}^{-0.25} {d_P}^{-0.6}$	(37)
Gel'perin *et al.* [44]	$\varepsilon_{l_{st}} = 5.47\ 10^{-2}\ {u_g}^{0.24} L^{0.14} {H_{st}}^{-0.08} {\rho_l}^{-1} {\rho_P}^{-0.1}$	(38)
Bruce & Krishnaiah [45]	$\varepsilon_{l_{st}} = 1.36\ {Fr_l}^{1.44}\ {Re_l}^{-0.927}\left(\frac{H_{st}}{d_p}\right)^{-0.593}\left(\frac{\varphi d}{D}\right)^{-0.213}\ (Type\ II)$	(39)
Barile & Meyer [46]	$\varepsilon_{l_{st}} = 1160\ {Fr_l}^{0.78}\ {Re_l}^{-0.51} {H_{st}}^{-0.36} {d_p}^{0.36}$	(40)
Tarat *et al.* [47]	$\varepsilon_{l_{st}} = 8.38\ 10^{-2}\ {H_{st}}^{-1} L^{0.96} {u_g}^{1.04} {\rho_g}^{1.04}$	(41)
	Correlations for gas holdup (ε_g)	
Kito *et al.* [17]	$\varepsilon_g = 0.19\left(\frac{d_p {U_g}^2 \rho_l}{\sigma}\right)^{0.11}\left(\frac{U_g}{\sqrt{gD_C}}\right)^{0.20}$	(42)
Bensebia *et al.* [25]	$\varepsilon_g = 0.276\ {Fr_g}^{0.325}\left(\frac{L}{G}\right)^{-0.014} \varphi^{-0.137}$	(43)
Kito *et al.* [39]	$\varepsilon_g = 0.417\ {U_g}^{0.44}$	(44)
Gel'perin *et al.* [43]	$\varepsilon_g = 0.93\left(\frac{d_p {U_g}^* \rho_g}{\mu_g}\right)^{0.4}\left(\frac{{d_p}^3(\rho_p - \rho_g)\rho_g}{{\mu_g}^2}\right)^{-0.2}\left({U_g}^* = \frac{U_g}{1-\varepsilon_{l_{st}}(H_{st}/H_d)}\right)$	(45)
Soundarajan & Krishnaiah [48]	$\varepsilon_g = 0.322\ {Fr_g}^{*0.22} \quad \left(Fr_g^* = (U_g/\varphi)/\sqrt{gd_p}\right)$	(46)
Vunjak-Novakovic *et al.*[49]	$\varepsilon_g = \frac{U_g}{U_{g_{mf}}}\varepsilon_0 - 4.43\ 10^{-3}\left(\frac{H_{st}}{D_C}\right)^{0.433} d_P^{-0.494} L^{0.812}\left(\frac{\rho_p}{\rho_l}\right)^{0.090} - 0.02\ (partial\ fluidization\ type\ II)$ $\varepsilon_g = 0.628 {U_g}^{0.237}\ (Fully\ fluidization\ types\ II)$	(47)

Table 3. Pairs ($\varepsilon_{l,st}$, ε_g) used for predicting bed expansion according to Eq. 9.

	Authors	ε_g					
		Kito *et al.*[17]	Bensebia *et al.* [25]	Kito *et al.* [39]	Gel'Perin *et al.* [43]	Soundarajan & Krishnaiah [48]	Vunjak-Novakovic *et al.* [49]
ε_{lst}	Vunjak-Novakovic *et al.*[14]	Eqs. (22, 42)	Eqs. (22, 43)	Eqs. (22, 44)	Eqs. (22, 45)	Eq. (22, 46)	Eq. (22, 47)
	Chen and Douglas [19]	Eqs. (23, 42)	Eqs. (23, 43)	Eqs. (23, 44)	Eqs. (23, 45)	Eq. (23, 46)	Eq. (23, 47)
	Balabekov *et al.* [21]	Eqs. (24, 42)	Eqs. (24, 43)	Eqs. (24, 44)	Eqs. (24, 45)	Eq. (24, 46)	Eq. (24, 47)
	Ushida *et al.* [23]	Eqs. (25, 42)	Eqs. (25, 43)	Eqs. (25, 44)	Eqs. (25, 45)	Eq. (25, 46)	Eq. (25, 47)
	Handl [24]	Eqs. (26, 42)	Eqs. (26, 43)	Eqs. (26, 44)	Eqs. (26, 45)	Eq. (26, 46)	Eq. (26, 47)
	Rama *et al.* [26]	Eqs. (27, 42)	Eqs. (27, 43)	Eqs. (27, 44)	Eqs. (27, 45)	Eq. (27, 46)	Eq. (27, 47)
	Lyashuk [34]	Eqs. (28, 42)	Eqs. (28, 43)	Eqs. (28, 44)	Eqs. (28, 45)	Eq. (28, 46)	Eq. (28, 47)
	Shackley [35]	Eqs. (29, 42)	Eqs. (29, 43)	Eqs. (29, 44)	Eqs. (29, 45)	Eq. (29, 46)	Eq. (29, 47)
	Gimenes & Handley [36]	Eqs. (30, 42)	Eqs. (30, 43)	Eqs. (30, 44)	Eqs. (30, 45)	Eq. (30, 46)	Eq. (30, 47)
	Aksel,rod & Yakovenko [37]	Eqs. (31, 42)	Eqs. (31, 43)	Eqs. (31, 44)	Eqs. (31, 45)	Eq. (31, 46)	Eq. (31, 47)
	Kito *et al.* [39]	Eqs. (32, 42)	Eqs. (32, 43)	Eqs. (32, 44)	Eqs. (32, 45)	Eq. (32, 46)	Eq. (32, 47)
	Paterson and Clift [40]	Eqs. (33, 42)	Eqs. (33, 43)	Eqs. (33, 44)	Eqs. (33, 45)	Eq. (33, 46)	Eq. (33, 47)
	Petrov & Tassaev [41]	Eqs. (34, 42)	Eqs. (34, 43)	Eqs. (34, 44)	Eqs. (34, 45)	Eq. (34, 46)	Eq. (34, 47)
	Soundarajan & Krishnaiah [42]	Eqs. (35, 42)	Eqs. (35, 43)	Eqs. (35, 44)	Eqs. (35, 45)	Eq. (35, 46)	Eq. (35, 47)
	Gel'perin *et al.* [43]	Eqs. (36, 42)	Eqs. (36, 43)	Eqs. (36, 44)	Eqs. (36, 45)	Eq. (36, 46)	Eq. (36, 47)
	Gel'perin *et al.* [43]	Eqs. (37, 42)	Eqs. (37, 43)	Eqs. (37, 44)	Eqs. (37, 45)	Eq. (37, 46)	Eq. (37, 47)
	Gel'perin *et al.* [44]	Eqs. (38, 42)	Eqs. (38, 43)	Eqs. (38, 44)	Eqs. (38, 45)	Eq. (38, 46)	Eq. (38, 47)
	Bruce and Krishnaiah [45]	Eqs. (39, 42)	Eqs. (39, 43)	Eqs. (39, 44)	Eqs. (39, 45)	Eq. (39, 46)	Eq. (39, 47)
	Barile and Meyer [46]	Eqs. (40, 42)	Eqs. (40, 43)	Eqs. (40, 44)	Eqs. 40,45)	Eq. (40, 46)	Eq. (40, 47)
	Tarat *et al.* [47]	Eqs. (41, 42)	Eqs. (41, 43)	Eqs. (41, 44)	Eqs. (41, 45)	Eq. (41, 46)	Eq. (41, 47)

Model evaluation

In addition to having a consistent theoretical basis, the quality of a predictive model is closely linked to the results of evaluating the precision, accuracy, and reliability of the correlation deduced from this model. The evaluation of the discrepancies between the experimental data and the predictions, according to the proposed approach, was estimated using the mean absolute error in percentage (MAPE), the root mean square error (RMSE), the coefficient of correlation (ρ_{XY}) and explained variance (VE_{CV}). The statistical indicators used were defined as follows:

$$MAPE\,(\%) = \frac{100}{n}\sum_{i=1}^{n}\frac{\left|\left(H_d / H_{st}\right)_{(\exp)_i} - \left(H_d / H_{st}\right)_{(\mathrm{pred})_i}\right|}{\left(H_d / H_{st}\right)_{(\exp)_i}} \quad (48)$$

$$RMSE\,(\%) = \sqrt{\sum_{i=1}^{n}\frac{1}{n}\left(\left(H_d / H_{st}\right)_{(\exp)_i} - \left(H_d / H_{st}\right)_{(\mathrm{pred})_i}\right)^2} \quad (49)$$

$$\rho_{XY} = \frac{\sum_{i=1}^{n}\left(\left(H_d / H_{st}\right)_{(\exp)_i} - \overline{\left(H_d / H_{st}\right)_{(\exp)}}\right)\left(\left(H_d / H_{st}\right)_{(\mathrm{pred})_i} - \overline{\left(H_d / H_{st}\right)_{(pred)}}\right)}{\sqrt{\sum_{i=1}^{n}\left(\left(H_d / H_{st}\right)_{(\exp)_i} - \overline{\left(H_d / H_{st}\right)_{(\exp)}}^{\,2}\right)\left(\left(H_d / H_{st}\right)_{(\mathrm{pred})_i} - \overline{\left(H_d / H_{st}\right)_{(pred)}}\right)^2}} \quad (50)$$

$$VE_{CV} = \left[1 - \frac{\sum_{i=1}^{n}\left(\left(H_d / H_{st}\right)_{(\exp)_i} - \left(H_d / H_{st}\right)_{(\mathrm{pred})_i}\right)^2}{\sum_{i=1}^{n}\left(\left(H_d / H_{st}\right)_{(\exp)_i} - \overline{\left(H_d / H_{st}\right)_{(\exp)}}\right)^2}\right]100\% \quad (51)$$

where $\left(\frac{H_d}{H_{st}}\right)_{(\exp)_i}$ and $\left(\frac{H_d}{H_{st}}\right)_{(\mathrm{pred})_i}$ are respectively, the ith experimental data and predicted values of bed expansion, among the n data, and $\overline{\left(\frac{H_d}{H_{st}}\right)_{(\exp)}}$ and $\overline{\left(\frac{H_d}{H_{st}}\right)_{(\mathrm{pred})}}$ are, respectively, the mean of the experimental data and predicted values.

Two different ways have been used for bed expansion prediction: i) with the different correlations presented in Table 1, ii) using the model based on Eq.9

and the correlations of liquid and gas holdups presented in Table 2.

Evaluation of the correlations of the different authors

All the bed expansion correlations presented in Table 1 were tested with the experimental values obtained under the experimental conditions of the present work. In Fig. 4, where an example of a given experimental system is presented, it is easy to notice that Eqs. 10, 13, 15, 18, 20, and 21 overestimate the bed expansion compared to the experimental data, while Eqs. 14, 17, and 19 underestimate the expansion to different degrees. Remarkably, the best estimate is given by Eq. 11 of Tichy and Douglas [20], which is one of the simplest and among the first.

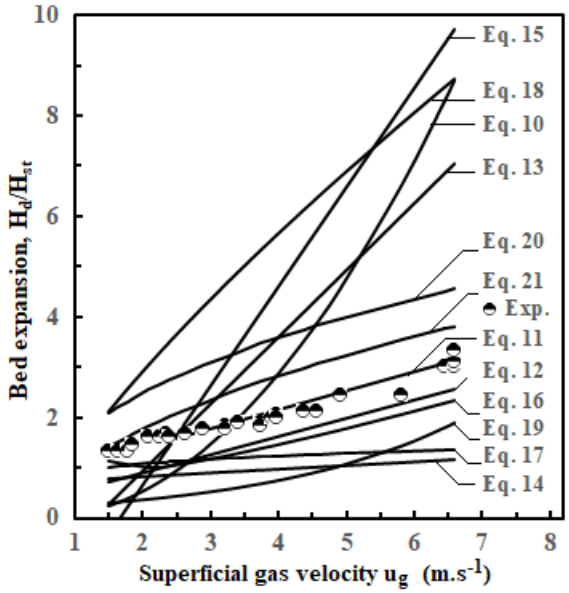

Figure 4. Comparison of experimental bed expansion (H_d/H_{st}) data and predictions by different bed expansion correlations (Eqs. 10–21) for system II.3 (ρ_{Pl}=868 kg m^{-3}, d_{Pl}=0.010 m, H_{st}=0.090 m, φ=0.56, L=15.84 kg m^{-2} s^{-1}).

Fig. 4 compares experimental results obtained from a specific system (System II.3 with L = 15.84 kg m^{-2} s^{-1}) with those of the 13 experimental systems investigated in the present study. To conduct a comprehensive analysis of the comparison results, encompassing all correlations (Eqs. 10–21) and the entirety of the experimental data (i.e., the 13 systems representing the various experimental conditions), the percent mean absolute error (MAPE), root mean square error (RMSE), correlation coefficient (ρ_{XY}), and variance explained (VE_{CV}) were determined.

The results for the experimental data set (1604 data) confirm that Eq. 11 of Tichy and Douglas [20] and Eq. 16 of Khanna [33] gave the best predictions for the expansion of the fluidized bed in TBC.

Table B1 in Appendix B presents the prediction results for all the correlations studied.

Evaluation of the predictions according to Eq. 9 and correlations for $\varepsilon_{l,st}$ and ε_g

The bed expansion prediction results (H_d/H_{st}) were obtained for all the systems using the evaluation criteria: MAPE, RMSE, ρ_{XY}, and VE_{CV}. For presentation, Table 4 shows only the results of systems with a MAPE error of less than 25%. Fig. 5a shows the experimental data of bed expansion for all experimental points (1604 points) with the proposed correlations (Eqs. 26 and 43).

The results in Table 4 show that among the 120 pairs studied, 15 pairs (correlations for $\varepsilon_{l,st}$, ε_g) gave predictions with MAPE errors lower than 25%.

Among the correlations for estimating gas holdup (ε_g), Eqs 42, 43, and 46 gave the best results for bed expansion (H_d/H_{st}). It should be noted that these Eqs

Table 3. Statistical results of comparison of bed expansion (H_d/H_{st}) data and predictions based on Eq. 9 and correlations of $\varepsilon_{l,st}$ (Eqs. 23, 26, 34, 36, and 37) and ε_g (Eqs. 42, 43, and 46).

Eqs. for ε_g		Statistical functions	Eqs. for $\varepsilon_{l,st}$				
N° Eq.	Authors		Eq. 23 Chen & Douglas [19]	Eq. 26 Handl [24]	Eq. 34 Petrov & Tassaev [41]	Eq. 36 Gel'perin *et al.* [43]	Eq. 25 Ushida *et al.* [23]
Eq. 42	Kito *et al.* [17]	MAPE (%)	20.26	15.33	24.75	22.68	33.04
		RMSE	0.70	0.55	0.72	0.75	0.73
		$\rho_{(x,y)}$	0.97	0.83	0.97	0.98	0.95
		VEcv (%)	49.95	64.86	55.88	42.31	40.69
Eq. 43	Bensebia *et al.* [25]	MAPE (%)	16.86	18.57	20.00	17.31	16.07
		RMSE	0.52	0.45	0.56	0.56	0.53
		$\rho_{(x,y)}$	0.86	0.65	0.83	0.86	0.84
		VEcv (%)	55.76	67.42	49.03	49.09	54.81
Eq. 46	Soundarajan & Krishnaiah [48]	MAPE (%)	15.66	16.46	17.05	16.47	15.79
		RMSE	0.52	0.41	0.53	0.57	0.55
		$\rho_{(x,y)}$	0.71	0.40	0.75	0.72	0.67
		VEcv (%)	56.02	73.24	54.24	47.49	51.31

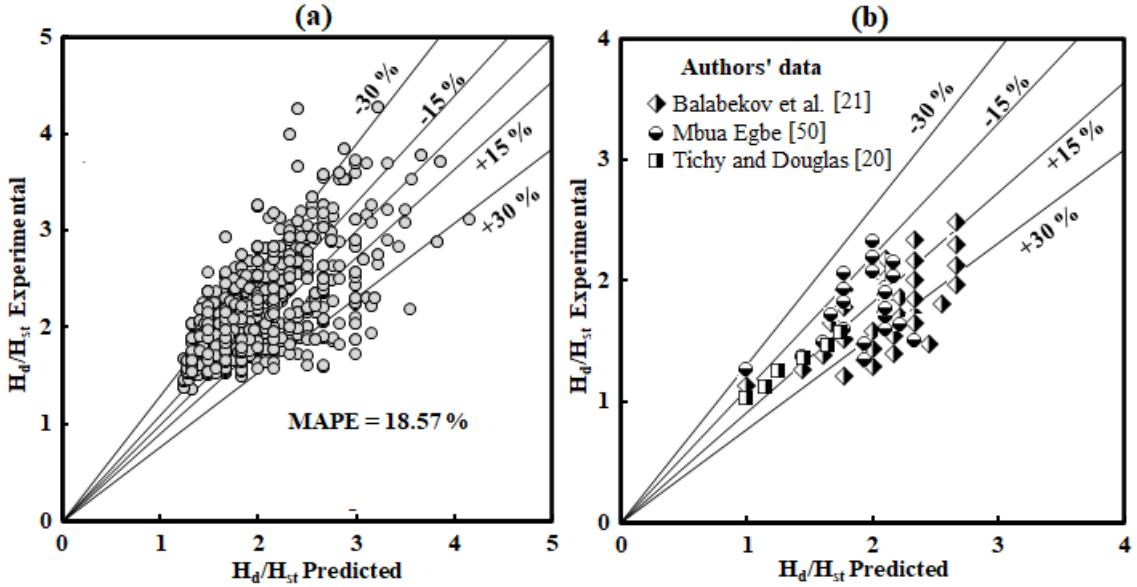

Figure 5. a) Comparison of experimental data of bed expansion (H_d/H_{st}) with predictions calculated by Eq. 9 with Eqs. 26 and 43 for all series (ρ_{PI}=868 k m^{-3}, d_{PI}=0.010 m, ρ_{PII}=736 kg m^{-3}, d_{PII}=0.015 m, Hst=0.06, 0.09, 0.12 m, φ=0.32, 0.56, 0.82). b) Comparison of experimental bed expansion (H_d/H_{st}) data with the predictions of Balabekov et al. [21], Tichy and Douglas [20], and Mbua Egbe [50].

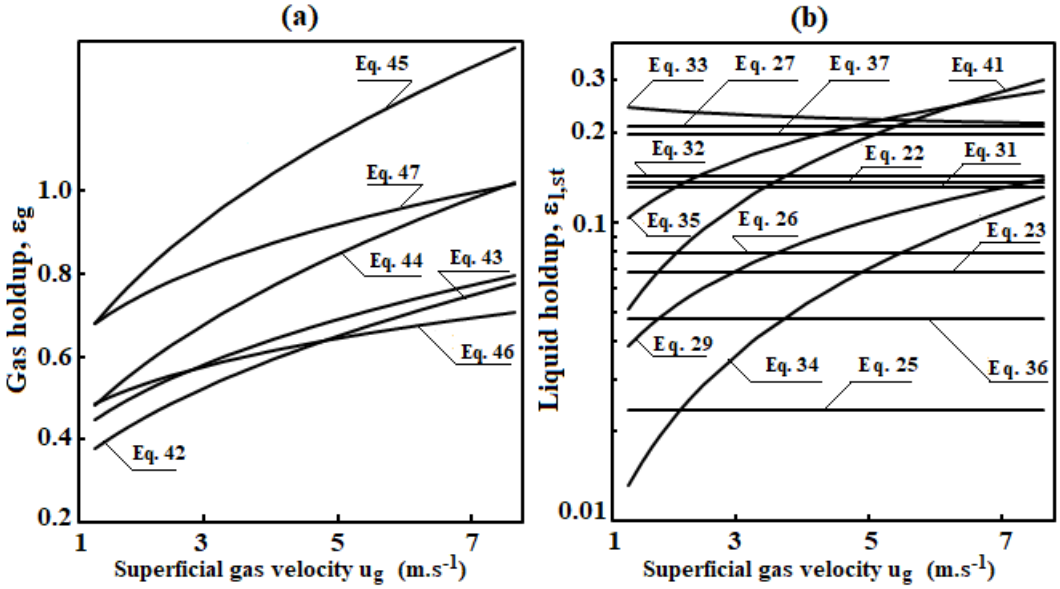

Figure 6. a) Gas holdup (ε_g) predictions with different correlations (Eqs. 42–47) for (ρ_{PII}=736 kg m^{-3}, d_{PII}=0.015 m, H_{st}=0.12 m, φ=0.56, L=4.57 kg m^{-2} s^{-1}). b) Liquid holdup predictions ($\varepsilon_{l,st}$) with different correlations for (ρ_{PII}=736 kg m^{-3}, d_{PII}=0.015 m, H_{st}=0.12 m, φ=0.56, L=4.57 kg m^{-2} s^{-1}).

equations gave substantially similar predictions of gas holdup (ε_g) with lower values than those given by the other equations (44, 45, and 47). This feature is well shown in Fig. 6a, which presents an example of the results of gas holdup predictions (ε_g) for a given experimental case.

Eqs. 42, 43, and 46, which gave the best predictions for bed expansion, gave significantly lower values of gas holdup (ε_g) than those given by Eqs 44, 45, and 47. Regarding the liquid holdup ($\varepsilon_{l,st}$), it was noticed that the correlations that give the lowest predictions for the liquid holdup (Eqs. 23, 25, 26, 34, and 36) gave the best estimates of the fluidized bed expansion.

Fig. 6b, which illustrates the evolution of the liquid holdup with the superficial velocity, using the different correlations of Table 2, highlights this peculiar where it is illustrated that Eqs. 23, 25, 26, 34, and 36 gave the lowest predictions for the liquid holdup.

The complete results of the comparison of experimental data obtained from the 13 series of bed expansion with predictions made using Eq. 9 and correlations for liquid holdup (Eqs. 22–41) and gas holdup (Eqs. 43–47) have been presented in Table B.2 within Appendix B.

Comparison of predictions with experimental values from other authors

The bed expansion prediction procedure developed in this work and based on Eq. 9 was tested using experimental data from different authors. The use of the correlations proposed in this work (Eqs. (26, 43), Eqs. (35, 43), Eqs. (36, 43)) to correlate the data of Tichy and Douglas [20], Balabekov *et al.* [21], and Mbua Egbe [50], gave satisfactory results as shown in Fig 5b. In Fig 5b, the comparison of the experimental and predicted values of Tichy and Douglas [20], Balabekov *et al.* [21], and Mbua Egbe [50], using the approach proposed in this work is presented. The experimental conditions used by the authors of the considered works are presented in Table C1, Appendix C.

CONCLUSION

The analysis of the experimental data showed that the bed expansion (H_d/H_{st}) increased with the gas velocity and the liquid flux. It was also observed that the bed expansion is favored by the decrease of the free surface of the support grid and that the static bed height did not affect the bed expansion.

The second part of this work, analyzing the results of expansion prediction using correlations from different authors, allowed the selection of the most suitable expressions based on a systematic evaluation using appropriate statistical indicators. Among the correlations for the prediction of H_d/H_{st}, the equations of Tichy and Douglas [20] and Khanna [33] gave the best predictions. It should be noted that these correlations involve the gas and liquid fluxes and the particle diameter without including the static bed height.

Analysis of the predictions using the model based on the basic theoretical fluidized bed expansion Eq. 9 yielded the best predictions using Eqs. 42, 43, and 46 for gas holdup estimation and Eqs. 23, 25, 26, 34, and 36 for liquid holdup estimation. Specifically, combinations of Eqs. 46 and 23 and Eqs. 42 and 26 yielded the best-fluidized bed expansion prediction.

NOMENCLATURE

D_C	Column inside diameter, m
d_p	Packing diameter, m
g	Acceleration due to the gravity, m s^{-2}
G	Mass flow rate of gas per unit area, kg m^{-2} s^{-1}
H_d	Expanded bed height, m
H_{st}	Static bed height, m
L	Liquid mass flow rate per unit area, kg m^{-2} s^{-1}
$-\Delta P_c$	Total pressure drop across the entire column, Pa
u_g	Superficial gas velocity, m s^{-1}
u_{gmf}	Minimum fluidization velocity, m s^{-1}
u_l	Liquid velocity, m s^{-1}
V_d	Volume of the expanded bed, m^3
V_g	Volume of the gas in the bed, m^3
V_l	Volume of the liquid in the bed, m^3
V_p	Volume of the packing in the bed, m^3
v_p	Volume of the individual particle of packing, m^3
ε_0	Voidage of the static bed without gas-liquid flow, m^3 m^{-3}
ε_g	Gas holdup ($V_g/\Omega H_d$), m^3 m^{-3}
ε_l	Liquid holdup based on expanded bed height (V_l/V_d), m^3 m^{-3}
$\varepsilon_{l,st}$	Liquid holdup based on static bed height (V_l/V_d), m^3 m^{-3}
ε_p	Packing holdup based on expanded bed height(V_p/V_d),m^3m^{-3}
$\varepsilon_{s,st}$	Packing holdup based on static bed height (V_p/V_d), m^3 m^{-3}
φ	Free-open area of the supporting grid
Ω	Cross-sectional area of the column ($nD_C^2/4$), m^2
ρ_g	Gas density, kg m^{-3}
ρ_l	Liquid density, kg m^{-3}
ρ_p	Packing density, kg m^{-3}
ψ_v	Sphericity

REFERENCES

[1] Z. Arsenijević, T. K. Radoičić, M. Đuriš, Z. Grbavcic, Chem. Ind. Chem. Eng. Q. 21 (4) (2015) 519–526. https://core.ac.uk/download/pdf/299291518.pdf.

[2] S. J. Kulkarni, A. K. Goswami, Int. Res. J. Eng. Tech, 02 (05) (2015) 279–282. https://www.irjet.net/archives/V2/i5/IRJET-V2I551.pdf.

[3] M. L. Gimenes, D. Handley, M. G. C. Silva, Braz. J. Chem. Eng. 24 (1) (2007) 37–45. https://doi.org/10.1590/S0104-66322007000100004.

[4] S. Deagan, Rev. Chim., 70 (11) (2019) 4040–4046. https://doi.org/10.37358/RC.70.19.11.7698.

[5] F.-M. Ilea, A-M. Cormos, S. Dragan, C.-C. Cormos, Chem. Eng. J. 449 (1) (2022) 137674. https://doi.org/10.1016/j.cej.2022.137674.

[6] K. Muroyama, L.-S. Fan, AIChE 31 (1) (1985) 1–34. https://doi.org/10.1002/aic.690310102.

[7] S. Durga Jeevitha, A. Annam Renita, K. Soundarajan, K. Krishnaiah, J. Abbas Mohaideen, Int. J. Appl. Bioeng. 2 (1) (2008) 77–79. https://doi.org/10.18000/ijabeg.10028.

[8] H. A. Khalifeh, M. Alkhedher, S. Fernandes, 8th International Conference on Modeling Simulation and Applied Optimization (ICMSAO) (2019) 1–4. https://dspace.adu.ac.ae/handle/1/2777.

[9] S. S. J. Gillani, A. Ullah, M. Zaman, I. R. Chugtai, M. H Inayat, Particuology, 35 (2017) 51–67. https://doi.org/10.1016/j.partic.2016.10.008.

[10] M. Imran, A. Ullah, S. W Ahmad, H. G. Qutab, M. Hameed, Arab. J. Sci. Eng., 45 (2020) 7477–7485. https://doi.org/10.1007/s13369-020-04605-4.

[11] A. Ullah, A. Amanat, M. Imran, S. S. J. Gillani, M. Kilic, A. Khan, Chem. Eng. Process., 156 (2020) 108101. https://doi.org/10.1016/j.cep.2020.108101.

[12] A. Ullah, K. Hong, S. Chilton, W. Nimmo, Powder Technol., 281 (2015) 129–137. https://doi.org/10.1016/j.powtec.2015.03.016.

[13] B. K. O'Neill, D. J. Nicklin, N. J. Morgan, L. S. Leung, Can. J. Chem. Eng. 50 (1972) 595–601. https://doi.org/10.1002/cjce.5450500507.

[14] G. V. Vunjak-Novakovic, D. V. Vukovic, H. Littman, Ind. Eng. Chem. Res. 26 (5) (1987b) 958–966. https://doi.org/10.1021/ie00065a019.

[15] I. P. Levsh, N. I. Krainev, M. I. Niyazov, Int. Chem. Eng. 8 (2) (1968a) 311–312. https://archive.org/details/sim_international-chemical-engineering_1968_8_index-contents/page/n5/mode/2up.

[16] M. Kito, M. Shimada, T. Sakai, S. Sugiyama, C. Y. Wen, in Fluidization Technology, D. L. Kearns (ed.), Hemisphere Publishing Co Washington, (1976b), p. 411–429. ISBN: 089116006X, 9780891160069.

[17] M. Kito, T. Monma, Y. Kayama, T. Sakai, S. Sugiyama, Kagaku Kogaku Ronbunshu 2 (5) (1976a) 476–478. https://doi.org/10.1252/kakoronbunshu.2.476.

[18] M. Kito, K. Tabei, K. Murata, Ind. Eng. Chem. Proc. Design Develop. 17 (4) (1978) 568–571. https://doi.org/10.1021/i260068a030.

[19] B. H. Chen, W. J. M. Douglas, Can. J. Chem. Eng. 46 (1968) 245–249. https://doi.org/10.1002/cjce.5450460406.

[20] J. Tichy, A. Wong, W. J. M Douglas, Can. J. Chem. Eng. 50 (1972) 215–220. https://doi.org/10.1002/cjce.5450500213.

[21] O.S. Balabekov, P.G. Ramankov, E.Ya. Tarat, M.F. Mikhalev, J. Appl. Chem. U.S.S.R. (Engl. Transl.) 42 (1969) 1454–1458. https://searchworks.stanford.edu/view/365872.

[22] O.S. Balabekov, E.Ya. Tarat, P.G. Romankov, M.F. Mikhalev, J. Appl. Chem. USSR 42 (1969a) 1068–1074. Translated from Zhurnal Prikladnoi Khimii 44 (5) (1969) 1061–1068.

[23] S. Ushida, C.S. Wong, C. Y. Wen, Can. J. Chem. Eng. 55 (4) (1977) 392–396. https://doi.org/10.1002/cjce.5450550405.

[24] R. Handl, Ph.D. Thesis, Technischen Universitat Clausthal, R.R.G. (1976).

[25] B. Bensebia, F-Z. Chaouche, S. Kouadri Moustefaï, Kem. Ind. 71 (9–10) (2022) 557–567. https://doi.org/10.15255/KUI.2021.094.

[26] O. P Rama, D.P. Rao, V.S. Rao, Can. J. Chem. Eng. 61 (1983) 863–868. https://doi.org/10.1002/cjce.5450610614.

[27] K. Soundarajan, K. Krishnaiah, Can. J. Chem. Eng. 72 (4) (1994) 569–575. https://doi.org/10.1002/cjce.5450720403.

[28] I. G. Blyakher, L.Ya. Zhivaikin, N.A. Yurovskaya, Chem. Eng. 7 (3) (1967) 485–490. https://doi.org/10.1007/bf01150061.

[29] J. Tichy, W.J.M Douglas, Can. J. Chem. Eng., 50 (1972) 702–706. https://doi.org/10.1002/cjce.5450500604.

[30] B.K. O'Neill, D.J. Nicklin, L.S. Leung, Fluidization and its Applications, Ed. by H. Angelo, J.P. Couderc, H. Gilbert, C. Laguerie, (Ed.), Cepadues-Editions-Toulouse. (1973), 365–371.

[31] G.B. Wallis, One Dimensional Two-Phase Flow. McGraw-Hill Book Company, New York. 1969, 408. https://doi.org/10.1017/S0022112070211362.

[32] B.Z. Uysal, Ph.D. Thesis, McGill, Montreal, 1978. https://escholarship.mcgill.ca/downloads/2227ms35b.pdf.

[33] R.T. Khanna, Ph.D. Dissertation, McGill University. PhD:198, Montreal 1971. https://escholarship.mcgill.ca/downloads/41687j305.pdf.

[34] A. Lyashuk, Research, J. Chem. Pet. Eng. 37 (3–4) (2001) 125–133. https://doi.org/10.1023/A:1017607026104.

[35] I. Shackley, Ph.D. Thesis, Department of Chemical and Process Engineering, University of Sheffield 2000. http://prr.hec.gov.pk/jspui/bitstream/123456789/1974/1/1439S.pdf.

[36] M.L. Gimenes, D.A. Handley, Chem. Eng. Res. Des. 76 (A7): (1998) 855–863. https://doi.org/10.1205/026387698525478.

[37] L.A. Aksel'rod, M.M. Yakovenko, Theor. Found. Chem. Eng. 3 (1969) 124–126. https://link.springer.com/article/10.1023/A:1017607026104.

[38] A. Ul-Haq, Ph.D. Thesis, Pakistan Institute of Engineering and Applied Sciences Nilore Islamabad, Pakistan, 2012. http://prr.hec.gov.pk/jspui/handle/123456789/1974 (accessed 31 May 2014).

[39] M. Kito, M. Sawada, M. Shimada, M. Takada, T. Sakai, S. Sugiyama, Int. Chem. Eng. 16 (2) (1976c) 701. https://doi.org/10.1252/kakoronbunshu.2.12.

[40] A.H.J. Paterson, R. Clift, Canadian Journal of Chemical Engineering. 65 (1987) 10–17. https://doi.org/10.1002/cjce.5450650103.

[41] P. Petrov, Sh. Tassaev, Chem. Ing. Tech. 50 (11) 887–888 (1978). https://doi.org/10.1002/cite.330501118.

[42] K. Soundarajan, K. Krishnaiah, Indian. J. of Chem. Technol. 5 (4) (1998) 179–186. http://nopr.niscpr.res.in/bitstream/123456789/30839/1/IJCT%205%284%29%20179-186.pdf (accessed 22 January 2023).

[43] N.I. Gel'Perin, V.I. Savshenko, V.Z. Grishko, Theor. Chem. Eng. 2 (1) (1968) 65–71. https://istina.msu.ru/workers/39330694/.

[44] N.I. Gelperin, V.A. Liferenko, ,V.Z. Grishko, V.I. Sokolov. Prom. Sanit. Ochistka Gazov (1976) 3 14.

[45] A.E.R. Bruce, P.S.T. Sai, K. Krishnaiah, Chem. Eng. J., 99 (3) (2004) 203–212. https://doi.org/10.1016/j.cej.2003.10.004.

[46] R.G. Barile, D.W. Meyer, Chem. Eng. Prog. Symp. Ser. No 119, Vol. 67, (1971) 134–141. https://nepis.epa.gov/Exe/ZyPURL.cgi?Dockey=20014PYW.TXT.

[47] E.Y. Tarat, V.S. Burkat, V.S. Durodova, Journal of Applied Chemistry USSR 47 105–108 (1974). https://searchworks.stanford.edu/view/365872.

[48] K. Soundarajan, K. Krishnaiah, Ind. J. Chem. Technol. 6 (3) (1999) 152–160.

http://nopr.niscpr.res.in/handle/123456789/16916.

[49] G.V. Vunjak-Novakovic, D.V. Vukovic, H. Littman, Ind. Eng. Chem. Res. 26 (5) (1987a) 967–972. https://doi.org/10.1021/ie00065a020.

[50] L. Mbua Egbe, Ph.D. Thesis, Middlesex University UK, 2001. https://eprints.mdx.ac.uk/id/eprint/8005 (accessed 16. November 2021).

BENSABER BENSEBIA[1]
FATMA-ZOHRA CHAOUCHE[1]
OUAHIDA BENSEBIA[2]
SOUMIA KOUADRI MOUSTEFAÏ[3]

[1]Laboratory of Plant Chemistry-Water-Energy, Department of Process Engineering, Faculty of Technology, Hassiba Benbouali University, Chlef, Algeria

[2]Industrial Process Engineering Sciences Laboratory, Houari Boumediene University of Sciences and Technology, Bab Ezzouar, Algeria

[3]Department of Process Engineering, Faculty of Technology, Hassiba Benbouali University, Chlef, Algeria

NAUČNI RAD

EKSPANZIJA SLOJA U TURBULENTNOM KONTAKTORU: EKSPERIMENTI I PREDVIĐANJE

U ovom radu, hidrodinamika turbulentnog kontaktoru (TBC) je proučavana u smislu ekspanzije sloja (H_d/H_{st}) koristeći poseban pristup za predviđanje ovog važng svojstva za projektovanje takve opreme. Studija je zasnovana na 1604 eksperimentalnih podataka o ekspanziji sloja, dobijenih variranjem operativnih varijabli (brzina gasa, raspršivanje tečnosti, karakteristike pakovanja, statička visina sloja i slobodna površina noseće mreže. Predviđanje širenja sloja zahteva procenu zadržavanja gasa i tečnosti. Da bi se to postiglo, korišene su različite korelacije iz literature, i to šest jednačina za zadržavanje gasa i dvadeset jednačina za zadržavanje tečnosti. Od ukupno 120 slučajeva, procenjeno je širenje sloja, a tačnost modela je procenjena izračunavanjem srednje apsolutne greške u procentima (MAPE), srednje kvadratne greške (RMSE), koeficijenta korelacije (rKSI) i objašnjene varijanse (VECV). Ovom studijom su identifikovane odgovarajuće korelacije za gas i tečnost. Štaviše, statistička analiza je korišćena u sledećoj fazi studije da bi se utvrdile najprikladnije korelacije za predviđanje ekspanzije sloja među onima koje su predložili različiti autori.

Ključne reči: trofazna fluidizacija, turbulentni kontaktor sa fludizovanim slojem, ekspanzija sloja, zadržavanje gasa, zadržavanje tečnosti.

CI&CEQ
Chemical Industry & Chemical Engineering Quarterly

Available online at
Association of the Chemical Engineers of Serbia AChE
www.ache.org.rs/CICEQ

Chem. Ind. Chem. Eng. Q. 30 (1) 59–72 (2024) CI&CEQ

ASLI DÖNMEZ
ÇETIN KADAKAL

HOT-AIR DRYING AND DEGRADATION KINETICS OF BIOACTIVE COMPOUNDS OF GILABURU (*Viburnum opulus* L.) FRUIT

Article Highlights

- Thermal degradation of selected bioactive compounds were fitted to the first-order kinetic model
- The drying rate of gilaburu fruit was highly influenced by drying temperature
- The effective diffusion coefficient increased with increasing drying temperature
- Selected bioactive compounds of gilaburu were reduced by the drying process
- The Parabolic and Page models were determined to predict the experimental drying best

Department of Food Engineering, Faculty of Engineering, Pamukkale University, Denizli, Turkey

Abstract

This study aims to determine whether drying is a suitable preservation method for gilaburu fruit and the changes in the bioactive components of gilaburu fruit (Viburnum opulus L.) at the end of the drying process. In this study, gilaburu fruits were dried in a cabinet dryer at different temperatures (50 °C, 60 °C, and 70 °C). The analyses of trans-resveratrol, water-soluble vitamins, organic acids, and phenolic compounds were made using the HPLC method, while total phenolic contents and antioxidant activity were spectrophotometric. As a result of drying of gilaburu fruit at 50 °C, 60 °C, and 70 °C, the highest component loss was observed at 70 °C. Losses of 73.64% and 84.08%, respectively, were detected in the total phenolic substance and antioxidant capacity content of gilaburu fruit after drying at 70 °C. While the trans-resveratrol content was 1.26±0.05 (g/100 g dry weight (DW)) in fresh fruit, it reduced to 0.31±0.03, 0.30±0.01 and 0.21±0.01 after drying at 50 °C, 60 °C and 70 °C, respectively. In terms of vitamins, the highest loss was seen in niacin. The contents of ascorbic acid, pyridoxine, niacin and thiamine contents of fresh gilaburu fruit decreased after drying at 50 °C, 60 °C and 70 °C. In addition, drying kinetics of water-soluble vitamins, total phenolic contents, antioxidant activity, and trans-resveratrol were modeled. The Page model best described the drying behavior of fruits at 70 °C, and the parabolic model at both 50 °C and 60 °C. Thermal degradation of water-soluble vitamins, total phenolic contents, antioxidant activity, and trans-resveratrol were fitted in the first-order kinetic model.

Keywords: antioxidant capacity, drying kinetic, gilaburu, trans-resveratrol, total phenolic content, water-soluble vitamins.

SCIENTIFIC PAPER

UDC 66.047: 582.5/.9

Fruits contain many nutritive and non-nutritive bioactive components such as flavonoids, phenolic acids, tannins, carotenoids, vitamins, sugars, minerals, and essential oils [1]. Edible wild fruits have played an important role in nutrition with their rich biodiversity since the beginning of humanity [2]. Gilaburu (*Viburnum opulus*) is one of the wild fruits originating from North Africa, North Asia, and Europe grown mainly in the Central Anatolia Region in Turkey and does not require high climatic features and can be grown in

Correspondence: Ç. Kadakal, Department of Food Engineering, Faculty of Engineering, Pamukkale University, Denizli, Turkey.
E-mail: ckadakal@pau.edu.tr
Paper received: 14 June, 2022
Paper revised: 27 March, 2023
Paper accepted: 8 June, 2023

https://doi.org/10.2298/CICEQ220614011D

almost every region where there is water [3]. Gilaburu plant (*Viburnum opulus* L.), which is from the Caprifoliaceae (Honeysuckle) family of the Dipsacales (Rubiales) team, has more than 230 species, most of which are endemic [4]. Four different species of Viburnum (*Viburnum tinus* L., *Viburnum lantana* L., *Viburnum orientale* P., and *Viburnum opulus* L.) are grown in Turkey [5]. While it is known by various names such as European cranberrybush, American cranberry bush, and cranberry tree worldwide, it is known as gilaburu in Turkey [6].

The ripening of the gilaburu fruit is completed in September-October, and clusters with 30–40 fruits are formed. The gilaburu plant's ripe fruits are bright red, round-oval in shape, single-seeded, thin-shelled, and juicy. Ripe fruits are acidic and bitter [7,8]. Gilaburu fruits can be consumed as they are plucked from the branch. However, since it has a bitter and acrid taste, it is preferred to be consumed in brine or fruit juice by adding sugar and water [9–11].

In recent years, the use of isolated plants has become popular in the world [12]. The gilaburu plant, which has been cultivated since the "16th century", has also been used in the treatment of many diseases such as stomach pain, gall bladder disorders, kidney stones, liver diseases, diuretics, menstrual pain, prevention of miscarriage and bleeding, mumps, diabetes, hemorrhoids using the fruit, leaves, and shells [13–15]. Gilaburu fruit is a good source of vitamin C. Also, it contains vitamins A and E, micronutrients (Cu, Mn, Fe, and Zn) and macronutrients (P, K, Mg, Ca, and N), organic acids, fatty acids, and phenolic compounds [16–20]. Phenolic compounds act as natural antioxidants which protect the plant from external factors. *Trans*-resveratrol, a phenolic acid in a *trans*-isomer structure, has many health benefits since it is an anticarcinogen, anti-inflammatory, antioxidant, heart protective, and vasodilator [21–23].

Drying is one of the most common preservation methods for fruits and vegetables [24]. Commonly used drying methods are natural drying in the sun and industrial drying in tray cabinet dryers. Although sun drying is a process that requires low cost, it has some disadvantages [25]. Although drying with cabinet dryers is more costly than sun drying, there is minimal loss of nutritional value and better physical preservation thanks to adjustable time and temperature parameters, a fast drying process, and homogeneous drying [26,27]. Almost half of the worldwide dried fruit market consists of raisins, followed by figs, apricots, peaches, and apples [28]. Gilaburu is a fruit that is generally used after brining. It is important to investigate the potential of dried gilaburu fruit. In the literature, studies investigate the pH, titration acidity, total phenolic content, antioxidant capacity, color, and texture values of the fruit after drying [29–31]. However, there is a dearth of information on the water-soluble vitamins, organic acids, *trans*-resveratrol, and phenolic compounds of dried gilaburu fruit. The current study presents the importance of changes in vitamin, organic acid, total phenolic content, and antioxidant capacity of gilaburu fruit due to drying with hot air. In addition, there is no data on the *trans*-resveratrol content of gilaburu fruit in previous scientific studies.

This study aims to determine the effect of drying on selected biochemical compounds and kinetic characteristics of gilaburu fruit for industrial purposes. In addition, determining the drying characteristics and creating mathematical models to determine the most suitable drying parameters at different temperatures are targeted.

MATERIAL AND METHODS

Sample collection

In this study, *Viburnum opulus* L. species of gilaburu fruit was used as material. The samples were obtained from Kayseri province (Kayseri Pazarı Bio Herbal Products Limited Company). Gilaburu fruits were collected homogeneously from 10 randomly selected plants in a private garden and brought to the laboratory by a refrigerated vehicle. The ripe fruits used in the analysis were selected. Fresh fruits were stored at -18 °C until analysis [32].

Drying process

Gilaburu fruits were dried in a drying cabinet (Yücebaş Makine Tic. LTD. ŞTİ. İzmir, Turkey) until the moisture content of samples reached up to 18%–20% on a wet basis. The tray cabinet dryer consisted of a resistance heater providing the temperature, a temperature control panel, and a fan providing the airflow (EUC442 model, ENDA, Turkey). The cabin, which has dimensions of 70 cm x 55 cm x 100 cm, operates in the temperature range of 40 °C–120 °C, air flow rate of 2 m/s, and relative humidity of 20%–95%. The drying process was carried out at three different temperatures, (50, 60, and 70) °C. The drying process was applied three times, including a preliminary trial drying for all three temperature values. Before drying, the cabinet was preheated until it reached the specified drying temperature. Drying tests were carried out with 200 g samples to determine the time norms of the temperature parameters. The samples (2000 g) were distributed homogeneously on the drying trays (25 cm x 20 cm x 3 cm). Average air velocity and relative humidity of 2 m/s and 20% were recorded, respectively. Gilaburu fruits were spread homoge-

neously as a single layer on the drying tray. During the drying process, fruits were weighed every half hour for the first 5 hours and then at one-hour intervals for the additional hours. The drying rate was calculated by recording these data.

Drying characteristics of gilaburu fruit

Knowing the moisture content is an important parameter for calculating mathematical models. Eq. (1) was used to calculate the humidity ratio:

$$MR = \frac{M_t - M_e}{M_i - M_e} \quad (1)$$

where MR is the moisture ratio of samples (dimensional), M_i and M_t are the initial and actual (at time t) moisture content of the sample (g water g^{-1} DW), respectively, and M_e is the equilibrium moisture content of example at t time (g water g^{-1} DW).

To determine the moisture content in the food drying process, M_t, M_i, and M_e values are compared. Since the M_e value is very low compared to the others, it is accepted as 0 in the calculations, and the humidity ratio is calculated using Eq. (2) [33]:

$$MR = \frac{M_t}{M_i} \quad (2)$$

The drying rate is determined by using Eq. (3).

$$Drying\ rate = \frac{M_{t+\Delta t} - M_t}{\Delta t} \quad (3)$$

where M_t is the moisture content of the sample for any time (g water g^{-1} DW), $M_{t+\Delta t}$ is the moisture content of the sample at any t+Δt time (g water g^{-1} DW), and Δt is the time difference between two measurements (hours).

Mathematical models examine the effects of ambient conditions such as air temperature, humidity, and flow rate [34]. The coefficient of determination (R^2), estimated standard error (RMSE), and chi-square ($\chi 2$) values are used when explaining the relationship between the estimated and experimental data of the samples dried at different temperatures. The model with the highest R^2 value and the lowest $\chi 2$ and RMSE should be selected to determine the best model for explaining the relationship between experimental and predicted data. MATLAB (R2015a) program was used to calculate the mathematical modeling data. The mathematical models used in this study are given in Table 1.

The RMSE and the chi-square ($\chi 2$) value were calculated by using Eqs (4) and (5), respectively.

$$RMSE = \left[\frac{1}{N}\sum_{i=0}^{N}\left(MR_{pre,i} - MR_{\exp,i}\right)^2\right]^{1/2} \quad (4)$$

$$\chi^2 = \frac{\sum_{i=0}^{N}\left(MR_{pre,i} - MR_{\exp,i}\right)^2}{N - n} \quad (5)$$

where $MR_{pre,i}$ and $MR_{exp,i}$ are the predicted and experimental moisture ratios, respectively, N is the number of experimental data, and n is the constants of thin layer drying models.

Table 1. Mathematical models.

Model name	Model	References
Parabolic	$a + bt + ct^2$	[33]
Logarithmic	$aexp(-kt) + c$	[35]
Lewis	$exp(-kt)$	[36]
Henderson and Pabis	$aexp(-kt)$	[37]
Page	$exp(-kt^n)$	[37]
Wang and Sing	$1 + at + bt^2$	[38]

Calculation of effective moisture diffusion and activation energy in hot air drying

The drying process is based on the principle that water molecules move from the place where the density of the molecules is more to the place where it is less. This situation is explained by Fick's law of diffusion [39]. Crank [40] proposed Eq. (6) to calculate the effective moisture diffusion in spherical products, provided there is no shrinkage in the dried material, and the effective diffusion is constant [41]:

$$MR = \frac{6}{\pi^2}\sum_{n=1}^{\infty}\frac{1}{n^2}\exp\left(\frac{-n^2\pi^2 D_{eff}t}{r^2}\right) \quad (6)$$

where D_{eff} is the effective moisture diffusivity (m^2 s^{-1}), and r is the arithmetical average of the radius of samples at measured intervals (m).

Eq. (6) was shortened to Eq. (7) [37]:

$$\ln(MR) = \ln\left(\frac{6}{\pi^2}\right) - \left(\frac{\pi^2 D_{eff}t}{r^2}\right) \quad (7)$$

The slope of the graph drawn by Eq. (7) was calculated by Eq. (8):

$$Slope = -\frac{\pi^2 D_{eff}}{r^2} \quad (8)$$

The Arrhenius equation was used to calculate the activation energy in the hot air drying process [42]:

$$D_{eff} = D_0\exp\left(\frac{-E_a}{RT}\right) \quad (9)$$

where R is the universal gas constant (8.314 J mol^{-1} K^{-1} or 1.987 cal mol^{-1} K^{-1}, T is the actual temperature (K), E_a is the activation energy (kJ mol^{-1} or kcal mol^{-1}), and D_0 is the constant before exponential (m^2 s^{-1}).

Eq. (10) is obtained using the natural logarithm of

Eqs. (8) and (9):

$$\ln D_{eff} = \ln D_0 - \frac{E_a}{RT} \quad (10)$$

The slope of the graph plotted against T^{-1} of the natural logarithm of the effective diffusion coefficient gives the activation energy.

Analysis of *trans*-resveratrol

Trans-resveratrol, a phenolic component, was analyzed according to the method suggested by Singh and Pai [43]. Methanol was used to extract gilaburu fruits, which are dried at different temperatures. An HPLC device (SHIMADZU LC20AD) consists of a column oven (SHIMADZU CTO-20A), column (ACE C18 (7.8 mm x 300 mm)), a pump (SHIMADZU LC-20AD), a degasser (SHIMADZU DGU-20A3), and a photodiode array (PDA) detector (SPDM20A), was used for *trans*-resveratrol analysis.

The calibration curve of the *trans*-resveratrol standard was prepared at (5, 10, 25, 50, 75, and 100) mg/L concentrations. Calculations were made using the equation (y=177599x-308529) of the calibration curve with a high R^2 (0.9985) value drawn with these concentrations. The method used for *trans*-resveratrol analysis is given in Table 2.

Analysis of water-soluble vitamins

An HPLC device (SHIMADZU LC20AD) was used to analyze water-soluble vitamins. The water-soluble vitamin analysis was carried out by modifying the method suggested by Otağ [19]. The method used in the analysis is given in Table 2. The water-soluble vitamin content was calculated using the equation obtained from the calibration curve with a high R^2 value using the stock solutions prepared at different concentrations (5, 10, 25, 50, 75, and 100) mg/L. The R^2 values obtained for ascorbic acid, pyridoxine, niacin, and thiamine were found to be 0.9984 (y=83790x-432582), 0.9997 (y=36871x+11924), 0.9999 (y=30299x+11105), and 0.9993 (y=62655x+128944), respectively.

Analysis of organic acids

Organic acid analysis was carried out by modifying the method proposed by Soyer et al. [44]. The method of this analysis performed with an HPLC device (SHIMADZU LC20AD) is given in Table 2. Standard calibration curves of organic acids were created with standards prepared at 100, 250, 500, 750, and 1000 mg/L concentrations. The R^2 values of the calibration curves were found to be 0.9998 (y=1520.9x+3100.3), 0.9999 (y=1065.9x-1974), and 0.9998 (y=857.83x-40.273) for tartaric, citric and malic acid, respectively. Calculations were made with the equation obtained from this calibration curve.

Analysis of phenolic compounds

Methanol extraction of the phenolic component composition of gilaburu samples dried at different temperature parameters was carried out, modifying the method suggested by Choi *et al.* [45]. The modification of the method suggested by Gao *et al.* [46] was finally used to extract phenolic compounds. Phenolic compounds were identified by modifying the method proposed by Bansal *et al.* [47]. Two different mobile phases (gradient) were used in this method. The operating conditions of the HPLC device (SHIMADZU LC20AD) used to detect phenolic compounds are given in Table 2. Standard calibration curves of phenolic compounds were prepared at (5, 10, 25, 50, and 100) mg/L concentrations. Calculations were made using the calibration curve equation with a high R^2 value. The highest R^2 values detected for chlorogenic, ellagic, p-coumaric, caffeic acid, and rutin were 0.9998 (y=64035x-63331), 0.9998 (y=178344x-306186), 0.9999 (y=283357x-230476), 1 (y=120497x-40235), and 1 (y=61226x-26563), respectively.

Total phenolic content and antioxidant activity analysis

The total phenolic content (TPC) of gilaburu samples, which were dried at different temperature parameters, was determined spectrophotometrically by modifying the method suggested by Singleton and Rossi [48]. The gallic acid curve created for the calculations was prepared using (25, 50, 75, and 100) mg/L standards. Calculations were made using the equation of the calibration curve (y=0.0097x+0.0834; R^2=0.9977) drawn with these concentrations. The absorbances of the samples were read in a spectrophotometer (PG Instruments T80 UV/VIS, UK) at a wavelength of 760 nm. Analysis results are given as mg gallic acid equivalent (GAE)/100 g DW.

The extracts used in the total antioxidant activity (AC) analysis of gilaburu samples were prepared using the same method as the methanol extracts prepared to determine phenolic compounds. Analysis was performed spectrophotometrically by the method of DPPH (2.2 diphenyl-1-picrylhydrazyl) proposed by Thaipong et al. [49]. The absorbances of the samples and standards were read in a spectrophotometer (PG Instruments T80 UV/VIS, UK) at a wavelength of 515 nm. The results were calculated in mmol Trolox equivalent (mmol TE)/g DW according to the equation obtained by preparing the standard curve (y=-0.017x+1.0278; R^2 =0.9853) of Trolox (Sigma-Aldrich Chemie gmbh) at (10, 20, 25, 30, and 50) mg/L.

Table 2. Methods used in chromatographic analyses.

		Column	Flow rate	Oven temperature	Wavelength	Mobile phase
Water-Soluble Vitamins	Ascorbic acid	ACE C18	0.8 ml/min	40°C	254 nm	0.1 M KH_2P0_4+0.1 M KOH
	Pyridoxine				324 nm	
	Niacin				261 nm	
	Thiamin				234 nm	
Organic Acids	Tartaric Acid		1.0 ml/min	25°C	214 nm	0.01 N H_2SO_4
	Citric Acid					
	Malic Acid					
Phenolic Compounds	Chlorogenic acid		0.5 ml/min		280 nm	0.1 orto-H_3PO_4:C_2H_3N
	Ellagic acid				254 nm	
	p-Coumaric acid				280 nm	
	Caffeic acid					
	Rutin				360 nm	
Trans-resveratrol			0.8 ml/min	30°C	306 nm	Metanol:10mM KH_2PO_4: C_2H_3N

Statistical analysis

SPSS software statistical package program (SPSS ver. 23, SPSS Inc., Chicago, IL, USA) was used to analyze the data. One-way analysis of variance (ANOVA) was used to evaluate differences between treatments with a significance level of $p<0.05$. Duncan's multiple comparison test was used to determine the difference between groups. All analyses were carried out in duplicate.

RESULTS AND DISCUSSION

Drying characteristic of whole gilaburu fruits during hot air drying

The moisture ratio (A) and drying rate (B) of gilaburu fruits during hot air drying are shown in Figure 1. Initially, the moisture content of gilaburu fruit was determined as 83.95%. A decrease in moisture content was observed over time during drying with hot air. An increase was observed depending on the drying rate of the gilaburu fruits with hot air. Accordingly, the drying time was reduced to 75 (4500 min), 17 (1020 min), and 7 h (420 min) for (50, 60, and 70)°C, respectively (air velocity 2 m s^{-1}). In a study conducted with gilaburu samples obtained from the Kayseri region, the samples were dried at an air velocity of 1.3 m/s. The (60, 70 and 80) °C drying process was completed in (2663, 856, and 420) minutes, respectively [29]. Considering the air velocity, it was observed that the drying times were similar. Heat transfer is provided by increasing the temperature difference [50]. As the temperature difference increases, more energy is transferred to fresh gilaburu fruits, and thus more water evaporates from the content of gilaburu fruits per unit of time. In addition, the increase in temperature decreased the relative humidity of the drying air, so the water transfer from the structure of gilaburu fruits to the drying air accelerated. In this case, the shortening of the drying time due to the increase in temperature can be explained by the increase in mass transfer [51].

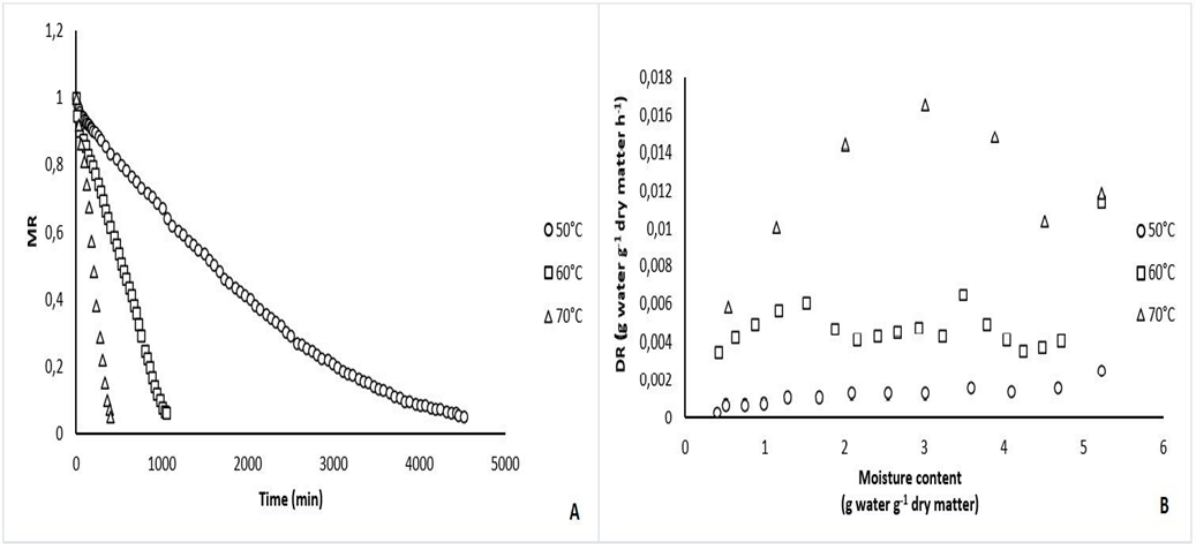

Figure 1. Moisture ratio (MR) and drying rate (DR) of whole gilaburu fruits during hot air drying.

The moisture ratio of gilaburu fruits during hot air drying was used to be fitted with mathematical models. The models used are listed in Table 1. The most suitable mathematical model giving the lowest RMSE and χ^2 and the highest R^2 value was preferred [37]. The parabolic model best describes the experimental MR of gilaburu fruits dried at 50 and 60 °C. In addition, the Page model was the best model to describe the experimental MR of fruits dried at 70 °C (Table 3).

Effective moisture diffusivity and activation energy of whole gilaburu fruits during hot air drying

Table 4 presents the D_{eff} and E_a values of gilaburu fruits. It was observed that the effective diffusion coefficient increased in accordance with the temperature increase [52]. The effective diffusion coefficient is a positive indicator of dehydration efficiency. A high D_{eff} value indicates a fast drying process [53]. The increase in the D_{eff} value because of the increase in temperature indicates that the moisture will be removed from the gilaburu fruit more easily.

In the literature, the D_{eff} and E_a values of drying of gilaburu fruits have not been found; however, there are similar studies. As a result of the calculations, the E_a value was determined to be 133.81 kJ mol^{-1}. In a study conducted with goji berry fruit, similar to gilaburu fruit, the E_a value was 48.37 kJ mol^{-1} [42]. It is thought that

Table 3. Thin-layer mathematical models, models constants, and statistical parameters of thin-layer drying curves.

Models	Temperature	Model constants			χ^2	RMSE	R^2
Parabolic	50°C	a= 0.977	b= -0.0003537	c= 0.00000003274	0.000044974	0.0066	0.9996
	60°C	a= 0.9589	b= -0.0008386	c= -0.00000003899	0.00019453	0.0133	0.9979
	70°C	a= 1.025	b= -0.0027	c= 0.000000478	0.001380291	0.0332	0.9915
Logarithmic	50°C	k= 0.0005596	a= 0.9708	c= 0.0529	0.002201172	0.0461	0.9791
	60°C	k= 0.001814	a= 0.9984	c= 0.0606	0.006625917	0.0780	0.927
	70°C	k= 0.005076	a= 1.069	c= 0.051	0.012675613	0.1007	0.9151
Lewis	50°C	k= 0.0004904			0.001366086	0.0367	0.9865
	60°C	k= 0.001529			0.005459036	0.0728	0.9345
	70°C	k= 0.004131			0.010951296	0.1011	0.9078
Henderson	50°C	k= 0.0004996	a= 1.016		0.001341656	0.0362	0.9871
and Pabis	60°C	k= 0.001628	a= 1.053		0.005281129	0.0706	0.9401
	70°C	k= 0.004654	a= 1.116		0.009891817	0.0926	0.9283
Page	50°C	k= 0.0001023	n= 1.204		0.000527738	0.0227	0.9949
	60°C	k= 0.0000786	n= 1.463		0.002212666	0.0457	0.9749
	70°C	k= 0.00004651	n= 1.821		0.001070552	0.0304	0.9922
Wang and Singh	50°C	a= -0.0003746	b= 0.00000003662		0.00015759	0.0124	0.9985
	60°C	a= -0.0009923	b= 0.00000008021		0.000439509	0.0204	0.995
	70°C	a= -0.002465	b= 0.00000001802		0.001294131	0.0335	0.9906

Table 4. Effective moisture diffusivity and activation energy of gilaburu.

Temperature	D_{eff} (m^{2}s^{-1})	E_a (kJ mol^{-1})
50°C	1.82x10^{-11}	
60°C	4.01x10^{-11}	133.814
70°C	3.38x10^{-10}	

the differences between E_a values might be due to different drying conditions and fruit types. D_{eff} values obtained from drying gilaburu fruit increased depending on the temperature increase. In a study with grapes, the drying process was examined at (30, 35, 40, and 45) °C, and the highest D_{eff} value was at 45 °C, the highest drying temperature [54]. It was seen that the analyzed data supported the present study. The Arrhenius equation correlating D_{eff} and T^{-1} is presented in Fig. 2.

The effect of the drying process

Changes in trans-resveratrol contents

In this study, the *trans*-resveratrol content of fresh fruits was determined to be 1.26 g/100 g. *Trans*-resveratrol content decreased due to the drying of gilaburu fruit with hot air at (50, 60, and 70) °C. The highest loss of *trans*-resveratrol content of gilaburu fruits was 82.90% at 70 °C, while the lowest loss was 75.02% at 50 °C. There is no study on the *trans*-resveratrol content of gilaburu fruit in the literature. However, in a study using blueberry juice, a spray drying process was applied, and the effect of the drying process on *trans*-resveratrol was evaluated. In this study, an average of 96% loss was observed in the *trans*-resveratrol content of the samples [55]. When the results were compared, it was observed that the temperature application caused a decrease in *trans*-

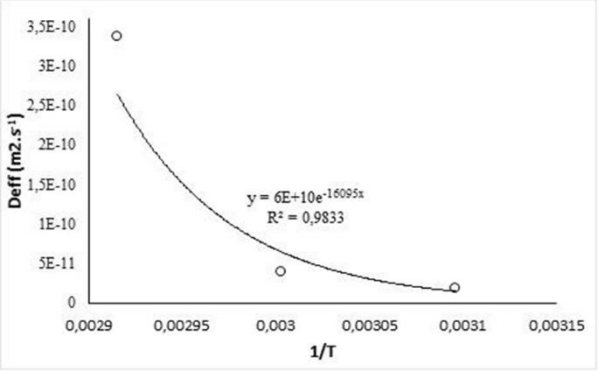

Figure 2. Arrhenius-type equation between D_{eff} and T^{-1}.

resveratrol. This decrease is because *trans*-resveratrol is a lipophilic polyphenol sensitive to thermal degradation [56].

Changes in water-soluble vitamin contents

Preserving heat-sensitive vitamins during drying is considered an indicator of food quality [57]. Especially ascorbic acid is a critical quality parameter. In general, if the loss of ascorbic acid is low after the applied process, it is thought that the loss of other nutritional elements is also low [58]. The change in water-soluble vitamin contents of gilaburu fruits at different drying temperatures is shown in Table 5. Ascorbic acid (vitamin C), thiamine (B1), niacin (B3), and pyridoxine (B6) analyses were performed in gilaburu fruits and the dominant vitamin was found to be ascorbic acid. In a study, it was determined that gilaburu fruit contains high levels of ascorbic acid [59]. A significant decrease in vitamin content was observed in parallel with the increase in drying temperature.

The ascorbic acid content of fresh gilaburu fruit was determined to be 0.78 g/100 g DW. In a study by Akbulut *et al.*, the ascorbic acid content of fresh gilaburu fruit was 0.59 g/100 g DW [60]. The ascorbic acid content of gilaburu fruits dried at (50, 60, and 70) °C were found to be (0.35, 0.30, and 0.24) g/100 g DW, respectively. In a study conducted with jujube fruits, it was reported that there was a decrease in the amount of ascorbic acid depending on the temperature increase [61]. This decrease in the ascorbic acid content of fruits is due to the low thermal sensitivity of ascorbic acid [56]. In the current study, the pyridoxine content of fresh gilaburu fruits was determined to be 3.14 mg/100 g DW. After drying at 70 °C, the pyridoxine content was decreased to 0.75 mg/100 g DW. The thiamine content decreased from 0.30 mg/100 g DW to 0.14 mg/100 g DW after drying at 70 °C. Heat treatment applied at high temperatures easily breaks the molecular ring structures and methylene group chemical bonds of thiamine, causing devitaminization [62]. The lowest amount of niacin was found in fresh fruits (0.12 mg/100 g DW). As a result of drying at 70 °C, niacin could not be detected. Niacin is a heat-stable compound due to the pyrimidine ring in its structure. However, due to the low initial niacin content of gilaburu fruit and the long drying time, niacin could not be detected at the end of drying [62]. In the literature, no study has been found investigating the vitamin B content of gilaburu fruit. These types of vitamins were found in a similar study with caper fruit [63]. In addition, in the study conducted by Duman with rosehip fruits, it was reported that there was a decrease in the content of thiamine and riboflavin after drying the rosehip fruit [64]. In a study, there was a decrease in vitamin values due to drying the jujube fruit at different temperatures [65].

Changes in organic acids contents

The dominant organic acid of gilaburu fruit was tartaric acid. In addition, the fresh fruit contains malic and citric acids. A study examining the organic acid content of gilaburu fruit reported that the dominant organic acid was tartaric acid [1]. Tartaric, citric, and malic acid contents of fresh gilaburu fruit were 11.06±0.23, 6.74±0.37, and 8.62±0.05, respectively. In a study conducted with 11 different gilaburu samples grown in different parts of the country, the amount of malic acid was between (578.0 and 2090.0) mg/100 g [66]. The same study reported that the amount of citric acid was in the range of (270.0–1630.0) mg/100 g. In another study, the dominant organic acid of fresh fruit was malic acid. In addition, tartaric, citric, and malic acid contents were reported to be 0.37±0.02, 3.09±0.01, and 3.13±0.02, respectively [67]. The results recorded in this study and the literature samples differ due to the factors, such as species diversity, climatic conditions, and soil properties, affecting the composition.

The changes in organic acid content after drying gilaburu fruits at different temperatures are shown in Table 5. While the tartaric acid value in fresh fruit was 11.06 g/100 g DW, after drying at (50, 60, and 70) °C, this value was (10.67, 10.54, and 10.35) g/100 g DW, respectively. While the malic acid value was 8.62 g/100 g DW in fresh fruit, it decreased to 8.11 g/100 g DW as the result of drying at 70 °C. Similarly, while the citric acid value in fresh fruit was 6.74 g/100 g DW, it decreased to 6.02 g/100 g DW after drying at 70 °C.

Generally, decreases in the organic acid values were observed with the increase in drying temperature. Adiletta *et al.* stated that the organic acid amount of red and white grapes decreased after drying at 50 °C [68] due to the decrease in organic acids and oxidation reactions [69].

Changes in phenolic components

The phenolic components of gilaburu fruit are shown in Table 5. Chlorogenic acid, ellagic acid, p-coumaric acid, caffeic acid and rutin analyses were carried out in gilaburu fruit. However, chlorogenic acid could not be detected. The dominant phenolic component of fresh fruits was caffeic and ellagic acid. After drying at all temperatures, the amount of phenolic compounds decreased. While the value of caffeic acid, the dominant phenolic component, was 0.64 g/100 g DW in fresh fruits, it decreased to 0.41 g/100 g DW after drying at 70 °C. Ellagic acid, the other dominant phenolic acid, decreased to 0.25 g/100 g DW after drying at 70 °C.

In a study conducted with fresh fruit, the chlorogenic, caffeic, and *p*-coumaric acid contents were in the ranges of (23.64–30.33, 14.82–19.92, and 6.38–11.18) mg/100 mL, respectively [70]. In another study, the flower, bark, and fruit of gilaburu were examined, and chlorogenic acid (752.59±2.07 mg/100 g) and rutin (5.39±0.03 mg/100 g) were detected in the fruit, but *p*-coumaric acid could not be detected [67]. In the literature, no study has been found on the changes in the phenolic composition of gilaburu fruit due to drying, but there are studies conducted with different fruits. In a study investigating the effect of drying with hot air on phenolic compounds, orange peel and pulp were used as materials. As a result, long-term heat treatment at high temperatures destroyed the phenolic compounds [71] because phenolic compounds have an easily oxidized structure [72].

Changes in total phenolic content and antioxidant capacity

The total phenolic content and antioxidant capacity values of gilaburu fruit are shown in Table 5. The increase in drying temperature decreased the total phenolic content of gilaburu fruits. While total phenolic content was 568.96 mg GAE/100 g DW in fresh fruit, that value decreased to 149.89 mg GAE/100 g DW after drying at 70 °C. A significant decrease was observed in the total phenolic content of gilaburu fruits dried at three different temperatures, depending on the drying process. The decrease in antioxidant activity due to the drying process is the loss of antioxidant compounds during drying [73]. Zarifikhosroshahi [17] determined the TPC value as 1009.89 mg GAE/100 g DW in gilaburu samples from the Kayseri region. This value was higher than the value obtained as a result of the present study. In another study conducted with gilaburu fruits obtained from the Kayseri region, the TPC value was determined as 633.56 mg GAE/100 g DW [74], which is close to the result of the present study. The antioxidant capacity of fresh fruit was detected at 15.08 µmol TE/g DW, and it decreased to 2.40 µmol TE/g DW after the drying process at 70 °C.

Table 5. Changes in the composition of gilaburu fruit after drying.

Analysis		Fresh	50 °C	Reduction %	60 °C	Reduction %	70 °C	Reduction %
Total phenolic content (mg GAE/100g DW)		568.97±21.33^{a}	351.46±6.18^{b}	38.22	233.80±7.52^{c}	58.90	149.96±4.87^{d}	73.64
Antioxidant capacity (mmol TE/g DW)		15.08±0.001^{a}	2.81±0.001^{b}	81.36	2.51±0.001^{d}	83.35	2.40±0.001^{c}	84.08
Ascorbic acid (g/100 g DW)	Ascorbic acid	0.78±0.32^{a}	0.35±0.04^{b}	55.12	0.30±0.01^{b}	61.53	0.24±0.07^{b}	69.23
Group B vitamins (mg/100 g DW)	Pyridoxine	3.14±0.18^{a}	1.01±0.55^{b}	67.83	0.85±0.03^{c}	72.92	0.75±0.18^{c}	76.11
	Niacin	0.12±0.02^{a}	0.09±0.06^{b}	25	0.05±0.01^{b}	58.33	Nd	100
	Thiamine	0.30±0.04^{a}	0.18±0.01^{b}	40	0.16±0.01^{b}	46.66	0.14±0.02^{c}	53.33
Organic acids (g/100 g DW)	Tartaric acid	11.06±0.23^{a}	10.67±0.43^{ab}	3.52	10.54±0.27^{ab}	4.70	10.35±0.14^{b}	6.41
	Citric Acid	6.74±0.37^{a}	6.58±0.21^{ab}	2.37	6.39±0.11^{ab}	5.19	6.02±0.08^{b}	10.68
	Malic Acid	8.62±0.05^{a}	8.59±0.17^{ab}	0.34	8.42±0.08^{ab}	2.32	8.11±0.04^{b}	5.91
Phenolic compounds (g/100 g DW)	Chlorogenic acid	Nd	Nd	Nd	Nd	Nd	Nd	Nd
	Ellagic acid	0.64±0.03^{a}	0.47±0.01^{b}	26.56	0.43±0.12^{b}	32.81	0.25±0.07^{c}	60.93
	p-Coumaric acid	0.57±0.17^{a}	0.21±0.03^{b}	63.15	0.33±0.07^{b}	42.10	0.13±0.04^{c}	77.19
	Caffeic acid	0.64±0.05^{a}	0.59±0.01^{a}	7.81	0.47±0.03^{bc}	26.56	0.41±0.06^{c}	35.93
	Rutin	0.26±0.02^{a}	0.11±0.04^{b}	57.69	0.03±0.01^{c}	88.46	0.09±0.01^{b}	65.38
Resveratrol (g/100 g DW)		1.26±0.05^{a}	0.31±0.03^{b}	75.02	0.30±0.01^{b}	75.98	0.21±0.01^{c}	82.90

*Nd: Not detectable. TPC: Total phenolic content. AC: Antioxidant capacity. Different letters on the same line indicate statistical difference ($p < 0.05$).

Determination of kinetic parameters

Kinetic parameters of trans-resveratrol

Thermal degradation of *trans*-resveratrol in gilaburu fruit was examined at (50, 60, and 70) °C. Arrhenius plots and the first-order reaction model obtained for *trans*-resveratrol during hot-air drying of gilaburu fruits at different temperatures are shown in Figure 3. As seen in Figure 3, the thermal degradation of *trans*-resveratrol in dried gilaburu fruits fitted the first-order kinetic model.

The values of k, $t_{1/2}$, Q_{10}, and E_a of the *trans*-resveratrol in dried gilaburu fruits are shown in Table 7.

The activation energy (E_a) indicates the reaction's sensitivity to temperature, which refers to the energy required to activate the reaction. Likewise, the reaction rate constant (k) value also indicates the thermal sensitivity of the reaction. The Q_{10} value represents the effect of every 10 °C change on the reaction, and the $t_{1/2}$ value represents the half-life of the reaction. The k value was increased with increasing drying temperature. The highest k value was identified at 70 °C. A decrease in the $t_{1/2}$ value was observed due to increased temperature. The lowest $t_{1/2}$ was 2.58 hours at 70 °C. The highest Q_{10} value was 4.25 for the studied temperature range (60 °C –70 °C).

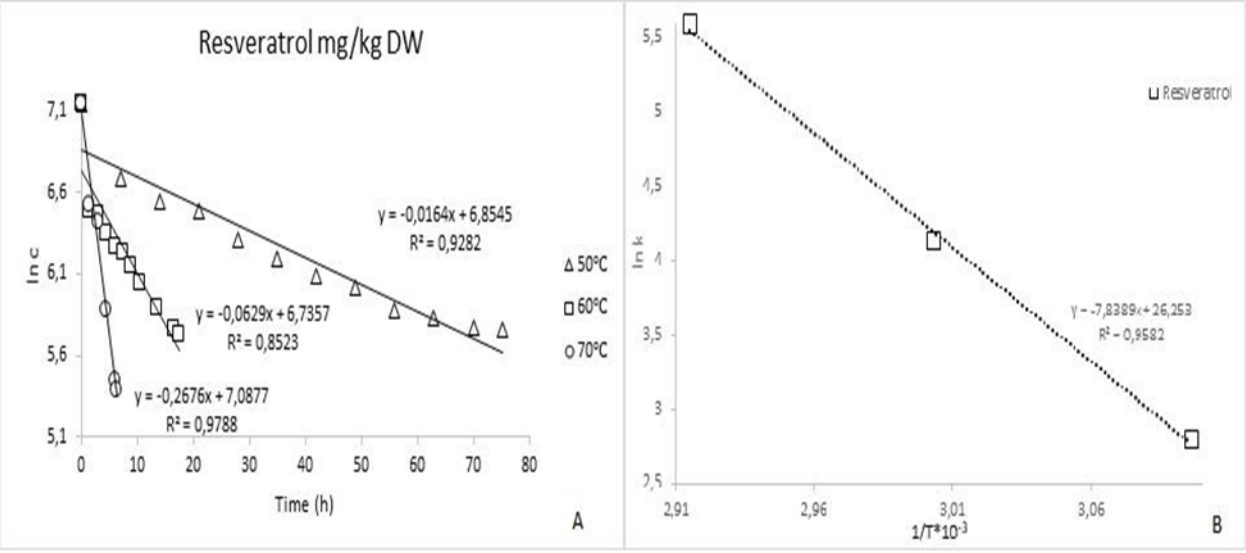

Figure 3. First order plots (A) and Arrhenius plots (B) of trans-resveratrol during drying of gilaburu fruits.

Kinetic parameters of water-soluble vitamins

Thermal degradation of water-soluble vitamins of gilaburu fruits was analyzed at (50, 60, and 70) °C. Thermal degradation of water-soluble vitamins fitted the first-order kinetic model (Figure 4). Thermal degradation of ascorbic acid and thiamine fit the first-order kinetic model in different dried fruits during hot-air drying [75].

The Arrhenius plots obtained for the thermal degradation of water-soluble vitamins during the drying of gilaburu fruits in different temperatures are presented in Figure 5.

The kinetic parameter values of water-soluble vitamins are shown in Table 6. The k value of all vitamins increased with increasing temperature. The lowest rate constant value was calculated for ascorbic acid. The $t_{1/2}$ value decreased depending on the increase in temperature. This result indicates that vitamins decompose more at high temperatures. The lowest $t_{1/2}$ value for water-soluble vitamins was at 70 °C.

For all water-soluble vitamins in gilaburu fruits, the Q_{10} value was calculated for temperatures between 50 °C and 70 °C. The highest Q_{10} value for ascorbic acid, thiamine, and pyridoxine was calculated at (50–60) °C while for niacin at (60–70) °C. This result shows that the decomposition reaction gets more affected by the changes in temperature.

As shown in Table 6, niacin has the highest E_a value (40.45 kcal mol^{-1}); the rest were thiamine, ascorbic acid, and pyridoxine.

Kinetic parameters of TPA and AC

The present study first reported data on the thermal degradation of TPC and AC of gilaburu fruits. Thermal degradation of TPC and AC followed the first-order kinetic model. Similarly, Tepe and Ekinci [41] have reported a first-order reaction of jujube fruits during hot drying. First-order graphics of TPC (A) and AC (B) are presented in Figure 6, while Arrhenius graphs of TPC and AC during hot air drying of gilaburu fruits at different temperatures are shown in Figure 7.

The degradation kinetics data of TPC and AC are given in Table 7. The k value of TPC and AC increased

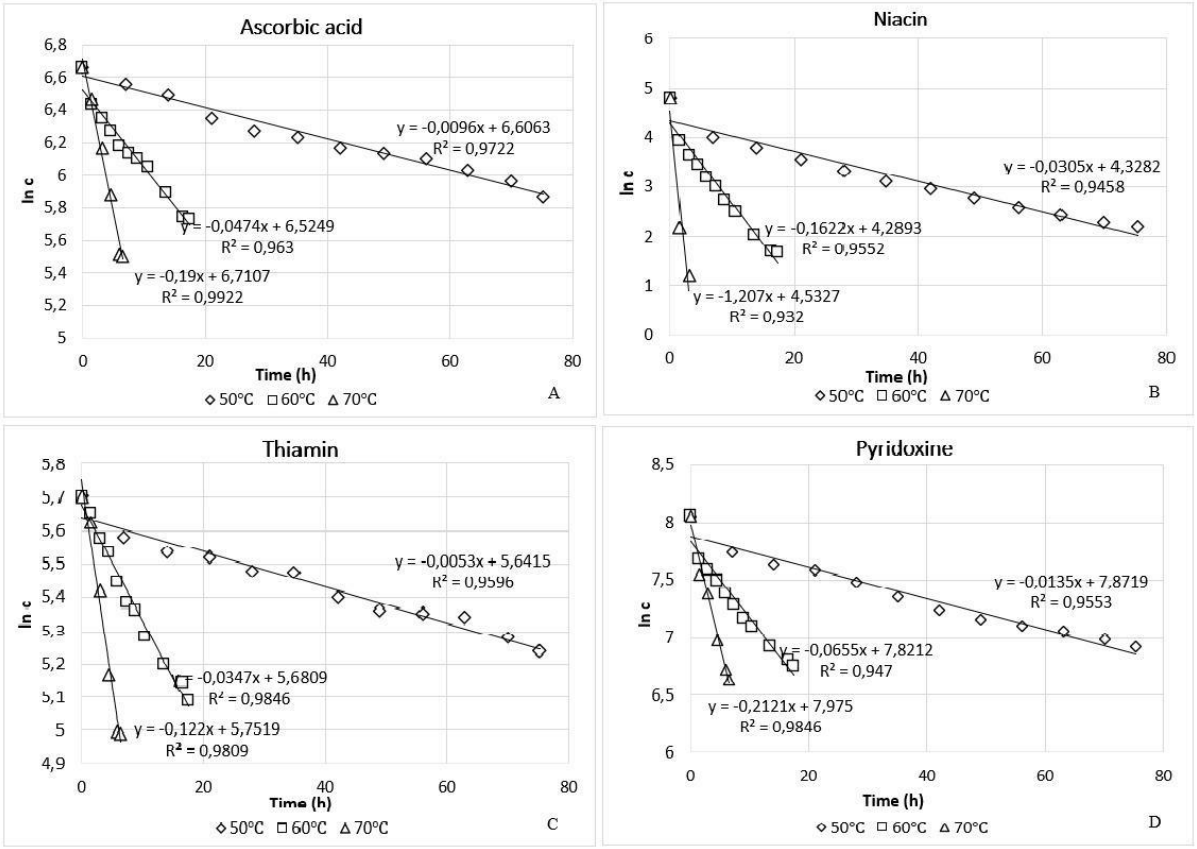

Figure 4. First-order kinetics of ascorbic acid (A), niacin (B), thiamine (C), and pyridoxine (D) of dried gilaburu fruits.

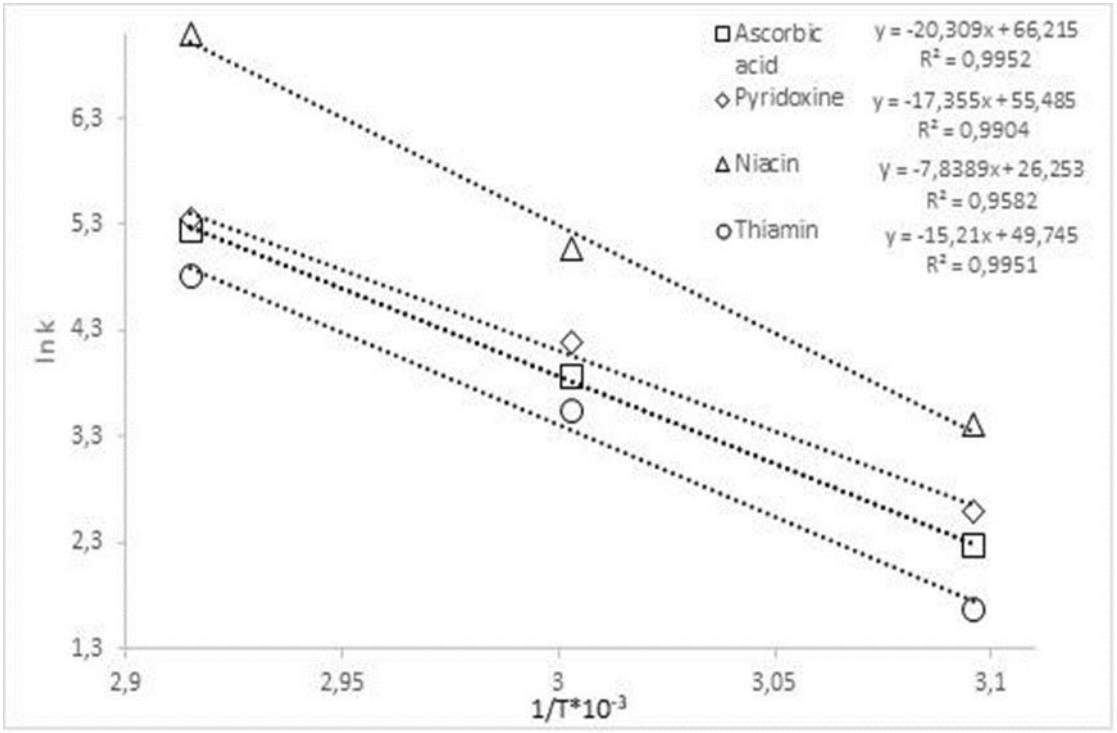

Figure 5. Arrhenius plots of water-soluble vitamins of dried gilaburu fruits.

Table 6. First-order kinetic parameters of water-soluble vitamins.

	T (°C)	k (h^{-1})	$t_{1/2}$ (h)	D (h)	Q_{10} (50–60) °C	Q_{10} (60–70) °C	E_a (kcal mol^{-1})	E_a (kJ mol^{-1})
	50	0.0096	72.18	239.89				
Ascorbic acid	60	0.0474	14.62	48.58	4.93	4.00	32.87	137.53
	70	0.1900	3.64	12.12				
	50	0.0305	22.72	75.50				
Niacin	60	0.1622	4.27	14.19	5.31	7.44	40.45	169.27
	70	1.207	0.57	1.90				
	50	0.0053	130.75	434.52				
Thiamine	60	0.0347	19.97	66.36	6.54	3.51	34.57	144.68
	70	0.1220	5.68	18.87				
	50	0.0135	51.33	170.59				
Pyridoxine	60	0.0655	10.58	35.16	4.85	3.23	30.30	126.80
	70	0.02121	3.26	180.85				

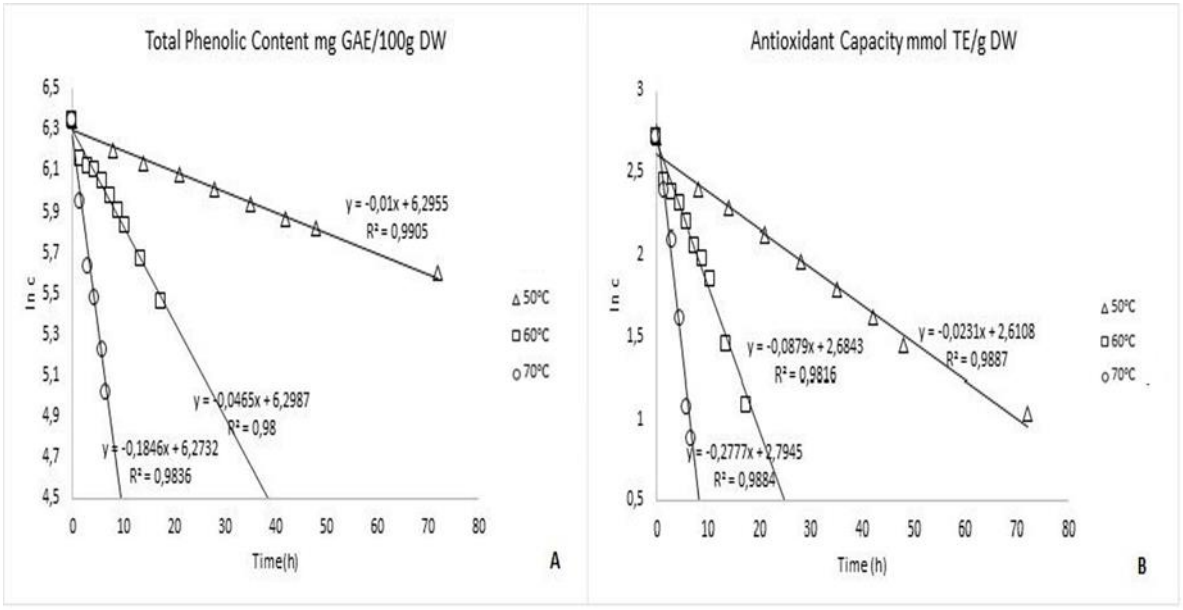

Figure 6. First-order kinetics of TPC (A) and AC (B) of dried gilaburu fruits.

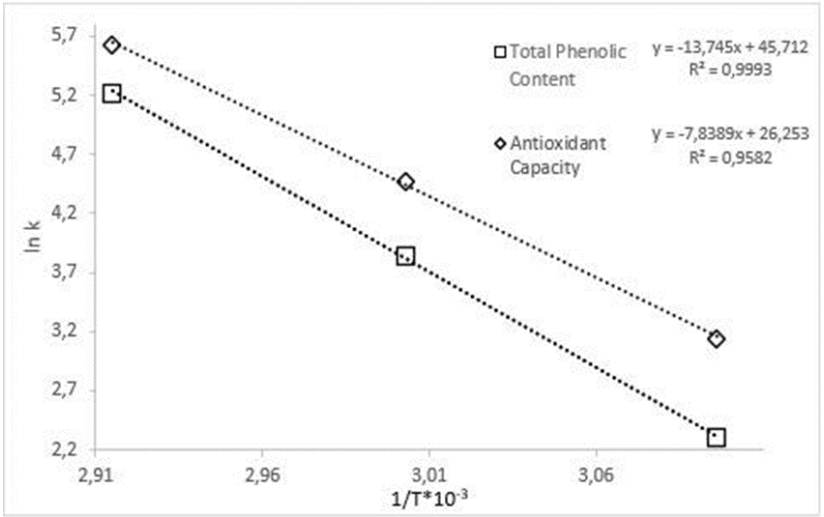

Figure 7. Arrhenius plots of TPC and AC of dried gilaburu fruits.

depending on the increment in temperature. Accordingly, a decrease in the $t_{1/2}$ value was observed. The highest D value was calculated at 50 °C. The highest Q_{10} value of TPC and AC content was 4.65 and 3.80 hours, respectively, at 50-60 °C. E_a values were 32.10 kcal mol^{-1} for TPC and 27.38 kcal mol^{-1} for AC.

The Q_{10} values from 50°C to 60 °C and from 60 °C to 70 °C were found to be 1.53 and 2.17, respectively. On the other hand, the high Q_{10} value between (60–70) °C shows that the thermal degradation of AC is more sensitive in this range than the increase between (50–60) °C.

Table 7. First-order kinetic parameters of TPC, AC and resveratrol.

	T (°C)	k (h^{-1})	$t_{1/2}$ (h)	D (h)	Q_{10} (50–60) °C	Q_{10} (60–70) °C	E_a (kcal mol^{-1})	E_a (kJ mol^{-1})
TPC	50	0.010	69.3	230.3	4.65	3.96	32.10	134.31
	60	0.0465	14.90	14.19				
	70	0.1846	3.75	1.90				
AC	50	0.0231	30.00	99.69	3.80	3.15	27.38	114.57
	60	0.0879	7.88	26.20				
	70	0.2777	2.49	8.29				
Trans-resveratrol	50	0.0164	42.25	140.42	3.83	4.25	30.71	128.50
	60	0.0629	11.01	36.61				
	70	0.2676	2.58	8.60				

CONCLUSION

The study shows that the drying temperature significantly affects the drying and moisture ratio of gilaburu fruits due to the drying process losses in TPC, AC, organic acids, water-soluble vitamins, phenolic components, and *trans*-resveratrol content. While the highest loss rates were observed at 70 °C, it was revealed that the components in the gilaburu fruits were better preserved as a result of the drying process at 50 °C. Therefore, when evaluated in terms of quality losses, it was observed that the best drying temperature was 50 °C. The degradation reaction at all compounds was carried out per the first-order kinetic model. In addition, further research should be conducted on different drying methods and pre-treatment (such as immersing citric acid and ethanol solution, hot water blanching, and ultrasound) in addition to hot air drying to ensure less loss of components of gilaburu fruits and a shorter drying time. Moreover, color kinetics can be inspected with dried fruits. Consequently, the drying data of gilaburu fruit obtained by this study has created an alternative to the different evaluation of gilaburu fruit consumed only as brine and fruit juice.

REFERENCES

[1] N. Ersoy, S. Ercisli, M. Gundogdu, J. Hortic. 29 (2) (2017) 181–188. https://doi.org/10.1515/fhort-2017-0017.

[2] J. S. Singh., A. S. Raghubanshi, C.K. Varshney, Curr. Sci. 66 (2) (1994) 109–112. https://www.jstor.org/stable/24109236.

[3] T. Baytop, Additive, Nobel Medicine Bookstores, İstanbul (1999), p. 198.

[4] A. Lobstein, G. Haan-Archipoff, J. Englert, J.G. Kuhry, R. Anton, Phytochemistry 50 (7) (1999) 1175–1180. https://doi.org/10.1016/S0031-9422(98)00681-5.

[5] N. Gulesci, Gelisim Univ. J. Health Sci. 9 (2019) 920–928. https://doi.org/10.38079/igusabder.594480.

[6] E. Ozer, İ.H. Kalyoncu, J. Selcuk Univ. Fac. Agric. 21 (2007) 46–52. http://sjafs.selcuk.edu.tr/sjafs/article/view/341.

[7] E. Ozer, MSc. Thesis, Selcuk University, Institute of Science, Konya, (2000) Turkey

[8] E. Orakcı, Graduation Thesis, Erciyes University, Faculty of Pharmacy, Kayseri, (2010) Turkey.

[9] M.C. Witmer, Ecol. Soc. Am. 82 (11) (2001) 3120–3130. https://doi.org/10.1890/0012-9658(2001)082[3120:NIAFRC]2.0.CO;2.

[10] L. Česonienė, R. Daubaras, J. Vencloviene, P. Viškelis, Open Life Sci. 5 (6) (2010) 864–871. https://doi.org/10.2478/s11535-010-0088-z.

[11] M. Soylak, L. Elci, S. Saracoglu, U. Divrikli, Asian J. Chem. 14 (2002) 135–138. http://www.scopus.com/inward/record.url?eid=2-s2.0-0036325673&partnerID=MN8TOARS.

[12] C. Ustun, Ph.D. Thesis, Ege University, Institute of Health Sciences, Izmir, (1998) Turkey.

[13] A. Yuruker, Ph.D. Thesis, Hacettepe University, Institute of Health Sciences, Ankara, (1993) Turkey.

[14] M. Cam, MSc. Thesis, Erciyes University, Institute of Science, Kayseri, (2005) Turkey.

[15] N. Arslan Burnaz, MSc. Thesis, Karadeniz Technical University, Institute of Science, Trabzon, (2007) Turkey.

[16] E. Coteli, F. Karatas, Gumushane Univ. J. Sci. Inst. 6 (2) (2016) 61–66. https://doi.org/10.17714/gufbed.2016.06.007.

[17] M. Zarifikhosroshahi, MSc. Thesis, Cukurova University, Institute of Science, Adana (2015) Turkey.

[18] M. Zarifikhosroshahi, E. Kafkas, J. Cukurova Univ. Sci. Eng. 35 (5) (2018) 41–51. https://fbe.cu.edu.tr/storage/fbeyedek/makaleler/2017/G%C4%B0LABURU%20(Viburnum%20opulus%20L.)%20MEYVELER%C4%B0NDE.pdf.

[19] M.R. Otag, Ph.D. Thesis, Pamukkale University, Institute of Science, Denizli, (2015) Turkey.

[20] M.A. Gundesli, S.H. Attar, I. Degirmenci, G. Nogay, N.E. Kafkas, J. Sci. Eng. Res. 5 (11) (2018) 222–227. https://www.researchgate.net/publication/329802862_Total_Phenol_and_Antioxidant_Activity_of_Kabarcik'_Grape_Vitis_vinifera_L_Variety.

[21] J. Sun, Y.F. Chu, R.H. Liu, X. Wu, J. Agric. Food Chem. 50 (2002) 7449–7454. https://doi.org/10.1021/jf0207530.

[22] L.M. Hung, J.K. Chen, S.S. Huang, R.S. Lee, M.J. Su, Cardiovasc. Res. 47 (3) (2000) 549–555. https://doi.org/10.1016/S0008-6363(00)00102-4.

[23] N. Kocabey, MSc. Thesis, Inonu University, Institute of Science, Malatya, (2013) Turkey.

[24] O. Taskın, G. İzli, N. İzli, J. Agric. Sci. 24 (2018) 349–358. https://doi.org/10.15832/ankutbd.456654.

[25] L. Gokayaz, Z. Yıldız, J. Food Feed Sci. Technol. 22 (2019) 29–36. https://dergipark.org.tr/en/download/article-file/778922.

[26] E. Demiray, Y. Tulek, Heat Mass Transfer 48 (2012) 841–847. https://link.springer.com/article/10.1007/s00231-011-0942-1.

[27] A. Aboud, Pak. J. Nutr. 12 (3) (2013) 250–254. http://pjbs.org/pjnonline/fin2577.pdf.

[28] M. J. Sadler. S. Gibson, K. Whelan, M. A. Ha, J. Lovegrove, J. Higgs, Int. J. Food Sci. Nutr. 70 (6) (2019) 675–687. https://doi.org/10.1080/09637486.2019.1568398.

[29] F. F. Dal, E. Karacabey, Turkish J. Agric. Food Sci. Technol. 9 (sp) (2021) 2547–2551. https://doi.org/10.24925/turjaf.v9isp.2547-2551.4924.

[30] A. Ozcan Aykutlu, E. Yurteri, H. Kuplemez, F. Seyis, Effects Of Drying Methods On Total Phenolic Content And Antioxidant Activity Of Guelder Rose (*Viburnum Opulus* L.) Collected From Different Altitudes, 2 st -International Congress On Modern Sciences, Tashkent, Uzbekistan (2022) p. 320. https://www.researchgate.net/publication/367168497.

[31] O. Taskin, G. Izli, N. Izli, Int. J. Fruit Sci. 21 (1) (2021) 1008–1017. https://doi.org/10.1080/15538362.2021.1971141.

[32] M. Cam, Y. Hisil, A. Kuscu, Chem. Nat. Compd. 43 (2007) 460–461. https://doi.org/10.1007/s10600-007-0161-7.

[33] J. Bi, A. Yang, X. Liu, X. Wu, Q. Chen, Q. Wang, J. Lv, X. Wang, LWT-Food Sci. Technol. 60 (2) (2015) 1136–1142. https://doi.org/10.1016/j.lwt.2014.10.006.

[34] W.C. Chiang, J.N. Petersen, Int. J. Food Sci. Technol. 20 (1) (1985) 67–78. https://doi.org/10.1111/j.1365-2621.1985.tb01904.x.

[35] I. Doymaz, Heat Mass Transfer 47 (3) (2011) 277–285. https://doi.org/10.1007/s00231-010-0722-3.

[36] W. K. Lewis, J. Ind. Eng. Chem. 13 (5) (1921) 427–432. https://doi.org/10.1021/ie50137a021.

[37] E. Demiray, A. Seker, Y. Tulek, Heat Mass Transfer 53 (5) (2017) 1817–1827. https://doi.org/10.1007/s00231-016-1943-x.

[38] I. Doymaz, J. Food Process. Preserv. 35 (2011) 280–289. https://doi.org/10.1111/j.1745-4549.2009.00454.x.

[39] X. Liu, S.K. Schnell, J.M. Simon, D. Bedeaux, S. Kjelstrup, A. Bardow, T.J.H. Vlugt, J. Phys. Chem. 115 (44) (2011) 12921–12929. https://doi.org/10.1021/jp208360s.

[40] J. Crank, The Mathematics of Diffusion, Clarendon Press, Oxford (1975), p. 100.

[41] B. Tepe, R. Ekinci, Ital. J. Food Sci. 33 (1) (2021) 1–15. http://doi.org/10.15586/ijfs.v33i1.1947.

[42] H.S. Batu, C. Kadakal, Ital. J. Food Sci. 33 (1) (2021) 16–28. https://doi.org/10.15586/ijfs.v33i1.1949.

[43] G. Singh, R.S. Pai, Int. Scholarly Res. Not. 2014 (2014) 248635. https://doi.org/10.1155/2014/248635.

[44] Y. Soyer, N. Koca, F. Karadeniz, J. Food Compos. Anal. 16 (5) (2003) 629–636. https://doi.org/10.1016/S0889-1575(03)00065-6.

[45] S.H. Choi, J.B. Ahn, H.J. Kim, N.K. Im, N. Kozukue, C.E. Levin, M. Friedman, J. Agric. Food Chem. 60 (41) (2012) 10245–10255. https://doi.org/10.1021/jf302848u.

[46] Q.H. Gao, C.S. Wu, J.G. Yu, M. Wang, Y.J. Ma, C.L. Li, J. Food Sci. 77 (11) (2012) C1218–C1225. https://doi.org/10.1111/j.1750-3841.2012.02946.x.

[47] V. Bansal, A. Sharma, C. Ghanshyam, M.L. Singla, J. Liq. Chromatogr. Relat. Technol. 38 (5) (2015) 619–624. https://doi.org/10.1080/10826076.2014.936608.

[48] V.L. Singleton, J.A. Rossi, Am. J. Enol. Vitic. 16 (1965) 144–158. http://doi.org/10.5344/ajev.1965.16.3.144.

[49] K. Thaipong, U. Boonprakob, K. Crosby, L. Cisneros-Zevallos, D.H. Byrne, J. Food Compos. Anal. 19 (6–7) (2006) 669-675. https://doi.org/10.1016/j.jfca.2006.01.003.

[50] A. Zhu, X. Shen, Int. J. Heat Mass Transfer 72 (2014) 345–351. https://doi.org/10.1016/j.ijheatmasstransfer.2014.01.001.

[51] H.S. Batu, PhD Thesis, Pamukkale University, Institute of Science, Denizli, (2021) Turkey.

[52] F. B. Tepe, Turkish J. Agric. Food Sci. Technol. 10 (10) (2022) 1877–1883. https://doi.org/10.24925/turjaf.v10i10.1877-1883.5360.

[53] Y. Chen, A. Martynenko, M. Mainguy, Wine Grape Dehydration Kinetics: Effect of Temperature and Sample Arrangement, CSBE/SCGAB 2016 Annual Conference, Halifax, Nova Scotia, Canada (2016), CSBE16-063.

[54] Y. H. Dong, R. Y. Yang, J. Wei, Y. Xue, R. X. Wang, Z. T. Zhang, L. W. Yang, Advanced Materials Research, Trans Tech Publications Ltd., Switzerland (2013), p. 3038.

[55] C. Leyva-Porras, M. Z. Saavedra-Leos, E. Cervantes-González, P. Aguirre-Bañuelos, M. B. Silva-Cázarez, C. Álvarez-Salas, Antioxidants, 8 (10) (2019) 437. https://doi.org/10.3390/antiox8100437.

[56] I. Choi, N. Li, Q. Zhong, Int. J. Biol. Macromol. 194 (2022) 982–992. https://doi.org/10.1016/j.ijbiomac.2021.11.157.

[57] E. Demiray, Y. Tulek, Y. Yılmaz, LWT Food Sci. Technol. 50 (2013) 172–176. https://doi.org/10.1016/j.lwt.2012.06.001.

[58] T. K. Tepe, C. Kadakal, J. Food Process. Preserv. 46 (6) (2022) e16544. https://doi.org/10.1111/jfpp.16544.

[59] O. Rop, V. Reznicek, M. Valsikova, T. Jurikova, J. Mlcek, D. Kramarova, Molecules, 15 (2010) 4467–4477.

https://doi.org/10.3390/molecules15064467.

[60] M. Akbulut, S. Calisir, T. Marakoglu, H. Coklar, Asian J. Chem. 20 (3) (2008) 1875–1885. https://asianjournalofchemistry.co.in/User/ViewFreeArticle.aspx?ArticleID=20_3_32.

[61] A. Wojdyło, A. Figiel, P. Legua, K. Lech, Á. A. Carbonell-Barrachina, F. Hernández, Food Chem. 207 (2016) 170–179. https://doi.org/10.1016/j.foodchem.2016.03.099.

[62] D. Kim, H. S. Kim, S. J. Hong, J. J. Cho, J. Lee, E. C. Shin, Appl. Biol. Chem. 61 (2018) 449–458. https://doi.org/10.1007/s13765-018-0381-5.

[63] S. Y. Inagamov, G. M. Tajibaev, Z. B. Tursunova, N. B. Sadikova, K. K. Shadmanov, IOP Conf. Ser.: Earth Environ. Sci. 723 (2021) p. 022021.

[64] T. Duman, MSc. Thesis, Pamukkale University, Institute of Science, Denizli, (2014) Turkey.

[65] F. Yasa, MSc. Thesis, Pamukkale University, Institute of Science, Denizli, (2016) Turkey.

[66] I. B. Perova, A. A. Zhogova, A. V. Cherkashin, K. I. Éller, G. V. Ramenskaya, I. A. Samylina, Pharm. Chem. J. 48 (2014) 332–339. https://doi.org/10.1007/s11094-014-1105-8.

[67] D. Polka, A. Podsędek, M. Koziołkiewicz, Plant Foods Hum. Nutr. 74 (2019) 436–442. https://doi.org/10.1007/s11130-019-00759-1.

[68] G. Adiletta, W. Senadeera, L. Liguori, A. Crescitelli, D. Albanese, P. Russo, Food Nutr. Sci. 6 (2015) 355–364. https://doi.org/10.4236/fns.2015.63036.

[69] O. Levent, Ph.D. Thesis, Inonu University, Institute of Science, Malatya, (2017) Turkey.

[70] A. M. Colak, K. Mertoglu, F. Alan, T. Esatbeyoglu, I. Bulduk, E. Akbel, I. Karamanoglu, Foods, 11 (11) (2022) 1614. https://doi.org/10.3390/foods11111614.

[71] M. C. Garau, S. Simal, C. Rossello, A. Femenia, Food Chem. 104 (3) (2007) 1014–1024. https://doi.org/10.1016/j.foodchem.2007.01.009.

[72] M. McSweeney, K. Seetharaman, Crit. Rev. Food Sci. Nutr. 55 (5) (2015) 660–669. https://doi.org/10.1080/10408398.2012.670673.

[73] L. Méndez-Lagunas, J. Rodríguez-Ramírez, M. Cruz-Gracida, S. Sandoval-Torres, G. Barriada-Bernal, Food Chem. 230 (2017) 174–181. https://doi.org/10.1016/j.foodchem.2017.03.010.

[74] O. Taskın, G. Izli, N. Izli, Ankara Univ. J. Agric. Sci. 24 (3) (2018) 349–358. https://doi.org/10.15832/ankutbd.456654.

[75] C. Kadakal, T. Duman, R. Ekinci, Food Sci. Technol. 38 (4) (2018) 667–673. https://doi.org/10.1590/1678-457X.11417.

ASLI DÖNMEZ
ÇETIN KADAKAL

Department of Food Engineering, Faculty of Engineering, Pamukkale University, Denizli, Turkey

KINETIKA SUŠENJA I RAZGRADNJE BIOAKTIVNIH NUTRITIVNIH JEDINJENJA PLODA CRVENE KALINE (*Viburnum opulus* L.)

Ovaj rad ima za cilj da utvrdi da li je sušenje pogodna metoda konzervisanja ploda crvene kaline (Viburnum opulus L.) i kakve su promene u njegovim bioaktivnim komponentama na kraju procesa sušenja. U ovoj studiji, plodovi crvene kaline su sušeni u sušari na različitim temperaturama (50, 60 i 70) °C. Analize trans-resveratrola, vitamina rastvornih u vodi, organskih kiselina i fenolnih jedinjenja vršene su HPLC metodom, a sadržaj ukupnih fenola i antioksidaciona aktivnost spektrofotometrijski. Kao rezultat sušenja plodova crvene kaline na (50, 60 i 70) °C, najveći gubitak komponenti zabeležen je na 70 °C, pri čemu gubici u sadržaju ukupnih fenola i antioksidacione aktivnosti ploda crvene kaline nakon sušenja na 70 °C iznose 73,64% i 84,08%, redom. Sadržaj trans-resveratrola je bio 1,26±0,05 (g/100 g suve mase u svežem voću), a smanjio se na 0,31±0,03, 0,30±0,01 i 0,21±0,01 nakon sušenja na (50, 60 i 70) °C, redom. Što se tiče vitamina, najveći gubitak je zabeležen u niacinu. Sadržaj askorbinske kiseline, piridoksina, niacina i tiamina u svežem plodu crvene kaline smanjen je nakon sušenja na 50°C, 60 °C i 70 °C. Pored toga, modelovana je kinetika sušenja u pogledu vitamina rastvornih u vodi, sadržaja ukupnih fenola, antioksidacione aktivnosti i trans-resveratrol. Model Pejdža najbolje opisuje kinetiku sušenja voća na 70 ℃, a parabolnki model na 50 ℃ i 60 ℃. Termička degradacija vitamina rastvornih u vodi, sadržaja ukupnih fenola, antioksidacione aktivnosti i trans-resveratrola prati kinetički model prvog reda.

NAUČNI RAD

Ključne reči: antioksidacioni kapacitet, kinetika sušenja, gilaburu, trans-resveratrol, sadržaj ukupnih fenolna, vitamini rastvorni u vodi.

CI&CEQ
Chemical Industry & Chemical Engineering Quarterly

Available online at
Association of the Chemical Engineers of Serbia AChE
www.ache.org.rs/CICEQ

Chem. Ind. Chem. Eng. Q. 30 (1) 73–79 (2024) CI&CEQ

RONDANG TAMBUN
ANGGARA DWITA BURMANA
BODE HARYANTO
VIKRAM ALEXANDER

Department of Chemical Engineering, Faculty of Engineering, Universitas Sumatera Utara, Medan, Indonesia

THE EFFECT OF VACUUM PROCESS ON BIODIESEL PRODUCTION FROM PALM KERNEL FATTY ACID DISTILLATE

Article Highlights

- Producing biodiesel under vacuum condition reduce costs and energy consumption
- The operating temperature is low in producing biodiesel at vacuum pressure
- Production of biodiesel from PFAD at a vacuum pressure by using PTSA catalyst

Abstract

This study examines the operating pressure effect on the manufacture of biodiesel from Palm Kernel Fatty Acid Distillate (PKFAD) by using para-Toluene Sulfonic Acid (PTSA) catalyst. The operating pressures studied are the vacuum pressures of 70 kPa, 80 kPa, 90 kPa, and 100 kPa, which varied with PTSA concentrations of 5%, 10%, 15%, 20%, and 25%, and the molar ratios of methanol and PKFAD are 5:1, 6:1, 7:1, 8:1, 9:1, and 10:1. Biodiesel production from PKFAD was carried out with reaction duration of 120 minutes and reaction temperature at 50 ^{0}C. The amounts of fatty acids converted to biodiesel were calculated based on the initial and acid numbers after the esterification reaction. The results show that a vacuum pressure of 70 kPa to 100 kPa provides a conversion above 96% for all catalyst concentrations and all methanol and PKFAD molar ratios. The highest conversion of PKFAD to biodiesel of 98.6% is obtained at an operating pressure of 80 kPa, a catalyst concentration of 25%, and the molar ratio of methanol and PKFAD is 10:1. The biodiesel characteristics obtained in this study have met the standards of the American Society for Testing Materials.

Keywords: biodiesel production, palm kernel fatty acid distillate, vacuum process.

SCIENTIFIC PAPER

UDC 662.756.3:338.2:633.844:66

Biodiesel production as a substitute for diesel from fossil materials has been widely carried out by utilizing vegetable and animal oils [1–5]. This biodiesel production process usually uses a catalyst to speed up the reaction, both homogeneous and heterogeneous catalysts [6–10]. Biodiesel production is generally carried out at operating pressures above 101.325 kPa (1 atm), both esterification and transesterification [6,11,12].

Palm Kernel Fatty Acid Distillate (PKFAD) was examined in the present study at a vacuum pressure to produce biodiesel (methyl ester). PKFAD is a by-product of the physical refining process of crude palm kernel oil [13]. It has the availability and low price so that this waste material can be used to produce biodiesel at low cost [14,15]. This vacuum pressure condition is intended to save energy for making biodiesel that has occurred so far. In the vacuum pressure condition, the operating temperature will be lower because the boiling point of a liquid will be lower so that the energy required for heating is also low. It agrees with the ideal gas equation, which shows that pressure and temperature have a relationship, that is, if the pressure is lowered, the temperature will decrease. The catalyst used in this study is an inexpensive

Correspondence: R. Tambun, Department of Chemical Engineering, Faculty of Engineering, Universitas Sumatera Utara, Medan, Indonesia.
E-mail: rondang@usu.ac.id
Paper received: 26 October, 2022
Paper revised: 17 March, 2023
Paper accepted: 8 June, 2023

https://doi.org/10.2298/CICEQ221026012T

homogeneous catalyst, namely *para*-Toluene Sulfonic Acid (PTSA, $C_7H_8O_3S$) [6,9,16–18]. It is a strong organic acid compound that is non-oxidizing, colorless (white), solid, and easily soluble in water, alcohol, and organic solutions.

The reaction of making biodiesel from PKFAD is shown in Reaction (R1):

$$\underset{\text{PKFAD}}{RCOOH} + \underset{\text{methanol}}{CH_3OH} \leftrightarrow \underset{\text{methylester}}{RCOOR} + \underset{\text{water}}{H_2O} \quad \text{(R1)}$$

In this reaction, a decrease in acid number (acid value) is used to describe the amount of fatty acid that is converted into biodiesel because the raw materials used are fatty acids, so the acid number in the reaction product can be used to calculate the amount of fatty acid that is not converted to biodiesel. The lower acid number obtained indicates that the PKFAD conversion to biodiesel will be higher. In this study, the acid number at the end of the esterification reaction reflects the PKFAD content that is not changed to biodiesel.

Several things that affect biodiesel production are also varied in this study, such as the molar ratio of reactants, catalyst concentration, reaction time, reaction temperature, and vacuum pressure. The characteristics of PKFAD as feedstock are shown in Table 1.

Table 1. PKFAD Characteristics.

Characteristics	Measurement results	Unit	Test Method
Density at 25 °C	0.904	g/cm^3	ASTM D1298
Color	0.9R	5¼ in Lovibond	AOCS Cc 13e-92
	7.9Y	5¼ in Lovibond	AOCS Cc 13e-92
Acid Value	336	mg KOH/g	AOCS Te 2a-64
Iodine Value	4.36	g I_2/100 g	AOCS TI 2a-64
Sulfur	2.05	ppm	ASTM D5453
Water content	0.02	%	ASTM D2705
C_6	0.06	%	ASTM D6584
C_8	31.95	%	ASTM D6584
C_{10}	60.23	%	ASTM D6584
C_{12}	0.50	%	ASTM D6584
C_{14}	0.17	%	ASTM D6584
C_{16}	0.27	%	ASTM D6584
C_{18}	1.89	%	ASTM D6584
C_{20}	1.89	%	ASTM D6584
unknown	2.12	%	ASTM D6584

MATERIAL AND METHODS

The fatty acid used consists of PKFAD; the composition and characteristics can be seen in Table 1. The PKFAD used in this study came from an oleochemical factory in North Sumatra Province, Indonesia. The PKFAD is the result of the refinery and is used directly without further treatment. The majority component of PKFAD consists of C_8 ($CH_3(CH_2)_6COOH$) or caprylic acid and C_{10} ($CH_3(CH_2)_8COOH$) or capric acid. Besides caprylic acid and capric acid, the PKFAD also contains caproic acid (C_6), lauric acid (C_{12}), myristic acid (C_{14}), palmitic acid (C_{16}), stearic acid (C_{18}), and arachidic acid (C_{20}). The alcohol is 99% methanol (Merck Chemicals Ltd), while the PTSA catalyst is purchased from Navdeep Chemicals Pvt Ltd. In this biodiesel production, the raw material and catalyst were heated on a hot plate to 50 ^{0}C and a speed of 300 rpm.

The biodiesel production from PKFAD consists of several variations, including variations in vacuum pressure (70 kPa, 80 kPa, 90 kPa, and 100 kPa) compared to the operating pressure at 110 kPa), variations in the concentration of catalysts on PKFAD (5%, 10%, 15%, 20%, and 25 %), variations in the molar ratios of methanol to PKFAD (5:1, 6:1, 7:1, 8:1, 9:1, and 10:1), reaction temperature (35 ^{0}C, 40 ^{0}C, 45 ^{0}C, 50 ^{0}C, and 55 ^{0}C), and variations in reaction time (60 minutes, 75 minutes, 90 minutes, 105 minutes, and 120 minutes). Eq. (1) is used to calculate the amount of fatty acids converted into biodiesel [19–22]:

$$y(\%) = \frac{BA_0 - BA_1}{BA_0} 100\% \quad (1)$$

where y is the fatty acids conversion into biodiesel, BA_0 is the initial acid number (mg KOH/g), and BA_1 is the acid number after the esterification reaction at a certain time (mg KOH/g). The biodiesel's composition was analyzed using Gas Chromatography-Mass Spectrometry (GC-MS) with the details of the Agilent Technologies 7890A system (SN CN11051074) using hydrogen as a carrier.

RESULTS AND DISCUSSION

Effect of vacuum pressure on the acid number without the addition of a catalyst

Biodiesel can be formed from PKFAD in the esterification reaction at various vacuum pressures. Fig. S1 (Supplementary material) shows the acid number obtained at various operating pressure performed with a molar ratio of 10:1, a reaction temperature of 50 ^{0}C, and a reaction time of 120 minutes. The results showed that the highest acid number of 122 mg KOH/g was obtained at an operating pressure of 80 kPa. Using Eq. (1), the conversion of PKFAD to biodiesel at an operating pressure of 80 kPa reaches 63.69%, while at operating pressures of 70 kPa, 90 kPa, and 100 kPa are 62.50%, 60.71%, and 57.74%, respectively. The absence of a catalyst reduced the ability to enhance the reaction of the reactants by the role of a catalyst. The results obtained in Fig. S1 indicate that biodiesel production from PKFAD under vacuum conditions without the addition of a catalyst can occur but with a low conversion rate.

At a non-vacuum operating pressure of 110 kPa, the acid number was higher than at vacuum pressure, or the conversion value of PKFAD to biodiesel was lower. The acid number obtained at 110 kPa was 148 mg KOH/g or the PKFAD conversion to biodiesel reached 55.95%. The results obtained indicate that it is necessary to make efforts to increase the reaction rate. The treatment to be carried out included adding a catalyst and increasing the temperature of the esterification reaction. These treatments were varied with the molar ratio of methanol to PKFAD.

Effect of reaction temperature on the acid number

Fig. S2 shows the reaction temperature effect on the acid number obtained at a molar ratio of 10:1, an operating pressure of 80 kPa, a catalyst concentration of 25%, and a reaction time of 120 minutes. It can also be seen that the lowest acid number was at 50 ^{0}C, which was 4.72 mg KOH/g, or the PKFAD conversion to biodiesel reached 98.60%, while at 35 ^{0}C, 40 ^{0}C, 45 ^{0}C, and 55 ^{0}C, the conversion of PKFAD to biodiesel were 98.06%, 98.37, 98.51%, and 98.37%, respectively. The absence of a catalyst reduced the ability to enhance the reaction of the reactants by the role of a catalyst. These results indicate that the operating temperature close to room temperature at a vacuum pressure of 80 kPa can provide a conversion result of PKFAD to biodiesel above 98%. Hence, operating pressure in vacuum conditions can save energy consumption in biodiesel production from PKFAD, and the conversions of PKFAD to biodiesel in vacuum pressure conditions are higher than operating in non-vacuum pressure conditions using various catalysts [14–17, 20–23].

Reaction time and catalyst concentration effect on the acid number

Fig. 1 shows the reaction time effect and catalyst (PTSA) concentration effect on the acid number at the operating pressure of 80 kPa, the molar ratio of methanol to PKFAD of 10:1, and the reaction temperature of 50 ^{0}C. The results showed that the acid number decreased with increasing reaction duration. Biodiesel production using a homogeneous catalyst is generally carried out with reaction times between 60 minutes and 120 minutes. However, a longer reaction time can lower the acid value [27]. Likewise, with the catalyst concentration, a decrease in acid number occurs with an increase in the catalyst concentration. It can be seen in Fig. 1 that the reaction time and catalyst concentration greatly affect the acid number obtained. The lowest acid number of 4.72 mg KOH/g was obtained at a reaction time of 120 minutes and a concentration of 25%, which means that 98.6% of PKFAD was converted into biodiesel. For all catalyst concentrations at the reaction time of 120 minutes, the amount of PKFAD converted into biodiesel is above 97%. The results obtained in this study are comparable to those of other researchers who were able to achieve the conversion of fatty acids into biodiesel up to 97.1% by Guan *et al.* [9], 87% by Liu *et al.* [10], 96% by Marchetti [26], and 95% by Metere [19]. All these researchers used acid catalysts to catalyze fatty acids and/or triglycerides as raw materials for biodiesel production, but all these studies were conducted at non-vacuum pressure. Hence, the addition of PTSA catalysts significantly increases the esterification reaction rate of the PKFAD into biodiesel.

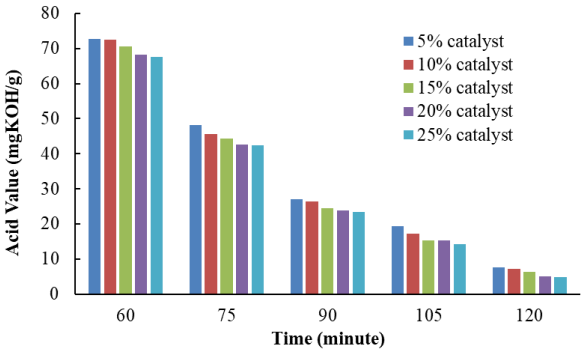

Figure 1. Reaction time and catalyst concentration effect on acid value at a molar ratio of 10: 1 and an operating pressure of 80 kPa.

Effect of operating pressure and a molar ratio of methanol and PKFAD on the acid number

In Fig. 2, the operating pressure effect on acid number is presented at various molar ratios of methanol and PKFAD with a catalyst concentration of 5% and a

reaction time of 120 minutes. Operating pressure did not significantly affect the acid number, but the acid number under vacuum gave better results than in non-vacuum conditions. The higher molar ratio generally produces a lower acid value [28]. In all molar ratios of methanol and PKFAD for all vacuum pressures, the conversion of PKFAD to biodiesel was above 96%, and the highest was at a molar ratio of 10:1, which could reach above 97%.

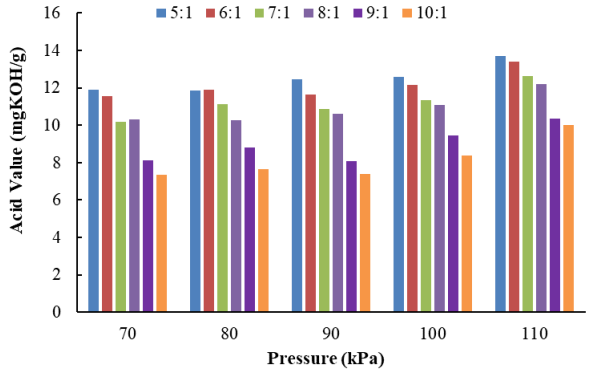

Figure 2. Effect of operating pressure and a molar ratio of methanol and PKFAD on acid value at a catalyst concentration of 5% in a reaction time of 120 minutes.

Fig. 3 shows the effect of operating pressure on the acid number at various methanol and PKFAD molar ratios with a catalyst concentration of 10% and a reaction time of 120 minutes.

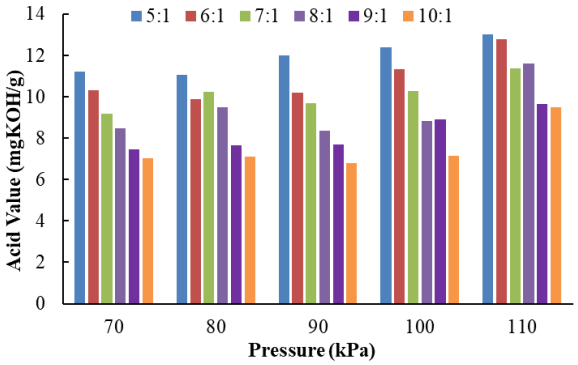

Figure 3. Effect of operating pressure and a molar ratio of methanol and PKFAD on acid value at a catalyst concentration of 10% in a reaction time of 120 minutes.

Similar to Fig. 2, the operating pressure did not significantly affect the acid number, but the acid number obtained under vacuum pressure gave better results than the non-vacuum pressure condition. In all molar ratios of methanol and PKFAD for all vacuum pressures, the conversion of PKFAD to biodiesel was above 96%, and the highest was at a molar ratio of 10:1, which could achieve conversions above 97%.

In Fig. 4, the effect of operating pressure on the acid number is presented at various molar ratios of methanol and PKFAD with a catalyst concentration of 15% and a reaction time of 120 minutes. In all molar ratios of methanol and PKFAD for all vacuum pressures, the conversion of PKFAD to biodiesel was above 96%, and the highest was at a molar ratio of 10:1, which could reach above 98% for all operating pressure variations.

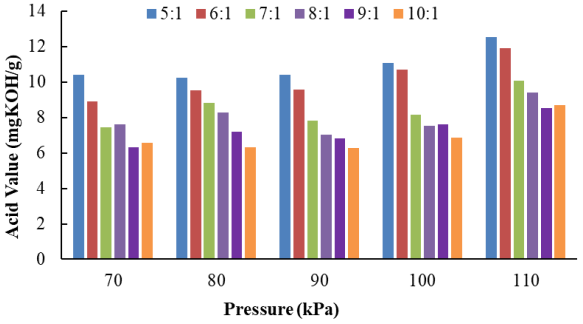

Figure 4. Effect of operating pressure and a molar ratio of methanol and PKFAD on acid value at a catalyst concentration of 15% in a reaction time of 120 minutes.

In Fig. 5, the effect of operating pressure on acid number is presented at various molar ratios of methanol and PKFAD with a catalyst concentration of 20% and a reaction time of 120 minutes. In all molar ratios of methanol and PKFAD for all vacuum pressures, the conversion of PKFAD to biodiesel was above 96%, and the highest was at a molar ratio of 10:1, which could reach above 98%.

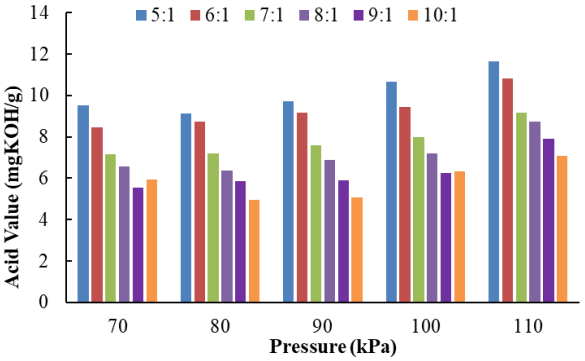

Figure 5. Effect of operating pressure and a molar ratio of methanol and PKFAD on acid value at a catalyst concentration of 20% in a reaction time of 120 minutes.

In Fig. 6, the effect of operating pressure on acid number is presented at various molar ratios of methanol and PKFAD with a catalyst concentration of 25% and a reaction time of 120 minutes. In all molar ratios of methanol and PKFAD for all vacuum pressures, the conversion of PKFAD to biodiesel was above 97%, and the highest was at a molar ratio of 10:1, which reached above 98%.

The lowest acid number of 4.72 mg KOH/g was obtained at an operating pressure of 80 kPa and a

molar ratio of methanol and PKFAD of 10:1, or the conversion of PKFAD to biodiesel reached 98.60% (Fig. 6). This conversion was higher than at other pressures including non-vacuum pressures. At 110 kPa, the lowest acid number of 6.54 mg KOH/g was obtained at a catalyst concentration of 25%, and the molar ratio of methanol and PKFAD was 10:1. Under this operating pressure condition, the conversion of PKFAD to biodiesel reached 98.05 %.

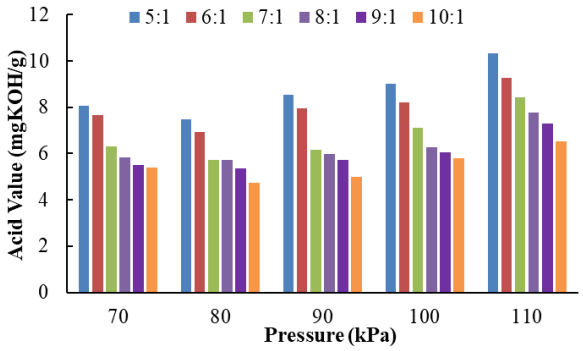

Figure 6. Effect of operating pressure and a molar ratio of methanol and PKFAD on acid value at a catalyst concentration of 25% in a reaction time of 120 minutes.

According to Figs. 2–6, a vacuum pressure of 70 kPa to 100 kPa gave a conversion that was not much different for each of the same methanol and PKFAD molar ratios. However, the vacuum pressure that gave the highest conversion of PKFAD to biodiesel was a pressure of 80 kPa. The conversion results of PKFAD to biodiesel for all vacuum pressures, all catalyst concentrations, and all molar ratios of methanol and PKFAD in the present study were above 96%. Figs. 2–6 show that the acid number obtained under vacuum pressure is better than that obtained at non-vacuum pressure (110 kPa).

Based on the results of the GC-MS analysis in Table 2, it can be seen that the composition of the biodiesel obtained is similar to the composition of PKFAD used as raw material (Table 1), where C_8 and C_{10} are the main compositions of biodiesel. The composition of C_{14} and C_{16} at a pressure of 90 kPa was not obtained, while the composition of the raw material was 0.17% of C_{14} and 0.27% of C_{16}. The loss of C_{14} and C_{16} at 90 kPa was caused by the decomposition of carbon atoms in the esterification reaction, which caused the reading on GC-MS to increase the number of unknowns. In contrast, at 90 kPa, the number of unknown compositions in biodiesel increased to 3.11% from 2.12% on raw materials.

Table 3 shows biodiesel's neutralized characteristics, namely biodiesel obtained from the experiment at an operating pressure of 80 kPa, 10:1 of methanol and PKFAD molar ratios, the amount of catalyst 25%, and the reaction duration of 120 minutes. These results indicate that the biodiesel obtained from this study has met the American Society for Testing Materials (ASTM) standards.

Table 2. Composition of biodiesel by using GC-MS Analysis at a molar ratio of methanol and PKFAD 10:1 and a catalyst concentration of 25%.

Pressure (kPa)	Component (%)								
	C_6	C_8	C_{10}	C_{12}	C_{14}	C_{16}	C_{18}	C_{20}	Unknown
70	0.05	32.31	61.49	0.23	0.15	0.21	1.29	2.18	2.09
80	0.04	32.91	61.95	0.42	0.03	0.31	0.82	1.38	2.14
90	0.03	32.79	62.08	0.26	0	0	0.66	1.07	3.11
100	0.03	32.64	61.53	0.41	0.07	0.20	0.80	1.27	3.05
110	0.04	32.91	62.26	0.27	0.03	0.16	0.94	1.56	1.83

Table 3. Characteristics of biodiesel at an operating pressure of 80 kPa, a molar ratio of methanol and PKFAD of 10: 1, and a catalyst concentration of 25%.

Characteristic	Measurement results	ASTM Standard
Ester content	97.8% (m/m)	>96.5%
Density at 25°C	895 kg/m^3	860-900 kg/m^3
Viscosity at 40 °C	2.3 mm^2/s	1.9-6.0 mm^2/s
Flash point	156 °C	≥130 °C
Water content	0,02% (v/v)	≤0.05% (v/v)
Acid value	0.35 mg KOH/g	≤0.50 mg KOH/g
Methanol content	0.01% (m/m)	≤0.02% (m/m)

CONCLUSION

Biodiesel production from PKFAD at a vacuum pressure of 70 kPa to 100 kPa achieves conversions above 96% for all PTSA catalyst concentrations and all methanol and PKFAD molar ratios. The highest conversion of PKFAD to biodiesel of 98.6% was obtained at a vacuum pressure of 80 kPa, with a catalyst concentration of 25%, a reaction time of 120 minutes, and the molar ratio of methanol and PKFAD is 10:1. The characteristics of biodiesel obtained in this study met the American Society for Testing Materials (ASTM) standards. The results show that the ability to produce biodiesel under vacuum conditions will reduce production costs and energy consumption because the operating temperature is lower than in non-vacuum conditions.

ACKNOWLEDGMENT

We are greatly thankful to the Ministry of Research and Technology/National Research and Innovation Agency of the Republic of Indonesia for Research Grant for the fiscal year 2020.

REFERENCES

[1] I. Ambat, V. Srivastava, M. Sillanpää, Renewable and Sustainable Energy Rev. (2018) 356–369. https://dx.doi.org/10.1016/j.rser.2018.03.069.

[2] G. Baskar, R. Aiswarya, Renewable and Sustainable Energy Rev. 57 (2016) 496–504. https://dx.doi.org/10.1016/j.rser.2015.12.101.

[3] J.M. Fonseca, J.G. Teleken, V. de Cinque Almeida, C. da Silva, Energy Convers. Manage. 184 (2019) 205–218. https://dx.doi.org/10.1016/j.enconman.2019.01.061.

[4] F. Shahidi, Bailey's Industrial Oil and Fat Products, Set, Wiley, Canada (2005), 2–20. 9780471678496.

[5] D. Singh, D. Sharma, S.L. Soni, S. Sharma, P. Kumar Sharma, A. Jhalani, Fuel 262 (2020) 1–15. https://dx.doi.org/10.1016/j.fuel.2019.116553.

[6] S. Dechakhumwat, P. Hongmanorom, C. Thunyaratchatanon, S.M. Smith, S. Boonyuen, A. Luengnaruemitchai, Renewable Energy 148 (2020) 897–906. https://dx.doi.org/10.1016/j.renene.2019.10.174.

[7] A. García, C. Cara, M. Moya, J. Rapado, J. Puls, E. Castro, C. Martín, Ind. Crops Prod. 53 (2014) 148–153. https://dx.doi.org/10.1016/j.indcrop.2013.12.029.

[8] S.N. Gebremariam, J.M. Marchetti, Energy Convers. and Manage. 174 (2018) 639–648. https://dx.doi.org/10.1016/j.enconman.2018.08.078.

[9] G. Guan, K. Kusakabe, N. Sakurai, K. Moriyama, Fuel 88 (2009) 81–86. https://dx.doi.org/10.1016/j.fuel.2008.07.021.

[10] J. Liu, Y. Nan, L.L. Tavlarides, Fuel 193 (2017) 187–196. https://dx.doi.org/10.1016/j.fuel.2016.12.058.

[11] Z. Helwani, N. Aziz, M.Z.A. Bakar, H. Mukhtar, J. Kim, M.R. Othman, Energy Convers. Manage. 73 (2013) 128–134. https://dx.doi.org/10.1016/j.enconman.2013.04.004.

[12] P. Rechnia-Gorący, A. Malaika, M. Kozłowski, Diamond Relat. Mater. 87 (2018) 124–133. https://dx.doi.org/10.1016/j.diamond.2018.05.015.

[13] S.P. Yeong, Y.S. Chan, M.C. Law, J.K.U. Ling, J. Bioresour. Bioprod. 7 (2022) 43–51. https://dx.doi.org/10.1016/j.jobab.2021.09.002.

[14] A.O. Esan, S.M. Smith, S. Ganesan, Process Saf. Environ. Prot. 166 (2022) 402–413. https://dx.doi.org/10.1016/j.psep.2022.08.040.

[15] M.S.A. Farabi, M.L. Ibrahim, U. Rashid, Y.H. Taufiq-Yap, Energy Convers. Manage. 181 (2019) 562–570. https://dx.doi.org/10.1016/j.enconman.2018.12.033.

[16] W. Xu, L. Gao, S. Wang, G. Xiao, Bioresour. Technol. 159 (2014) 286–291. https://dx.doi.org/10.1016/j.biortech.2014.03.004.

[17] A.D. Burmana, R. Tambun, B. Haryanto, V. Alexander, IOP Conf. Ser.: Mater. Sci. Eng. 1003 (2020). https://dx.doi.org/10.1088/1757-899X/1003/1/012134.

[18] R. Tambun, A.D. Burmana, V. Alexander, Journal of Engineering Science and Technology 17 (2022) 257–266. https://jestec.taylors.edu.my/Vol%2017%20Issue%201%20February%20%202022/17_1_19.pdf.

[19] A. V. Metre, K. Nath, Pol. J. Chem. Technol. 17 (2015) 88–96. https://dx.doi.org/10.1515/pjct-2015-0013.

[20] A. Hykkerud, J.M. Marchetti, Biomass Bioenergy 95 (2016) 340–343. https://dx.doi.org/10.1016/j.biombioe.2016.07.002.

[21] Z. Zhou, X. Zhang, F. Yang, S. Zhang, J. Cleaner Prod. 215 (2019) 13–21. https://dx.doi.org/10.1016/j.jclepro.2018.12.279.

[22] D.T. Melfi, K.C. dos Santos, L.P. Ramos, M.L. Corazza, J. Supercrit Fluids 158 (2020). https://dx.doi.org/10.1016/j.supflu.2019.104736.

[23] S.K. Sangar, C.S. Lan, S.M. Razali, M.S.A. Farabi, Y.H. Taufiq-Yap, Energy Convers. Manage. 196 (2019) 1306–1315. https://dx.doi.org/10.1016/j.enconman.2019.06.073.

[24] I.M. Lokman, U. Rashid, Y.H. Taufiq-Yap, R. Yunus, Renewable Energy 81 (2015) 347–354. https://dx.doi.org/10.1016/j.renene.2015.03.045.

[25] U. Rashid, S. Soltani, T.S.Y. Choong, I.A. Nehdi, J. Ahmad, C. Ngamcharussrivichai, Catalysts 9 (2019) 1–15. https://dx.doi.org/10.3390/catal9121029.

[26] J.M. Marchetti, A.F. Errazu, Biomass and Bioenergy 32 (2008) 892–895. https://dx.doi.org/10.1016/j.biombioe.2008.01.001.

[27] V.B. Veljković, S.H. Lakićević, O.S. Stamenković, Z.B. Todorović, M.L. Lazić, Fuel 85 (2006) 2671–2675. https://dx.doi.org/10.1016/j.fuel.2006.04.015.

[28] Y.C. Sharma, B. Singh, Fuel 87 (2008) 1740–1742. https://dx.doi.org/10.1016/j.fuel.2007.08.001.

RONDANG TAMBUN
ANGGARA DWITA BURMANA
BODE HARYANTO
VIKRAM ALEXANDER

Department of Chemical Engineering, Faculty of Engineering, Universitas Sumatera Utara, Medan, Indonesia

NAUČNI RAD

EFEKAT VAKUUMA NA PROIZVODNJU BIODIZELA OD DESTILATA MASNIH KISELINA PALMI

Ova studija istražuje efekat radnog pritiska na proizvodnju biodizela iz destilata masnih kiselina palminog jezgra (PKFAD) korišćenjem para-toluen sulfonske kiseline (PTSA) kao katalizatora . Istraživannja su sprovedena pri radnim pritiscima (vakuum) od 70 kPa, 80 kPa, 90 kPa i 100 kPa, koncentracijama PTSA od 5%, 10%, 15%, 20% i 25% i molskim odnosima metanola i PKFAD od 5:1, 6:1, 7:1, 8:1, 9:1 i 10:1. Proizvodnja biodizela iz PKFAD-a je trajala 120 minuta na 50 °C. Količine masnih kiselina pretvorenih u biodizel izračunate su na osnovu početnog i kiselinskog broja nakon reakcije esterifikacije. Rezultati pokazuju da vakuum od 70 kPa do 100 kPa obezbeđuje konverziju iznad 96% za sve koncentracije katalizatora i sve molske odnose metanola i PKFAD. Najveća konverzija PKFAD u biodizel od 98,6% se postiže pri radnom pritisku od 80 kPa, koncentraciji katalizatora od 25%, a molskom odnosu metanola i PKFAD od 10:1. Karakteristike biodizela dobijene zadovoljavaju standarde Američkog društva za ispitivanje materijala.

Ključne reči: proizvodnja biodizela, destilat masnih kiselina palminog jezgra, process pod vakuumom.

CI&CEQ
Chemical Industry & Chemical Engineering Quarterly

Available online at
Association of the Chemical Engineers of Serbia AChE
www.ache.org.rs/CICEQ

Chem. Ind. Chem. Eng. Q. 30 (1) 81–88 (2024) CI&CEQ

LOGANATHAN GOKULANATHAN[1]
JEGAN ANNAMALAI[2]

Department of Mechanical Engineering, Sona College of Technology, Salem, Tamil Nadu, India

AVS College of Technology, Salem

EXPERIMENTAL INVESTIGATION OF MICRO-ECM ON MONEL 400 ALLOY USING PARTICLES MIXED ELECTROLYTE

Article Highlights

- The micro-holes were fabricated over the MONEL 400 alloy
- The various electrolytes used here are MGAE, MPME, and CPME
- The parameters are electrolyte type, concentration, machining voltage, and duty cycle
- The results are optimized using MOORA and VIKOR techniques
- The best parameter for machining is 28 g/l of electrolyte, 11V machining voltage, and 50% duty cycle

Abstract

The machining of extremely hard material in conventional machining requires high energy. Therefore stress-free, burr-free, and high-accuracy machining technique like Electro Chemical Micro Machining (ECMM) with extra features is recommended. To improve efficiency, various electrolytes such as Magnet Associated Electrolytes (MGAE), Metal Particle Mixed Electrolytes (MPME), and Carbon Pellets Mixed Electrolytes (CPME) are employed. The micro-holes were drilled over the work material MONEL 400 alloy. The parameters for the studies are electrolyte type, concentration (g/l), machining voltage (V), and duty cycle (%). The responses of ECMM are estimated through material removal rate (MRR) in µm/sec and overcut in µm. The results are optimized using Multi-objective optimization based on ratio analysis (MOORA) and VIseKriterijumska Optimizacija I Kompromisno Resenje (VIKOR). Both techniques produce the same optimal parameter, 18th experiment CPME, 50% duty cycle, 11 V machining voltage, and 28 g/l electrolyte concentration. It is the best optimal parameter solution for machining. According to the ANOVA table of both, the type of electrolyte plays a 62.6% and 60.37% contribution, respectively, to machining performance. Furthermore, the scanning electron microscope (SEM) image analysis perused on the micro holes to extend the effect of different electrolytes on machining surfaces.

Keywords: carbon pellets, MOORA, VIKOR, ECMM, metal particles, magnet.

SCIENTIFIC PAPER

UDC 544.6:669.24.017/.018

ECMM creates numerous applications in different manufacturing sectors, such as medical, electronics, automobiles, and microelectromechanical systems. The machining of micro features in all kinds of components is essential nowadays. Therefore, this paper mainly focuses on fabricating micro holes via the ECMM process [1]. The precision of micro-hole and machining performance of ECMM is acquired based on various factors such as electrical, nature of electrolyte, electrode, and adoption of the new technique. Also, it is mandatory in the fast-developing and challenging manufacturing sector to suppress the irregularity of machining and improve the machining performance simultaneously [2]. In line up with that, to improve micro-hole accuracy and machining performance, various research attempts are made by researchers worldwide. Therefore, Singh *et al.* [3] conducted experiments in the electrochemical discharge machin-

Correspondence: L. Gokulanathan, Department of Mechanical Engineering, Sona College of Technology, Salem, Tamil Nadu, India -636005.
E-mail: lgokulanathan@gmail.com
Paper received: 15 November, 2022
Paper revised: 19 May, 2023
Paper accepted: 21 June, 2023

https://doi.org/10.2298/CICEQ221115013G

ing process with multiple tooltip electrodes to investigate the effect of electrical frequency and duty cycle. They noted nonhomogeneous tool wear on the electrode due to the pulse variations in the sulfuric acid electrolyte. The frequency of 50 kHz is optimal for a better uniform machining rate and surface finish. Zhao *et al*. [4] conducted the experiment in ECMM with a curved voltage signal to improve the machining accuracy and derived a mathematical model. They noted the better agreement for curved pulse signals with experimental results. Also, they compared the results of pulse signals, such as rectangular and parabolic, to the experimental outputs and suggested parabolic signals. The parabolic signals diminish the machining gap ten times less, contributing to a better surface finish. Sharma *et al*. [5] investigated the effect of pulsed current between the tool and electrode and noted the suitable current distributions technique for the ECM process using simulation and experimental. The waveforms such as rectangular, sinusoidal, and triangular are employed in experimentations. They suggested that triangular waveforms produce a better surface finish and two times better machining rate than the normal waveforms. Panda *et al*. [6] employed the sulfuric acid electrolyte with rectangular electric pulses in ECMM of titanium alloy. They noted that machining voltage 13V–17 V produces better MRR with short pulses. Also, the taper of hole and overcut are reduced by around 83.99% and 51.39%, respectively, with this short pulse power supply. VinodKumaar *et al*. [7] studied the ECMM performance with metal particles of copper mixed electrolyte on SS 316 work metal using the citric acid electrolyte. In addition, they employed the stirring mechanism to accelerate the movement of the ions in the electrolyte. They noted that employing an additional mechanism induces the unwanted surface finish due to the excess migration of electrons. Gokulanathan *et al*. [8] conducted experiments in ECMM on Monel 400 alloy with a pulsed air supply system to understand the effect of pulsed sir suspension on machining performance. They noted that the micro stirring effect increases the electron's movement and leads to a better machining rate. Also, optimization techniques such as TOPSIS and COPRAS methods are employed to identify the optimal parameter solution. Kumaar *et al*. [9] tried various organic electrolytes to study the machining performance of ECMM on SS 316 material. The electrolytes such as citric acid, tartaric, and mixed organic acid (citric acid and tartaric) in equal proportion are employed for the experiment. They noted that overcut of micro-hole was reduced by around 170% with tartaric acid, and MRR increased to 110% with mixed acid electrolyte. Also, the organic acids note very few surface irregularities over the work material. Arul *et al*. [10] employed the aluminum composite electrode in the ECMM process to investigate surface accuracies. The square micro-hole is fabricated using a composite electrode, and the edges of the micro-hole are obtained neatly due to the uniform current distribution. Also, they noted that 43% improved over cut and 70% higher MRR with composite electrode than SS tool electrode. Vats *et al*. [11] fabricated the high-aspect micro holes using a hollow tube electrode through the ECMM process on nickel-based Inconel alloy. They noted lesser stray cuts and uniform current distribution in the machining zone. The inter-electrode gap provides a better way to dispel the dissolved parts from the machining zone because of the hollow tool. The surface roughness of the micro-hole significantly improved by around 20% with a hollow tube electrode than a normal tool. Rajkeerthi *et al*. [12] conducted experiments using a hollow taper tool and cylindrical hollow toll in the ECMM process on nickel-based superalloy. They noted that the tapered hollow tool reduces the over-cut by up to 2.5% and increases the MRR by around 24% more than normal cylindrical hollow tools. Thanigaivelan *et al*. [16] tried different mixed electrolytes, such as plain sodium nitrate, plain sodium chloride, and mixed sodium nitrate and sodium chloride, for the ECMM process. They noted significant improvement in MRR due to the solution's accelerated electron movements. Wang *et al*. [17] used acoustic emission to improve the ECM process's machining performance. It has been noted that two times better overcut with this mechanism, and ultrasonic vibrations dispel the machined products from the machining zone quickly, leading to a better surface finish. Liu *et al*. [18] tried the heat-treated copper electrodes in the ECMM process using sodium nitrate electrolyte. They mentioned that lesser overcut was obtained with heat-treated electrodes than with normal electrodes due to the high electrical conductivity of the electrode. Zhan *et al*. [19] investigated the machining performance of ECM with a gas-assisted tool electrode. The assistance of gas surrounding the electrode act as insulation, preventing unwanted material removal and causing lesser overcut. The literature discussed above clearly notes that many researchers employed electrolytes and electrodes to enhance ECMM performance. The electrolytes are fabricated by mixing magnets, metal powder, and carbon pellets in different ranges to enhance the machining performance. The results of these electrolytes, such as MGAE, MPME, and CPME, are compared. Also, these mixing elements are successfully employed in other sectors such as electrical batteries, metal coating, electrical discharge machining, etc. [20,21,22]. Although magnets and metal mixed studies exist in the literature, it is not adequate data for commercial execution, and carbon pellets are employed in electrolytes for the first time in

this attempt. Carbon materials naturally stimulate electrolyte conductance when mixed in water. Also, the process parameters are optimized through the most prominent optimization techniques, such as MOORA and VIKOR methods. Furthermore, SEM figures analysis is carried out to show the performance of the machining process, and microholes are affected by various electrolytes. Matsuzawa *et al*. [28] ECM can be performed on any workpiece regardless of its hardness. However, the machining direction is confined to the gravitational direction because ECM uses electrolytes. The electrolyte is frozen using a Peltier device. This method uses the principle of the Peltier device to freeze the electrolyte and seal it in an electrode. Wang *et al*. [29] Electrochemical machining (ECM) is widely employed to machine tough materials. A non-conductive solid porous ball is used as an electrolyte absorption material in ECM. Ge *et al*. [30] Casing parts are considered key components of aero-engines. Most casing parts are attached to convex structures of different shapes, whose heights range from hundreds of microns to tens of millimeters. It indicates that the back-pressure method is suitable and effective for the electrochemical machining of highly convex structures with blocky electrodes. From the literature mentioned above section, the research gap is found that pulsed air supply for this electrochemical micromachining is proposed in this work along with the many different electrolytes like MGAE, MPME, and CPME going to be tested in the proposed methodology.

MATERIAL AND METHODS

For the experiment shown in Fig. 1, an ECMM setup that was autonomously manufactured was used. The experimental setup included various sub-components, a voltage rectifier, a tool transmission system, and an electrolyte recycling supply arrangement. Considering the demand for Monel 400 in various fields, this paper employed a 0.8 mm thick plate as work material. SS material is considered for all three electrodes with a length of 4.5 cm and a diameter of 500 µm. The pulsed air supply system is employed in all experiments. The experiments are planned with different methods of electrolytes. Hence, commercially available ferrite (Fe_2O_3) permanent magnets (40 mm x 20 mm x 5 mm in size) are fixed on the electrolyte tank for both sides of the wall and considered MGAE. The experimental setup and MGAE method are presented in Fig. 1. The activated carbon pellets in sizes of 2 mm dia, 5 mm length, and 25 grams are mixed with the electrolyte. Activated carbon pellets exist commercially, and this electrolyte is termed CPME. The 25-gram Nano-sized zinc metal particle is mixed with the standard electrolyte, MPME [23]. The total machining time is noted to evaluate the machining rate. The differences in diameter between the tool and micro hole are measured using an optical microscope to find the overcut of the micro-hole. The hole formation was noted by the witness of hydrogen bubbles beneath the micro-hole. The range of machining parameters and the design of the experiment are presented in Tables 1 and 2, respectively.

Table 1. Machining factors and their levels.

Machining factors	Levels
Type of Electrolyte	MGAE, MPME, CPME
Electrolyte Concentration in g/l	24, 26, 28
Machining voltage in v	9, 11, 13
Duty Cycle in %	50, 75, 90

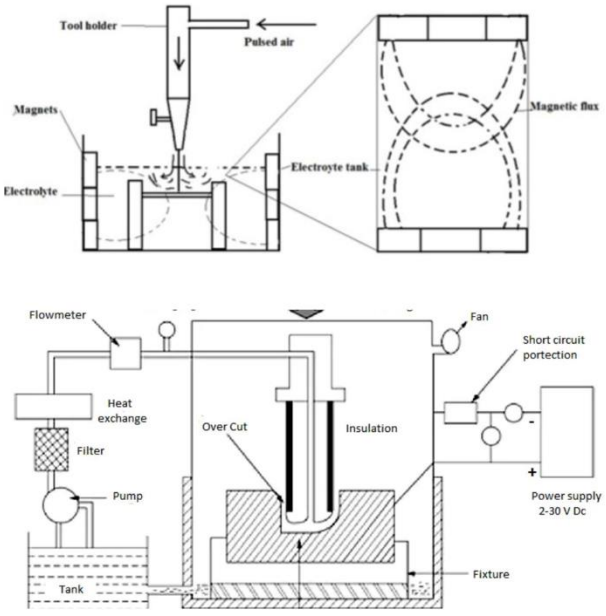

Figure 1. Experimental setup (a) Magnet-associated electrolyte (b) Carbon pellets.

Table 2. Design of experiments and outcomes.

Ex. No	Type of Electrolyte	Elet. Con. in g/l	Mach. Volt in V	Du. Cycle in %	MR in µm / sec	Overcut in µm
1	MGAE	24	9	50	0.6197	152.05
2	MGAE	26	11	75	0.7279	210.04
3	MGAE	28	13	90	0.8070	201.66
4	MPME	24	9	75	0.4655	100.43
5	MPME	26	11	90	0.8514	126.85
6	MPME	28	13	50	0.9296	186.86
7	CPME	24	11	50	0.8556	110.84
8	CPME	26	13	75	0.7365	124.45
9	CPME	28	9	90	0.8863	116.04
10	MGAE	24	13	90	0.6089	135.84
11	MGAE	26	9	50	0.8090	187.85
12	MGAE	28	11	75	0.7274	205.58
13	MPME	24	11	90	0.5046	96.68
14	MPME	26	13	50	0.6637	102.77
15	MPME	28	9	75	0.8573	182.46
16	CPME	24	13	75	0.6987	104.55
17	CPME	26	9	90	0.8183	114.47
18	CPME	28	11	50	0.8491	100.87

OPTIMIZATION

VIKOR

VIKOR is one of the most robust and reliable techniques for multi-criteria optimization to find the optimal parameter solution. The following steps are followed to evaluate the best machining combination [24] which are;

Step 1. Different dimensioned values are converted into single form by normalization using Eqs. 1 and 2. Also, a positive sign was assigned for MR, and a negative sign was assigned for minimization.

$$S_m = \begin{bmatrix} T_{11} & T_{12} & T_{13} & T_{1n} \\ T_{21} & T_{22} & T_{23} & T_{2n} \\ T_{31} & T_{32} & T_{33} & T_{3n} \\ T_{m1} & T_{m2} & T_{m3} & T_{mn} \end{bmatrix} \quad (1)$$

$$t_{ij} = \frac{T_{ij}}{\sqrt{\sum_{i=1}^{m} T_{ij}^2}},\ j = 1,2,\ldots,n. \quad (2)$$

Step 2. The uppermost and least values are noted from the decision matrix to find the *Ci* and *Di* using Eqs. 3 and 4, respectively.

$$C_i = \sum_{j=1}^{n} R_j \left[\left(b_{ij}\right)_{\max} - \left(b_{ij}\right) \right] / \left[\left(b\right)_{\max} - \left(b\right)_{\min} \right] \quad (3)$$

$$D_i = Max^n \left\{ \frac{\left[R_j \left(b\right)_{\max} - \left(b_{ij}\right) \right]}{\left[\left(b\right)_{\max} - \left(b\right)_{\min} \right]} \right\},\ j = 1,2,\ldots,n. \quad (4)$$

where R_j is the weighted value (equal weight assigned).

Step 3- *Pi* values are estimated through *Ci* and *Di* using Eq. 5.

$$P_i = R \frac{C_i - C_{i-\min}}{C_{i-\max} - C_{i-\min}} + (1-R) \frac{D_i - D_{i-\min}}{D_{i-\max} - D_{i-\min}} \quad (5)$$

Step 4. Lowest *Pi* values are considered the best solution, and others are followed in the rank order.

MOORA

MOORA is another excellent and straightforward technique to identify the suitable parameter solution from a certain number of experiments [25].

Step 1. Normalization is carried out by the Eqs. 1 and 2.

Step 2. Values are added for higher needs and have to subtract for lesser needs using Eq. 6.

$$J_i = \sum_{j=1}^{g} M_{ij} - \sum_{j=g+1}^{n} m_{ij} \quad (6)$$

Step 4. Equal weights are assigned to all outputs, multiplied by w_j in the Eq. 7.

$$T_i = \sum_{j=1}^{g} w_j M_{ij} - \sum_{j=g+1}^{n} w_j m_{ij},\ j = 1,2,\ldots,n. \quad (7)$$

Finally, *Ti* values are graded, and higher values are ranked as one and termed as the best optimal combination.

RESULTS AND DISCUSSION

Influences of input parameters on overcut

The overcut of all input parameters is drawn as a graph and presented in Fig. 2. The data sets of the

graph are prepared according to the mean values of overcut. The graph infers that overcut increases when increasing input parameter ranges. Also, it indicates that MGAE produced the least overcut among the different electrolytes, and the highest overcut was found to be with the MPME. MGAE and CPME produce 35.08% and 11.61% lesser overcut, respectively, than MPME. In one of our previous experiments, plain air-assisted electrolyte [8] obtained 124.23 µm overcut for the first optimal combination, whereas, in the present study, the MGAE produces 111.87 µm overcut. This value is 9.9% lesser than the plain air-assisted electrolyte. Fig. 3a presents the SEM image of the micro-hole machined under the MGAE, which shows the precise circumference and micropores surface.

The use of magnets in the electrolyte induces magnetic flux pressure over the movement of the ions at the machining zone. Hence, continuous sludge removal is carried between the tool and electrode, which ensures the unwanted electric current conduct among electrolytes. Also, the uniform electric current flow passage settled among the movement of the electron, as explained in Fig. 1. This phenomenon is caused for the lesser overcut in the MGAE. Also, in MGAE, additional substances are not mixed, which enables the homogeneous current conductivity and causes the best surface finish and lesser over-cut. The CPME produces 152.38 µm overcut. The second least overcut in the experiment. SEM images of a micro hole machined with CPME and MPME are presented in Fig. 3b and Fig. 3c. Carbon particles conduct electricity smoothly and uniformly by their soft crystallographic nature [20].

On the other hand, metal particles create a strong conduction bridge in the electrolyte which induces the turbulent ion movement [26], which causes the excess material removal and leads to a lesser overcut with CPME than MPME. The case of other machining parameters produces the magnified overcut when increasing the levels. It is oblivious that the dissolution range increase or decreases based on the input ranges supplied to the machining zone.

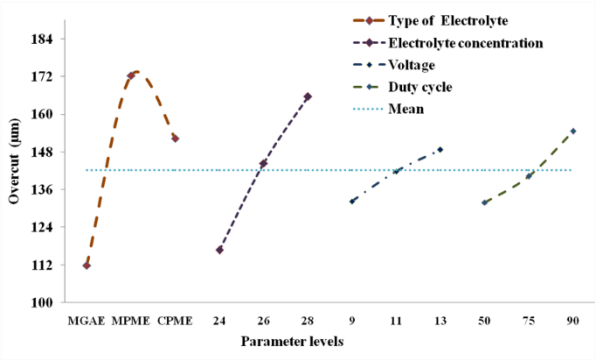

Figure 2. Influences of different parameters on overcut.

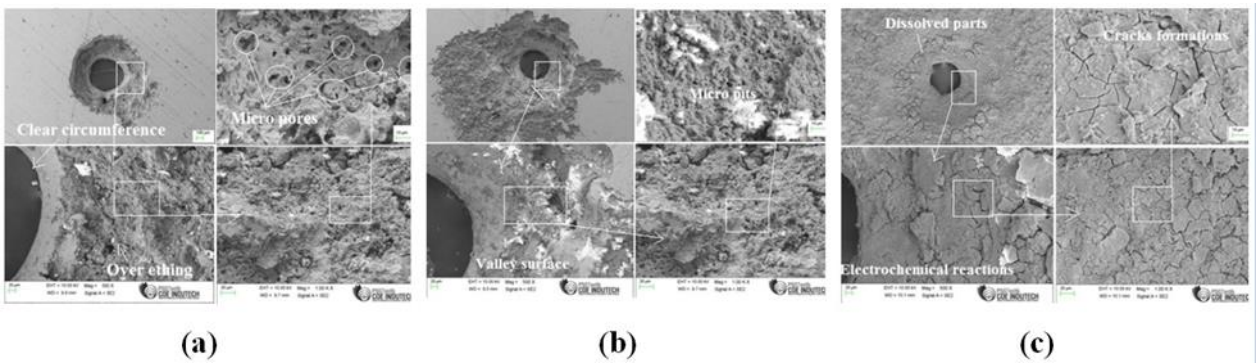

Figure 3. SEM image of micro holes (a) MGAE (b) CPME (C) MPME.

Influences of input parameters on MRR

The influences of various input parameters on MRR and its values are presented as a graph in Fig. 4. The graph indicates that a range of input parameters increases the MRR. Among those uses, different electrolytes contribute more MRR than other parameters. Based on that, MPME produces the highest MRR among different electrolytes and the lowest MRR obtained with MGAE. The MPME and CPME produce 27.92% and 17.93% higher MRR, respectively, than the MGAE. Although, the MGAE produces 6.57% higher MRR than the literature [8], which is obtained for the optimal solution. The primary cause for the highest MRR with MPME is Nano metal particles. Since the Nano metal particle creates the connection pathway for the vibrant electrons movement in the electrolyte by its range of size, this character of electrolyte implies faster ion migration, leading to the highest MRR than others. The CPME produces the second-highest MRR. Since the carbon pellets post up the conductivity of the electrolyte due to the series connections, it acts like a storage barrier that transmits the electric energy to the electrolyte between the pulses on time [20]. This phenomenon of carbon-mixed electrolytes causes a higher MRR. Also, the graph shows the increasing trend concerning all ranges of

levels. It is because the high state of the machining parameter enables rapid ion oscillation. Also, in the higher range of machining, the dissolved particle of the work plate merges with the electrolyte and induces electric conductivity among the electrolyte.

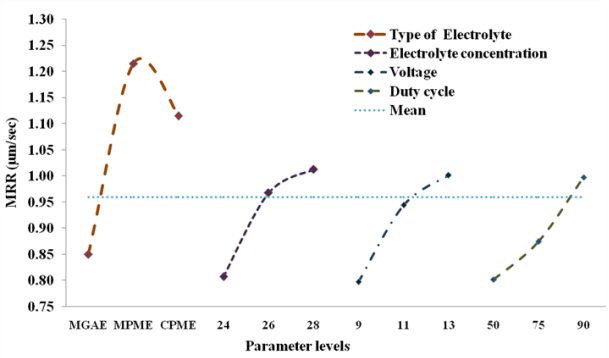

Figure 4. Influences of different parameters on MRR.

Estimation of optimal combinations

VIKOR

The perfect parameter value is determined by the VIKOR method [24]. Equal weights are provided to the output responses. The VIKOR compromised values are ranked as lowest is best and furthest is the worst solution, presented in Table 3a. Based on the table, the least compromised value was obtained in experiment no 18. Hence, the 18th experiment parameter solution of CPME, electrolyte level of 28 g/l, machining voltage of 11 V, and duty cycle of 50% is considered a suitable parameter solution for machining. Experiments 9 and 7 show the next ranking orders and are considered the 2nd and 3rd optimal combinations for machining.

ANOVA table estimated the preference values used to investigate the machining performance statically [27]. The VIKOR study involves the ANOVA values to find the most critical parameter in machining, presented in Table 4a. Based on the table, electrolyte type plays a 62.6% contribution to machining performance. The machining voltage and duty cycle contribute 12.63% and 12.38%, respectively, to the performance. The very least contribution was obtained with the electrolyte concentration factor.

MOORA

MOORA method estimates the suitable parameter combination for ECMM with different electrolytes and machining parameters [27]. The obtained MOORA values and their ranking are presented in Table 3b. The Eqs. 1, 2, 6 and 7 are used for the MOORA values. An equal weight of 0.5 is assigned for both output values. The uppermost MOORA value is taken as an optimal solution and termed first grade to obtain a better machining outcome.

Table 3. a) Ranking of responses in VIKOR; b) MOORA and its ranking.

Ex. No	R_i	S_i	VIKOR (T_i)	Rank
1	0.5781	0.6749	0.7903	15
2	0.7173	0.7879	1.0000	18
3	0.5952	0.6892	0.8165	16
4	0.5165	0.6226	0.6956	12
5	0.2174	0.3346	0.2068	5
6	0.3978	0.5162	0.5083	9
7	0.1423	0.2469	0.0710	3
8	0.3306	0.4520	0.3989	8
9	0.1321	0.2341	0.0519	2
10	0.5183	0.6241	0.6983	13
11	0.5321	0.6360	0.7198	14
12	0.6981	0.7728	0.9715	17
13	0.4579	0.5710	0.6039	11
14	0.3133	0.4350	0.3703	7
15	0.4563	0.5696	0.6015	10
16	0.2835	0.4049	0.3205	6
17	0.1984	0.3134	0.1733	4
18	0.1052	0.1989	0.0000	1

Table 3b.

Ex. No	Normalized Responses		MOORA value (Yi)	Rank
	MR	OC		
1	0.1932	0.2423	0.4433	14
2	0.2269	0.3348	0.2995	18
3	0.2515	0.3214	0.3846	16
4	0.1451	0.1601	0.5468	10
5	0.2654	0.2022	0.7685	5
6	0.2898	0.2978	0.5095	12
7	0.2667	0.1767	0.8607	2
8	0.2295	0.1984	0.6822	8
9	0.2762	0.1850	0.8553	3
10	0.1898	0.2165	0.5175	11
11	0.2521	0.2994	0.4289	15
12	0.2267	0.3277	0.3074	17
13	0.1573	0.1541	0.5775	9
14	0.2069	0.1638	0.6854	7
15	0.2672	0.2908	0.4836	13
16	0.2178	0.1666	0.7148	6
17	0.2551	0.1824	0.8074	4
18	0.2646	0.1608	0.8904	1

In line with that, the 18th experiment carried the farthest MOORA grade, 0.8904. 18th experimental run parameter combinations present 0.8491 µm/sec MRR and 100.87 µm overcut. Hence, based on the MOORA method, these experiment parameter characteristics: CPME, 11 V machining voltage, 28 g/l electrolyte concentration, and 50% duty cycle is considered suitable parameter solution for machining. Also, experiments 7th and 9th are optimal parameter combinations for better outcome machining.

Table 4. a) ANOVA of VIKOR; b) ANOVA for MOORA.

Machining parameter	DOF	SS	MS	F	% OF CON
Type of electrolyte	2	0.3920	0.196	39.357	62.81
Electrolyte concentration	2	0.0406	0.0203	4.0779	6.51
Machining voltage	2	0.0788	0.0394	7.9153	12.63
Duty cycle	2	0.0773	0.0386	7.7598	12.38
Error	9	0.0448	0.005		5.66
Total	17	0.6336	0.0373		100

Table 4b.

Machining parameter	DOF	SS	MS	F	% OF CON
Type of electrolyte	2	1.0206	0.5103	41.562	60.37
Electrolyte concentration	2	0.1987	0.0993	8.0899	11.75
Machining voltage	2	0.1206	0.0603	4.9108	7.13
frequency	2	0.2450	0.1225	9.9773	14.49
Error	9	0.1105	0.0123		6.26
Total	17	1.6953	0.0997		100

CONCLUSION

The primary objective of this investigation is to emphasize the machining process of ECMM using different inorganic materials mixed electrolytes along with a pulsed air supply system for Monel 400 alloy. The results of the machining process are optimized through VIKOR and MOORA methods.

MPME produces the highest MRR and lowest MRR obtained with MGAE. MPME and CPME produce 27.92% and 17.93% higher MRR, respectively, than the MGAE.

MGAE produces the least overcut and highest overcut found in MPME. MGAE and CPME produce 35.08% and 11.61% lesser overcut, respectively, than MPME.

CPME produces 152.38 µm overcut, the second least overcut in the experiment. Carbon particles conduct electricity smoother and more uniformly through their soft crystallographic nature.

Both optimization techniques, VIKOR and MOORA, produce the same optimal parameter for machining as the 18th experiment parameter solution, CPME 50% duty cycle, an 11 V machining voltage, and a 28 g/l electrolyte concentration.

SEM image analysis extends the understanding of the effect of different electrolytes on the micro holes, which presents the over-etching surface near the micro holes due to the synergetic effect of electrochemical reactions.

REFERENCES

[1] T.S. Srivatsan, T.S. Sudarshan, K. Manigandan, Textbook of Manufacturing Techniques for Materials: Engineering and Engineered (1st ed.), CRC Press, Boca Raton (2018), p. 814. https://doi.org/10.1201/b22313.

[2] M. Soundarrajan, R. Thanigaivelan, Russ. J. Electrochem. 57 (2021) 172–182. https://doi.org/10.1134/S1023193521020117.

[3] T. Singh, D.K. Mishra, P. Dixit, J. Appl. Electrochem. 52 (2022) 667–682. https://doi.org/10.1007/s10800-021-01662-x.

[4] C. Zhao, T. Huang, J. Wang, L. Xu, Int. J. Adv. Manuf. Technol. 121 (2022) 3067–3078. https://doi.org/10.1007/s00170-022-09482-9.

[5] V. Sharma, P. Gupta, J. Ramkumar, J. Manuf. Processes. 75 (2022) 110–124. https://doi.org/10.1016/j.jmapro.2022.01.006.

[6] H. S. Panda, K. Mishra, B. Bhattacharyya, J. Electrochem. Soc. 169 (2022). https://doi.org/10.1149/1945-7111/ac6e8e.

[7] J.R. VinodKumaar, R. Thanigaivelan, M. Soundarrajan, Mater. Manuf. Processes. (2022) 1–14. https://doi.org/10.1080/10426914.2022.2030874.

[8] L. Gokulanathan, A. Jegan, Int. J. Electrochem. Sci. 17 (2022) 2. https://doi.org/10.20964/2022.08.55.

[9] J.R.K.V. Kumaar, R. Thanigaivelan, M. Soundarrajan, Chem. Ind. Chem. Eng. Q. 28(4) (2022) 329–337. https://doi.org/10.2298/CICEQ211204007V.

[10] T.G. Arul, V. Perumal, R. Thanigaivelan, Chem. Ind. Chem. Eng. Q. 28 (2022) 247–253. https://doi.org/10.2298/CICEQ210501036A.

[11] A. Vats, A. Dvivedi, P. Kumar, Mater. Manuf. Processes. 36 (2021) 677–692. https://doi.org/10.1080/10426914.2020.1866189.

[12] E. Rajkeerthi, P. Hariharan, N. Pradeep, Mater. Manuf. Processes. 36 (2021) 488–500. https://doi.org/10.1080/10426914.2020.1843672.

[13] M. Soundarrajan, R. Thanigaivelan, S. Maniraj, In Advances in Industrial Automation and Smart Manufacturing, Springer, Singapore (2021), p. 367–376.

https://doi.org/10.1007/978-981-15-4739-3_30.

[14] R. Shanmugam, M. Ramoni, G. Thangamani, M. Thangaraj, Metals. 11 (2021) 778. https://doi.org/10.3390/met11050778.

[15] M. Soundarrajan, R. Thanigaivelan, Mater. Manuf. Processes. 35 (2020) 775–782. https://doi.org/10.1080/10426914.2020.1740252.

[16] V. Subburam, S. Ramesh, R.M. Arunachalam, R. Thanigaivelan, In Proceedings of the second international conference on advances in materials processing and characterisation-AMPC (2013), p. 799–806.

[17] G. Wang, Y. Zhang, H. Li, J. Tang, Materials. 13 (2020) 5780. https://doi.org/10.3390/ma13245780.

[18] S. Liu, T. Geethapriyan, T. Muthuramalingam, R. Shanmugam, Ramoni, Arch. Civ. Mech. Eng. 22 (2022) 1–15. https://doi.org/10.1007/s43452-022-00478-6.

[19] S. Zhan, Y. Zhao, J. Mater. Process. Technol. 291 (2021) 117049. https://doi.org/10.1016/j.jmatprotec.2021.117049.

[20] M. Deraman, S. Zakaria, R. Omar, A.A. Aziz, Jpn. J. Appl. Phys. 39 (2000) L1236. https://doi.org/10.1143/JJAP.39.L1236.

[21] P. Kapitza, Proc. R. Soc. London, Ser. A, 123 (1929) 292–341. https://doi.org/10.1098/rspa.1929.0072.

[22] Jadidi, R.B. Azhiri, R. Teimouri, Int. J. Lightweight Mater. Manuf. 3 (2020) 265–276. https://doi.org/10.1016/j.ijlmm.2020.02.004.

[23] R. Kumar, R. Thanigaivelan, G.K. Rajanikant, T. Jagadeesha, J. Das, J. Aust. Ceram. Soc. 57 (2021) 107–116. https://doi.org/10.1007/s41779-020-00517-6.

[24] Jahan, F. Mustapha, M. Y. Ismail, S. M. Sapuan, M. Bahraminasab, Mater. Des. 32 (2011) 1215–1221. https://doi.org/10.1016/j.matdes.2010.10.015.

[25] M. Soundarrajan, R. Thanigaivelan, In Advances in Micro and Nano Manufacturing and Surface Engineering, Springer, Singapore (2019), p. 423–434.

[26] Pramanik, Int. J. Mach. Tools Manuf. 86 (2014) 44–61. https://doi.org/10.1016/j.ijmachtools.2014.07.00.

[27] H. Majumder, K. Maity, Measurement. 118 (2018) 1–13. https://doi.org/10.1016/j.measurement.2018.01.003.

[28] K. Matsuzawa, S. Oka, M. Uchiyama, Procedia CIRP. 113 (2022) 483–487. https://doi.org/10.1016/j.procir.2022.09.204.

[29] J. Wang, W. Natsu, Precis. Eng.77 (2022) 307–319. https://doi.org/10.1016/j.precisioneng.2022.06.012.

[30] Z. Ge, W. Chen, Chin. J. Mech. Eng. 35 (2022) 98. https://doi.org/10.1186/s10033-022-00752-x.

LOGANATHAN GOKULANATHAN[1]

JEGAN ANNAMALAI[2]

Department of Mechanical Engineering, Sona College of Technology, Salem, Tamil Nadu, India

AVS College of Technology, Salem

NAUČNI RAD

EKSPERIMENTALNO ISTRAŽIVANJE ELEKTROHEMIJSKE MIKRO OBRADE LEGURE MONEL 400 KORIŠĆENJEM ELEKTROLITA SA ČESTICAMA

Konvencionalna mašinska obrada izuzetno tvrdog materijala zahteva veliku energiju. Zbog toga se preporučuje tehnika obrade bez naprezanja, bez ivica i visoke preciznosti, kao što je elektrohemijska mikro obrada (sa dodatnim funkcijama. Da bi se poboljšala efikasnost, koriste se različiti elektroliti, kao što su elektroliti sa magnetima, elektroliti sa metalnim česticama i elektroliti sa ugljeničnim peletama (CPME). Mikro-rupe su izbušene u radnom materijalu, tj. legui MONEL 400. Parametri istraživanja su tip elektrolita, koncentracija (g/l), napon obrade (V) i radni ciklus (%). Rezultati elektrohemijske mikro obrade se procenjuju putem brzine uklanjanja materijala u µm/sec i prekoračenja u µm. Rezultati su optimizovani korišćenjem višeciljne optimizacije zasnovane na analizi odnosa i višekriterijumske optimizacije i kompromisnog resenja. Obe tehnike određuju iste optimalne parameter: 18ti eksperiment CPME, radni ciklus 50%, napon obrade 11 V i koncentracija elektrolita 28 g/l. To je najbolje optimalno parametarsko rešenje za mašinsku obradu. ANOVA je pokazala da oba tipa elektrolita doprinose performansama obrade sa 62,6% i 60,37%. Štaviše, skenirajućim elektronskim mikroskopom pregledane su mikro rupe da bi se proširio efekat različitih elektrolita na obrađene površine.

Ključne reči: ugljenične pelete, višeciljna optimizacija zasnovana na analizi odnosa, višekriterijumska optimizacija i kompromisno resenje, elektrohemijska mikro obrada , metalne čestice, magnet.